Titre: Title:	Flow and heat transfer Analysis in Granular beds for Injection Molding
Auteur: Author:	Yixun Sun
Date:	2021
Type:	Mémoire ou thèse / Dissertation or Thesis
Référence: Citation:	Sun, Y. (2021). Flow and heat transfer Analysis in Granular beds for Injection Molding [Ph.D. thesis, Polytechnique Montréal]. PolyPublie. https://publications.polymtl.ca/10250/

POLYTECHNIQUE MONTRÉAL

affiliée à l'Université de Montréal

Flow and Heat Transfer Analysis in Granular Beds for Injection Molding

YIXUN SUN

Département de génie mécanique

Thèse présentée en vue de l'obtention du diplôme de *Philosophiæ Doctor*

Génie mécanique

Décembre 2021

POLYTECHNIQUE MONTRÉAL

affiliée à l'Université de Montréal

Cette thèse intitulée :

Flow and Heat Transfer Analysis in Granular Beds for Injection Molding

présentée par **Yixun SUN**

en vue de l'obtention du diplôme de *Philosophiæ Doctor*

a été dûment acceptée par le jury d'examen constitué de :

Njuki MUREITHI, président
François TROCHU, membre et directeur de recherche
Brahim BENMOKRANE, membre et codirecteur de recherche
Philippe CAUSSE, membre et codirecteur de recherche
Sébastien LECLAIRE, membre
Cyprien SOULAINE, membre externe

ACKNOWLEDGEMENTS

I would like to express my warmest and deepest thanks to my supervisor Professor François Trochu, who offered me the opportunity to come to Canada and carry out this work. He always guided me so positively and always made me feel confident in my abilities to overcome challenges throughout my PhD. This work would not have been possible without his support and expert advice.

I would also wish to express my gratitude to my co-supervisors, Professor Philippe Causse, Professor Cédric Béguin and Professor Brahim Benmokrane for their continuous support, valuable suggestions and constructive feedback which have contributed greatly to the improvement of the research project.

My sincere thanks also goes to Christian-Charles Martel, the technical staff of SDI-Plomberie, Wei Huang, Bin Yang, Sami Hillal, Zaynab Grofti, Yuwei Feng, Lingyu Yue and Xiao Fan for all the support provided, no matter in research or in daily life. Polytechnique Montréal is also acknowledged in providing the access to the laboratories, libraries, and sports facilities.

Finally, special thanks goes to my wife. Xuewei, thank you for giving me the courage during this tough journey and thank you for your continuous support and love. My thanks are extended to my parents who have no doubt supported me in every possible way since I was born.

RÉSUMÉ

Dans la fabrication de composites, des moules avec capacité de chauffage et refroidissement intégrés ont été développés au cours des dernières années pour éviter l'utilisation de l'autoclave ou de fours en raison des limitations de taille et de coût. Cette thèse étudie un concept innovant pour la conception de tels moules à base de matériaux granulaires. La surface du moule est conçue pour être chauffée ou refroidie en passant un fluide à travers le matériau granulaire contenu dans le boîtier du moule. Ce concept présente des avantages en termes de réduction des coûts d'outillage et permet de fabriquer des pièces de géométrie complexe. De plus, l'écoulement à travers le matériau granulaire peut fournir un chauffage plus continu et uniforme de la cavité de moulage que les moules utilisant des sources de chauffage linéaires comme des conduites avec liquide caloporteur ou des éléments résistifs.

La performance du chauffage doit être étudiée pour ce nouveau concept d'outillage. À cette fin, des simulations numériques seront effectuées avec la méthode de *Reynolds-Averaged Navier-Stokes* (RANS) en *Computational Fluid Dynamics* (CFD), qui fournit une description raisonnable des phénomènes de transport moyen dans les milieux poreux sans demander trop de ressources de calcul. Cependant, cela reste un défi car la présence d'une paroi pose deux problèmes principaux dans la modélisation. Premièrement, la porosité change rapidement près de la paroi. Différents modèles de porosité ont été proposés pour effectuer des simulations RANS-CFD, mais sans règles spécifiques pour sélectionner un modèle. Deuxièmement, les variables calculées par moyenne volumique dans les milieux granulaires ne correspondent pas aux valeurs ponctuelles définies sur la paroi, par exemple les valeurs de température à l'interface entre la paroi et le milieu granulaire. Cet obstacle empêche de définir correctement des conditions aux limites pour la simulation numérique.

Cette thèse propose un cadre général de modélisation de l'écoulement et du transfert de chaleur dans des milieux granulaires confinés par une paroi solide, qui permet d'étudier numériquement la performance de chauffage des moules. Cet objectif est atteint à travers la préparation des 5 articles suivants (dont un article en deux parties) :

1. Une nouvelle méthode de caractérisation de la perméabilité est proposée dans l'Article 1, appelée « *modified falling head test* ». Par rapport à la méthode conventionnelle, cette approche permet d'élargir la plage de l'essai et permet de mesurer la perméabilité de matériaux

granulaires de perméabilité de l'ordre de 10^{-8} m^2. Cette étude montre que l'équation d'Ergun revisitée prédit la perméabilité avec précision, et permet donc de calculer la perte de charge à travers le milieu granulaire.

2. La première partie de l'Article 2 résout deux problèmes critiques précédemment mentionnés : la détermination du profil de porosité et l'incompatibilité des variables physiques définies à l'interface avec la paroi. On dérive les équations qui gouvernent l'écoulement et le transfert de chaleur pour un volume élémentaire représentatif non constant (« *Representative Elementary Volume* » - REV).

3. Dans la partie 2 de l'Article 2, les équations qui gouvernent l'écoulement et le transfert de chaleur sont validées expérimentalement en comparant des mesures expérimentales de la température et du flux de chaleur avec les prédictions numériques. Une analyse plus détaillée montre l'importance de modéliser la turbulence, qui joue ici un rôle critique, particulièrement près de la paroi.

4. À partir des équations dérivées et validées à l'Article 2, une étude paramétrique est présentée dans l'Article 3 pour analyser l'effet de différents paramètres de conception dans un tube chauffé rempli de billes. Pour raccourcir le temps nécessaire pour atteindre l'uniformité de la température, la réduction de l'épaisseur en paroi ou l'utilisation de matériaux à faible capacité thermique jouent un rôle majeur.

5. Dans le cadre de modélisation développé dans les études précédentes, l'Article 4 étudie par simulation numérique les moules granulaires pour deux matériaux du moule : un matériau polymère renforcé par des fibres et l'aluminium. On peut vérifier que la température de la surface du moule devient uniforme dans un délai raisonnable dans les deux cas pour des conditions d'essai réalistes. Cela est comparable aux outils chauffants conventionnels avec des conduits.

Avec les méthodes numériques et expérimentales développées dans cette thèse, le concept innovant d'outillage chauffé à base de matériaux granulaires a pu être étudié dans le but de développer des applications. Les résultats confirment la performance de cette méthode de chauffage et favorisent des développements ultérieurs.

ABSTRACT

In composite manufacturing, a number of heated tools were developed over the past decades to avoid the use of autoclaves or ovens due to size and cost limitations. This thesis investigates an innovative concept of heated tool based on granular materials. The mold surface is designed to be heated or cooled by circulating a fluid through the granular material packed in the mold case. This concept has advantages in saving tooling costs and allows conforming parts of complex geometry. Furthermore, the flow through the granular material can provide a more continuous and uniform heating of the part than molds using discrete heating sources like ducts or resistive wires.

The heating performance needs to be examined for this new tooling concept. To do this, *Reynolds-Averaged Navier-Stokes* (RANS) *Computational Fluid Dynamics* (CFD) simulations will be performed. This method provides a reasonable description of the averaged transport phenomena in bead packings without too much computational resources. However, this remains a challenge because the presence of bounding walls causes two main issues in modelling. Firstly, the porosity changes rapidly near the wall. Various porosity models were proposed to conduct CFD simulations, without systematic guidelines to assist in selecting one. Secondly, volume-averaged variables in bead packings don't match with the pointwise wall values (e.g., wall temperature values) at the interface between the wall and the granular bed, which prevents from defining proper boundary conditions.

This thesis aims to propose a general modelling framework for the flow and heat transfer in wall-bounded granular beds, which allows studying numerically the heating performance of granular based molds. The objectives are achieved through 5 articles (including an article of two parts) as follows:

1. A new permeability characterization method is proposed in Article 1, called the "modified falling head test". Compared with the conventional one, it enlarges the test range, which allows measuring bead packings of relatively large permeability ($\sim 10^{-8}$ m^2). The result shows that the revisited Ergun's equation predicts permeability accurately, which yields the pressure drop through the granular bed.
2. Part 1 of the Article 2 addresses the two above-mentioned critical issues: determination of the porosity distribution in the packed bed and incompatibility of physical parameters defined at

the boundary. This is done by deriving equations governing the flow and heat transfer with a non-constant *Representative Elementary Volume* (REV).

3. In part 2 of Article 2, the governing equations are validated experimentally by comparing with the temperature and heat flux measurements. A more detailed analysis emphasizes the importance of modelling turbulence especially near the wall.
4. Based on the equations derived and validated in Article 2, a parametric study is presented in Article 3, which analyzes the effect of different design parameters in a heated pipe filled with beads. To shorten the time required to reach temperature uniformity, reducing the wall thickness, or using low thermal inertia wall materials play a key role.
5. In the framework developed in previous studies, Article 4 investigates also numerically granular based molds containing beads with two types of mold casings made of *Fiber Reinforced Polymers* (FRP) and aluminum. The temperature of the mold surface with the part is shown to reach uniformity within a reasonable time in both cases under realistic test conditions. This time is comparable to that of conventional heated tools with ducts.

With the numerical and experimental methods developed in this thesis, the innovative concept of heated tool containing granular materials is studied. The results confirm the heating performance and fosters further developments.

TABLE OF CONTENTS

LIST OF TABLES

LIST OF FIGURES

CHAPTER 1 INTRODUCTION

Composite materials are composed of at least two elements to obtain properties that are superior to each of its components. Composites can be divided into three main families [1]: *Polymer Matrix Composites* (PMC), *Metal Matrix Composites* (MMC) and *Ceramic Matrix Composites* (CMC). Among these three types of materials, PMC, also known as *Fibre Reinforced Polymers* (FRP) have experienced a strong growth in different industrial fields in recent years. Structures made of FRP are lighter and possess a high rigidity and strength. The resin used in FRP is usually a thermosetting polymer. The initial state of these types of resin is usually liquid monomers or a mixture with additives (e.g., hardener, catalyst). As temperature increases, chemical reactions take place. The monomers begin to grow by building 3D cross-linked networks and become polymers. This irreversible chemical reaction is known as resin polymerization. A full and uniform cure of the resin represents a critical issue in high-performance composites to create structures with optimal mechanical properties. For that purpose, temperature must be controlled properly and as uniformly as possible in the mold cavity.

1.1 Heating methods

One commonly used approach consists of heating the composite part indirectly via gas (e.g., nitrogen) circulation inside an autoclave or an oven, which is well known and has been widely used [2, 3]. It allows curing composite parts of any shape, but with a limitation of size. As advanced composites gradually replace traditional materials in aircraft, vehicles and even infrastructure, composite parts are getting much larger. As a result, the size of autoclaves never seems large enough to process parts such as aircraft wings or wind blades. Meanwhile, the cost to acquire and operate large autoclaves is significantly expensive [3-6]. In fact, the effort to find alternative methods to autoclave went on for decades and various mold heating technologies have been developed and implemented for that purpose. Many of them embed heating elements in the mold and heat the part directly through its surface using heat transfer fluids, electrical circuits or magnetic induction, etc. These mold heating methods will be reviewed in detail in the next chapter. Progoulakis [7] reported a cost comparison (Table 1.1) between a heated tool using resistive heaters

and traditional methods (autoclave or oven) to fabricate a 12-metre-long composite wing spar. This clearly demonstrates the huge savings in cost of using heated tools.

Compared with other out-of-autoclave heating methods, using heat transfer fluids comes up with two main advantages: it is easy to control the maximum temperature and the heating system can be used ‘reversely’ for cooling [8]. The commonly used method is to have a heat transfer fluid flowing through ducts embedded (or drilled) in the mold. The disadvantages include the relatively high expenses of drilling in metallic molds to install ducts and maintaining the heating system. In addition, the pipe lines cannot always follow the shape of complex parts [9]. A more detailed analysis will be presented in the sequel.

Table 1.1 Cost comparison (negative percentage value indicates cost savings for heated tools) [7]

Cost data	Comparison of processing options	
	Heated tool / Autoclave	Heated tool / Oven
Estimated power requirements (kW)	-96%	-80%
Operating cost £/hour	-70%	-60%
Procurement costs (£)	-97%	-82%
Pre-production requirement costs (£)	+15%	+15%
Production requirements costs (£)	-18%	+1%

1.2 Granular mold

To overcome some of the limitations of heated tools while keeping the advantages of using a heat transfer fluid, a novel mold concept based on granular materials was proposed. The idea was tested by Désilets [10] (Figure 1.1). Note that patents were also taken on this topic by Borland [11, 12]. The idea is to fill the mold with solid particles to form a porous medium instead of using a solid material. It is covered by a rigid skin reproducing the shape of the molded part. The skin can be heated or cooled by circulating a fluid through the granular bed. This results in significant savings on tooling because a ribbed tool or a full steel mold with embedded heating and cooling ducts are no longer necessary. Besides, granular molds come with advantages in terms of geometrical conforming and improvements in thermal uniformity. This will be presented in detail in Chapter 2

after limitations of existing mold heating methods will have been clearly summarized. This analysis will help to understand better the improvements brought by granular materials.

Despite the early study performed by Désilets [10], predicting and controlling the temperature in a granular mold remain a challenge. As a new technique, the thermal performance of granular molds has not yet been analyzed. Therefore, our goal will be to verify if this new technology can be successfully applied in composite manufacturing based on injection molding.

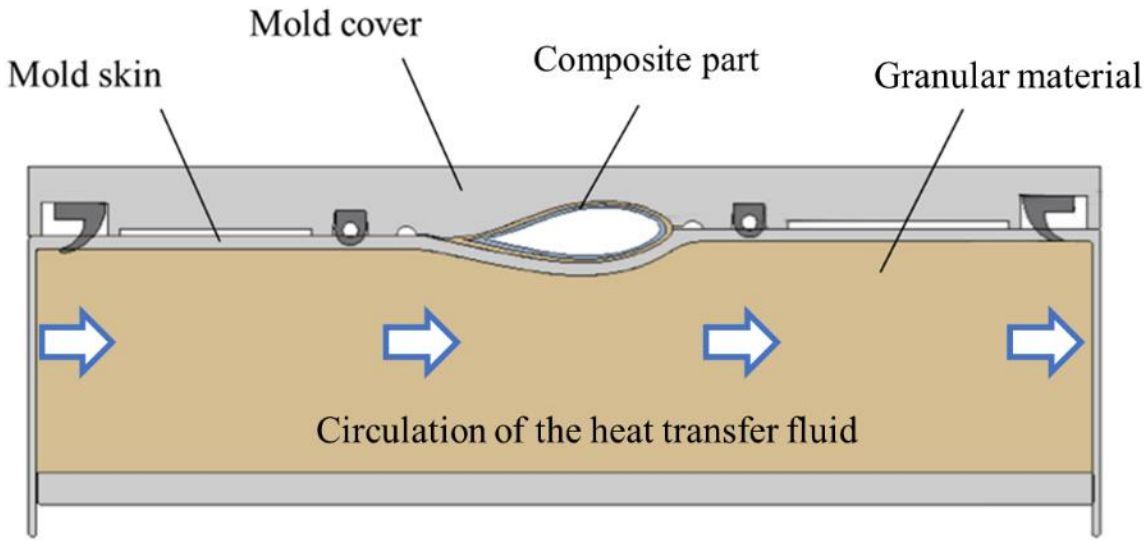

Figure 1.1: Schematics of a typical granular mold (adapted from [10]).

CHAPTER 2 LITERATURE REVIEW

As mentioned in the previous chapter, several mold heating methods other than autoclave or oven based were developed to circumvent size limitations and reduce fabrication costs. In the first part of the literature review, different mold heating techniques will be presented. Summarizing their respective advantages and limitations will help better understand the improvements brought by granular molds. Secondly, studies on flow and heat transfer in granular porous media will be reviewed to analyze key issues connected with modelling and predicting the temperature evolution in granular molds.

2.1 Mold heating techniques

2.1.1 Resistance heating

The resistive heaters use electrical current to generate heat. Cartridge heaters are commonly used resistive heating elements in molds. This type of heater is normally built in the shape of a rod and embedded in the mold [9] (Figure 2.1a). An example of a typical structure is given in Figure 2.1b, which consists of a container pipe, electrical insulation fillers and heating wires. These heaters are usually standard components, which gives a cost-effective solution for molds of simple geometry. Difficulties appear in molds of complex shape, since drilling holes and setting ducts following the mold contour are not easy tasks. Another important issue is temperature control. Brocks et al. [13] used cartridge heaters of 5 mm diameter for a RTM mold. They showed that the maximum temperature can reach up to 700 °C with electrical power of ~4000 W at 220 V. Therefore, cartridge heaters must be controlled in temperature with proper thermal contact with the mold to prevent overheating or burning out of the mold.

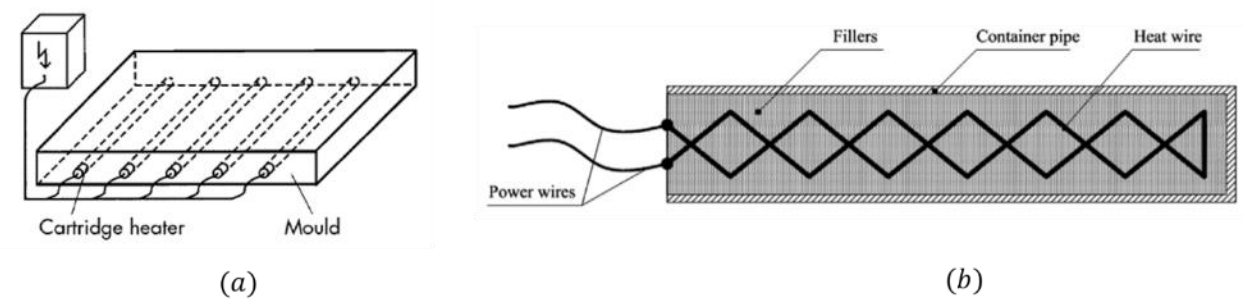

Figure 2.1: Cartridge heaters: (a) a schematic of the mold [9]; (b) a typical structure [14].

The TCX heating technology creates heating elements by spraying melted resistive elements on a coated substrate [15]. Smith et al. [16] cured prepregs using the *Vacuum-Bag-Only* (VBO) process with a flat aluminium tool (Figure 2.2). The heating elements were sprayed on the underside of the plate, so they were not in contact with the molded part. They showed that this method can achieve a faster heating ramp (50 °C/min) than conventional ovens (~6 °C/min), but large through-thickness thermal gradients appear since it is only heated from one side. They suggested to add an insulation layer on top of the laminate to mitigate this problem.

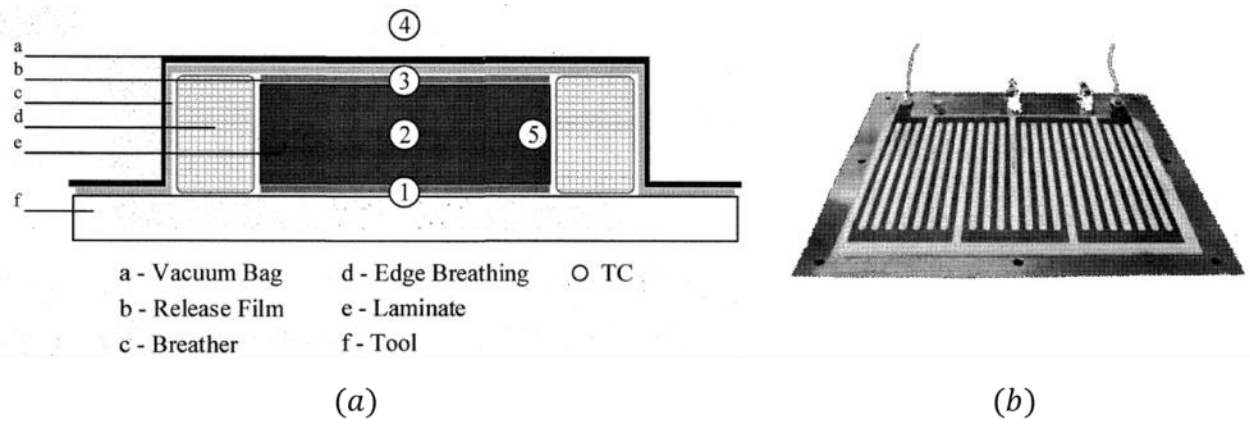

Figure 2.2: Experimental setup of heated tool with TCX heaters: (a) bagging configuration; (b) the underside of the tool plate [16].

The *Coal-based carbon foam* (CFOAM) was developed in the early 1990s by Touchstone Research Laboratories [17]. This material is rigid, light, electrically and thermally conductive, which makes

it suitable for heated tools. A typical structure is shown in Figure 2.3a where the CFOAM heating elements were adhesively bonded together with different layers. Blacker et al. [18] examined two molds: a flat mold (Figure 2.3b) and a mold of complex geometry (Figure 2.3c). The thermal performance of both heated tools was evaluated via curing tests. The results showed that both molds can provide a good thermal uniformity and cured composite parts were comparable to oven-cured ones in terms of mechanical properties. As all the layers are bonded together, shortcomings lie in managing joints between layers especially for molds of complex shape.

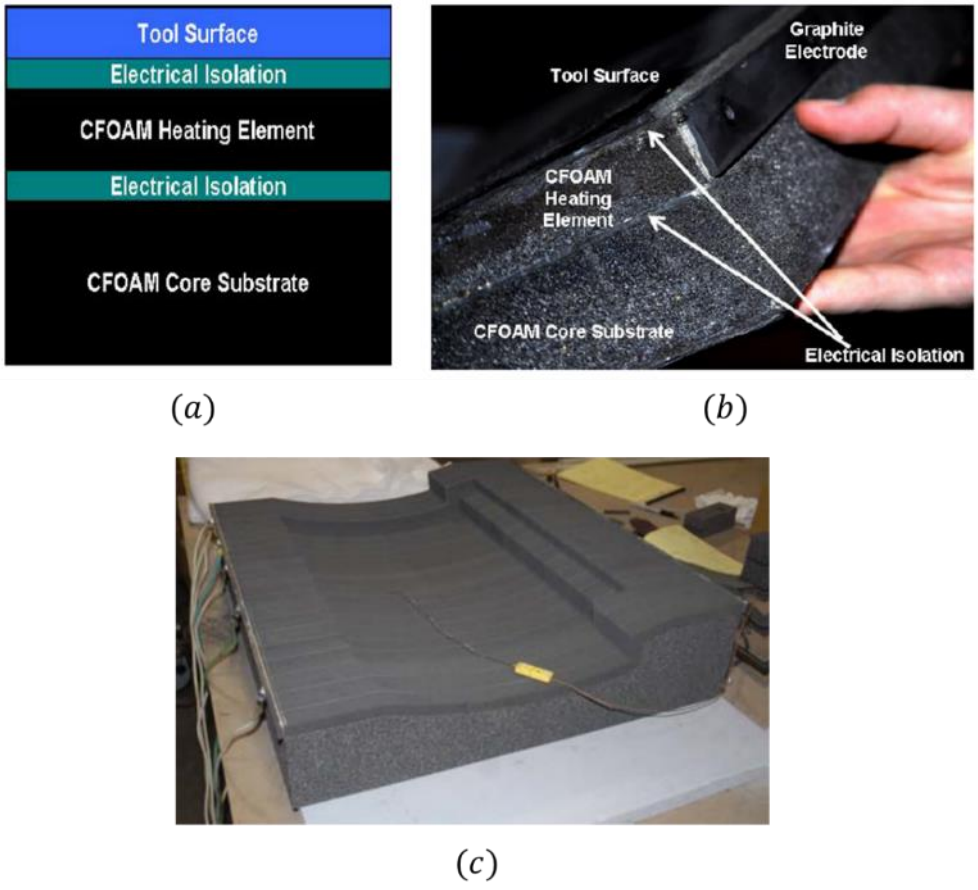

Figure 2.3: CFOAM heated tool: (a) schematic of the mold structure; (b) mold of flat surface; (c) mold of complex geometry [18].

2.1.2 Thermal fluid heating

Most heating systems use injected liquids as heat transfer fluid through ducts (or channels) embedded (or drilled) in the mold. The main advantage of this technique, contrary to electrical heating, lies in the additional capability of cooling down the composite part after cure (and not only heating up the mold). This reduces the cycle time and increases productivity. It is also useful in plastic manufacturing because molten plastic needs to solidify in the mold cavity [19]. For this reason, several studies combined cooling channels with resistive (or inductive) heaters to improve the overall efficiency (Figure 2.4) [14, 20, 21]. However, the presence of cooling channels affects the temperature uniformity during the heating process [20].

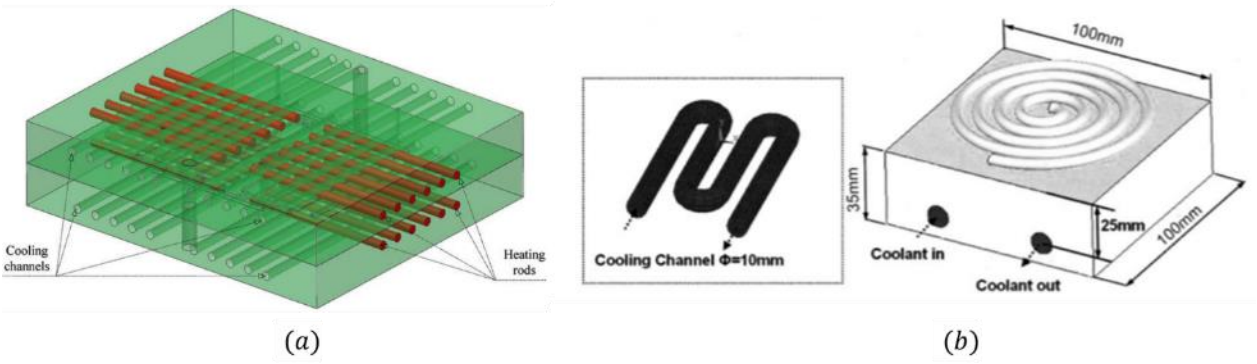

Figure 2.4: Combination of heating elements and cooling channels: (a) resistive heating rods [14]; (b) inductive coil in a spiral shape [21].

Abdalrahman et al. [22] studied numerically the heating performance of molds with heating ducts. Different channel layouts (Figure 2.5a) and shapes of duct cross-section (Figure 2.5b) were examined. The results show that the cross-sectional profile has little effect, while parallel layout is the most efficient way of heating. An oil-based heating system with parallel channels was studied by Ding et al. [23]. They showed that the time to reach thermal uniformity mainly depends on the flow rate. Compared with laminar flows (Re=2300), using a fully turbulent flow (Re=10000) leads to a much shorter heating time. There are disadvantages in molds with ducts, including tooling costs for installation and repair, considerable heat loss along the pipes [9] and difficulty to follow the shape of complex parts [10].

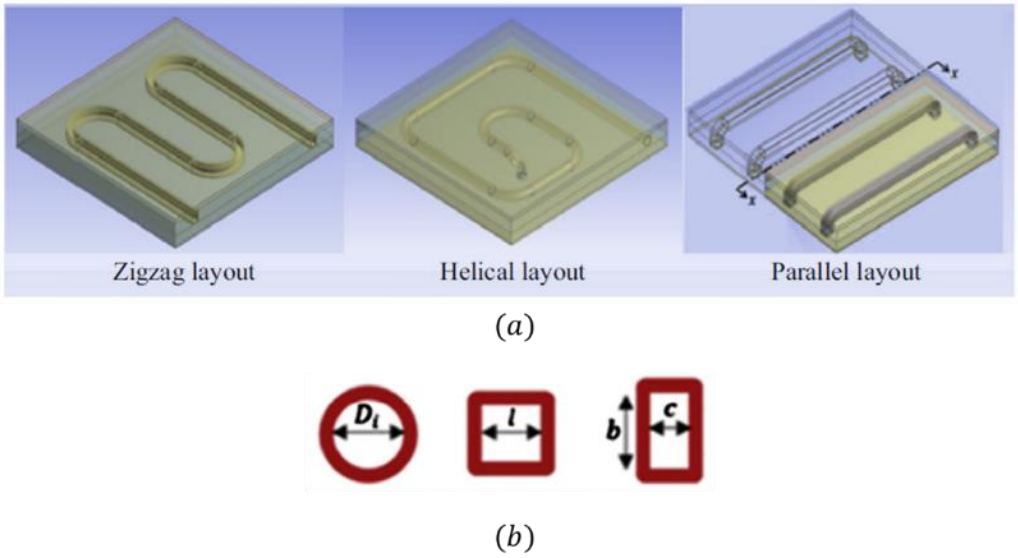

Figure 2.5: Numerical models of different heating systems: (a) channel layouts; (b) geometry of channel cross-section [22].

Apart from heating ducts, the idea of using flexible membranes has been explored and implemented in some heating systems. One main advantage of such structures consists of saving tooling costs since a solid mold is not necessary. A typical structure of a Quickstep mold with flexible membranes is shown in Figure 2.6. The molded part is confined in a pressurized chamber with a heat transfer fluid. Coenen et al. [24] showed a saving of 50% in cycle time and a tooling cost reduction of 82% compared to an autoclave. Davies et al. [25] showed that the mechanical properties of a part cured by Quickstep is similar to autoclave processed parts. Despite this, the size of the part is still limited to the pressure chamber. The stability of the system is another concern. When adapting this technology to some fabrication process (e.g., RTM) which requires high pressure, the flexible membrane deforms and causes instabilities in the resin flow resulting in improper filling of the cavity.

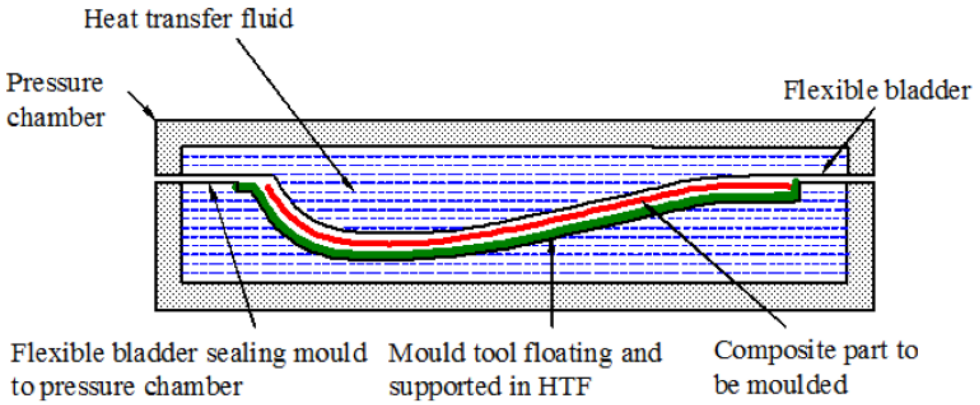

Figure 2.6: Schematics of the Quickstep process [26].

Another technology with flexible membrane is Flexible Injection [27]. This technique was especially devised for *Liquid Composite Molding* (LCM). A mold with a double cavity separated by a deformable membrane is shown in Figure 2.7a. The reinforcement is placed in the lower cavity, and the resin injected from the inlet port in the bottom cavity. Then a heated compaction fluid is injected from the top inlet to heat the part (Figure 2.7b) and complete the impregnation of the dry reinforcement by the resin, while compacting the saturated portion of the part. Studies showed that this method can reduce tooling costs and improve part quality [28, 29].

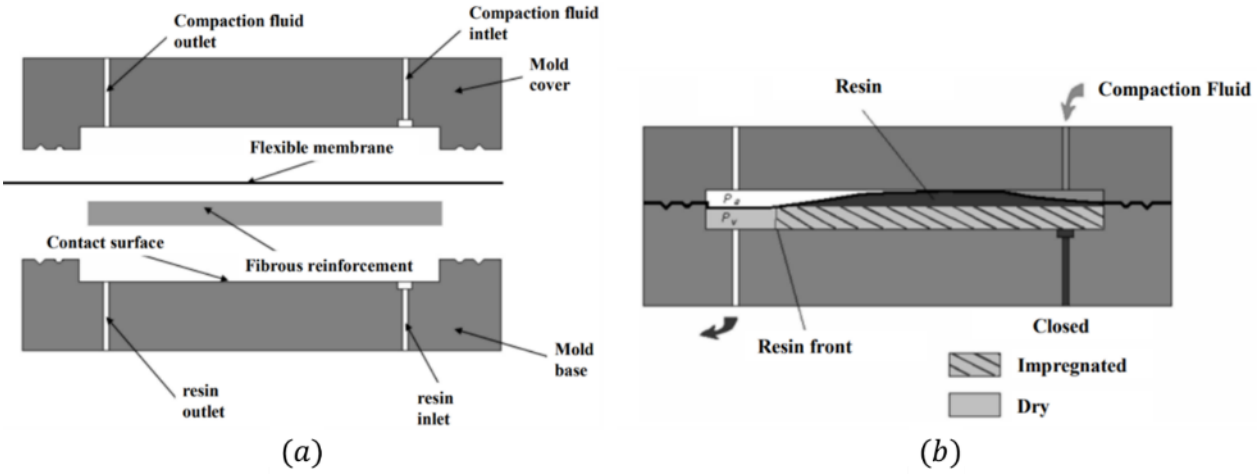

Figure 2.7: Schematics of Flexible Injection (FI): (a) mold components; (b) injection of resin and compaction fluid [29].

2.1.3 Induction heating

Inductive mold heating is achieved by applying alternating current to the induction coil. This creates an electromagnetic field around the coil inducing eddy currents to heat the mold. The coil can be placed inside the mold (i.e., internal inductor, Figure 2.8a) or above the mold surface (i.e., external inductor, Figure 2.8b). The main advantage is the fast heating rate. Chen et al. [21] showed that an AISI 4130 steel mold of 100×100×35 mm^3 (Figure 2.4b) can be heated at ~22.5°C/s with power supply of 1kW of the induction coil. The disadvantage is the high cost of the induction equipment, especially for large molds where high-power induction devices with long coils are needed [9, 30]. This heating method was adapted to the RTM process by RocTool [31]. The molded part is heated by the inductors and cooled by cooling channels (Figure 2.9). A lid is added to create a pressurized chamber, which can 'press' the part during the process. Because of the lid, the maximum size of the part is limited to 6 m^2 [32].

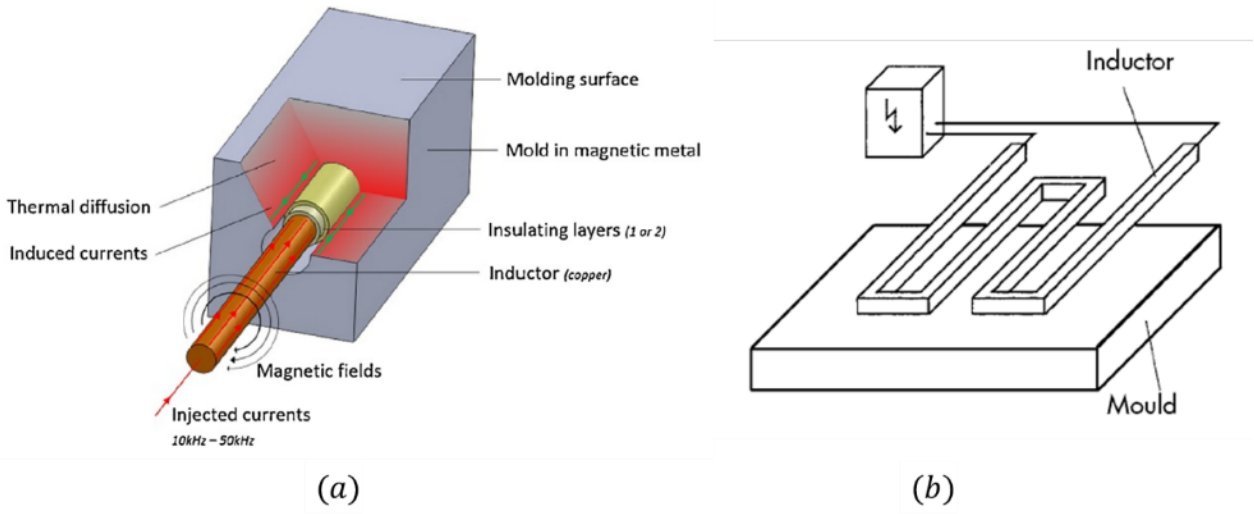

Figure 2.8: Mold structure with induction coil: (a) internal inductor; (b) external inductor [31].

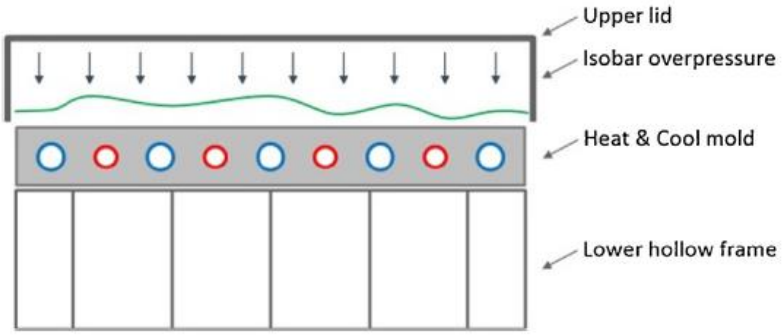

Figure 2.9: RocTool inductive heating technique for RTM [31].

2.1.4 Summary

Several mold heating methods have been reviewed in this section. They were developed because of high tooling costs connected with autoclaves or ovens. These methods heat the molded part directly through the mold surface other than via gas circulations. This increases heating efficiency. However, some drawbacks remain, which can be summed up as follows:

- Several heating elements are made in the shape of a rod and are embedded in the mold, such as heating ducts, resistive heating rods and induction coils. This usually requires drilling high-quality channels that follow the shape of the molded part. For molds of large size and complex geometry, this is not easy to achieve. In addition, installation of the system and repair come with significant costs.
- Heating layers (e.g., CFOAM) increase the uniformity of surface temperature compared with discrete heating elements. However, they bring benefits to molds of simple geometry and are not unsuited for complex shapes because of the difficulty of managing joints between bonded layers.
- Both resistive and inductive heating elements cannot be used to cool the mold. Although cooling ducts can be added, they affect temperature uniformity.
- Due to high heating ramps, the surface temperature of molds using inductive or resistive heaters must be carefully monitored to prevent overheating. Additional protective layers of electrical isolation are also necessary.

Among these methods, using heat transfer fluids comes with advantages to control the maximum temperature and can be used ‘reversely’ for cooling. As mentioned above, granular molds heat the part using a fluid, which keeps these two advantages. Secondly, the same granular chamber can be reused to make different parts by replacing only the rigid mold skin. This represents huge potential savings in terms of tooling costs. The geometrical conforming problem can also be solved because the granular material packed in the chamber can easily follow the geometry of a molded part. Furthermore, with granular mold fillers, no pipework is needed. Compared with a Quickstep mold, granular mold fillers can provide enough support for the mold skin to sustain high pressure. This feature opens up potential applications in RTM. Finally, continuous flow lines through the granular bed can also improve the heating uniformity without having joint problems like with heating layers.

2.2 Flow and heat transfer in wall-bounded granular beds

In the previous section, different mold heating methods have been reviewed and the improvements brought by the novel concept of granular molds have also discussed. Although this new heating approach is promising, its thermal performance needs to be investigated. Numerical simulation is a powerful and cost-effective tool to assist in this investigation. To perform numerical simulations, the fundamental flow and heat transfer problems in granular porous media need to be understood. Secondly, a key issue consists of modelling the heat exchange between the granular bed and the solid mold skin. At the pore scale, physical variables defined in the flow such as fluid pressure, velocity and temperature are not uniform. In fact, these variables are highly influenced by the microstructure of the granular porous medium. Due to the complex geometry of pores, macroscopic models based on volume averaging have been widely adopted to analyze transport processes in porous media for practical applications [33]. In this approach, the transport equations are integrated and averaged over a *Representative Elementary Volume* (REV) (Figure 2.10). As a result, the packing structure is not modelled explicitly and aggregate pore-scale transport processes are described through various effective parameters, such as porosity, permeability, averaged particle size, etc. The size of a typical REV should be large enough to obtain meaningful averaged values, but small enough compared with the whole calculation domain [34]. A more detailed discussion on REVs and spatial averaging of transport equations is given in Chapter 5.

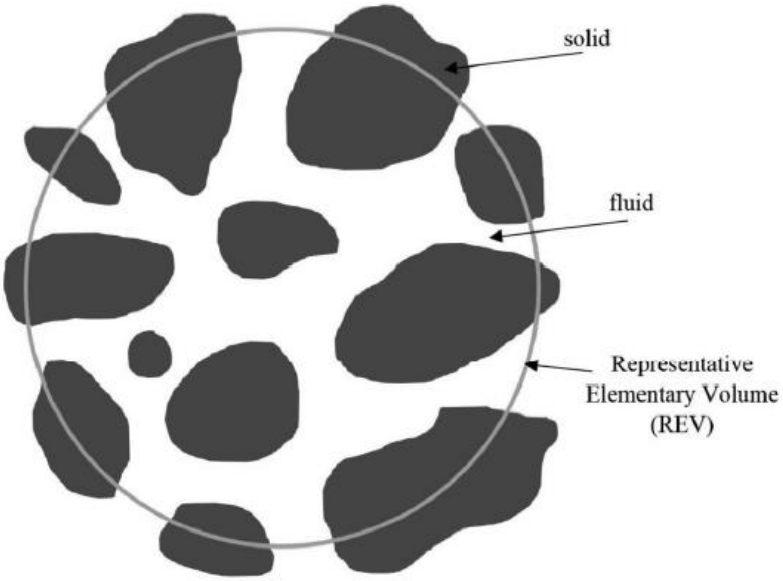

Figure 2.10: A typical REV used for spatial averaging in granular porous media [35].

2.2.1 Pressure drop through granular beds

As fluids flow through a granular bed, pressure drop appears due to the resistance created by the presence of granular materials. As shown in the macroscopic model in Chapter 5, the fluid flow is modelled by adding a source term (i.e., the pressure gradient induced by the granular material) to the standard volume-averaged momentum equation. It is therefore important to predict this pressure gradient. Darcy's law writes the pressure gradient ∇P as a function of superficial velocity v, permeability K and dynamic viscosity μ:

$$-\nabla P = \frac{\mu}{K}\, v \tag{2.1}$$

This equation was originally formulated from the famous experiment of Darcy [36]. The range of validity of Eq. (2.1) can be assessed by computing Reynolds number (Re):

$$\mathrm{Re} = \frac{\rho_f\, v\, L}{\mu} \tag{2.2}$$

where L is a characteristic length of the porous medium, and ρ_f is the fluid density. Darcy's law is considered as valid for Re lower than 10 [37]. An alternative correlation to Darcy's law was

proposed by Brinkman [38]. This equation includes the Darcy term and a Laplacian term like in Navier-Stokes equation:

$$\nabla P = -\frac{\mu}{K} v + \tilde{\mu}\, \nabla^2 v \tag{2.3}$$

where $\tilde{\mu}$ is the effective viscosity and Brinkman simplifies it as the fluid viscosity μ for practical use [33]. However, this is generally not true. Givler and Altobelli [39] showed the value of $\tilde{\mu}$ can be 7.5 times larger than μ at Re=17. The domain of validity of Brinkman's equation is quite restricted and a clear experimental checking is still missing [40].

For high Reynolds numbers, a nonlinear relationship exists between ∇P and v. Forchheimer [41] suggested that in this case an inertial term should be added to Darcy's equation:

$$-\nabla P = \frac{\mu}{K} v + \rho_f \beta v^2 \tag{2.4}$$

where β is the inertial factor. The value of β is determined experimentally. In 1952, Ergun [42] proposed the following equation for bead packings:

$$\nabla P = A \frac{(1-\phi_V)^2}{{\phi_V}^3} \frac{v\,\mu}{d_s^2} + B \frac{(1-\phi_V)}{{\phi_V}^3} \frac{v^2 \rho_f}{d_s} \tag{2.5}$$

where ϕ_V is the void fraction of the granular bed, d_s is the averaged particle diameter and A, B are empirical constants. Ergun's equation originates from Darcy's law and Kozeny-Carman equation [37]. Ergun suggested to take the values of A and B as 150 and 1.75 respectively, whereas Macdonald et al. [43] suggested 180 and 1.8 in the "revisited Ergun's equation".

We note that the knowledge of the coefficient with the linear velocity term is indispensable to predict the pressure gradient, no matter the value of Re, i.e., the permeability k for Eq. (2.1), Eq. (2.4) and Eq. (2.3) or the empirical constant A for Eq. (2.5). Two experimental methods are commonly used to characterize this coefficient: the constant head and the falling head methods. The first one measures the flow rate through the test material under a constant inlet pressure. To do this, liquid is supplied to the test rig with control of the inlet pressure [44]. The second method measures the flow rate under a variable pressure head. The falling head test is easier to implement and preferable for in-situ measurements. However, it has some limitations in terms of measurement range (usually for $K < 10^{-10}$ m^2) [45], which is only suited for packed beds with small grains. On the other hand, there is no range limitation in the constant head test, but it requires a more complex

experimental setup. In addition, it is not suited for in-situ measurements. A more detailed literature review and discussion on this topic will be presented in Article 1 (see Chapter 4).

2.2.2 Flow channeling and packing structure

For a typical wall-confined randomly packed granular bed, the flow velocity is not constant over the cross-section. Near the wall, the flow velocity increases, which is referred to as flow channeling (or wall channeling) [46]. Schwartz and Smith [47] measured the radial cross-sectional velocity profile (Figure 2.11) of a packed bed confined in a cylindrical pipe using a set of pitot tube anemometers. They mentioned that the variation of velocity is induced by the packing structure and influences the heat and mass transfer. Guo et al. [48] stated that additional turbulent energy can be generated due to an increase in velocity causing a higher heat transfer rate near the wall. It is therefore important to understand the packing structure.

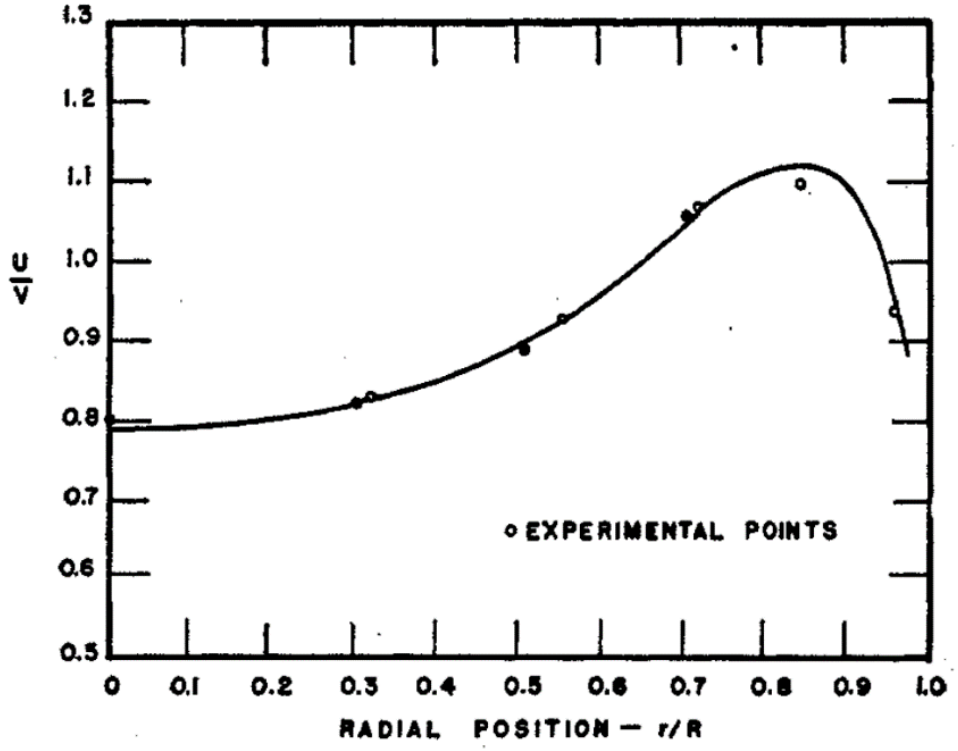

Figure 2.11: Radial velocity profile for a monodisperse granular bed (d_s = 0.25 inches) confined in a cylindrical pipe of 4 inches diameter (x-axis: dimensionless radial position, 0 is the bed center and 1 is at the wall; y-axis: local velocity over the superficial velocity; the solid line is the curve fitted to experimental data) [47].

A typical packing structure is shown in Figure 2.12 where the particle centers are projected onto the bottom plane. The particles which are immediately adjacent to the wall tend to form a structured circular layer. The next layer forms on the surface of the first layer and becomes less ordered. Then the successive layers are less and less ordered, and finally a fully random arrangement is achieved in the center area of the packing [49]. This explains the experimental results (Figure 2.11): the velocity tends to be constant towards the center as the packing structure becomes random. The liquid flows more easily through the gaps between the ordered layers located near the wall.

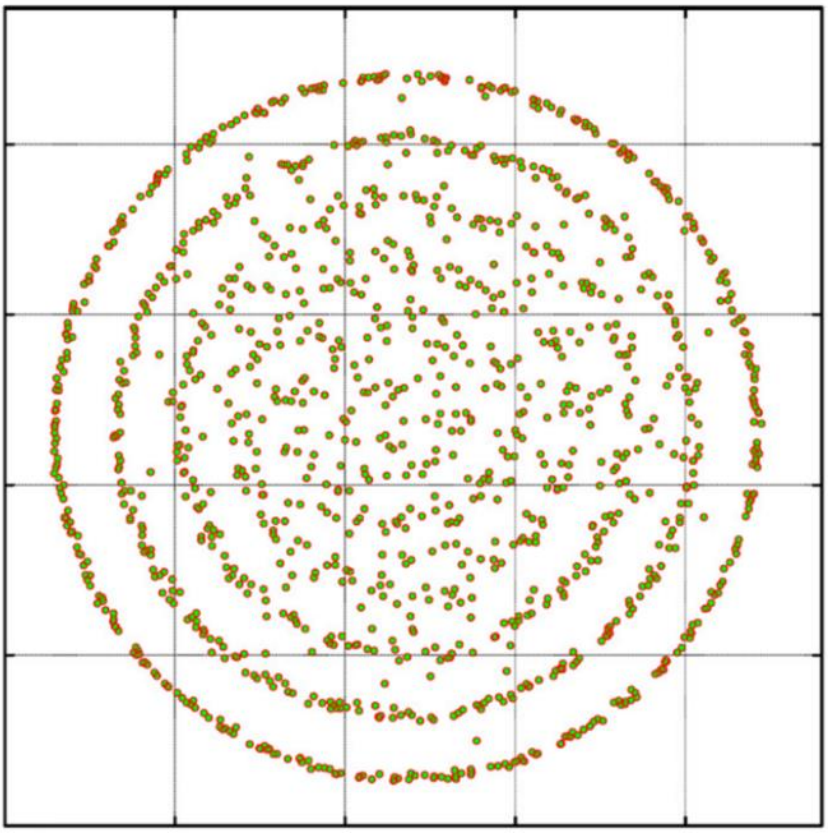

Figure 2.12: Distribution of particle centers projected onto the bottom plane of a randomly packed granular bed confined in a cylindrical pipe (the bed-to-particle size ratio D/d_p is 12.7 and the overall bed porosity is ~0.4) [50].

To measure the porosity variations of a cylindrical granular bed, a series of thin concentric annular columns can be considered. By measuring the void fraction of a certain column, the porosity

between its radial position r and $r + \Delta r$ is determined. When $\Delta r \to 0$, this represents the axially averaged local porosity [51]. Goodling et al. [52] used an epoxy resin to fill the voids of a cylindrical granular bed. The bed was then cut into multiple rings (Figure 2.13a) once the epoxy solidified. By weighing and measuring each ring, the local porosity was determined. Ridgway and Tarbuck [49] measured the porosity using a centrifugal device (Figure 2.13b). A closely packed bed was placed in a cylindrical drum with a known amount of water. The drum was then rotated at sufficient speed so water forms an annular layer on the inner surface of the drum. The local porosity can be determined by measuring the thickness of the annular layer. Klerk [53] summarized the results from different studies including the above-mentioned ones (Figure 2.14). These results are in good agreement: the porosity oscillates asymptotically from 1 at the wall to ~0.4 after the distance of 4 to 5 d_s towards the bed center. This is called the oscillatory porosity model.

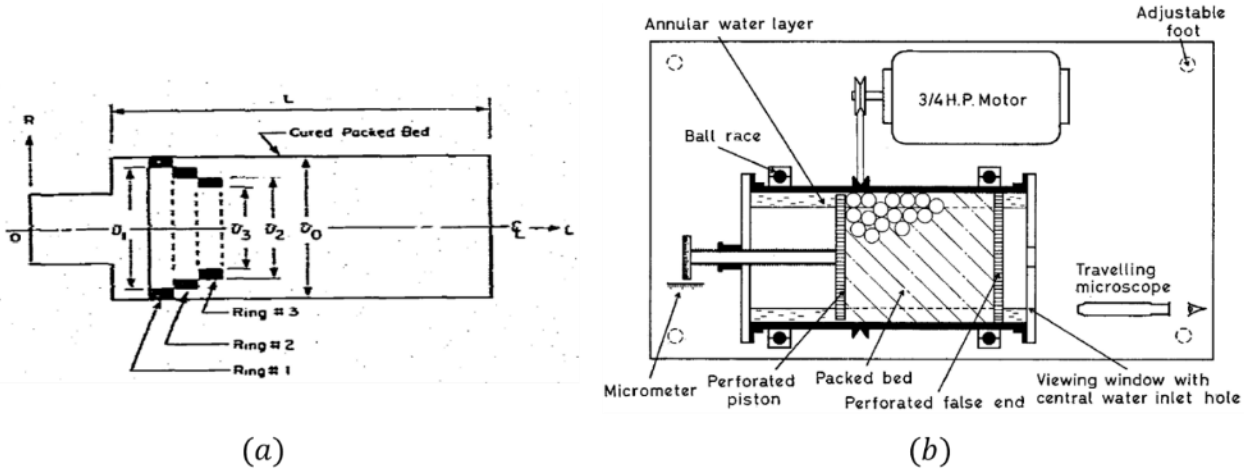

(a) (b)

Figure 2.13: Schematics of experimental devices measuring the local porosity of a cylindrical packed bed: (a) Goodling et al. [52]; (b) Ridgway and Tarbuck [49].

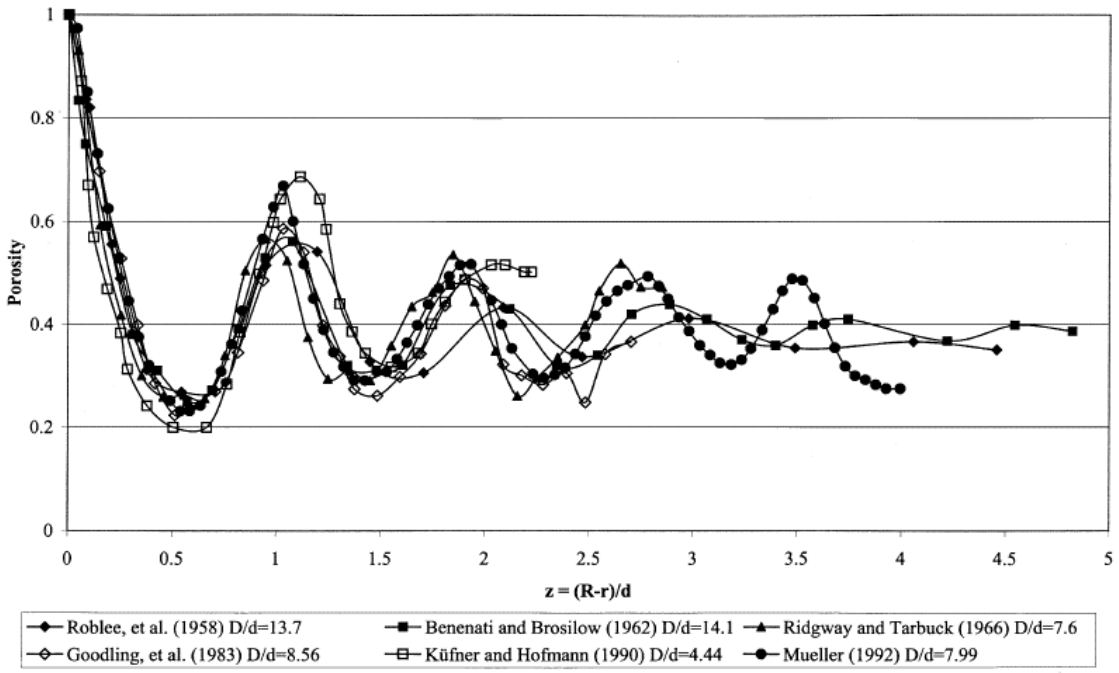

Figure 2.14: Radial bed porosity variation determined by different studies [53]. Note that the parameters R, r and d along the x-axis represent the radius of the granular bed, the radial position and the diameter of beads respectively.

In macroscopic models, the packing structure is modelled implicitly. The void fraction (i.e., porosity) is defined as the fluid volume in a REV over the entire REV volume. This is an average value and the above-mentioned local porosity is not suited. Therefore, an exponential model was proposed. This type of model assumes the radial porosity decreases exponentially from 1 at the wall to the bulk average porosity in the center of the packing. In fact, such model was obtained by solving the volume-averaged governing equations knowing the experimentally measured flow velocities [54, 55]. Antwerpen et al. [56] plotted different exponential models for the same annular granular bed (Figure 2.15). This shows disagreements from one exponential model to another.

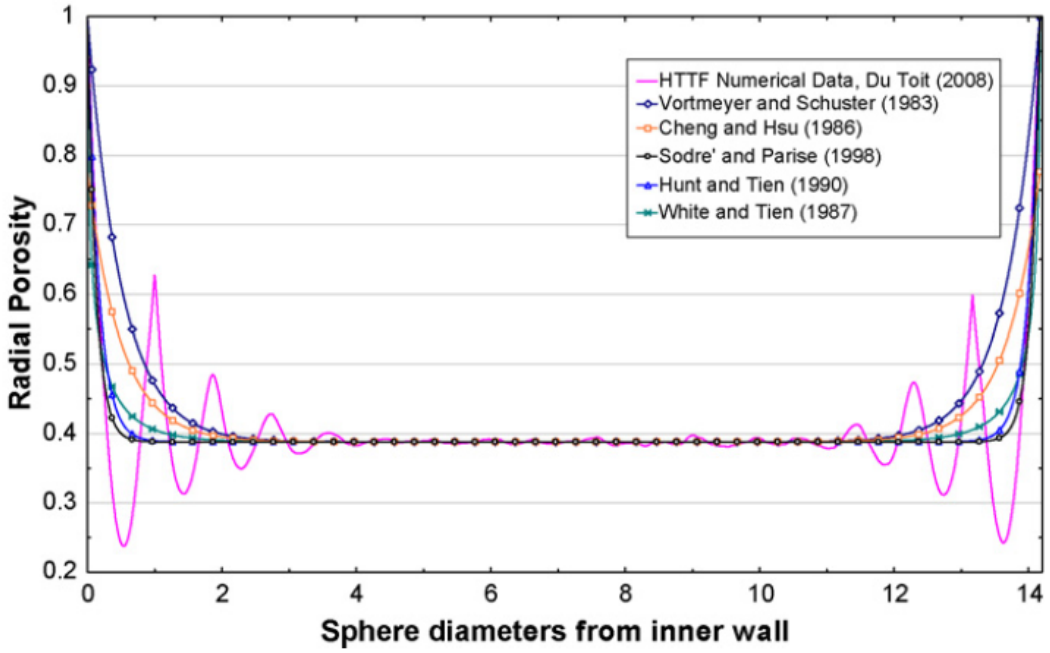

Figure 2.15: Comparison between radial exponential porosity models applied on the same annular granular bed [56]. The magenta curve is the well-agreed oscillatory porosity profile. The x-axis is the radial position from the inner wall in the unit of particle diameter.

2.2.3 Convective heat transfer

The *Local Thermal Non-Equilibrium* (LTNE) model is widely used [57-61] to model the energy transport inside packed beds. In LTNE, the fluid and solid particles are considered as two continua and the energy equations of each phase are developed separately by volume averaging. The energy equations are connected by the heat transfer coefficient between phases h_{sf}. A properly determined value of h_{sf} is required to predict the temperature profile in the granular bed [62, 63]. However, due to its complex nature, h_{sf} is obtained from empirical correlations of Nusselt number (Nu) based on experiments:

$$\mathrm{Nu} = \frac{h_{sf}\, d_s}{\lambda_f} \tag{2.6}$$

where λ_f represents the fluid thermal conductivity. Nie et al. [64] stated that, for packed beads, Nu can be written as a function of porosity (ϕ_V), particle Reynolds number ($\mathrm{Re_{d_p}}$) and Prandtl number (Pr):

$$\mathrm{Pr} = \frac{\mu\, C_f}{\lambda_f} \tag{2.7}$$

where C_f is the specific heat capacity of the fluid. Some empirical correlations found in the scientific literature are summarized in Table 2.1.

Table 2.1 Empirical correlations of Nusselt number in forced convective heat transfer through granular packed beds

Reference	Correlation	$\mathrm{Re_{dp}}$	Material	Fluid
[65]	$\mathrm{Nu} = \left\{\left(1.18\ \mathrm{Re_{dp}}^{0.58}\right)^4 + \left[0.23\ \frac{\mathrm{Re_{dp}}^{0.75}}{(1-\phi_V)^{0.75}}\right]^4\right\}^{1/4}$	1~10^5	Pebble beds	Air, He
[66]	$\mathrm{Nu} = \frac{\mathrm{Pr}^{1/3}}{\phi_V}\ \mathrm{Re_{dp}}\left(0.0108 + \frac{0.929}{\mathrm{Re_{dp}}^{0.58} - 0.483}\right)$	>20	Metallic particles	Air, CO_2, H_2
[67]	$\mathrm{Nu} = 1.1\ \frac{\mathrm{Pr}^{1/3}\ \mathrm{Re_{dp}}}{\mathrm{Re_{dp}}^{0.41} - 1.5}$	13~2136	Porous celite spheres	Air
[68]	$\mathrm{Nu} = 0.922\ \mathrm{Pr}^{1/3}\ \mathrm{Re_{dp}}^{0.66}$	15~161	Catalytic spheres	H_2O_2 vapor
[69]	$\mathrm{Nu} = 8.74 + 9.34\ [6\ (1-\phi_V)]^{0.2}\ \mathrm{Pr}^{1/3}\ \mathrm{Re_{dp}}^{0.2}$	50~120	ZrO_2 pellets	Flue gas
[64]	$\mathrm{Nu} = 0.052\ \frac{(1-\phi_V)^{0.14}}{\phi_V}\ \mathrm{Pr}^{1/3}\ \mathrm{Re_{dp}}^{0.86}$	2.5~175.6	Glass, lead and steel beads	Air
[70]	$\mathrm{Nu} = 0.048\ \frac{(1-\phi_V)^{0.3}}{\phi_V}\ \mathrm{Pr}^{1/3}\ \mathrm{Re_{dp}}^{0.7}$	20~100	Granular potash	Air

In front of such different correlations, the question arises on which one to select for a given application. In fact, such correlations may only be reliable for bead materials and original test

conditions [62]. To enlarge the validation range, Whitaker [71] collected various experimental data of heat transfer in randomly packed beds and proposed the following correlation for $\mathrm{Re_{dp}} > 50$:

$$\mathrm{Nu} = \left[0.5\ \mathrm{Re_{dp}}^{-0.1}\ \frac{(1-\phi_V)^{0.5}}{\phi_V} + 0.2\ \mathrm{Re_{dp}}^{\frac{1}{15}}\ \frac{(1-\phi_V)^{\frac{1}{3}}}{\phi_V}\right] \mathrm{Pr}^{1/3}\ \mathrm{Re_{dp}}^{0.6} \tag{2.8}$$

Wakao et al. [72] assembled the published heat transfer data for packed beds of spheres, cylinders, cubes and irregular shaped grains over a wide range of Reynolds number ($\mathrm{Re_{dp}}$) from 15 to 8500 with a porosity around 0.4. The following correlation is widely used in published investigations [57, 61, 73-75]:

$$\mathrm{Nu} = 2 + 1.1\ \mathrm{Re_{dp}}^{0.6}\ \mathrm{Pr}^{1/3} \tag{2.9}$$

Another issue appears at the interface between the granular bed and the wall. Volume-averaged variables in the granular bed are not consistent with pointwise values of the solid wall. This is referred to as the 'length scale mismatch' [76]. Such mismatch makes it difficult to properly define the boundary conditions. Hager et al. [77] studied a 1D case of heat transfer between a cylindrical bead packing and its bounding wall. The incompatibility at the boundary is avoided by using a cylindrical REV (Figure 2.16). This can be considered as a 'slice' of the system including the granular bed, the containing wall and the insulation layer. The wall temperature is not computed as pointwise values, but rather as an average value over the interface $A_{\gamma\eta}$ in Figure 2.16. Although this approach prevents inconsistency, it is limited to solve 1D problems because of the REV selected. To the best of our knowledge, no further study attempted to solve this issue.

2.2.4 Summary

The literature survey on flow and heat transfer in wall-bounded granular beds can be summed up as follows:

- The knowledge of permeability is necessary to describe fluids flow in granular porous media at the macroscopic scale. This parameter is characterized experimentally using the falling head or the constant head tests. Note that both test methods have different practical limitations.

- The analysis of the packing structure of a typical wall-bounded granular bed shows variations of porosity near the wall. This results in an uneven distribution of the cross-sectional flow velocity, which affects the flow and heat transfer. In the context of macroscopic models, the exponential porosity model was proposed. Note that the porosity variation should depend only on the packing structure. In the literature, however, the exponential porosity models were determined inversely using the experimentally measured radial flow velocity fields and show disagreement.
- The description of the convective heat transfer between the solid bead packing and the fluid relies on empirical correlations. As many have been proposed, it is important to select an appropriate model for a given application. However, there are no general guidelines to assist in such selection.
- An incompatibility in physical variables of the flow appears at the interface between the granular bed and the wall: volume-averaged variables in the granular bed are not consistent with pointwise values in the solid wall. This leads to a difficulty in defining boundary conditions for the numerical simulations. Note that only Hager et al. [77] investigated this problem and solved this issue for a 1D case.

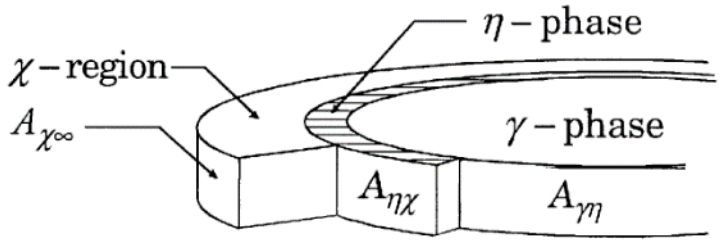

Figure 2.16: Cylindrical REV used by Hager et al. [77]. 'γ-phase' is the bead packing, 'η-phase' is the pipe wall, 'χ-region' is the insulation layer, $A_{\gamma\eta}$ is the interface between the granular packing and the wall, $A_{\eta\chi}$ is the interface between the wall and the insulation layer, $A_{\chi\infty}$ is the interface between the insulation layer and the environment. The temperature of the inner pipe wall is computed as an average value over $A_{\gamma\eta}$.

CHAPTER 3 RESEARCH ISSUES, OBJECTIVES AND OUTLINE

Based on the literature review, several research issues have been identified, from which objectives were derived as stated in the sequel. Finally, an outline is presented at the end of this chapter describing the four articles prepared with one in two parts (Article 2).

3.1 Research issues

Five issues related to the flow and heat transfer in porous media have been identified. Regarding the flow velocity prediction, the permeability (Issue 1) and porosity distribution (Issue 2) of the granular medium based on packed beads need to be properly determined. Secondly, two critical issues related to the heat transfer will be investigated: incompatibility of variables defined at the interface between the wall and granular bed (Issue 3) and determination of convective coefficient between the liquid and the solid particles (Issue 4). Finally, after resolving the above-mentioned issues, the thermal performance of the granular mold can be investigated (Issue 5).

3.1.1 Permeability measurement

The knowledge of permeability is important to predict flow velocity fields in porous media. Due to the complexity at the pore scale, permeability is usually characterized with experiments. For a typical granular bed, it is possible to use the methods proposed in the scientific literature (i.e., falling head or constant head methods), but with the following limitations:

- The falling head test is well suited for granular beds composed of small particles of permeability smaller than 10^{-10} m^2.
- Although the constant head test does not have a range limitation, a more complex apparatus with fluid supply system and inlet pressure measurements would be needed to keep the inlet pressure constant throughout the test.

3.1.2 Porosity profile near the wall

The second issue is the porosity variation near the wall. Studies on the packing structure and measurements of the cross-sectional flow velocity clearly indicate an increase in porosity near the containing wall. Two types of model have been proposed to describe such variation for monodisperse sphere backings, namely the oscillatory porosity model and the exponential porosity model. The oscillatory models obtained from different methods are in general agreement, whereas the exponential models used in macroscopic models deviate from one to another. This is likely caused by measurement errors in velocity, since the exponential models are not determined directly from packing structures, but calculated from the measured flow velocities. This disagreement makes it impossible to predict the flow velocity near the wall: to make accurate predictions, the porosity values near the wall is necessary. However, to select an appropriate porosity model, the flow velocity must be known.

3.1.3 Incompatibility of physical variables at the boundary

A clear definition of boundary conditions at the wall-bed interface is necessary to simulate the bed-to-wall heat transfer. As mentioned above, the main problem is the incompatibility of physical variables computed from different governing equations: the volume-averaged variables in the granular bed computed by the macroscopic model and pointwise values in the solid wall computed by the conventional heat conduction equation. Only one published paper proposed a solution for 1D cases, which cannot be applied in 3D as required to study heating processes in granular molds. The governing equations must be revisited, and a modelling framework needs to be proposed allowing to couple variables defined in neighbouring regions.

3.1.4 Convective heat transfer between the fluid and particles

The convective heat transfer coefficient between the fluid and particles is determined by empirical functions. The literature survey shows the uncertainty of selecting a proper correlation for a given application. Despite a clear preference for the function proposed by Wakao et al. [72], the experimental data available still remain limited to reach a final conclusion. This issue requires either devising a special characterization method or set up guidelines to assist in the selection of an appropriate model.

3.1.5 Heating performance of the granular mold

In the first part of the literature review, the advantages of granular beds over conventional heated molds have been analyzed. However, no study has yet analyzed the innovative tooling concept of granular molds. Having solved the above-mentioned issues, it will be possible to analyze by numerical simulations the heating performance of a granular mold. The effect of various design parameters (e.g., mold materials, liquid flow rate, particle size, etc.) will also be investigated.

3.2 Objectives

This thesis aims to investigate the flow and heat transfer in wall-bounded granular porous media. A modelling framework will be proposed, which allows analyzing the thermal performance of the innovative tooling concept of molds based on granular materials. More specifically, four objectives are listed:

1. To characterize the permeability of a typical granular bed, a simple and robust test method will be proposed to keep the simplicity of conventional falling head methods and enlarge the test range.
2. The second objective is to revisit the conventional volume-averaged governing equations in porous media and propose a new modelling framework which can be used to predict the flow and heat transfer in a wall-bounded granular bed. The following two issues need to be solved:
    a) Determination of the granular bed porosity profile (especially near the wall) directly from the packing structure.
    b) Incompatibility of averaged physical variables at the wall-bed interface.
3. Thirdly, the new modelling framework needs to be validated by experiments and more specific issues related to the heat transfer process can then be investigated, for example, the selection of the convection heat transfer correlations to model the heat transfer between different phases.
4. The final objective consists of analyzing the thermal performance of granular molds and studying the effect of different design parameters. This analysis will be performed numerically using the previously proposed modelling framework. This is an efficient way to evaluate the performance of this innovative tool design. Based on the results, future work is expected to apply this innovative concept in composite manufacturing.

3.3 Outline

This thesis is presented in 4 articles in the following chapters:

- Chapter 4 presents the first article published in *Journal of Engineering Mechanics*, which introduces a modified falling head test to measure the permeability of a typical granular bed. The range of this new approach is two orders of magnitude larger than the conventional one.
- Chapter 5 presents the Part I of the second article submitted to *Transport in Porous Media*, which presents the theoretical derivations of volume-averaged governing equations of wall-bounded granular porous media. This eliminates the incompatibility of physical variables defined on the wall and subsequently allows determining the porosity profile directly from the packing structure.
- Chapter 6 presents Part II of the second article submitted to *Transport in Porous Media*, which describes the experimental validation of the governing equations derived in Part I. Specific issues on modelling are also considered, including additional turbulence sources induced by the wall, the convective heat transfer coefficient between phases and the temperature boundary conditions on the wall.
- Chapter 7 presents the third article submitted to International Journal of Heat and Mass Transfer, which studies the influence of different design parameters for a typical bed-to-wall heat transfer process. The indicator used in this parametric study is the heating time, i.e., the time required to reach temperature uniformity on the wall. This study is conducted numerically using the modelling framework developed in the thesis and is expected to assist in the design of effective granular molds.
- Chapter 8 presents the fourth article submitted to Applied Thermal Engineering, which introduces the innovative concept of heated molds using granular materials. Its heating performance is tested numerically for realistic manufacturing conditions.
- Chapter 9 sums up the concluding remarks of this investigation, which provide a general synthesis of the work. Recommendations for future work are also given.

CHAPTER 4 ARTICLE 1: PERMEABILITY MEASUREMENT OF GRANULAR POROUS MATERIALS BY A MODIFIED FALLING HEAD METHOD

Yixun Sun, Philippe Causse, Brahim Benmokrane and François Trochu

Published in *Journal of Engineering Mechanics* on 18/06/2020

4.1 Chapter overview

This chapter presents the article published in *Journal of Engineering Mechanics*, which introduces the modified falling head method to measure the permeability of granular beds. Compared with the conventional methods, its originality lies in the data-processing approach and the selection of a different test liquid other than water. The characterization on permeability allows a proper determination of the pressure loss in the granular bed, which represents an important source term in the volume-averaged governing equation derived in Chapter 5. The results show that the revisited Ergun's equation [43] describes accurately the pressure loss. This conclusion will be used to validate the modelling framework in Chapter 6.

4.2 Abstract

Liquid flows through granular material are common phenomena in different engineering fields. Under certain conditions, this type of flow can be described by Darcy's law, which involves the permeability of the porous medium. Experimental characterization of this parameter is then of importance to many practical applications. The falling head permeability test is regarded as one of the most commonly used methods for that purpose. The required manipulations are easy and rapid, which makes it preferable especially for field tests. However, due to practical difficulties of carrying out such measurements, it is only applicable to porous materials with permeability values lower than 10^{-10} m^2. To enlarge the test range while keeping its advantages, a modified test procedure is proposed here to measure saturated permeability values two orders of magnitude

larger, namely around 10^{-8} m^2. Tests were performed on granular beds containing single-diameter and multiple-diameter beads. Experimental results showed that the saturated permeability can be accurately predicted by the revisited Ergun's equation with its first empirical constant equal to 180. Two important factors must be considered when performing these tests. The first one is the data processing method to compute the permeability from experimental data: both the gravity and pressure drop of the setup must be taken into account. The second one is the selection of test fluid. By comparing water and silicone oil, it was shown that the viscosity should be adapted depending on the permeability of the sample to ensure consistent and repeatable results.

KEYWORDS: Granular beds, beads, permeability, falling head method

4.3 Introduction

Granular materials represent a significantly important topic of investigation in many engineering fields. Over the past decades, investigations were conducted on granular packings because of their applications to study soil properties in Civil Engineering [78], fluidized bed reactors in Chemical Engineering [79], thermal features of nanofluids [80] and so on. A large number of these studies focused on liquid flows through granular packings composed of stationary beads. At the pore scale, the fluid velocity is not uniform and remains highly influenced by the geometrical shape of the pores and their connectivity [81, 82]. The flow is also affected by the shape and size of the grains, their distribution uniformity in the granular bed, the saturated flow conditions and the properties of the filtration liquid [83]. At the macroscopic scale, such complexity can be conveniently modelled using an averaged approach based on Darcy's law. The latter involves a key parameter of the porous material, namely the permeability (k).

Two types of experimental methods have been widely used to measure the saturated permeability of granular beds: the constant head and the falling head method [44, 84, 85]. The constant head test measures the flow rate through a granular bed under a constant inlet pressure, while the falling head test measures the flow rate under a variable pressure head. The falling head method is easier to implement and much more rapid, which makes it preferable especially for in-situ measurements [86, 87]. However, practical difficulties arise with the falling head method for materials of large

permeability [45]. As a matter of fact, most previous investigations with the falling head test are focused on samples with fine grains of permeability under 10^{-10} m^2 [88-90].

The goal of this work is to revisit the conventional falling head method and propose a modified version to evaluate the saturated permeability of bead packings of permeability in the range of 10^{-8} m^2. This modified falling head test was devised to enlarge the range of the conventional method while keeping its main advantages. The article is organized as follows. After a literature review on the falling head method, the experimental setup and the properties of test samples are presented. The experimental methodology and existing data processing methods are described in the following section. These approaches are compared to highlight the features of the modified approach. The selection of the test fluid is then discussed providing specific rules for similar measurements with other porous materials. Finally, the experimental results are presented and conclusions are drawn.

4.4 Literature review

The measure of permeability is based on Darcy's law, which describes fluid flows in porous media. Although Darcy's law originates from the experiments of Darcy on groundwater flows [36], it may also be derived from the conservation of momentum by volume averaging techniques [44]. For unidirectional flows, Darcy's law can be stated as follows:

$$v = -\frac{Q}{S} = -\frac{k}{\mu}\frac{\partial P}{\partial z} \tag{4.1}$$

where v denotes the superficial velocity (or Darcy's velocity) of the fluid, Q is the volumetric flow rate, S is the cross-sectional area of the porous medium perpendicular to the flow direction, μ is the dynamic viscosity of the fluid and $\partial P/\partial z$ is the pressure gradient through the porous medium. Note that this equation is only applicable at low fluid flow rate. The validity of Darcy's law can be verified by evaluating the Reynolds number based on the particle $R_p = \rho_f v d_p/\mu$, where d_p represents the equivalent particle diameter of the granular bed and ρ_f is the density of the fluid. Bear [44] suggested that Darcy's law is valid for R_p lower than some value between 1 to 10. For higher Reynolds numbers, a nonlinear relationship between the pressure gradient and the flow rate

should be taken into account [44]. For granular packings, Ergun [91] proposed a specific nonlinear equation giving an empirical relation between the flow rate and the pressure drop:

$$\nabla P = A\,\frac{(1-\phi_V)^2}{{\phi_V}^3}\,\frac{v\mu}{d_p^2} + B\,\frac{(1-\phi_V)}{{\phi_V}^3}\,\frac{v^2\,\rho_f}{d_p} \tag{4.2}$$

where ∇P is the pressure gradient in the flow direction, ϕ_V is the void fraction and A, B are empirical constants. Ergun's equation originates from combining Darcy's law with Kozeny-Carman equation [44]. Ergun suggested taking the values of A and B as 150 and 1.75 respectively. Later, Macdonald et al. [43] revisited this equation for smooth particles and proposed different values of 180 and 1.8 for A and B respectively.

In conventional falling head tests, a vertical standpipe of small sectional area is inserted into the saturated granular sample from the top (Figure 4.1). Water is used as test fluid and a high head is normally desired, which may vary from 0.9 to 4.5 meters [85, 89, 90, 92-94]. During the test, the water level falls from its initial position h_0 to a certain height h over a time interval Δt. The permeability is then calculated as [44]:

$$k = \frac{\mu}{\rho_f\,g} \times \frac{a\,L_{bed}}{S\,\Delta t} \times ln\,\frac{h_0}{h} \tag{4.3}$$

where a is the cross-sectional area of the standpipe, L_{bed} is the vertical length of the sample and g is the gravitational acceleration. The change in liquid position is usually recorded visually in time.

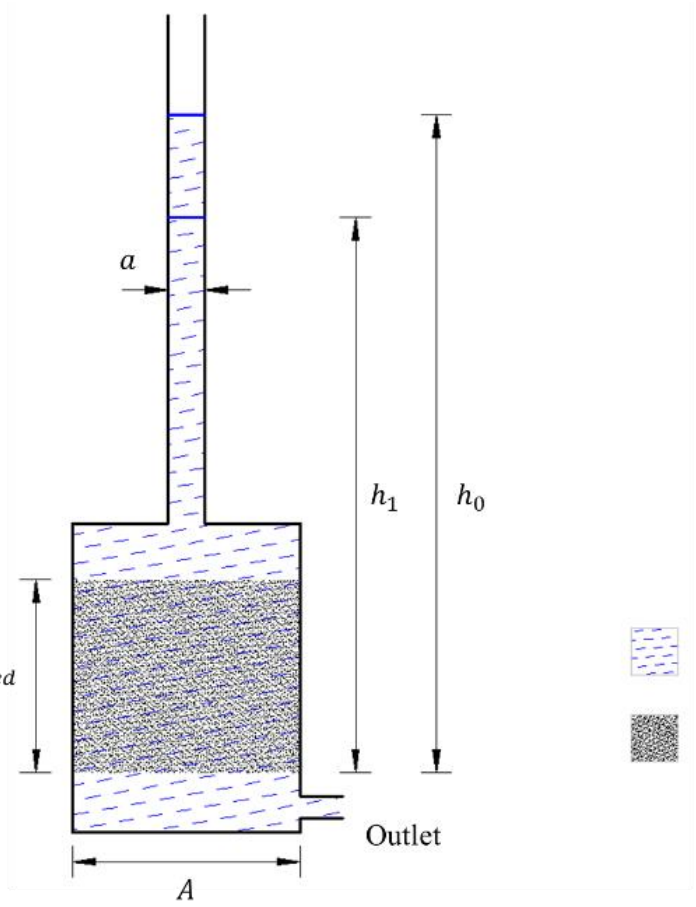

Figure 4.1: Schematic diagram of the conventional falling head test.

The falling head method has already been applied to a wide variety of porous materials such as soil [89], porous pavements [95], sand [96], gravels [94], porous stones [92], pervious concrete [97], glass-fiber wicks [88] and 3D printed porous media [98]. Nearly all investigations used water as test fluid and the water position changes rapidly in the experiments, especially when measuring very permeable samples. Fast changes in the positions of the liquid head during the tests increase the difficulties of performing accurate and consistent measurements [89]. Consequently, the falling head test has mainly been used to characterize porous materials of relatively low permeability (Table 4.1). It is generally not recommended when k is larger than 10^{-10} m^2 [45, 89, 99].

Table 4.1 Ranges of permeability characterized using the falling head test in the scientific literature

	Material tested	Permeability range (m^2)
Assaad and Harb [90]	mixed mortars and concrete	$10^{-15} < k < 10^{-14}$
Hall [85]	hot-mix asphalt pavements	$10^{-15} < k < 10^{-12}$
Lee et al. [98]	3D printed PPF scaffolds	$10^{-14} < k < 10^{-9}$
Pedescoll et al. [94]	constructed wetlands	$10^{-11} < k < 10^{-10}$
Galvan et al. [92]	porous building rocks	$10^{-17} < k < 10^{-13}$
Johnson et al. [89]	sand and silt loam	$10^{-14} < k < 10^{-11}$
Silva et al. [100]	fine-grained marine sediments	$10^{-18} < k < 10^{-15}$
Zarandi et al. [88]	glass-fiber wicks	$10^{-12} < k < 10^{-10}$

Several modifications have been proposed to improve the accuracy and efficiency of measurements made by the falling head method. Nightingale and Bianchi [101] installed a strain gage into the permeameter to measure the water pressure and transient displacement automatically. Fwa et al. [102] described a falling head permeameter with pressure transducers and automatic data loggers. Pressure transducers were positioned in the interior wall of the apparatus to perform automatic readings of time and pressure changes. This idea has also been used in the study of Johnson et al. [89]. Wilson et al. [93] described a device with several pairs of infrared emitters and detectors installed in the standpipe. The change in water level could then be detected, and hence the flow rate data calculated as a function of time. Noborio et al. [103] installed a laser distance meter on the top of the cylinder to measure temporal changes in hydraulic head. These techniques gave a good accuracy by avoiding manual readings of fast changing water head positions. However, additional work and cost are required for the installations and calibration of electronic devices. Note also that the use of Darcy's law in such measurements remains limited to flows at low R_p. For materials with coarse grains, flow may pass from laminar to transitional or turbulent, for which Darcy's law is no longer valid [84, 93, 95].

Apart from the experimental setup, the calculation of permeability also plays a key role in the falling head method. In the vast majority of published works, this parameter is computed by Eq. (4.3) [44, 45, 85, 88, 90, 92, 93, 104, 105]. By doing so, it is implicitly assumed that gravity and the pressure drop in the setup outlet can be neglected. Although Kaczmarek [106] considered gravity in Darcy's law and a recent paper suggested that the pressure drop of the permeameter should also be taken into account for higher permeability values [107], these approaches have not

yet been compared with the conventional falling test method. In particular, the possible implications in terms of permeability calculation have not been analyzed quantitatively. In the current study, experimental results will be processed by several methods and compared to evaluate the accuracy.

4.5 Experimental setup and materials

4.5.1 Experimental setup

The experimental setup is presented in Figure 4.2a and schematically depicted in Figure 4.2b. The granular bed is placed in a vertical transparent plastic pipe of inside diameter 101.6 mm (4 inches) and total length of 550 mm. The plastic pipe is graduated in height to measure h_0. Two identical metallic perforated plates and mesh layers (Figure 4.3) are placed at the top and bottom of the granular bed. The plates support the granular medium and help keeping the cylindrical shape and constant thickness, while the mesh layers create a transition zone between the perforated plates and the granular bed so as to generate a unidirectional flow through the sample. The granular bed, the perforated plates and the mesh layers are held by a plastic sleeve supported by the bottom cap. A rubber flex cuff is tightened around the main pipe and the bottom cap to ensure proper sealing of the device. An outlet valve and a small pipe serving as vent for the system are connected to the bottom cap. The outlet flow is collected in a recipient and weighed by an electronic scale SETRA EL-4100D. This instrument has a maximum capacity of 4.1 kg with a recording speed of up to 5 times per second. To reduce signal fluctuations caused by the electronic scale, both time and mass data were averaged over every 2 seconds. Let t_i and m_i be the i-th ($1 \leq i$) averaged time and mass value. The initial time and mass are denoted t_0 and m_0. On each interval, the volumetric flow rate Q_i, the fluid velocity v_i and the liquid level h_i were calculated as follows:

$$Q_i = \frac{m_i - m_{i-1}}{(t_i - t_{i-1})\rho_f} \tag{4.4}$$

$$v_i = -\frac{Q_i}{S} \tag{4.5}$$

$$h_i = h_0 - \frac{m_i - m_0}{\rho_f S} \tag{4.6}$$

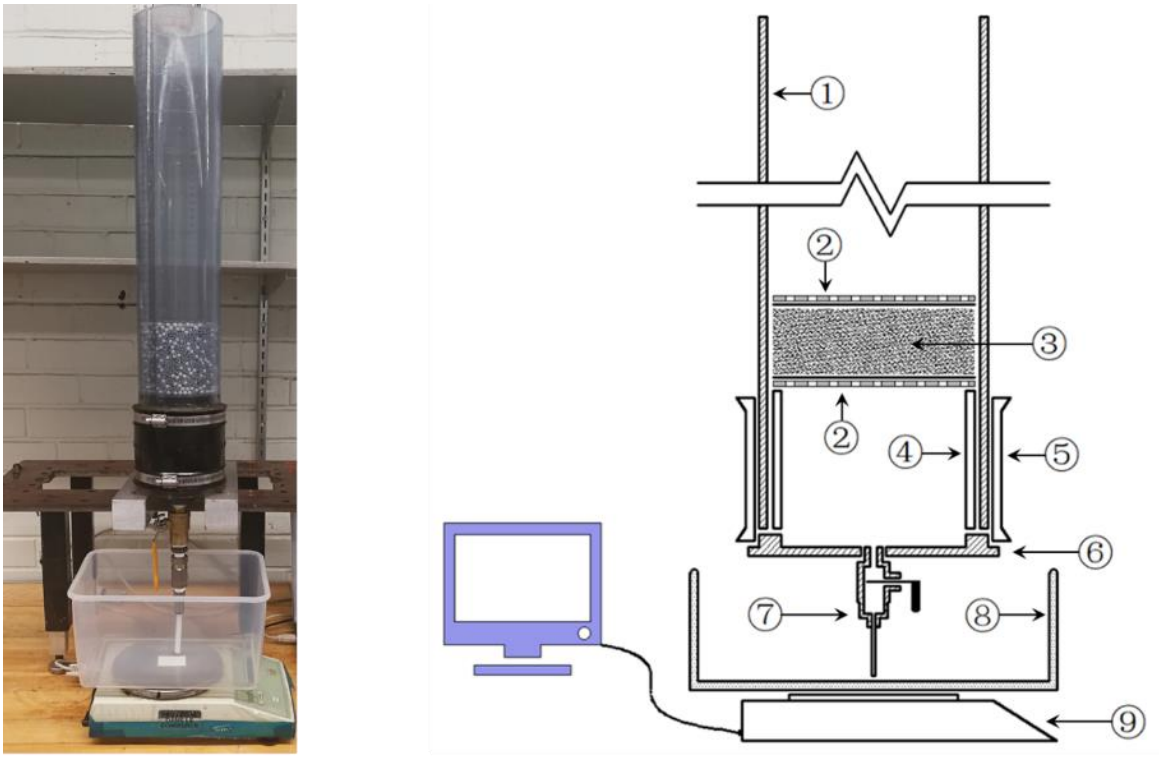

Figure 4.2: Experimental setup: (a) photograph of the setup with the transparent pipe containing the granular bed; (b) schematics of the setup: 1. plastic pipe of 4 inches inside diameter; 2. mesh layer and porous plate; 3. granular bed; 4. plastic ‘sleeve’; 5. rubber flex cuff; 6. plastic end cap; 7. outlet valve; 8. container; 9. electronic scale.

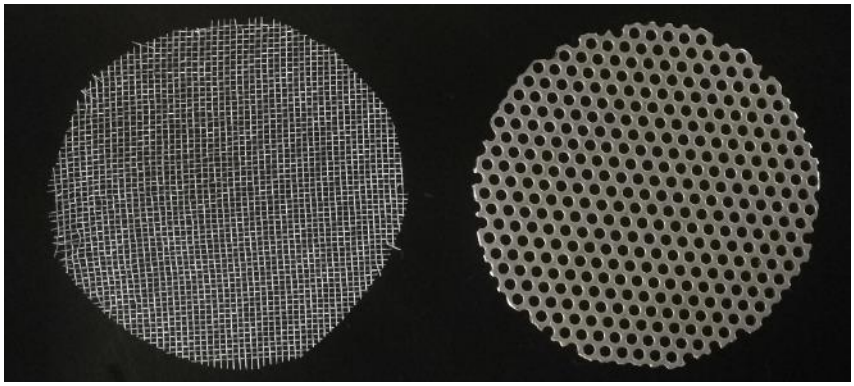

Figure 4.3: Mesh layer (left) and perforated plate (right) holding the granular bed at the top and bottom.

4.5.2 Materials

Two different materials were used during the experiments: ceramic beads (Figure 4.4a) and plastic beads in ABS (Figure 4.4b). Preliminary characterization tests were conducted to evaluate basic properties of the raw materials. The density of beads was measured using a buoyancy technique described in ASTM D792 [108]. The measurements were repeated 20 times for both materials. Mean values reported in Table 4.2 subsequently allowed evaluating the porosity of tested samples. The diameter of the particles is also an important factor to estimate porosity and compare the measured permeability to predictive models. The diameter of a large number of beads (more than 1500 for each type material) were measured by image processing. Firstly, randomly selected beads were photographed with an optical camera (the beads were placed on a graduated background to allow conversion between pixel and physical length). The images were then binarized by manual thresholding using the software ImageJ [109]. This allowed measuring the area of each particle, which was finally converted to diameter by assuming a perfect spherical shape. The size distributions are reported in Figure 4.4, which shows a rather significant scatter, especially for the ceramic beads. The mean diameter for each type of beads was then calculated by the following equation:

$$d_p = \frac{\sum d_i \ f_i}{\sum f_i} \tag{4.7}$$

where d_i is the diameter of particles of size i and f_i is the total number of spheres of size i. The mean diameters obtained for the two types of beads are reported in Table 4.2.

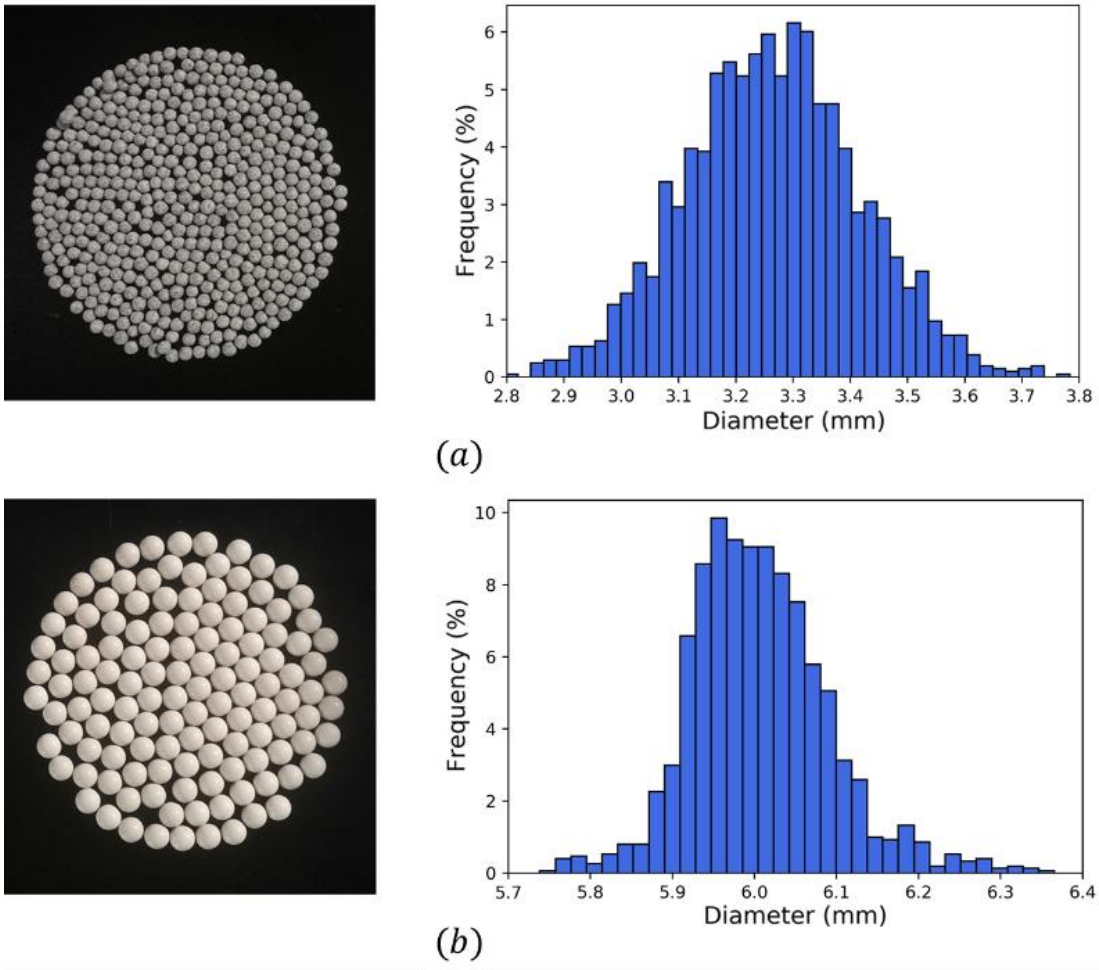

Figure 4.4: Photographs of test materials and size distribution: (a) ceramic beads; (b) ABS beads.

Table 4.2 Material properties

Material	Diameter range (mm)	Mean diameter (mm)	Standard deviation of bead diameter (mm)	Mean density (g/cm^3)	Standard deviation on density measurement (g/cm^3)
Ceramic	2.8 - 3.8	3.26	0.155	2.58	0.0133
ABS	5.73 - 6.36	6.02	0.088	2.24	0.0125

Five different cylindrical packings were considered during the permeability measurements. As reported in Table 4.3, the granular beds of the first two samples contain only one type of beads, while specimens 3 to 5 consisted of a mixture of the two materials. Before each permeability

measurement, the weight and height of the granular sample were measured, and the corresponding porosity was estimated knowing the densities of the two types of beads. Note that the diameter of the test column is more than 12 times larger than the sphere diameter. This ratio was suggested by Beavers et al. [110] to eliminate the influence of the wall when measuring the permeability of granular packings.

Table 4.3 Properties of the granular beds characterized during the permeability experiments

Granular bed	Material	Mass ratio (ceramic : ABS)	Mean diameter (mm)	Porosity
1	Ceramic	N/A	3.26	0.39
2	ABS	N/A	6.02	0.40
3	Ceramic + ABS	1:1	3.68	0.39
4	Ceramic + ABS	1:2	3.99	0.39
5	Ceramic + ABS	2:1	3.49	0.39

The test fluid was the XIAMETER™ PMX-200 calibrated silicone oil from Dow Corning. This liquid is commonly used to characterize the permeability of engineering fabrics used in structural composites [111]. It was notably selected as reference during the latest international benchmark on that topic [112]. It has stable properties and a relatively high viscosity, which facilitates measurements. It possesses several interesting properties such as strict Newtonian behavior and nearly no aging. At the test temperature considered in this investigation (23°C ±1°C), its density and dynamic viscosity are 0.966 g/cm^3 and 0.099 Pa·s respectively. This viscosity is two orders of magnitude higher than water, which is normally used as test liquid in the standard falling head method. The advantages of using a more viscous fluid will be discussed in detail in a subsequent section.

4.6 Test procedure and experimental data processing

The falling head setup presented above differs on two main points from previous studies: the initial head position is much lower (less than 300 mm) and the test fluid is much more viscous. Another particular feature in this work comes from the calculation of permeability. Preliminary experiments were conducted to determine the pressure drop caused by the setup and this effect was incorporated in the final data processing procedure to improve accuracy.

4.6.1 Baseline test

The pressure is not directly measured at the boundaries of the granular sample (points C and D in Figure 4.5). By neglecting viscous effects in the main cylinder, the pressure at point C (P_C) can be simply deduced from the liquid height. At point D, the pressure (P_D) is affected by the liquid flow between the sample and the outlet, but an additional pressure drop is also created by the change of section at the bottom of the test cylinder and in the outlet pipe and valve. To evaluate quantitatively this effect, experiments were performed without samples. Results are reported in Figure 4.6 for four repeated experiments. A linear relationship is observed between P_D and Q:

$$P_D = c_0\, Q + c_1 \tag{4.8}$$

where c_0 = 5.93 × 10^8 Pa·s·m^{-3} and c_1 = -2742 Pa are the fitting parameters obtained from experimental data. Eq. (4.8) describes the intrinsic pressure drop caused by the setup and will be used as baseline to correct the pressure gradient in the sample during a permeability experiment.

4.6.2 Experimental procedure

After performing the baseline tests, the granular beds described in Table 4.3 were characterized by the following experimental procedure. Firstly, a perforated plate and a mesh layer were placed on the top of the plastic sleeve. With the outlet valve closed, silicone oil was poured into the vertical plastic pipe. With the apparatus filled by silicone oil, beads are gradually poured from the top into the plastic pipe. For the granular beds 3 to 5 which contain different types of beads, the particles were thoroughly mixed before placing them in the test cylinder. Another mesh layer and porous plate is placed on top of the granular bed. During installation, the top plate is carefully tapped to reach proper positioning (i.e., perpendicular to the column axis). This ensures that the test packings are of constant thickness. After reading the value of h_0, the data acquisition is launched and the outlet valve opened. The test is stopped before the liquid level reaches the top surface of the sample. During the entire experiment, the mass is continuously recorded from the starting time of the test (i.e., when the mass begins to increase).

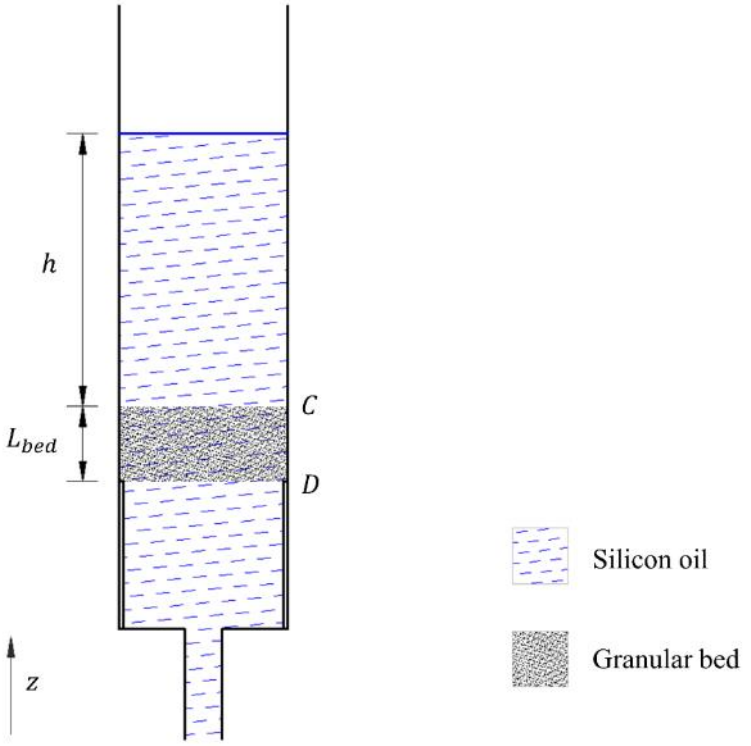

Figure 4.5: Schematic diagram of the modified falling head test.

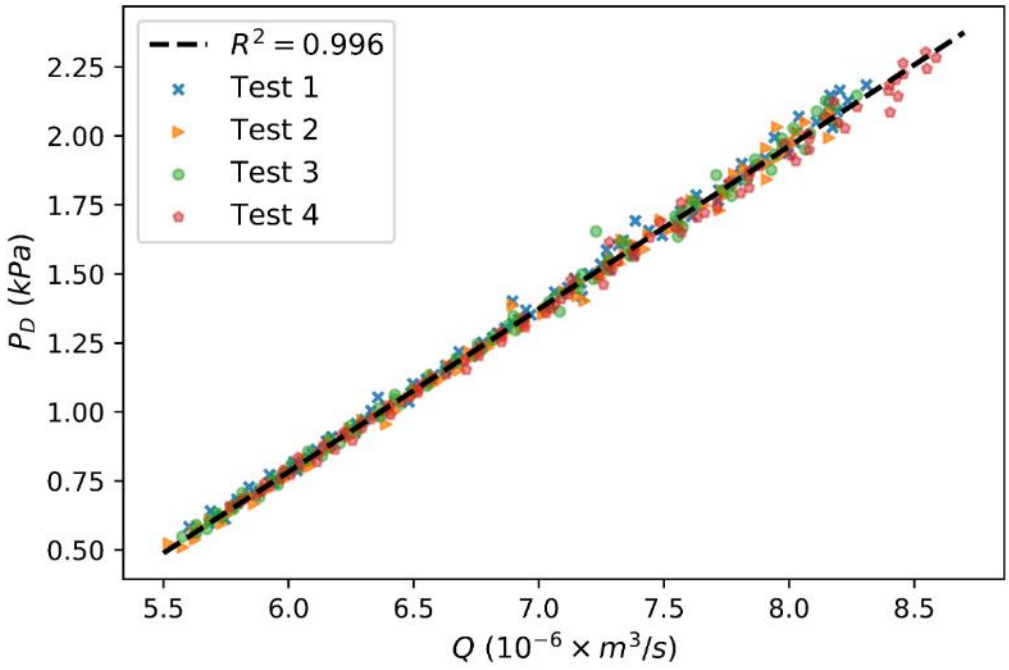

Figure 4.6: Determination of the intrinsic pressure drop caused by the experimental setup.

4.6.3 Experimental data-processing

Different approaches were considered to process the raw experimental results and calculate permeability. The first approach includes all the known physical concepts related to the experimental procedure. Darcy's law was used in its general form, including gravity [44]:

$$v = -\frac{Q}{S} = -\frac{k}{\mu}\left(\frac{\partial P}{\partial z} + \rho_f g\right) \tag{4.9}$$

For incompressible test fluids, $\partial P/\partial z$ writes as follows:

$$\frac{\partial P}{\partial z} = \frac{P_C - P_D}{L_{bed}} = \frac{\rho_f g h - P_D}{L_{bed}} \tag{4.10}$$

The value of P_D was evaluated in Eq. (4.8). Substituting Eq. (4.10) and Eq. (4.8) in Eq. (4.9) gives the permeability of the granular bed:

$$k = -\frac{v\,\mu\,L_{bed}}{\rho_f g\,(h + L_{bed}) - c_0 Q - c_1} \tag{4.11}$$

This equation can be used directly with the discrete values Q_i, v_i and h_i of Eq. (4.4), (4.5) and (4.6) to compute the permeability every 2 seconds. In the rest of this paper, this calculation is referred to as the "instantaneous method". The "global method" will also be considered, which uses the entire set of experimental data to derive a unique permeability from each test. In that case, the initial condition of the liquid level and the incompressibility assumption of the fluid must be considered:

$$h(0) = h_0,\ v = dh/dt \tag{4.12}$$

Thus, the analytical solution can be obtained by integration of Eq. (4.9) as follows:

$$ln\frac{h + L_{bed} - \frac{c_1}{\rho_f\, g}}{h_0 + L_{bed} - \frac{c_1}{\rho_f\, g}} = -\frac{\rho_f\, g}{\frac{\mu\, L_{bed}}{k} + c_0\, S}\, t \tag{4.13}$$

Eq. (4.13) describes the logarithmic variation of h in time during the test. Fitting Eq. (4.13) to the discrete measurement points (t_i , h_i) obtained by Eq. (4.4), (4.5) and (4.6) gives a global permeability value.

Eq. (4.11) and Eq. (4.13) were derived from the same approach. To illustrate the importance of considering gravity and the pressure drop caused by the setup, two simplified data-processing approaches will be examined in the sequel. In the second data-processing approach, the pressure drop of the setup and the gravity term in Darcy's law are both neglected. As discussed previously, this second approach was the most commonly used in past investigations using the falling head method. In that case, Eq. (4.11) and Eq. (4.13) reduce to:

$$k = -\frac{L_{bed}\,\mu\,v}{\rho_f\,g\,h} \tag{4.14}$$

$$ln\frac{h}{h_0} = -\frac{k\,\rho_f\,g}{\mu\,L_{bed}}\,t \tag{4.15}$$

A third data-processing approach will also be implemented following the method of Kaczmarek [106], who considered the gravity term in Darcy's law, but not the setup pressure (which was zero at the bottom of the granular bed). The "instantaneous" and "global" permeability for the third approach were determined by the following equations:

$$k = -\frac{L_{bed}\,\mu\,v}{\rho_f\,g\,(\,h\,+\,L_{bed}\,)} \tag{4.16}$$

$$ln\,\frac{h + L_{bed}}{h_0 + L_{bed}} = -\frac{k\,\rho_f\,g}{\mu\,L_{bed}}\,t \tag{4.17}$$

4.7 Results and discussions

4.7.1 Comparison of data-processing approaches

In this section, the differences between the data-processing approaches described above are compared with typical experimental data obtained for the first granular bed tested (see

monodisperse ceramic beads in the first line of Table 4.3). Note that similar results have been obtained for all the samples analyzed, but are not presented here for the sake of brevity. Figure 4.7a shows the permeability computed by the instantaneous method for the three data-processing approaches considered. Since permeability is an intrinsic property of the porous medium, it should remain constant during the whole test. This behavior is observed only with the first approach, which exhibits a stable average permeability throughout the test.

In the second approach, neglecting the pressure at the bottom of the sample overestimates the pressure gradient. Consequently, the permeability is much lower at the beginning of the test than in the first approach. As the liquid level approaches the top of the granular bed during the test, the overestimation of the pressure gradient becomes less important because neglecting gravity inside the sample tends to generate an opposite effect. Since the apparatus is placed vertically, gravity plays a role in dragging the liquid flow through the granular bed, especially when the liquid level is low.

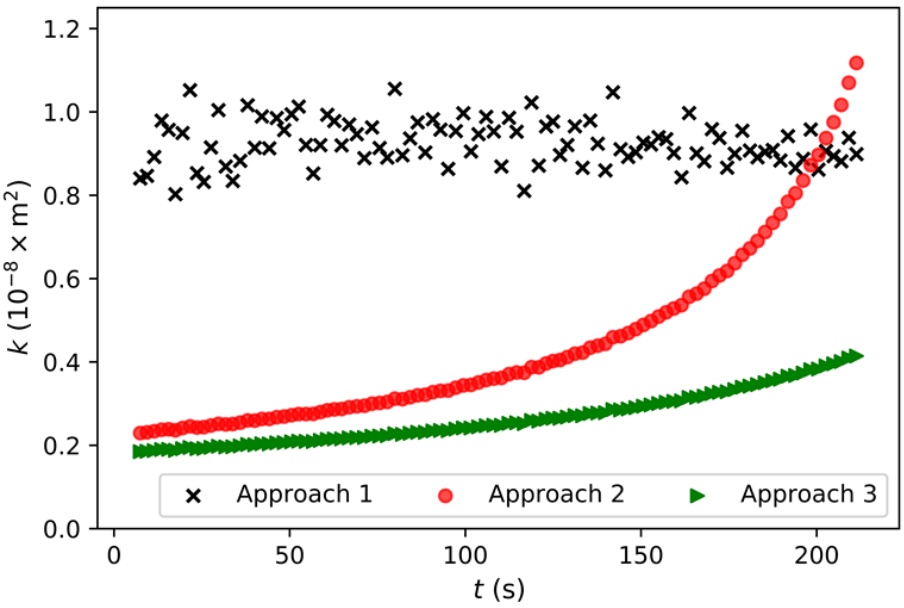

(a)

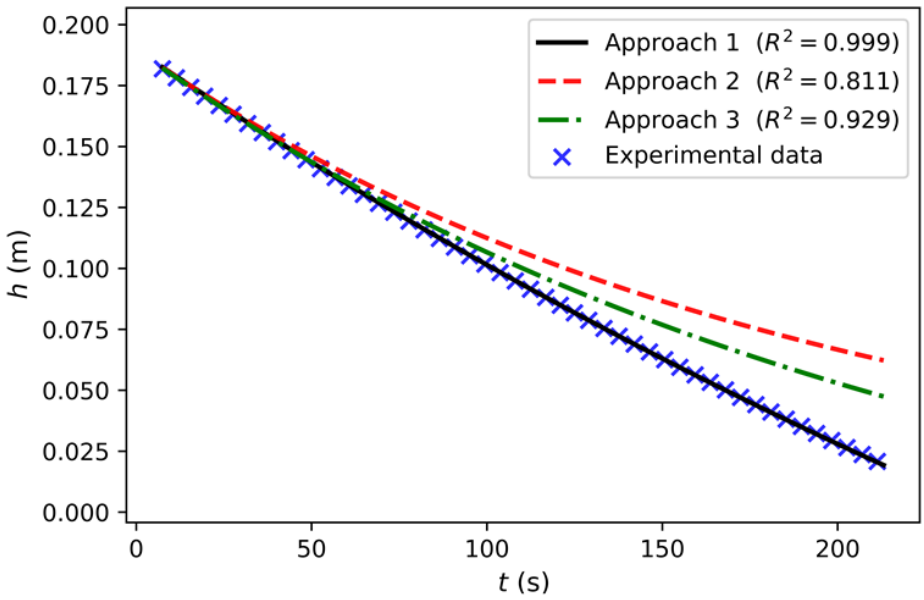

(b)

Figure 4.7: Processing results with three data-processing approaches for typical experimental data obtained with monodisperse ceramic beads of average diameter 3.26 mm: (a) instantaneous method; (b) global method: liquid positions are given in time and compared with experimental observations. 'Approach 1' refers to Eq. (4.11) and (4.13), 'Approach 2' refers to Eq. (4.14) and (4.15) and 'Approach 3' refers to Eq. (4.16) and (4.17).

Finally, adding a gravity term in Darcy's law in approach 3 gives a similar increase of permeability during the test, but with lower values of instantaneous permeability. These results show that the pressure drop of the setup and the effect of gravity should be considered in the evaluation of permeability from experimental results. This conclusion is confirmed by the analysis performed with the global permeability as illustrated in Figure 4.7b: only the first approach gives a good agreement with experiments. However, note that the curves of approaches 2 and 3 give satisfactory results at the beginning of the test. This shows that the complete data from one test must be considered to confirm the validity of the new data-processing approach proposed here. It is also clear that the R^2 coefficients are not satisfactory for approaches 2 and 3. Given their limitations, approach 1 will be used to determine the permeability of the bead packings listed in Table 4.3.

4.7.2 Test fluid selection

The results presented above show that an appropriate data processing methodology is required to characterize the permeability of the granular materials considered. Another key aspect is the selection of test fluids. From the literature review, water was used in previous falling head investigations. In fact, before adopting silicone oil, preliminary tests with water were performed with monodisperse ceramic beads of average diameter 3.26 mm. This allowed identifying difficulties related to the use of water to characterize the permeability of such granular porous media. The first concern is related to the fluid velocity (Figure 4.8). Using water with the proposed experimental setup resulted in values of Reynolds number between 10 and 20 during the entire test, which is out of the usual validity range of Darcy's law. Since experimental data are processed using Darcy's law, it is necessary to lower the fluid velocity. The first possible solution is to increase the thickness of the granular bed. However, this implies using a much bigger testing device and a larger quantity of beads, which is not practical. Another option is to increase the pressure drop of the setup. This was done by placing an additional valve on the outlet. During the test, the valve was kept partially open to generate sufficient pressure loss. In Figure 4.8, this modification resulted in an overall test duration close to a test with silicone oil. The Reynolds number is still high (between 4 and 5), but it is sufficiently low to consider Darcy's law valid as a first approximation.

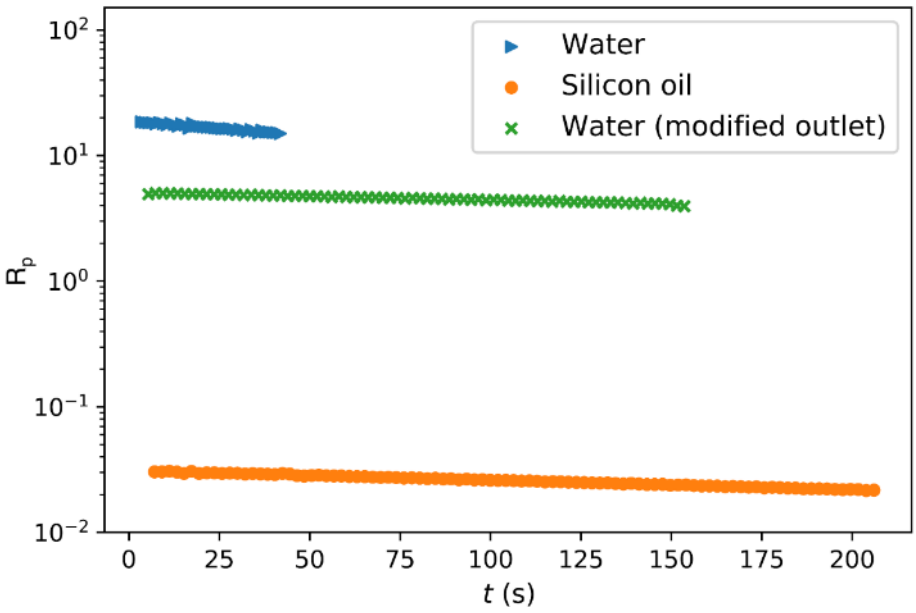

Figure 4.8: Evolution of Reynolds number during tests on ceramic bead packings (average diameter 3.26 mm) with different fluids and outlet conditions.

After modifying the outlet conditions, a baseline test was conducted with water and the permeability of the ceramic bead packing was determined using the global method. Results reported in Figure 4.9 indicate a satisfactory coefficient of determination of the curve fitting. However, the computed value of permeability is much lower than with silicone oil (see Table 4.5 and Figure 4.10). To explain this discrepancy, Figure 4.9 also plots the baseline obtained with water, which nearly coincides with the liquid position during the permeability test. This means that the pressure drop induced by the granular bed is very small compared to the pressure drop of the setup. It is then very difficult to quantify the pressure loss caused by the granular bed alone and estimate precisely the corresponding permeability. To correct this, the proportion of the bed induced pressure drop must be increased. Based on the physical conditions of the experiment, several solutions exist: increase the length of the sample, increase the diameter of the outlet valve, and increase the viscosity of the fluid. Based on the precedent analysis, using a more viscous test fluid is clearly preferable, which motivated the choice of silicone oil. In that case, the change of liquid position during the test is considerably different from the baseline (see Figure 4.10). This facilitates the detection of the pressure drop related to the sample and makes the calculation of permeability more precise and repeatable.

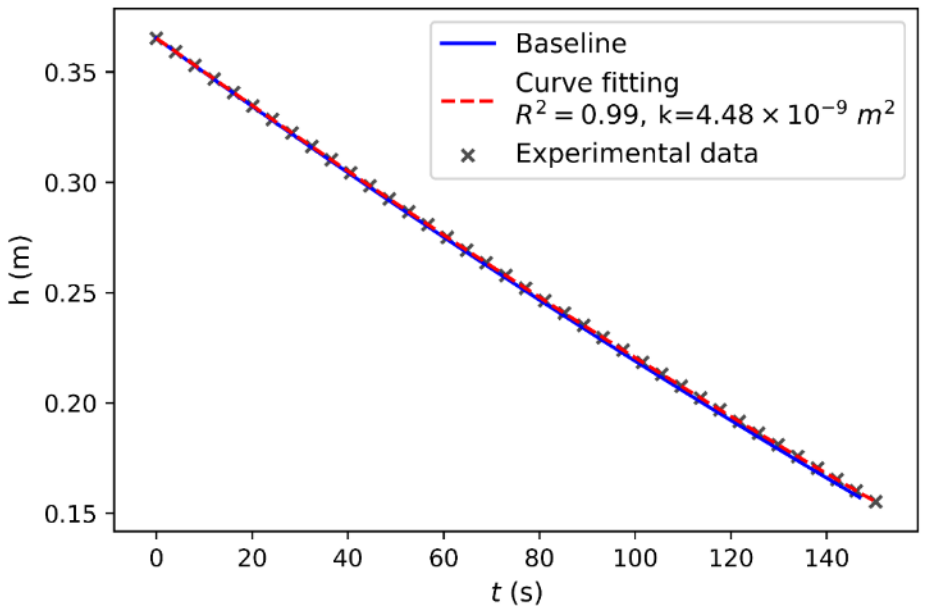

Figure 4.9: Experimental results with the ceramic beads (average diameter 3.26 mm) and setup baseline using water as test fluid and the modified outlet condition.

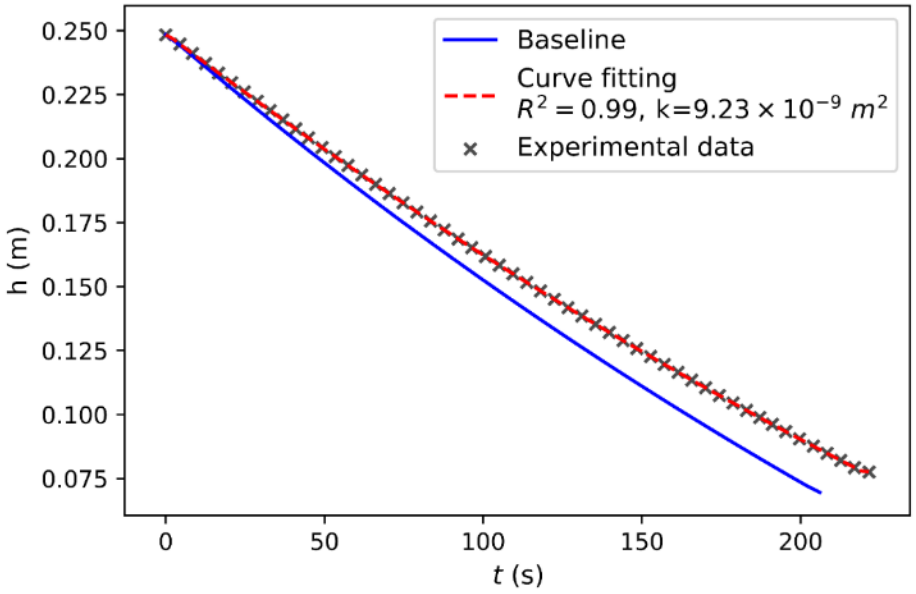

Figure 4.10: Experimental results with ceramic beads (average diameter 3.26 mm) and setup baseline using silicone oil as test fluid.

To understand the influence of liquid viscosity, a sensitivity study was conducted to assess the accuracy of the measurement. Only one possible source of error was considered during this analysis, namely the manual reading of h_0. Since the graduated plastic pipe used during the experiments possesses a minimum scale of 1 mm, the reading errors were estimated to be about ± 0.5 mm. All other parameters (fluid properties, length of the granular bed, geometry of the setup) were considered perfectly known and the acquisition system is assumed to give exact results of time and mass data. Under these assumptions, a series of virtual experiments were performed for L_{bed} = 101.6 mm and h_0 = 350 mm. A virtual experiment is a numerical calculation that reproduces a typical permeability test by following four steps:

1. For a given bed permeability k_{bed}, compute the duration of the test t_{end} using Eq. (4.13) giving the liquid position in time when gravity and the pressure drop of the experimental setup are considered.
2. Generate a time series from 0 to t_{end} with intervals of 2 seconds and calculate the liquid position at each time interval with Eq. (4.13).

3. Introduce an error of ±0.5 mm on h_0 and compute again a series of data points for the virtual experiment.
4. Apply the global method to obtain a simulated value of permeability k_{sim} with reading errors by fitting the liquid positions as a function of time.

Results of the sensitivity analysis are summarized in Figure 4.11 with k_{bed} varies from 10^{-10} to 10^{-6} m^2. The shaded areas represent the possible permeability regions for a reading error on h_0. At low permeability (10^{-10} m^2 and below), an error on the initial liquid position does not affect the measurement. In that case, water is recommended as test fluid because the overall measurement duration is shorter than silicone. Note also that water brings other additional advantages over silicone oil, namely low cost and easier reuse of the beads afterwards. However, the situation differs when the permeability of the sample increases. For example, when k_{bed} equals 10^{-8} m^2, the deviation between k_{bed} and k_{sim} is around 40% for water, but remains below 0.5% for silicone oil. This analysis is consistent with the experimental results of Figure 4.9 and Figure 4.10. For the permeability range considered in this study, the test procedure is too sensitive to experimental errors with water. On the other hand, the silicone oil selected appears to be a well-suited fluid for that particular application. However, this might not be necessarily true for granular packings composed of much larger beads. In that case, a liquid of higher viscosity may probably be recommended.

The above discussion shows that the test fluid should be carefully selected depending on the permeability of the sample to ensure an appropriate trade-off between the duration of the test and accuracy. It is important to mention that other factors can generate variability during practical tests. In order to improve fluid selection, future work could consider other sources of error from the acquisition system or from other parameters.

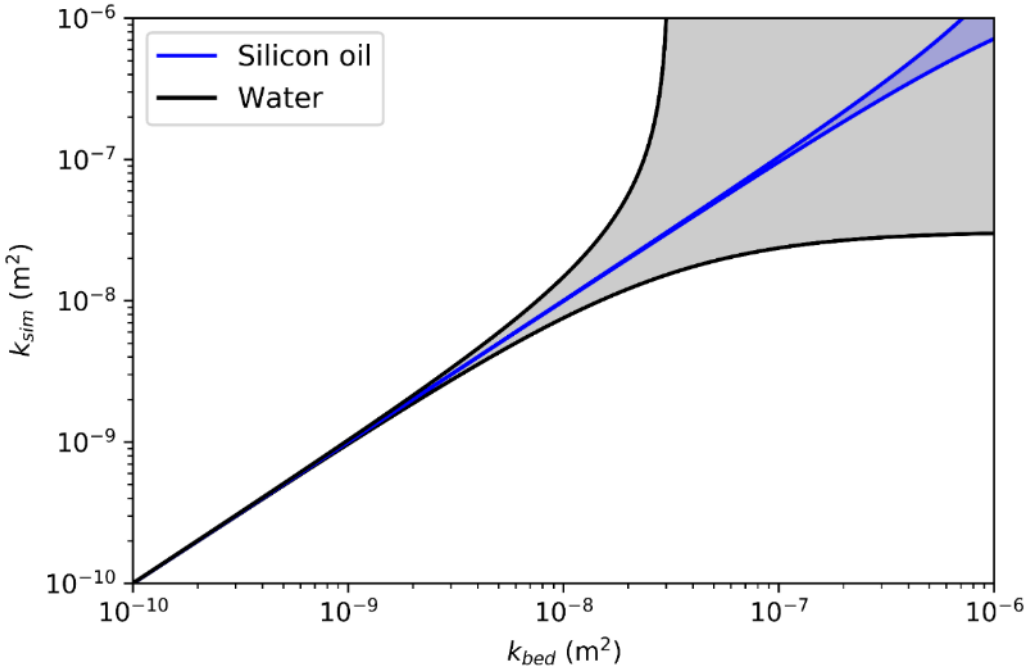

Figure 4.11: Estimation of the measurement accuracy considering errors of ±0.5 mm on the initial liquid position h_0. The graph plots the original permeability k_{bed} in abscissa and the simulated measured permeability k_{sim} in ordinate for water and silicone oil with test conditions representative of the actual experimental setup.

4.7.3 Permeability of bead packings

Figure 12 shows the instantaneous permeability determined from four repeated tests for the first set of beads listed in Table 4.3 (monodisperse ceramic beads of average diameter 3.26 mm). The overall repeatability appears satisfactory, although a scatter exists. Note that the time interval is relatively small (2 seconds), which prevents the noise of the balance signal to be thoroughly averaged. In the test illustrated in Figure 4.12, the average permeability is 9.7×10^{-9} m^2 with a standard deviation of 6.4×10^{-10} m^2 (computed from all the data points). Similar repeated tests were conducted with the other sets of beads and the results are summarized in Table 4.4. Note that low Reynolds numbers (R_p < 0.1) were calculated for all the tests, which validates the applicability of Darcy's law. Overall, the measurements show a good consistency and repeatability during the test since relatively low standard deviations are obtained in all the experiments. The results also show that the revisited Ergun's equation [43] predicts correctly the permeability within a deviation of 6%

whereas the original Ergun's equation [91] overestimates permeability by around 15% in these cases.

Table 4.4 Measured permeability of bead packings listed in Table 4.3 obtained by the instantaneous method and comparison with theoretical predictions

Granular bed	Average permeability (10^{-8} m^2)	Relative standard deviation (%)	Ergun's equation (Eq. (4.2), A=150, B=1.75)		Macdonald's equation (Eq. (4.2), A=180, B=1.8)	
			Prediction (10^{-8} m^2)	ε_{dev} (%)	Prediction (10^{-8} m^2)	ε_{dev} (%)
1	0.97	6.60	1.13	16.49	0.94	3.09
2	3.53	6.52	4.06	15.01	3.39	3.97
3	1.30	10.01	1.49	14.62	1.24	4.62
4	1.46	7.53	1.69	15.75	1.41	3.42
5	1.14	9.65	1.29	13.16	1.08	5.26

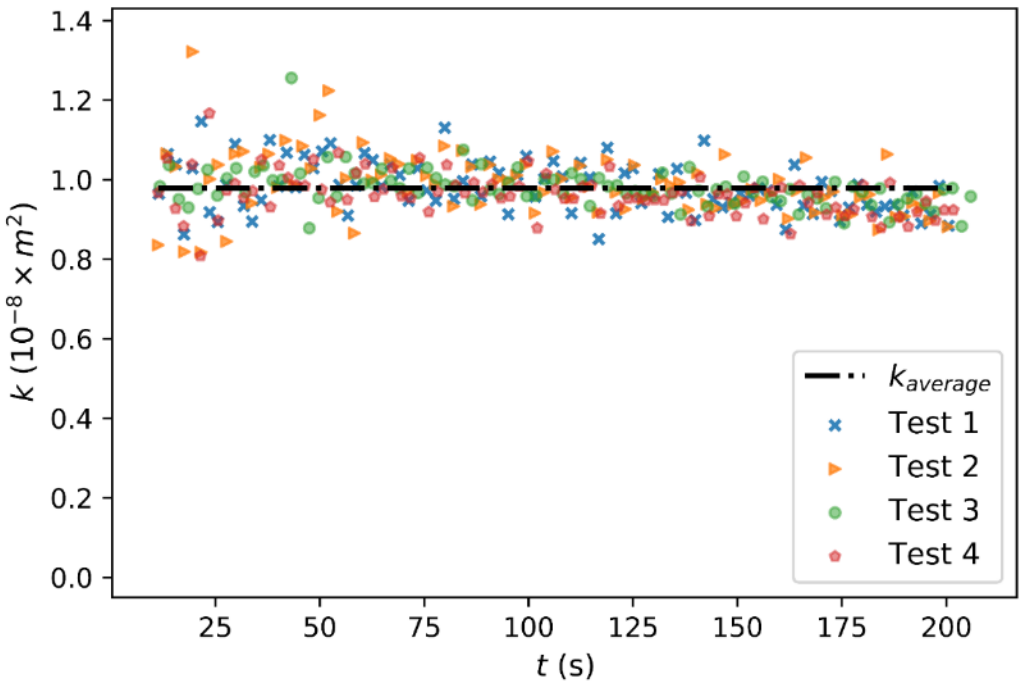

Figure 4.12: Instantaneous permeability for monodisperse ceramic beads of average diameter 3.26 mm.

The global permeability was obtained by fitting the liquid positions in time. The results are summarized in Table 4.5. The values of R^2 approximately equal 1 in all the tests. Compared with the instantaneous method, no evident difference can be observed on the average values of permeability, but the standard deviation is much lower (below 3%). Indeed, the global method considers the entire set of experimental data, which eliminates inherent fluctuations coming from the acquisition system. However, the two methods yield similar results. If simplification of the testing methodology is required, the instantaneous approach could be used by recording only the change in mass over a given time interval. This could be interesting to implement the test in a more practical environment. Finally, note that the permeability computed by the global approach is very close to the predictions of MacDonald's equation [43]. This confirms the ability of the revisited Ergun's equation to predict permeability in such granular porous media.

Table 4.5 Measured permeability of bead packings listed in Table 4.3 obtained by the global method and comparison with theoretical predictions.

Granular bed	Average permeability (10^{-8} m^2)	Relative standard deviation (%)	Ergun's equation (Eq. (4.2), A=150, B=1.75)		Macdonald's equation (Eq. (4.2), A=180, B=1.8)	
			Prediction (10^{-8} m^2)	ε_{dev} (%)	Prediction (10^{-8} m^2)	ε_{dev} (%)
1	0.93	1.38	1.13	21.51	0.94	1.08
2	3.43	3.06	4.06	18.37	3.39	1.17
3	1.27	1.34	1.49	17.32	1.24	2.36
4	1.39	1.87	1.69	21.58	1.41	1.44
5	1.15	1.48	1.29	12.17	1.08	6.09

4.8 Conclusions

In this study, a modified falling head method is proposed to measure the permeability of bead packings, which lies in the range of 10^{-8} m^2. The method does not require the installation of electronic devices on the apparatus, nor manual reading of the head loss. Hence, it is relatively easy to implement. The saturated permeability of five different granular beds filled with single-diameter and multi-diameter spherical beads were investigated experimentally. After comparing different

data-processing approaches, it was shown necessary to consider both gravity and the pressure drop of the setup to process experimental data. The choice of an appropriate test fluid is also a key parameter. Due to its low viscosity, water is not applicable for the tests considered. Hence, a more viscous silicone oil was used in the experiments which allowed measuring a higher range of permeability. With the test methodology described in the article, permeability results exhibit a good consistency and repeatability. The revisited Ergun's equation was recommended to predict the permeability of bead packings. Although the samples tested in this investigation are composed of spherical beads, the modified falling head method can be applied to other types of porous media over a wide range of permeability values. However, the data-processing approach and the viscosity of the test fluid must be carefully selected depending on the permeability of the material and the experimental setup.

4.9 Acknowledgments

This study was made possible thanks to financial support of NSERC (*Natural Sciences and Engineering Research Council*), FRQNT (*Fonds de recherche québécois sur la nature et la technologie*), CREPEC (*Research Center for High Performance Polymer and Composite Systems*) and the Engage project supported by René Matériaux Composites (RMC), St-Ephrem-de-Beauce (Quebec), who are gratefully acknowledged. The authors would also like to thank John and Spencer Borland for suggesting this investigation, for their guidance and for providing the beads. The technical assistant of the composite laboratories of Polytechnique Montreal, Christian-Charles Martel and the technical staff of SDI-Plomberie are also acknowledged for their efficient help to set up the experiments.

CHAPTER 5 ARTICLE 2: CONVECTIVE HEAT TRANSFER BETWEEN A BEAD PACKING AND ITS BOUNDING WALL: PART I - THEORY

Yixun Sun, Cédric Béguin, Philippe Causse, Brahim Benmokrane and François Trochu

Submitted to *Transport in Porous Media* on 22/04/2021

5.1 Chapter overview

This chapter is the first part of an article in two parts submitted to *Transport in Porous Media*, which presents the theorical derivation of volume-averaged governing equations in wall-bounded bead packings. This study addresses two critical issues summarized in Chapter 3 using a non-constant *Representative Elementary Volume* (REV): the determination of the exponential porosity profile and the incompatibility of physical quantities at the boundary. The derivation of the governing equations enables subsequent studies on this topic. An experimental validation and the investigation on the effect of various modelling parameters will be presented in Chapter 6.

5.2 Abstract

Forced convective heat transfer between fluid-saturated bead packings and the solid containing walls are important phenomena in different engineering fields. In practical applications, the volume-averaged governing equations and the use of *Reynolds-Averaged Navier-Stokes* (RANS) *Computational Fluid Dynamics* (CFD) simulations can provide a reasonable description of the averaged transport phenomena in bead packings without too much computational resources. However, it is still a challenge to treat conjugate problems because the presence of a bounding wall causes different modelling issues. Firstly, different exponential functions have been proposed for RANS CFD simulations to model the porosity variation of bead packings near the wall. These functions are usually determined by an inverse approach which solves the governing equations to approximate the physically measured flow fields (e.g., velocity, temperature). Given the variety of

existing porosity models, it is difficult to select the most appropriate one in a particular case. Secondly, the volume-averaged quantities of the bead packing are incompatible with the local point quantities of the wall. This largely increases the difficulty in defining the boundary conditions at the wall. In the present work, a modelling framework is presented to simulate the forced convective heat transfer from the bead packing to its containing wall. These two critical issues are addressed by deriving volume-averaged governing equations using a non-constant Representative Elementary Volume (REV). In Part I of the article, the theoretical derivations are presented in detail. A procedure is also developed to select an appropriate porosity model from the packing microstructure. Part II of the article completes the investigation by validating the predictive capability of the derived governing equations by experiments.

KEYWORDS: Bead packings, forced convection, volume averaging, wall-to-bed heat transfer

5.3 Introduction

Fluid flows through pipes and ducts are commonly encountered in heating and cooling systems used in different engineering fields. In such applications, a granular porous medium can be placed inside the fluid channel to intensify the mixing and enhance the heat transfer. Following this approach, the wall-to-bed heat transfer coefficient can be increased by 2 to 30 times [113-115]. For example, multi-tubular packed bed reactors were designed to conduct strong exothermic or endothermic chemical reactions [116]. In such reactors, pipes filled with catalyst particles are placed vertically inside a cooling or heating jacket. With gaseous reactants injected into the granular porous medium, heat is added or removed through the pipe wall. Similar studies were conducted for various applications such as electronics cooling [117], micro-porous heat exchangers for fuel cells [118], packed bed energy storage systems [119] and many more.

Numerical simulation is a powerful tool to assist in the design and control of such systems. Adequate modeling of the forced convective heat transfer between the bead packing and its bounding wall is therefore needed to ensure accurate predictions of transient temperature fields. On the pore scale, the flow quantities (e.g., velocity, pressure) are irregular and local on-site measurements are extremely difficult as the flow passages are small and complex. This also makes

it computationally demanding to solve the transport phenomena in a typical medium at a microscopic scale for practical applications. As a result, the macroscopic approach is widely adopted [35]. In this approach, the conservation equations of each phase in the porous medium are spatially averaged over a *Representative Elementary Volume* (REV). With the *Reynolds-Averaged Navier-Stokes* (RANS) *Computational Fluid Dynamics* (CFD) simulation, it provides low-cost and reasonable descriptions of the averaged transport phenomena in bead packings [58-61]. However, as it will be shown in the next section, it remains challenging to determine the porosity profile in the wall confined packed bed and to define properly the boundary conditions at the bounding wall.

The main objective of this study is to propose a framework to model the heat transfer between a random monodisperse bead packing and its bounding wall. In Part I of the article, the theoretical derivations of the volume-averaged governing equations using a non-constant REV are presented in detail. The proposed non-constant REV is also used to select an appropriate porosity profile directly from the packing structure (i.e., without measuring the corresponding flow fields). In Part II of the study, an experimental validation of the governing equations derived in Part I is performed with a cylindrical ceramic bead packing. The selection of appropriate parameters in the model will also be discussed. The Part I of the study begins by a literature review. The second section presents the detailed derivation of volume-averaged governing equations using a non-constant REV. This includes the mass, momentum and thermal energy conservation equations. The determination of the radial exponential porosity profile is presented in the third section. In the final section, the conclusions are drawn.

5.4 Literature review

Forced convective heat transfer in the homogeneous region of the bead packings (i.e., far away from the bounding walls) has been widely studied [60, 63, 120, 121]. In such studies, the porosity (ϕ_V) of the packing is normally considered as constant. However, in the near-wall region, the porosity changes rapidly causing variations in flow velocity [122]. This significantly influences the heat and mass transfer. It is therefore inappropriate to use a constant ϕ_V for the entire packing. Two different types of model have been proposed to describe such structural feature in monodisperse sphere packings, namely the oscillatory porosity model and the exponential porosity model. The

former was developed by measuring the void fraction of a series of thin concentric annular columns [122], which gives an oscillatory porosity profile. The results from published investigations of different particle diameters (d_s) are in good agreement: the porosity oscillates asymptotically from 1 at the wall to around 0.4 at a radial distance of 5 to 6 d_s towards the bed center [123]. On the other hand, the exponential model was proposed in the context of RANS CFD simulations, in which the packing structure is modelled implicitly. This type of model assumes the radial porosity decays exponentially from the wall to the bulk porosity at the bed center. Some exponential models published in the scientific literature are listed in Table 5.1.

Table 5.1. Exponential porosity models for monodisperse bead packings

Reference	Radial porosity correlation	Descriptions	
Hunt and Tien [124]	$\phi_V = \phi_b \left[1 + \left(\frac{1}{\phi_b} - 1\right) \exp\left(-b \frac{R_{bed} - r}{d_s}\right)\right]$	b is 6 for perfect spheres and 8 for slightly irregular particles.	(5.1)
Vortmeyer and Schuster [54]	$\phi_V = \phi_b \left[1 + \left(\frac{1}{\phi_b} - 1\right) \exp\left(1 - 2 \frac{R_{bed} - r}{d_s}\right)\right]$		(5.2)
White and Tien [125]	$\phi_V = \left[1 + \left(\frac{1}{\phi_b} - 1\right) \sqrt{1 - \exp\left(-2 \frac{R_{bed} - r}{d_s}\right)}\right]^{-1}$		(5.3)
Cheng and Hsu [126]	$\phi_V = \phi_b \left[1 + \exp\left(-2 \frac{R_{bed} - r}{d_s}\right)\right]$	It is valid when ϕ_b is ~0.4	(5.4)

(ϕ_V is the volume porosity, i.e., the void fraction of the REV, ϕ_b is the bulk porosity, R_{bed} is the radius of the granular bed, r is the radial coordinate and d_s is the particle diameter.)

Unlike the oscillatory models, not all exponential porosity models give 1 at the wall. For example, Eq. (5.4) proposed by Cheng and Hsu [126] gives ~0.8 at the wall. Given the variety of existing models, it is not straightforward to select a radial porosity profile for a typical RANS CFD simulation. Du Toit [127] evaluated different models by comparing the overall void fraction to a reference value given by a recognized oscillatory profile. The results showed possible over or under estimations from one exponential model to another. It should also be noted that these models, i.e.,

Eq. (5.1) to (5.4), are approximated inversely by solving the transport equations knowing the physically measured cross-sectional flow velocity or temperature fields. By doing so, uncertainties on the flow measurements can impact the porosity model, which is a possible limitation of the approach. In addition, the disagreement between different exponential models makes it difficult to predict the cross-sectional flow velocity field in the granular bed with RANS CFD simulation. If one wants to make a prediction, a radial porosity model is needed. To select an appropriate porosity model, the cross-sectional flow velocity distribution should be known. As a matter of fact, the porosity profile is a structural parameter that should only be determined by the packing arrangement, not by the associated flow fields.

Apart from the uncertainty in the porosity profile, an additional modelling difficulty lies in clearly defining the boundary conditions at the wall. At the interface, the volume-averaged quantities (i.e., velocity, temperature, pressure, etc.) in the granular bed confront with the point quantities of the solid wall. These two types of quantity are incompatible and difficult to be used in defining the boundary conditions. This is referred to as ‘the length scale mismatch’ by Ochoa-Tapia and Whitaker [76]. Hager et al. [77] studied a 1D case of heat and mass transfer between a cylindrical porous bead packing and its bounding wall. Volume-averaged equations were derived using a cylindrical REV with constant radius. This REV can be regarded as a ‘slice’ of the system perpendicular to the central axis of the granular bed. The incompatibility is avoided by calculating the area-averaged quantities at the interface. However, due to its geometrical feature, this approach is limited to solve 1D problems and cannot be applied for a complex geometry. To the best of our knowledge, no further attempts were made in the scientific literature to analyze such incompatibility at a typical solid-porous interface. For practical reasons, Cascetta et al. [57] simply assumed that the wall temperature equals to the volume-averaged fluid temperature at the interface. Despite the simplification, numerical results were in a good agreement with experimental data to predict the fluid and wall temperature fields.

In conclusion, the literature survey shows a disagreement on the radial porosity profile in RANS CFD simulations. It also points out the incompatibility of quantities at the interface. This increases the difficulty of defining the boundary conditions and modelling the wall-to-bed heat transfer in practical applications. In the following sections of the article, we demonstrate that both issues can be addressed by deriving the volume-averaged governing equations using a non-constant REV.

5.5 Volume averaging

A typical volume averaging process starts by averaging the point equations for the fluid and solid region over the REV. In most studies [120, 128-131], the size, shape and orientation of the REV are assumed as constant and independent of space and time. These studies confirmed that the transport phenomena in the homogeneous region of the packed bed (i.e., far away from the bounding wall) can be well described by the volume-averaged governing equations derived with a constant REV. However, such an assumption creates difficulties in the near-wall region. For a constant spherical REV of diameter D_{cst}, if the distance between the REV center and the wall is less than $0.5D_{cst}$, then the wall enters in the REV (Figure 5.1a). The volume averaged governing equations need to be reconsidered for a third phase (i.e., the wall) apart from the fluid and porous medium. The governing equations for the fluid and beads may also need to be adapted accordingly. This creates difficulties in defining the boundary conditions at the wall-bed interface. To deal with this problem, a non-constant spherical REV may be used with a diameter D calculates as follows:

$$D = \min(2d_{wall}\,,\, D_{max}) \tag{5.5}$$

where d_{wall} is the distance between the REV sphere center and the wall. A schematic diagram is given in Figure 5.1b. With such a definition, the REV contains only the fluid and beads phase. In the homogeneous region of the packed bed, the diameter of the REV is D_{max}, which is independent of space and time. At the wall, the porosity is 1 [51]. This can be regarded as a 'thin layer' of pure fluid and the volume-averaged quantities are the same as their corresponding pointwise values [76]. Therefore, the diameter of the REV at the wall is null. In the transition region (i.e., between the homogeneous region and the wall), the size of the REV varies and the volume-averaged equations derived with constant REV may not be valid. In this section, the conventional equations for granular porous media are then revisited to consider the size variation of the REV.

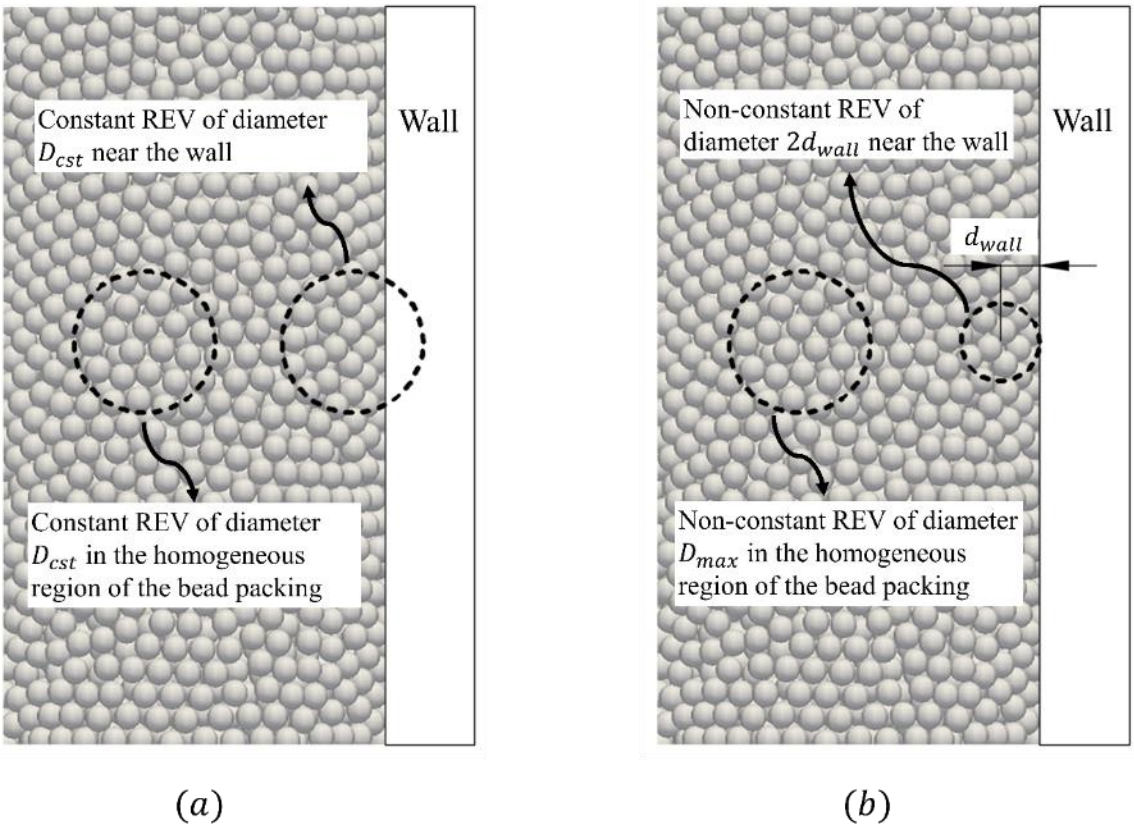

Figure 5.1: Macroscopic region of a wall-confined bead packing and associated averaging volumes in the homogeneous region of the packing and near the wall: (a) constant spherical REV; (b) non-constant spherical REV.

5.5.1 Continuity equation

The process of volume averaging is first conducted with the fluid phase continuity equation:

$$\frac{\partial \rho_f}{\partial t} + \nabla \cdot \left(\rho_f \, \boldsymbol{u_f}\right) = 0 \tag{5.6}$$

where ρ_f is the fluid density, $\boldsymbol{u_f}$ is the fluid velocity. For a given spherical REV, Eq. (5.6) is averaged over the volume V:

$$\frac{1}{V}\int_{V_f} \frac{\partial \rho_f}{\partial t}\, dV + \frac{1}{V}\int_{V_f} \nabla \cdot \left(\rho_f \, \boldsymbol{u_f}\right) dV = 0 \tag{5.7}$$

where V_f represents the fluid volume in the REV (Figure 5.2a). Since the REV is independent of time, the integration and differentiation of the first term in Eq. (5.7) is interchanged:

$$\frac{1}{V}\int_{V_f}\frac{\partial \rho_f}{\partial t}\,dV = \frac{\partial}{\partial t}\left(\frac{1}{V}\int_{V_f}\rho_f\,dV\right) \tag{5.8}$$

To interchange the integration and differentiation in the second term in Eq. (5.7), the theorem derived by Gray [132] for non-constant REV is applied:

$$\begin{aligned}\frac{1}{V}\int_{V_f}\nabla\cdot\left(\rho_f\,\boldsymbol{u_f}\right)dV \\ = \frac{1}{V}\nabla\cdot\int_{V_f}\rho_f\,\boldsymbol{u_f}\,dV + \frac{1}{V}\int_{A_{fs}}\boldsymbol{n_{fs}}\cdot\left(\rho_f\,\boldsymbol{u_f}\right)dA - \frac{\nabla V}{V}\frac{1}{A}\int_{A_f}\rho_f\,\boldsymbol{u_f}\,dA\end{aligned} \tag{5.9}$$

where A_{fs} is the interfacial area between the fluid and beads, $\boldsymbol{n_{fs}}$ is the unit normal vector on the interface pointing from the fluid to the beads, A is the bounding surface area of the REV and A_f denotes the area of A occupied by the fluid (Figure 5.2b). The first term on the right-hand side of Eq. (5.10) can be further expressed as:

$$\frac{1}{V}\nabla\cdot\int_{V_f}\rho_f\,\boldsymbol{u_f}\,dV = \nabla\cdot\left(\frac{1}{V}\int_{V_f}\rho_f\,\boldsymbol{u_f}\,dV\right) + \frac{\nabla V}{V}\frac{1}{V}\int_{V_f}\rho_f\,\boldsymbol{u_f}\,dV \tag{5.10}$$

We assume no mass transfer between the solid beads and fluid, therefore the second term on the right-hand side of Eq. (5.10) is null. Substituting Eq. (5.8) to (5.10) into Eq. (5.7) results in:

$$\begin{aligned}\frac{\partial}{\partial t}\left(\frac{1}{V}\int_{V_f}\rho_f\,dV\right) + \nabla\cdot\left(\frac{1}{V}\int_{V_f}\rho_f\,\boldsymbol{u_f}\,dV\right) \\ + \frac{\nabla V}{V}\left(\frac{1}{V}\int_{V_f}\rho_f\,\boldsymbol{u_f}\,dV - \frac{1}{A}\int_{A_f}\rho_f\,\boldsymbol{u_f}\,dA\right) = 0\end{aligned} \tag{5.11}$$

For the sake of brevity, we define the intrinsic volume average of a fluid phase quantity ψ as:

$$\langle\psi\rangle^f = \frac{1}{V_f}\int_{V_f}\psi\,dV = \frac{1}{\phi_V\,V}\int_{V_f}\psi\,dV \tag{5.12}$$

where ϕ_V is the void fraction of the REV, which is defined as:

$$\phi_V = \frac{1}{V}\int_{V_f} dV \tag{5.13}$$

Similarly, we define the intrinsic area averaging of the quantity ψ as:

$$\langle\psi\rangle_A^f = \frac{1}{A_f}\int_{A_f} \psi\, dA = \frac{1}{\phi_A\, A}\int_{A_f} \psi\, dA \tag{5.14}$$

where ϕ_A is the area porosity of the REV, which represents the fluid area fraction of the REV bounding surface:

$$\phi_A = \frac{1}{A}\int_{A_f} dA \tag{5.15}$$

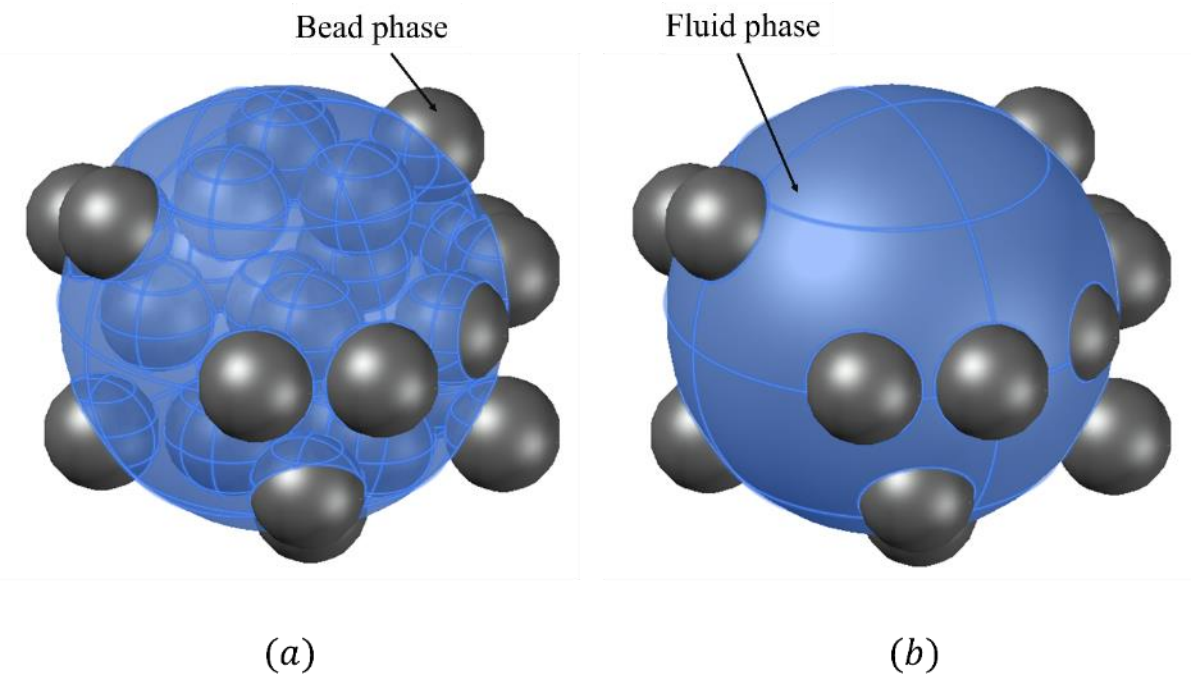

Figure 5.2: Schematic of a typical REV (i.e., the large sphere) used to illustrate: (a) the fluid occupied REV volume V_f (shaded volume in blue) and (b) the fluid occupied REV bounding area A_f (shaded area in blue).

We then rewrite Eq. (5.11) as follows:

$$\frac{\partial\left(\phi_V \langle\rho_f\rangle^f\right)}{\partial t} + \nabla \cdot \left(\phi_V \langle\rho_f \boldsymbol{u_f}\rangle^f\right) + \frac{\nabla V}{V}\left(\phi_V \langle\rho_f \boldsymbol{u_f}\rangle^f - \phi_A \langle\rho_f \boldsymbol{u_f}\rangle_A^f\right) = 0 \tag{5.16}$$

Ochoa-Tapia and Whitaker [76] have provided a detailed analysis of the term $\langle\rho_f \boldsymbol{u_f}\rangle^f$ assuming that spatial deviations of variables are neglected in the same REV. It can be decomposed into:

$$\langle\rho_f \boldsymbol{u_f}\rangle^f = \langle\rho_f\rangle^f \langle\boldsymbol{u_f}\rangle^f \tag{5.17}$$

Similarly, the term $\langle\rho_f \boldsymbol{u_f}\rangle_A$ writes:

$$\langle\rho_f \boldsymbol{u_f}\rangle_A^f = \langle\rho_f\rangle_A^f \langle\boldsymbol{u_f}\rangle_A^f \tag{5.18}$$

Ochoa-Tapia and Whitaker [133] suggested that the area-averaged quantity can be replaced as its corresponding volume-averaged quantity, thus resulting in:

$$\langle\rho_f\rangle_A^f \langle\boldsymbol{u_f}\rangle_A^f = \langle\rho_f\rangle^f \langle\boldsymbol{u_f}\rangle^f \tag{5.19}$$

Substituting Eq. (5.17) to (5.19) into Eq. (5.16) gives the local volume-averaged continuity equation as follows:

$$\frac{\partial\left(\phi_V \langle\rho_f\rangle^f\right)}{\partial t} + \nabla \cdot \left(\phi_V \langle\rho_f\rangle^f \langle\boldsymbol{u_f}\rangle^f\right) = -\frac{\nabla V}{V} \langle\rho_f\rangle^f \langle\boldsymbol{u_f}\rangle^f (\phi_V - \phi_A) \tag{5.20}$$

5.5.2 Momentum equation

The momentum conservation equation of the fluid is expressed as :

$$\frac{\partial}{\partial t}\left(\rho_f \boldsymbol{u_f}\right) + \nabla \cdot \left(\rho_f \boldsymbol{u_f}\boldsymbol{u_f}\right) = -\nabla p + \nabla \cdot \bar{\bar{\tau}} + \rho_f \boldsymbol{g} \tag{5.21}$$

where $\boldsymbol{u_f}\boldsymbol{u_f}$ represents the tensor product of the fluid velocity, p is the pressure, $\boldsymbol{g}$ is the gravitational acceleration and $\bar{\bar{\tau}}$ is the stress tensor described as follows:

$$\bar{\bar{\tau}} = \mu\left[\left(\nabla \boldsymbol{u_f} + \left(\nabla \boldsymbol{u_f}\right)^T\right) - \frac{2}{3}\nabla \cdot \boldsymbol{u_f} \boldsymbol{I}\right] \tag{5.22}$$

where $\boldsymbol{I}$ is the unit matrix. The phase-averaged momentum conservation equation is derived in Section 5.10 as follows:

$$\begin{aligned} &\frac{\partial}{\partial t}\left(\phi_V \langle\rho_f\rangle^f \langle \boldsymbol{u_f}\rangle^f\right) + \nabla \cdot \left(\phi_V \langle\rho_f\rangle^f \langle \boldsymbol{u_f}\rangle^f \langle \boldsymbol{u_f}\rangle^f\right) \\ &\qquad = -\phi_V \nabla\langle p\rangle^f + \nabla\left(\phi_V \langle\bar{\bar{\tau}}\rangle^f\right) + \phi_V \langle\rho_f\rangle^f \boldsymbol{g} - \\ &\nabla \cdot \left(\phi_V \langle\rho_f\rangle^f \langle \boldsymbol{u'_f u'_f}\rangle^f\right) + \frac{1}{V}\int_{A_{fs}} \boldsymbol{n_{fs}}\left(\bar{\bar{\tau}} - p'\right) dA \\ &\qquad + \frac{\nabla V}{V}\left(\phi_V - \phi_A\right)\left(\langle\bar{\bar{\tau}}\rangle^f - \langle\rho_f\rangle^f \langle \boldsymbol{u_f u_f}\rangle^f - \langle p\rangle^f\right) \end{aligned} \tag{5.23}$$

The term $\frac{1}{V}\int_{A_{fs}} \boldsymbol{n_{fs}}\left(\bar{\bar{\tau}} - p'\right) dA$ in Eq. (5.23) represents the interactive force between the phases. It is usually determined empirically. The term $\langle\rho_f\rangle^f \langle \boldsymbol{u'_f u'_f}\rangle^f$ represents the Reynolds stress which is calculated by turbulence modelling. Note that the turbulence model in porous media is carried out in two successive averaging steps, namely the time averaging and the spatial volume averaging. The parameters $\boldsymbol{u'_f}$ and p' represent the variation from the averaged flow velocity and pressure (see Section 5.10). Further discussion on these two terms will be given in the Part II of the study.

5.5.3 Thermal energy equations

In this study, we make use of the *local thermal non-equilibrium* assumption between the fluid and beads, i.e., the fluid and beads are considered as two continua and the energy equations of each phase are developed separately:

$$\frac{\partial}{\partial t}\left(\rho_f C_f T_f\right) + \nabla \cdot \left(\rho_f C_f T_f \boldsymbol{u_f}\right) = \nabla \cdot \left(\lambda_f \nabla T_f\right) \tag{5.24}$$

$$\frac{\partial}{\partial t}\left(\rho_s C_s T_s\right) = \nabla \cdot \left(\lambda_s \nabla T_s\right) \tag{5.25}$$

where λ_f, T_f and C_f represent the thermal conductivity, temperature and specific heat capacity of the fluid, while λ_s, T_s and C_s denote the thermal conductivity, temperature and specific heat capacity of the solid beads. The temperature and heat flux at the interface between the beads and the fluid are continuous, which sets the boundary conditions for Eq. (5.24) and Eq. (5.25). In Section 5.11, the volume-averaged energy equations are derived for the fluid phase with $\lambda_{f_{eff}}$, the effective thermal conductivity of the fluid:

$$\begin{aligned}\frac{\partial}{\partial t}\left(\phi_V \langle\rho_f\rangle^f \langle C_f\rangle^f \langle T_f\rangle^f\right) + \nabla\cdot\left(\phi_V \langle\rho_f\rangle^f \langle C_f\rangle^f \langle T_f\rangle^f \langle \boldsymbol{u_f}\rangle^f\right) \\ = \nabla\cdot\left(\phi_V\, \lambda_{f_{eff}} \nabla\langle T_f\rangle^f\right) + \frac{1}{V}\int_{A_{fs}} \boldsymbol{n_{fs}}\cdot\left(\lambda_f \nabla T_f\right) dA \\ + \frac{\nabla V}{V}(\phi_V - \phi_A)\left(\lambda_{f_{eff}} \nabla\langle T_f\rangle^f - \langle\rho_f\rangle^f \langle C_f\rangle^f \langle T_f\rangle^f \langle \boldsymbol{u_f}\rangle^f\right)\end{aligned} \tag{5.26}$$

and for the solid phase:

$$\begin{aligned}\frac{\partial}{\partial t}[(1-\phi_V)\langle\rho_s\rangle^s \langle C_s\rangle^s \langle T_s\rangle^s] \\ = \nabla\cdot[(1-\phi_V)\lambda_s \nabla\langle T_s\rangle^s] + \frac{1}{V}\int_{A_{fs}} \boldsymbol{n_{sf}}\cdot(\lambda_s \nabla T_s)\, dA \\ + \frac{\nabla V}{V}\lambda_s \nabla\langle T_s\rangle^s (\phi_A - \phi_V)\end{aligned} \tag{5.27}$$

The terms $\frac{1}{V}\int_{A_{fs}} \boldsymbol{n_{fs}}\cdot\left(\lambda_f \nabla T_f\right) dA$ and $\frac{1}{V}\int_{A_{sf}} \boldsymbol{n_{sf}}\cdot(\lambda_s \nabla T_s)\, dA$ in Eq (5.26) and (5.27) represent the interfacial heat exchange. These terms are normally expressed in a more explicit way with the convective heat transfer coefficient h_{sf} [120]:

$$\frac{1}{V}\int_{A_{fs}} \boldsymbol{n_{fs}}\cdot\left(\lambda_f \nabla T_f\right) dA = -a_v\, h_{sf}\left(\langle T_f\rangle^f - \langle T_s\rangle^s\right) \tag{5.28}$$

$$\frac{1}{V}\int_{A_{fs}} \boldsymbol{n_{sf}}\cdot(\lambda_s \nabla T_s)\, dA = -a_v\, h_{sf}\left(\langle T_s\rangle^s - \langle T_f\rangle^f\right) \tag{5.29}$$

where a_v is the interfacial area per unit volume. For sphere packings, a_v is expressed as:

$$a_v = \frac{6\,(1-\phi_V)}{d_s} \tag{5.30}$$

Due to the complex nature of h_{sf}, it is usually obtained from empirical correlations based on experiments. A detailed analysis will be provided in Part II of this study. Substitution of Eq. (5.28) and (5.29) into Eq (5.26) and (5.27) provides:

$$\begin{aligned}\frac{\partial}{\partial t}\left(\phi_V\,\langle\rho_f\rangle^f\,\langle C_f\rangle^f\,\langle T_f\rangle^f\right) + \nabla\cdot\left(\phi_V\,\langle\rho_f\rangle^f\,\langle C_f\rangle^f\,\langle T_f\rangle^f\,\langle \boldsymbol{u_f}\rangle^f\right)\\ = \nabla\cdot\left(\phi_V\,\lambda_{f_{eff}}\nabla\langle T_f\rangle^f\right) - a_v\,h_{sf}\left(\langle T_f\rangle^f - \langle T_s\rangle^s\right)\\ + \frac{\nabla V}{V}\left(\phi_V-\phi_A\right)\left(\lambda_{f_{eff}}\nabla\langle T_f\rangle^f - \langle\rho_f\rangle^f\,\langle C_f\rangle^f\,\langle T_f\rangle^f\,\langle \boldsymbol{u_f}\rangle^f\right)\end{aligned} \tag{5.31}$$

$$\begin{aligned}\frac{\partial}{\partial t}\left[(1-\phi_V)\,\langle\rho_s\rangle^s\,\langle C_s\rangle^s\,\langle T_s\rangle^s\right]\\ = \nabla\cdot\left[(1-\phi_V)\,\lambda_s\,\nabla\langle T_s\rangle^s\right] - a_v\,h_{sf}\left(\langle T_s\rangle^s - \langle T_f\rangle^f\right)\\ + \frac{\nabla V}{V}\,\lambda_s\,\nabla\langle T_s\rangle^s\,(\phi_A-\phi_V)\end{aligned} \tag{5.32}$$

Up to this point, the volume-averaged governing equations are derived using a non-constant REV. By doing this, the volume-averaged quantities in the homogeneous region (i.e., $d_{wall} > 0.5\,D_{max}$) of the granular bed gradually transform to point quantities as the REV approaches to the wall. This also prevents the wall from entering the REV in the near wall zone (i.e., $0 < d_{wall} < 0.5\,D_{max}$). The boundary conditions at the interface (e.g., no-slip condition at the wall) can then be clearly defined without any incompatibility of quantities. Additional source terms containing $\nabla V\,(\phi_V - \phi_A)$ appear in all the governing equations presented above, i.e., Eq. (5.20), (5.23), (5.31) and (5.32). These terms are induced by the size variation of the REV. Note that these terms only occur in the near wall region, since ∇V vanishes in the homogeneous region of the granular bed. A detailed analysis of these terms is presented in the sequel.

5.6 REV size variation induced source terms

5.6.1 Determination of the volume porosity ϕ_V and the area porosity ϕ_A

We now direct our attention to the source terms induced by the size variation of REV, i.e., terms containing $(\phi_V - \phi_A)$ in Eq. (5.20), (5.23), (5.31) and (5.32). The key issue is to analyze the difference between the volume porosity ϕ_V and the area porosity ϕ_A of the REV. To do so, a cylindrical granular bed of mono-sized spheres (Figure 5.3a) was generated using the open-source *Discrete Element Method* (DEM) package LIGGGHTS [134]. The diameter of the beads (d_s) and the packing (D_{bed}) are 6.27 mm and 101.6 mm respectively, which are measured experimentally and will be used in Part II to perform the experimental validation. In order to save computational resources and meanwhile be representative of the packing structure in z direction, the height of the cylinder (H_{bed}) is set as 200 mm. With 7461 beads generated, the volume porosity of the virtual granular bed is 0.406. The radial distributions of ϕ_V and ϕ_A of the granular bed are determined by the following five steps:

Step 1: A given cross-section of the granular bed is meshed by parallel lines of spacings dx and dy in the x and y directions respectively (Figure 5.3b). The center axis of the granular bed is at $x = 0, y = 0$ and the bottom of the virtual granular bed is at $z = 0$.

Step 2: Discard all the intersection grid points located outside the granular bed, i.e., when the radial distance to (0, 0) is larger the radius of the bed (R_{bed}).

Step 3: Calculate the spherical REV diameter D using Eq. (5.5) with its center located at each intersection point within the cross-section.

Step 4: Determine the value of ϕ_V and ϕ_A for each REV, knowing its diameter D and the positions of all the beads. The equations used in this step are given in Section 5.12.

Step 5: Repeat Steps 1 to 4 for different axial positions $z \in \left[\frac{D_{max}}{2}, H_{bed} - \frac{D_{max}}{2}\right]$ for the spacing dz. Calculate the average of ϕ_V and ϕ_A for each radial position r at different axial positions z.

Following the work of Clausnitzer and Hopmans [135] who showed that the minimum size of a typical REV in determining the porosity of a randomly packed bed is $5.15d_s$, the parameter D_{max} in Eq. (5.5) was taken as 34.5 mm ($5.5d_s$). Note that the averaged values of ϕ_V and ϕ_A calculated

in Step 5 are used to determine the radial porosity distribution of the granular bed. This prevents the fluctuations of ϕ_V and ϕ_A values at local positions and exhibits the averaged distribution of the entire granular bed. The results are plotted as a function of the dimensionless radial position d_{wall}/d_s and shown in Figure 5.4 with $dx = dy = dz = 5$ mm. The data points of ϕ_V and ϕ_A are fitted using two piecewise linear functions. The fitted function for ϕ_V is further considered as the radial porosity profile of the packing and will be used in the numerical simulation in Part II of the work. The profiles of ϕ_V and ϕ_A are rather similar and decrease exponentially from unity at wall to the bulk porosity ~0.4. In fact, they are nearly identical when the dimensionless radial position d_{wall}/d_s is smaller than 0.3. The values of ϕ_V and ϕ_A show an obvious discrepancy with a maximum difference of about 0.09 when $0.3 < d_{wall}/d_s < 2.75$. This difference between ϕ_V and ϕ_A will be taken into consideration in the numerical simulations in Part II.

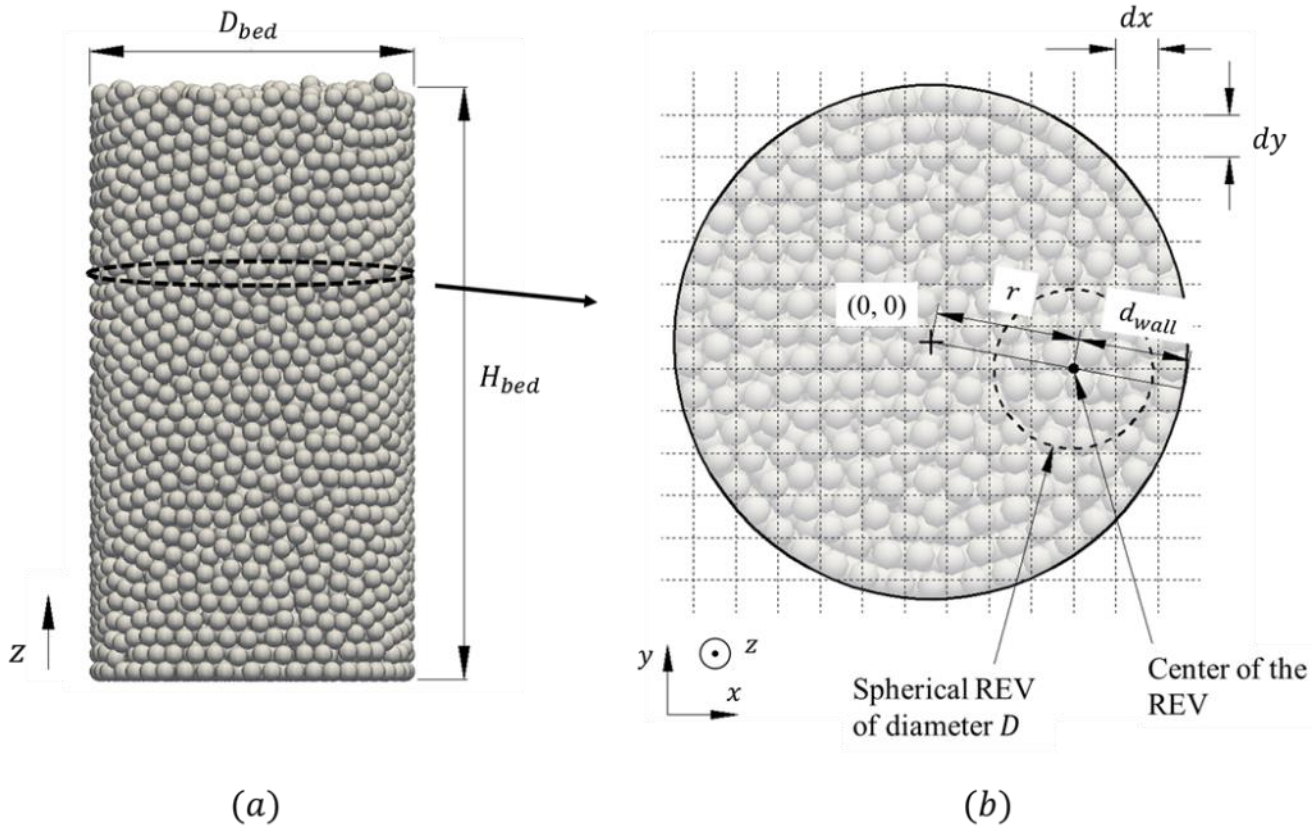

Figure 5.3: Virtual cylindrical monodisperse sphere packing generated with LIGGGHTS (d_s = 6.27 mm, D_{bed} = 101.6 mm, H_{bed} = 200 mm, overall granular bed void fraction = 0.406): (a) front view; (b) typical cross-section with rectangular grid applied.

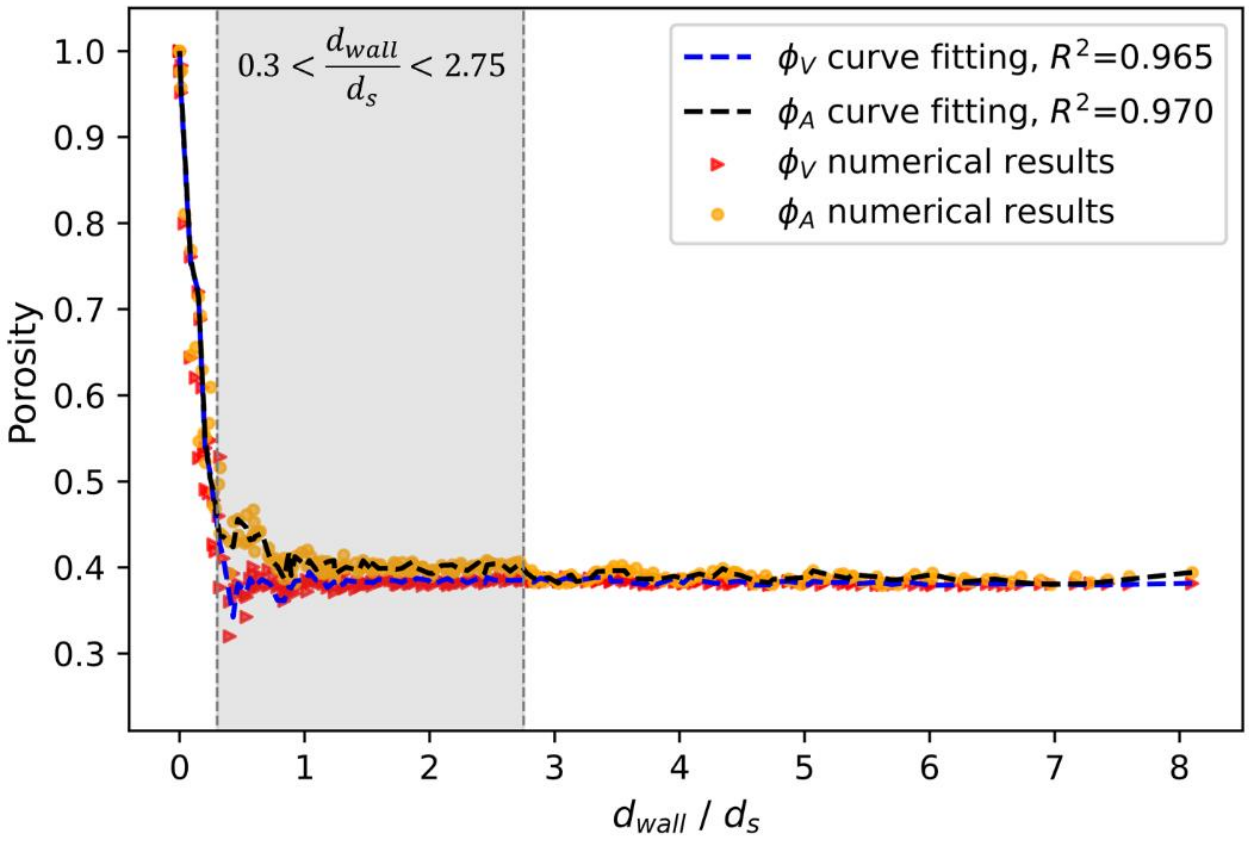

Figure 5.4: The volume (ϕ_V) and area porosity (ϕ_A) values determined with the virtual granular bed (Figure 5.3) as a function of d_{wall}/d_s. Two piecewise linear fitted curves for ϕ_V and ϕ_A are plotted. Note that the values of ϕ_V and ϕ_A show a significant difference in the shaded area (i.e., $0.3 < d_{wall}/d_s < 2.75$).

5.7 Independency of the exponential radial porosity profile

As mentioned in the literature survey, the porosity distribution of monodisperse packings is a structural dependent parameter and should be independent of flow fields. Different investigations [51, 53, 56] on the oscillatory porosity model confirmed that the radial porosity distribution is a function of d_{wall}/d_s only. Monodisperse sphere packings of different d_s should be described with the same correlation and the corresponding exponential profile should be the same. To verify this, the methodology presented in the above section is repeated and applied to two additional virtual

packings of different bead sizes (d_s), namely 3 mm and 9 mm. The other parameters remain unchanged, i.e., D_{bed} = 101.6 mm, H_{bed} = 200 mm, $dx = dy = dz = 5$ mm and overall packing void fraction = ~0.4. The results are plotted as a function of d_{wall}/d_s and shown in Figure 5.5. The data points are compared with the exponential porosity models (i.e., Eq. (5.1) to Eq. (5.4)) published in the literature by calculating the R^2 value for each model. The one proposed by Hunt and Tien [124] as well as the model of White and Tien [125] agree with current numerical results with R^2 values of 0.94 and 0.79 respectively.

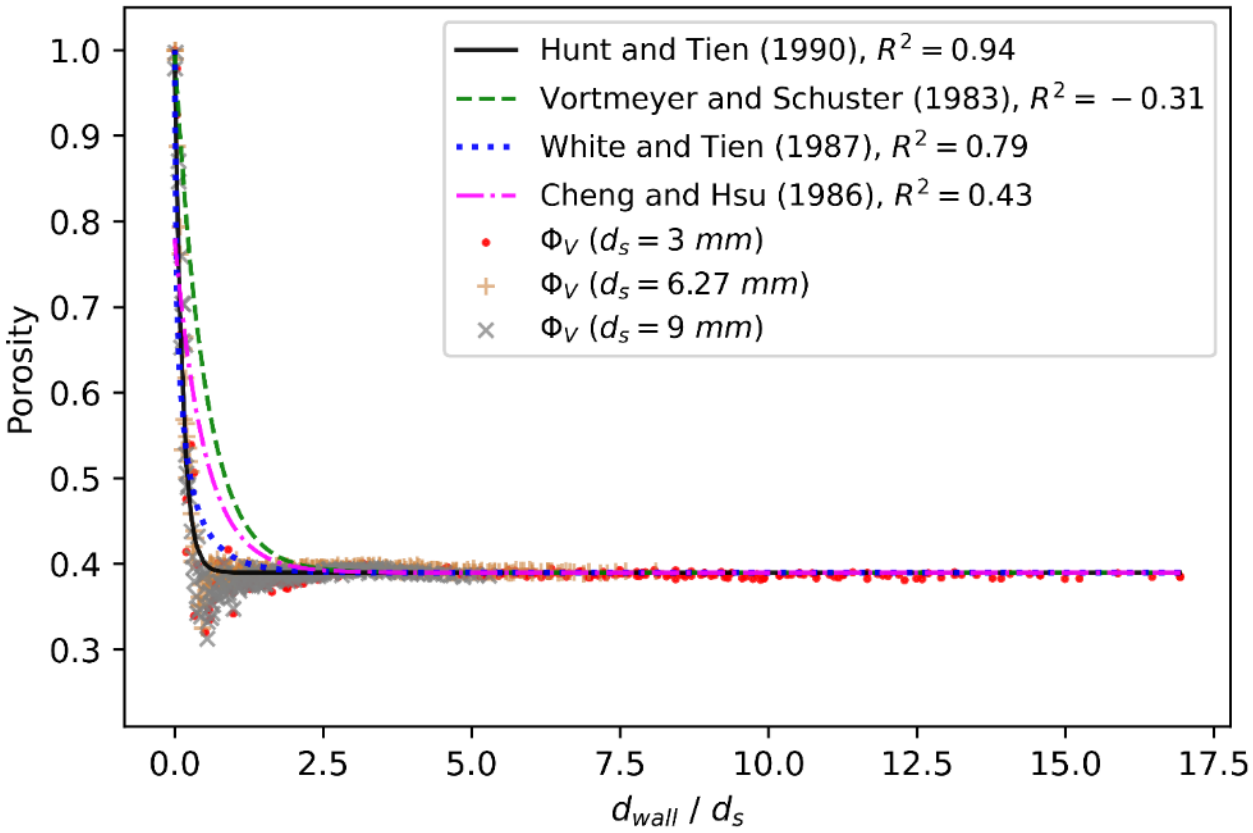

Figure 5.5: Volume porosity (ϕ_V) values determined with different virtual granular beds as a function of d_{wall}/d_s. The exponential porosity models published in the literature, i.e., Eq. (5.1) to Eq. (5.4), are also plotted.

5.8 Conclusion

The present article derived macroscopic transport equations for wall confined bead packings using the method of volume averaging and a non-constant REV. The main contributions are summarized as follows:

1. Compared with the conventional volume averaging method using a constant REV, the use of a non-constant REV prevents a third phase (i.e., the wall) from entering the REV near the containing wall. This theoretically simplifies the derivation of the macroscopic transport equations in a bead packing confined by a wall without necessarily considering the wall as a third phase.
2. With the non-constant REV, the incompatibility of quantities is eliminated at the wall by transforming the volume-averaged quantities in the granular bed to pointwise quantities at the interface. This allows a clear definition of boundary conditions at the interface between the bead packing and the wall.
3. The use of the non-constant REV subsequently allowed determining the exponential porosity profile directly from the packing structure. The profile is shown to be a function of d_{wall}/d_s only (Figure 5.5). This reduces the uncertainty in the selection of the porosity model and facilitates the modeling of transport phenomena in such wall-confined bead packings.

It should be noted that the model proposed by Hunt and Tien [124] is only valid for mono-sized spheres and the methodology presented in the literature to determine the oscillatory model is limited to axisymmetric geometries (e.g. cylinder). The analysis presented in this study is more general since it can be applied to packings of mixed spheres of different sizes and complex geometries, which could be studied in future investigations. In Part II of the study, a numerical simulation based on the governing equations derived in this paper (Eq. (5.20), (5.23), (5.31) and (5.32)) will be performed. The numerical predictions will be compared with experimental data and the important parameters in the model will be discussed.

5.9 Acknowledgements

This work was supported by the *National Science & Engineering Research Council of Canada* (NSERC) (Discovery Grants). Authors also gratefully acknowledge the *Research Center for High Performance Polymer and Composite Systems* (CREPEC) and the "*Fonds de recherche du Québec - Nature et technologies*" (FRQNT) for their partial financial support. Authors also express their sincere thanks to Christian-Charles Martel, technical assistant, for his support in the laboratory.

5.10 Appendix A. Volume-averaged momentum equation

We begin our analysis by averaging Eq. (5.21):

$$\frac{1}{V}\int_{V_f}\frac{\partial}{\partial t}\left(\rho_f\,\boldsymbol{u_f}\right)dV+\frac{1}{V}\int_{V_f}\nabla\cdot\left(\rho_f\,\boldsymbol{u_f}\boldsymbol{u_f}\right)dV = -\frac{1}{V}\int_{V_f}\nabla p\,dV+\frac{1}{V}\int_{V_f}\nabla\cdot\bar{\bar{\tau}}\,dV+\frac{1}{V}\int_{V_f}\rho_f\,\boldsymbol{g}\,dV \tag{5.33}$$

With Eq. (5.17), the first term on the left-hand side of Eq. (5.33) can be expressed as:

$$\frac{1}{V}\int_{V_f}\frac{\partial}{\partial t}\left(\rho_f\,\boldsymbol{u_f}\right)dV=\frac{\partial}{\partial t}\left(\phi_V\,\langle\rho_f\rangle^f\,\langle\boldsymbol{u_f}\rangle^f\right) \tag{5.34}$$

Using Gray's theorem [132] and considering no mass transfer between phases, the second term on the left-hand side of Eq. (5.33) writes:

$$\frac{1}{V}\int_{V_f}\nabla\cdot\left(\rho_f\,\boldsymbol{u_f}\boldsymbol{u_f}\right)dV = \nabla\cdot\left(\phi_V\,\langle\rho_f\,\boldsymbol{u_f}\boldsymbol{u_f}\rangle^f\right)+\frac{\nabla V}{V}\left(\phi_V\,\langle\rho_f\,\boldsymbol{u_f}\boldsymbol{u_f}\rangle^f-\phi_A\,\langle\rho_f\,\boldsymbol{u_f}\boldsymbol{u_f}\rangle_A^f\right) \tag{5.35}$$

We make use of the simplified form of $\langle\rho_f\,\boldsymbol{u_f}\boldsymbol{u_f}\rangle^f$ developed by Faghri and Zhang [136]:

$$\langle\rho_f\,\boldsymbol{u_f}\boldsymbol{u_f}\rangle^f=\langle\rho_f\rangle^f\,\langle\boldsymbol{u_f}\boldsymbol{u_f}\rangle^f=\langle\rho_f\rangle^f\left(\langle\boldsymbol{u_f}\rangle^f\langle\boldsymbol{u_f}\rangle^f+\langle\boldsymbol{u'_f}\boldsymbol{u'_f}\rangle^f\right) \tag{5.36}$$

where $\boldsymbol{u'_f}$ is the fluctuating part of $\boldsymbol{u_f}$ defined as $\boldsymbol{u'_f} = \boldsymbol{u_f} - \langle \boldsymbol{u_f} \rangle^f$. Following the development discussed in Eq. (5.19) and assuming low variations within the REV, $\langle \rho_f \, \boldsymbol{u_f u_f} \rangle_A$ writes:

$$\langle \rho_f \, \boldsymbol{u_f u_f} \rangle_A^f = \langle \rho_f \rangle_A^f \, \langle \boldsymbol{u_f u_f} \rangle_A^f = \langle \rho_f \rangle^f \, \langle \boldsymbol{u_f u_f} \rangle^f \tag{5.37}$$

Directing the attention to the right-hand side of Eq. (5.33), with Gray's theorem [132], the first term writes:

$$-\frac{1}{V}\int_{V_f} \nabla p \, dV = -\nabla \left(\phi_V \, \langle p \rangle^f\right) - \frac{\nabla V}{V} \, \langle p \rangle^f \, (\phi_V - \phi_A) - \frac{1}{V}\int_{A_{fs}} \boldsymbol{n_{fs}} \, p \, dA \tag{5.38}$$

The pressure p is then decomposed as an intrinsic averaged term $\langle p \rangle^f$ and a fluctuating part p', i.e., $p = \langle p \rangle^f + p'$. Eq. (5.38) is then expressed as:

$$\begin{aligned} -\frac{1}{V}\int_{V_f} \nabla p \, dV = & -\phi_V \, \nabla \langle p \rangle^f - \langle p \rangle^f \, \nabla \phi_V \\ & - \frac{\langle p \rangle^f}{V}\int_{A_{fs}} \boldsymbol{n_{fs}} \, dA - \frac{1}{V}\int_{A_{fs}} \boldsymbol{n_{fs}} \, p' \, dA - \frac{\nabla V}{V} \, \langle p \rangle^f \, (\phi_V - \phi_A) \end{aligned} \tag{5.39}$$

We make use of the equation proposed by Whitaker [120]:

$$\frac{1}{V}\int_{A_{fs}} \boldsymbol{n_{fs}} \, dA = -\nabla \, \phi_V \tag{5.40}$$

and write Eq. (5.39) as:

$$-\frac{1}{V}\int_{V_f} \nabla p \, dV = -\phi_V \, \nabla \langle p \rangle^f - \frac{1}{V}\int_{A_{fs}} \boldsymbol{n_{fs}} \, p' \, dA - \frac{\nabla V}{V} \, \langle p \rangle^f \, (\phi_V - \phi_A) \tag{5.41}$$

The second term on the right-hand side of Eq. (5.33) can be written as:

$$\frac{1}{V}\int_{V_f} \nabla \cdot \bar{\bar{\tau}} \, dV = \nabla \cdot \left(\phi_V \, \langle \bar{\bar{\tau}} \rangle^f\right) + \frac{\nabla V}{V} \, \langle \bar{\bar{\tau}} \rangle^f \, (\phi_V - \phi_A) + \frac{1}{V}\int_{A_{fs}} \boldsymbol{n_{fs}} \, \bar{\bar{\tau}} \, dA \tag{5.42}$$

As $\boldsymbol{g}$ is constant, the last term on the right-hand side of Eq. (5.33) can be written explicitly as:

$$\frac{1}{V}\int_{V_f}\rho_f\,\boldsymbol{g}\,dV\;=\;\frac{\boldsymbol{g}}{V}\int_{V_f}\rho_f\,dV=\phi_V\,\langle\rho_f\rangle^f\,\boldsymbol{g} \tag{5.43}$$

Substitution of Eq. (5.34) to (5.37) and Eq. (5.41) to (5.43) into Eq. (5.33) yields finally:

$$\begin{aligned}&\frac{\partial}{\partial t}\left(\phi_V\,\langle\rho_f\rangle^f\,\langle\boldsymbol{u_f}\rangle^f\right)+\nabla\cdot\left(\phi_V\,\langle\rho_f\rangle^f\,\langle\boldsymbol{u_f}\rangle^f\langle\boldsymbol{u_f}\rangle^f\right)\\&=-\phi_V\,\nabla\langle p\rangle^f+\nabla\left(\phi_V\,\langle\bar{\bar{\tau}}\rangle^f\right)+\phi_V\,\langle\rho_f\rangle^f\,\boldsymbol{g}-\nabla\\&\cdot\left(\phi_V\,\langle\rho_f\rangle^f\,\langle\boldsymbol{u'_f u'_f}\rangle^f\right)+\frac{1}{V}\int_{A_{fs}}\boldsymbol{n_{fs}}\,(\bar{\bar{\tau}}-p')\,dA\\&+\frac{\nabla V}{V}\,(\phi_V-\phi_A)\left(\langle\bar{\bar{\tau}}\rangle^f-\langle\rho_f\rangle^f\,\langle\boldsymbol{u_f u_f}\rangle^f-\langle p\rangle^f\right)\end{aligned} \tag{5.44}$$

This gives Eq. (5.23) in the main text.

5.11 Appendix B. Volume-averaged thermal energy equations

5.11.1 Fluid phase volume-averaged thermal energy equation

The following equation is obtained by averaging Eq. (5.24) over a REV of volume V:

$$\frac{1}{V}\int_{V_f}\frac{\partial}{\partial t}\left(\rho_f\,C_f\,T_f\right)dV+\frac{1}{V}\int_{V}\nabla\cdot\left(\rho_f\,C_f\,T_f\,\boldsymbol{u_f}\right)dV=\frac{1}{V}\int_{V_f}\nabla\cdot\left(\lambda_f\,\nabla T_f\right)dV \tag{5.45}$$

The integration and differentiation of the first term on the left-hand side of Eq. (5.45) can be interchanged, due to the independency in time:

$$\frac{1}{V}\int_{V_f}\frac{\partial}{\partial t}\left(\rho_f\,C_f\,T_f\right)dV=\frac{\partial}{\partial t}\left(\frac{1}{V}\int_{V_f}\rho_f\,C_f\,T_f\,dV\right)=\frac{\partial}{\partial t}\left(\phi_V\,\langle\rho_f\,C_f\,T_f\rangle^f\right) \tag{5.46}$$

Based on Gray's theorem [132] for non-constant REV and the assumption that no mass transfer occurs between phases, the second term on the left-hand side of Eq. (5.45) writes:

$$\frac{1}{V}\int_{V_f} \nabla \cdot \left(\rho_f\, C_f\, T_f\, \boldsymbol{u_f}\right) dV$$
$$= \nabla \cdot \left(\phi_V\, \langle \rho_f\, C_f\, T_f\, \boldsymbol{u_f} \rangle^f\right) + \frac{\nabla V}{V}\left(\phi_V\, \langle \rho_f\, C_f\, T_f\, \boldsymbol{u_f} \rangle^f - \phi_A\, \langle \rho_f\, C_f\, T_f\, \boldsymbol{u_f} \rangle_A^f\right) \tag{5.47}$$

We make use now of the analysis presented by Whitaker [120] and Ochoa-Tapia and Whitaker [133] to simplify the terms $\langle \rho_f\, C_f\, T_f\, \boldsymbol{u_f} \rangle$, $\langle \rho_f\, C_f\, T_f\, \boldsymbol{u_f} \rangle_A$ and $\langle \rho_f\, C_f\, T_f \rangle$ as follows:

$$\langle \rho_f\, C_f\, T_f \rangle^f = \langle \rho_f \rangle^f\, \langle C_f \rangle^f\, \langle T_f \rangle^f \tag{5.48}$$

$$\langle \rho_f\, C_f\, T_f\, \boldsymbol{u_f} \rangle_A^f = \langle \rho_f \rangle^f\, \langle C_f \rangle^f\, \langle T_f \rangle^f\, \langle \boldsymbol{u_f} \rangle^f \tag{5.49}$$

$$\langle \rho_f\, C_f\, T_f\, \boldsymbol{u_f} \rangle^f = \langle \rho_f \rangle^f\, \langle C_f \rangle^f\, \langle T_f \rangle^f\, \langle \boldsymbol{u_f} \rangle^f \tag{5.50}$$

Using Gray's theorem [132] another time, the term on the right-hand side of Eq. (5.45) writes as follows:

$$\frac{1}{V}\int_{V_f} \nabla \cdot \left(\lambda_f\, \nabla T_f\right) dV$$
$$= \nabla \cdot \left(\phi_V\, \lambda_{f_{eff}}\, \nabla \langle T_f \rangle^f\right) + \frac{\nabla V}{V}\, \lambda_{f_{eff}}\, \nabla \langle T_f \rangle^f\, (\phi_V - \phi_A) \tag{5.51}$$
$$+ \frac{1}{V}\int_{A_{fs}} \boldsymbol{n_{fs}} \cdot \left(\lambda_f\, \nabla T_f\right) dA$$

where $\lambda_{f_{eff}}$ is the effective thermal conductivity of the fluid. Considering the turbulence of the flow, $\lambda_{f_{eff}}$ is computed as:

$$\lambda_{f_{eff}} = \lambda_f + \frac{\langle C_f \rangle^f\, \mu_t}{\mathrm{Pr_t}} \tag{5.52}$$

where μ_t is the eddy viscosity, and $\mathrm{Pr_t}$ the turbulent Prandtl number. The effect of turbulence modelling will be discussed in detail in Part II. Substituting Eq. (5.46) to (5.51) into Eq. (5.45) provides:

$$\frac{\partial}{\partial t}\left(\phi_V \langle\rho_f\rangle^f \langle C_f\rangle^f \langle T_f\rangle^f\right) + \nabla\cdot\left(\phi_V \langle\rho_f\rangle^f \langle C_f\rangle^f \langle T_f\rangle^f \langle \boldsymbol{u_f}\rangle^f\right)$$
$$= \nabla\cdot\left(\phi_V \lambda_{f_{eff}} \nabla\langle T_f\rangle^f\right) + \frac{1}{V}\int_{A_{fs}} \boldsymbol{n_{fs}}\cdot\left(\lambda_f \nabla T_f\right) dA \qquad (5.53)$$
$$+ \frac{\nabla V}{V}(\phi_V - \phi_A)\left(\lambda_{f_{eff}} \nabla\langle T_f\rangle^f - \langle\rho_f\rangle^f \langle C_f\rangle^f \langle T_f\rangle^f \langle \boldsymbol{u_f}\rangle^f\right)$$

This gives Eq. (5.26) in the main text.

5.11.2 Solid phase volume-averaged thermal energy equation

Averaging Eq. (5.25) over a REV of volume V gives:

$$\frac{1}{V}\int_{V_s}\frac{\partial}{\partial t}(\rho_s C_s T_s)\, dV = \frac{1}{V}\int_{V_s}\nabla\cdot(\lambda_s \nabla T_s)\, dV \qquad (5.54)$$

where V_s is the volume of solid beads in the REV. The solid phase intrinsic volume average of a quantity ψ is defined as:

$$\langle\psi\rangle^s = \frac{1}{V_s}\int_{V_s}\psi\, dV = \frac{1}{(1-\phi_V)\, V}\int_{V_s}\psi\, dV \qquad (5.55)$$

The integration and differentiation of the term on the left-hand side of Eq. (5.54) can be interchanged. Applying the simplification proposed by Whitaker [120] and Ochoa-Tapia and Whitaker [133] gives:

$$\frac{1}{V}\int_{V_s}\frac{\partial}{\partial t}(\rho_s C_s T_s)\, dV = \frac{\partial}{\partial t}\left[(1-\phi_V)\langle\rho_s\rangle^s \langle C_s\rangle^s \langle T_s\rangle^s\right] \qquad (5.56)$$

The term on the right-hand side of Eq. (5.54) may be expressed in the same way as the term in fluid phase equation:

$$\frac{1}{V}\int_{V_s} \nabla \cdot (\lambda_s \nabla T_s)\, dV$$

$$= \nabla \cdot \left[(1-\phi_V)\, \lambda_s \nabla \langle T_s \rangle^s\right] + \frac{\nabla V}{V}\, \lambda_s \nabla \langle T_s \rangle^s\, (\phi_A - \phi_V) \tag{5.57}$$

$$+ \frac{1}{V}\int_{A_{sf}} \boldsymbol{n_{sf}} \cdot (\lambda_s \nabla T_s)\, dA$$

Substitution of Eq. (5.56) and (5.57) into Eq. (5.54) results in:

$$\frac{\partial}{\partial t}\left[(1-\phi_V)\, \langle \rho_s \rangle^s\, \langle C_s \rangle^s\, \langle T_s \rangle^s\right]$$

$$= \nabla \cdot \left[(1-\phi_V)\, \lambda_s \nabla \langle T_s \rangle^s\right] + \frac{1}{V}\int_{A_{sf}} \boldsymbol{n_{sf}} \cdot (\lambda_s \nabla T_s)\, dA \tag{5.58}$$

$$+ \frac{\nabla V}{V}\, \lambda_s \nabla \langle T_s \rangle^s\, (\phi_A - \phi_V)$$

This gives Eq. (5.27) in the main text.

5.12 Appendix C. Calculation of the volume and area porosity from LIGGGHTS data

To determine the value of ϕ_V and ϕ_A for a given REV, we firstly loop through all the beads in the packing and calculate the distance between each bead center and the REV. If a bead is located entirely out of the REV, it will be excluded from the following calculation. For the other beads, there are two possible situations: the bead is located entirely and partially inside the REV. In the first situation, the entire bead's volume will be used to calculate ϕ_V and ϕ_A without any surface area term. In the second situation, the intersection volume (V_{ins}) and surface area (A_{ins}) are calculated by the following equations:

$$V_{ins} = \frac{\pi}{12\, d_{ss}}\, (R + r_s - d_{ss})^2 (d_{ss}^2 + 2\, d_{ss}\, r_s - 3\, r_s^2 + 2\, d_{ss}\, R + 6\, r_s\, R - 3R^2) \tag{5.59}$$

$$A_{ins} = 2\,\pi\,R\,\frac{r_s^2 - (R - d_{ss})^2}{2\,d_{ss}} \tag{5.60}$$

where d_{ss} is the distance between the two sphere centers, R is the radius of the spherical REV and r_s is the radius of the bead. A schematic diagram is given in Figure 5.6. We calculated and summed up the volume and area of each single bead to obtain the total beads occupied volume and bounding area for the REV. Then the value of ϕ_V and ϕ_A can be determined.

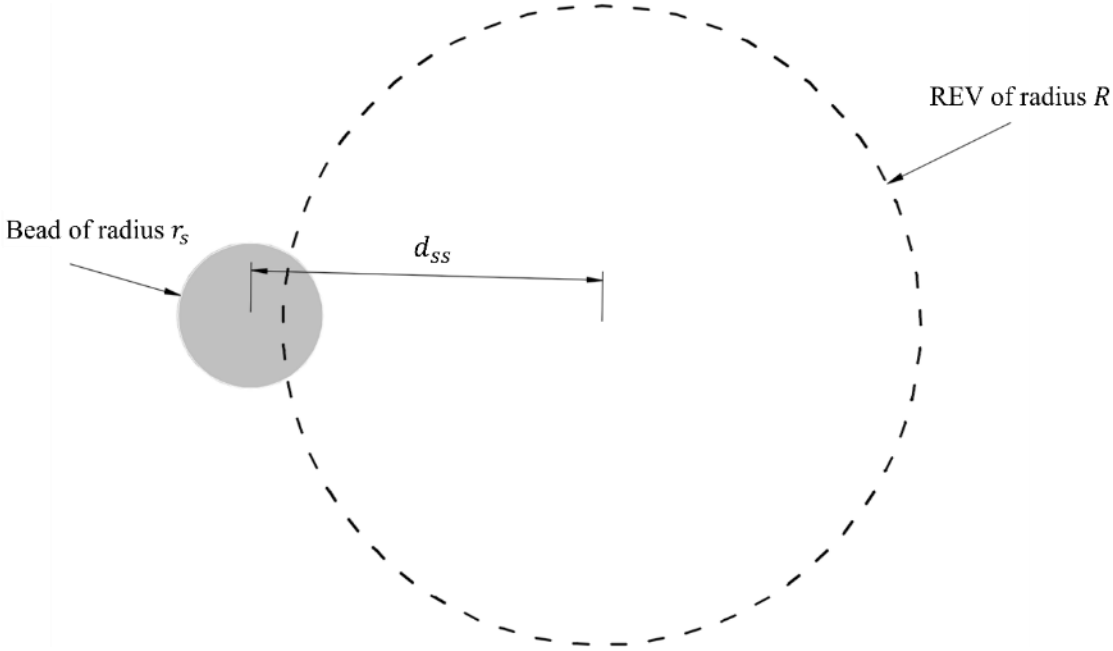

Figure 5.6: Schematic of a typical spherical REV that intersects with a bead.

CHAPTER 6 ARTICLE 3: CONVECTIVE HEAT TRANSFER BETWEEN A BEAD PACKING AND ITS BOUNDING WALL: PART II – NUMERICAL ANALYSIS AND EXPERIMENTAL VALIDATION

Yixun Sun, Cédric Béguin, Philippe Causse, Brahim Benmokrane and François Trochu

Submitted to *Transport in Porous Media* on 22/04/2021

6.1 Chapter overview

This chapter is the second part of the article in two parts submitted to *Transport in Porous Media*. An experimental study is presented to validate the governing equations derived in Chapter 5 by comparing with the measured temperature and heat flux values in a wall-bounded cylindrical bead packing. The empirical parameters used in the numerical model are discussed, which includes the convective heat transfer coefficient and the turbulent source near the wall. This completes the modelling framework and will be used in the following chapters to analyze the thermal performance of granular molds and study the effect of different design parameters.

6.2 Abstract

The volume averaged transport equations for wall confined bead packings were derived in Part I using a non-constant *Representative Elementary Volume* (REV). This eliminates the incompatibility of the volume averaged quantities of the bead packing and pointwise quantities of the wall at the interface. This also allowed determining the exponential porosity profile directly from the packing structure for *Reynolds-Averaged Navier-Stokes* (RANS) *Computational Fluid Dynamics* (CFD) simulations. In Part II, the governing equations proposed in Part I are used to simulate the forced convective heat transfer from the bead packing to its containing wall. The predictive capability of the model is validated by comparing with experimentally measured temperature and heat flux values. Further discussion shows that a close agreement between

numerical and experimental results can be achieved if additional turbulence source terms induced by the presence of beads are properly modelled.

KEYWORDS: Bead packings, forced convection, volume averaging, wall-to-bed heat transfer

6.3 Introduction

In Part I of this article, two main challenges were summarized in modelling the convective heat transfer between a random monodisperse bead packing and its bounding wall: (1) the incompatibility of quantities at the interface where the volume averaged quantities in the granular bed confront with the pointwise quantities of the solid wall; and (2) the selection of the exponential porosity model for a typical *Reynolds-Averaged Navier-Stokes* (RANS) *Computational Fluid Dynamics* (CFD) simulation. These two issues were addressed by deriving volume averaged transport equations using a non-constant *Representative Elementary Volume* (REV). The second part of the study completes this investigation by performing numerical simulations based on the derived governing equations and by validating the numerical model experimentally.

In the present Part II, specific issues related to performing numerical simulations of forced convection in packed beds are studied and discussed. The first one is the disagreement on temperature continuity at the wall-bed interface. As a matter of fact, some studies reported large temperature differences between the fluid and wall sides at the interface [137, 138]. Due to practical difficulties, the fluid temperature at the wall was extrapolated from measured temperature values at different radial positions, whereas the wall temperature was measured directly. However, Tsotsas and Schlünder [139] questioned the existence of such heat transfer resistance at the wall. They showed that the ‘temperature jump’ could be caused by an unmixed sublayer of fluid located in the immediate vicinity of the wall. A continuous temperature profile was also considered at the interface in some numerical studies [57, 140].

Secondly, as demonstrated in Part I, several terms appearing in the governing equations are determined empirically to facilitate the modelling process, such as the interactive force between phases in momentum equations and the interfacial heat exchange between the fluid and the beads in the energy conservation equations. Justification of the empirical parameters selection is therefore

needed to provide specific rules for similar modelling process. Part II of the study begins by presenting the setup and test procedure used to gather experimental data for model validation. The numerical implementation of the governing equations is presented in the second section, including a presentation of the empirical parameters used in the numerical model. In the final section, the numerical predictions are compared with experiments and the selection of appropriate empirical parameters is discussed.

Note also that the current investigation was conducted for large bed-to-particle ratios, namely around 16.2, for which the variations of porosity near the wall do not affect the flow and heat transfer in the middle of the granular bed. This agrees with Winterberg and Tsotsas [141], who demonstrated the applicability of Ergun's equation and exponential radial porosity model to predict the pressure drop if the bed-to-particle ratio is higher than 10. For smaller bed-to-particle ratios, the concept of volume averaging may be not suited. However, it is important to determine the local porosity oscillation near the wall, since a non-uniform local velocity distribution appears and affects significantly the flow behavior [53, 142]. The heat transfer mechanism is also different. For small bed-to-particle ratios (i.e., smaller than 10), the conduction in the beads becomes important and Nusselt number exhibits a strong dependency of the size ratio [139, 143]. As presented in section 4.2, such a dependency does not appear in correlations for large bed-to-particle ratios.

6.4 Experimental setup and test procedure

6.4.1 Experimental setup

An experimental setup was designed and built to study the heating of a cylindrical packed bed and its bounding wall under forced convection. The system, which consists of a heating circuit and a test section, is schematically depicted in Figure 6.1. The testing fluid (air) is supplied by the laboratory compressed air system and the flow rate (Q_{ro}) is controlled and measured by a valve and a rotameter. A pressure sensor and a thermocouple are used to measure the pressure (P_{ro}) and temperature (T_{ro}) at the rotameter. Before entering the test section, the air flow passes through a heat exchanger connected to a closed heating circuit filled with thermal oil (Ucon 50HB-660, Dow Inc.). The heating circuit comprises an oil tank, a pump and an electrical heater to control the oil temperature (T_{oil}). All the pipes and the oil tank are insulated to reduce the heat loss.

Figure 6.2 schematically describes the details of the test section. The packed bed is composed of ceramic beads placed in a vertical transparent acrylic pipe of inside diameter 101.6 mm (4 inches). The density of the beads (ρ_s) was measured at room temperature (~23℃) following the buoyancy technique described in ASTM standard D792 [108]. This subsequently allowed evaluating the particle size, which is determined by weighing a large number of randomly selected beads (more than 1500 beads) one by one. Assuming the perfect spherical shape, the diameter of each single bead was calculated. The mean diameter (d_s) is determined as 6.27 mm. The total length of the granular bed is 625 mm. A 12.7 mm (0.5 inch) thick insulation layer is installed to cover the pipe. Two identical metallic perforated plates and mesh layers are placed at the top and bottom of the granular bed. The lower perforated plate is held by an acrylic sleeve of outside diameter 101.6 mm (4 inches) and total height of 200 mm. Note that insulation layers are also placed to cover the inner surface of the sleeve and the acrylic pipe above the upper plate. This can avoid excessive heating of the pipe wall. A pressure sensor is installed 20 mm below the lower plate to measure the inlet pressure (P_{in}). A metallic rack equipped with 8 K-type thermocouples is fixed vertically on the lower perforated plate along the central axis of the cylinder. Among these thermocouples, one is placed 10 mm below the lower perforated plate to measure the inlet air temperature (T_{in}). Four are located along the centerline of the cylinder with an interval of 125 mm to measure the axial fluid temperature of the granular bed. The others are positioned at the same axial position of z = 250 mm from the lower plate to measure the radial fluid temperature profile. The fluid temperature on the wall is measured by a thermocouple fixed on the heat flux sensor (PHFS-01 FluxTeq, thickness 0.38 mm) which is mounted at the same axial position on the inner surface of the pipe. It measures the heat flux passing through the wall and is also equipped with a thermocouple to determine the inner wall surface temperature. Four heat flux sensors are also mounted on the outer pipe surface at different axial positions (i.e., z = 125, 250, 375 and 500 mm) to measure the temperature evolution and the heat loss fluxes caused by natural convection.

The positioning error for all the sensors is considered to be ± 0.5 mm in the radial and axial directions. All the signals are detected by two National Instrument data acquisition cards (PCI-6036E, 16-Analog-Input Multifunction DAQ) plugged into the PCI (Peripheral Component Interconnect) of a computer. A LabVIEW interface was programmed to operate the system (i.e., electrical heater and pump) and perform the data acquisition.

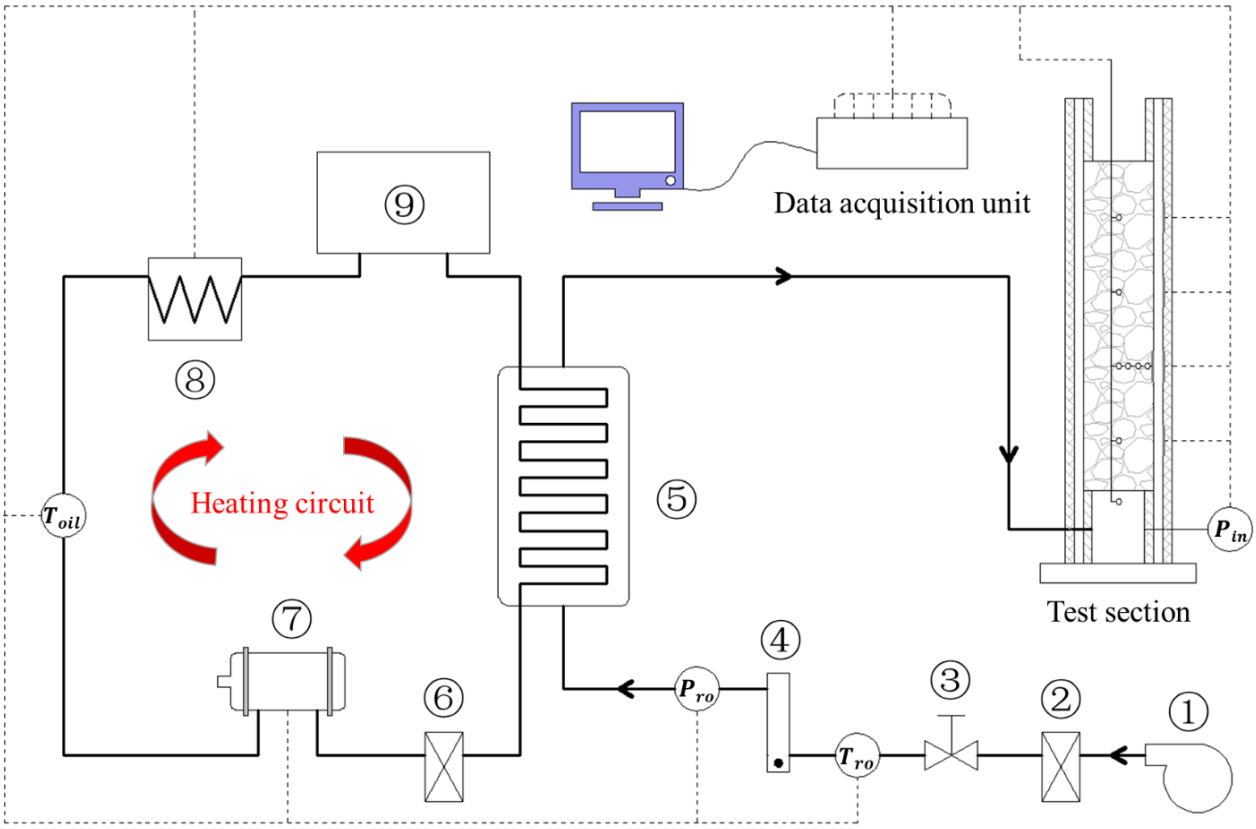

Figure 6.1: Schematic of the experimental system: (1) laboratory compressed air supply; (2) air filter; (3) valve; (4) rotameter; (5) heat exchanger; (6) hydraulic filter; (7) pump; (8) electrical heater; (9) oil tank. The dashed lines represent the wires.

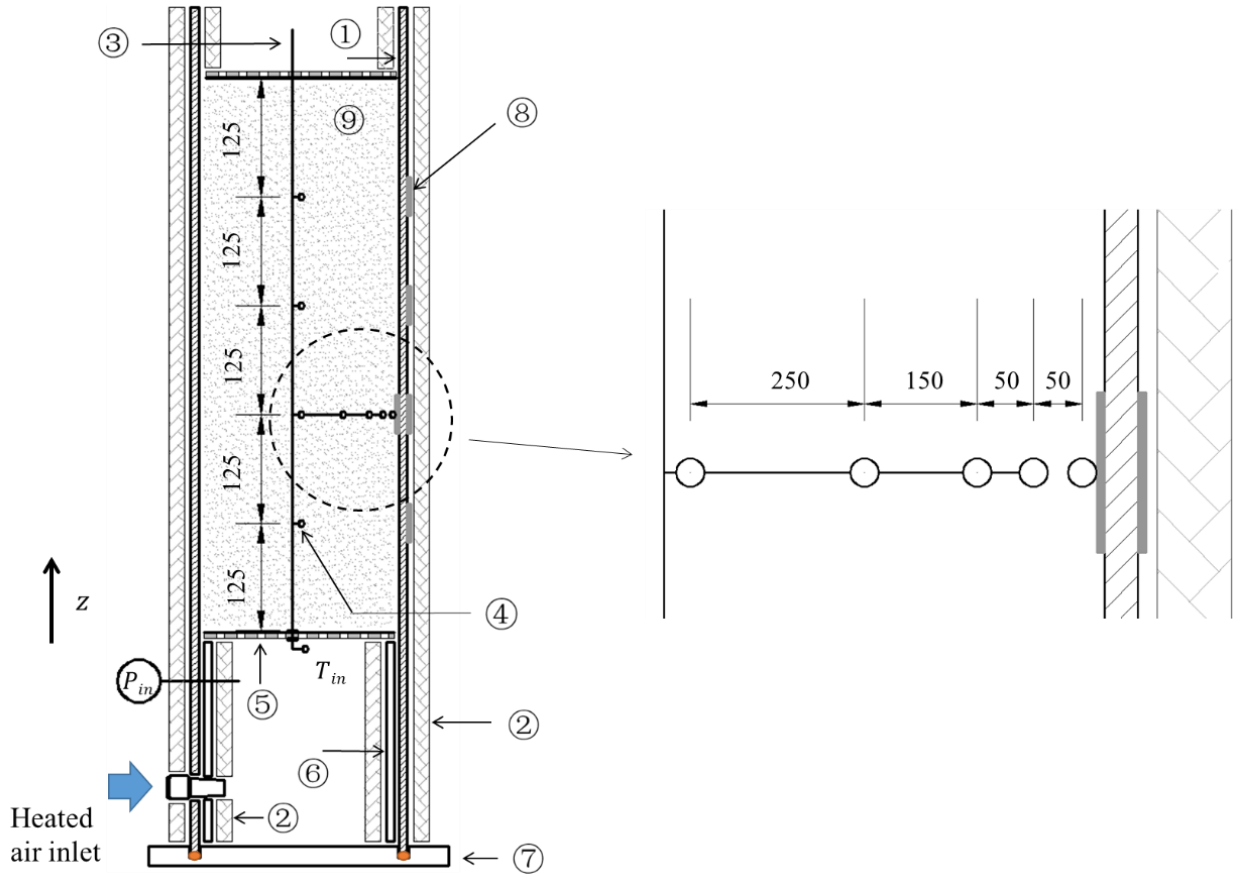

Figure 6.2: Schematic of the test section (unit: mm): (1) acrylic pipe of 4 inches inside diameter; (2) insulation layer; (3) metallic rack; (4) thermocouple; (5) mesh layer and porous plate; (6) acrylic ‘sleeve’; (7) acrylic base with groove and O-ring; (8) heat flux sensor; (9) ceramic bead packing (bed height = 625 mm, bed diameter = 101.6 mm).

6.4.2 Test procedure

The test starts by circulating the thermal oil in the heating circuit at a constant speed. The PID controller automatically operates the electrical heater to reach a temperature of 65 ± 0.8℃ throughout the test. The valve is then opened and air flows in at temperature T_{ro} and a fixed flow rate Q_{ro} of 9 SCFM. Note that the observed reading of the air volumetric flow rate Q_{ro} at the rotameter is measured for the pressure P_{ro} and temperature T_{ro}. This value should be corrected to obtain the flow rate under standard conditions (21℃, 101325 Pa) for further use. This will be presented in detail in a subsequent section. Passing through the heat exchanger, air is heated from T_{ro} to 60 ± 1.5 ℃ and enters the test section. During a typical test, all the temperature, pressure and heat flux values are measured and recorded every second. The test stops when the difference in the temperature measured by the heat flux sensors on the outer pipe surface at z = 125 and 500 mm becomes less than 2 ℃. The heating experiment was repeated three times with similar conditions. Overall, the repeatability of the test was quite satisfactory, and the experimental results reported in this study are averaged values.

6.5 Numerical analysis

The derived volume averaged governing equations were implemented in the commercial software Ansys Fluent and a transient 2D axisymmetric simulation case was created for the granular bed described in Figure 6.2. The computational domain takes only the granular bed and its containing wall into account, namely from the lower to the upper surface of the granular bed excluding the insulation layer. The simulation was performed using the standard $k - \epsilon$ turbulence model with the “enhanced wall treatment” option activated. Due to the low temperature range, thermal radiation is neglected. The simulation was performed using the standard $k - \epsilon$ turbulence model with the “enhanced wall treatment” option activated automatically in the software. The enhanced wall treatment in Fluent is a near-wall modeling method that combines the traditional two-layer model with wall functions. If the near-wall mesh is fine enough to completely resolve the viscous sublayer with $y^+ \approx 1$, then the enhanced wall treatment is identical to the two-layer model [144]. In this study, due to the presence of large solution gradients (e.g., temperature and velocity gradient), the near-wall region is fully resolved with $y^+ = 0.78$. The governing equations, the

associated empirical parameters, the input material properties and the boundary conditions used in the simulation are presented in the sequel.

6.5.1 Governing equations

In Part I of the study, the mass, momentum and energy conservation equations for the wall confined granular bed were developed based on the concept of a non-constant REV and local volume averaging technique. For the sake of brevity, only the final forms of the governing equations are presented in this section:

- Mass conservation equation:

$$\frac{\partial\left(\phi_V \langle\rho_f\rangle^f\right)}{\partial t} + \nabla \cdot \left(\phi_V \langle\rho_f\rangle^f \langle \boldsymbol{u_f}\rangle^f\right) = -\frac{\nabla V}{V} \langle\rho_f\rangle^f \langle \boldsymbol{u_f}\rangle^f (\phi_V - \phi_A) \tag{6.1}$$

where ρ_f is the air density, t the time, $\boldsymbol{u_f}$ the air velocity, ϕ_V the volume porosity, ϕ_A the area porosity, and V the volume of a non-constant REV. As presented in Part I, the radial distribution of ϕ_V is computed from the numerical results obtained for the virtual cylindrical sphere packing. The piecewise linear function for ϕ_V (i.e., the blue curve in Figure 5.4) is implemented in the simulation with *User Defined Functions* (UDFs). The symbol $\langle\,\rangle^f$ represents the fluid phase intrinsic volume average. For a given quantity ψ, the following equation can be written:

$$\langle\psi\rangle^f = \frac{1}{V_f}\int_{V_f} \psi \, dV = \frac{1}{\phi_V \, V}\int_{V_f} \psi \, dV \tag{6.2}$$

where V is the volume of the REV and V_f represents the fluid volume in the REV. Similarly, the solid bead phase intrinsic volume average writes:

$$\langle\psi\rangle^s = \frac{1}{V_s}\int_{V_s} \psi \, dV = \frac{1}{(1-\phi_V) \, V}\int_{V_s} \psi \, dV \tag{6.3}$$

where V_s represents the beads volume in the REV.

- Momentum conservation equation:

$$\begin{aligned}&\frac{\partial}{\partial t}\left(\phi_V\,\langle\rho_f\rangle^f\,\langle\boldsymbol{u_f}\rangle^f\right)+\nabla\cdot\left(\phi_V\,\langle\rho_f\rangle^f\,\langle\boldsymbol{u_f}\rangle^f\langle\boldsymbol{u_f}\rangle^f\right)\\&=-\phi_V\,\nabla\langle p\rangle^f+\nabla\left(\phi_V\,\langle\bar{\bar{\tau}}\rangle^f\right)+\phi_V\,\langle\rho_f\rangle^f\boldsymbol{g}-\\&\nabla\cdot\left(\phi_V\,\langle\rho_f\rangle^f\langle\boldsymbol{u'_f u'_f}\rangle^f\right)-\left(\frac{\phi_V^2\,\mu_f}{K}\,\langle\boldsymbol{u_f}\rangle^f+\frac{\phi_V^3\,C}{2}\langle\rho_f\rangle^f\left|\langle\boldsymbol{u_f}\rangle^f\right|\langle\boldsymbol{u_f}\rangle^f\right)\\&+\frac{\nabla V}{V}\,(\phi_V-\phi_A)\left(\langle\bar{\bar{\tau}}\rangle^f-\langle\rho_f\rangle^f\,\langle\boldsymbol{u_f u_f}\rangle^f-\langle p\rangle^f\right)\end{aligned}\tag{6.4}$$

where $\langle\boldsymbol{u_f}\rangle^f\langle\boldsymbol{u_f}\rangle^f$ represents the tensor product of the averaged fluid velocity, p is the pressure, $\boldsymbol{g}$ is the gravitational acceleration, μ_f is the fluid viscosity, K is the permeability of the granular bed, C is the inertial resistance factor and $\bar{\bar{\tau}}$ is the stress tensor calculated as follows with $\boldsymbol{I}$ the unit matrix:

$$\bar{\bar{\tau}}=\mu\left[\left(\nabla\boldsymbol{u_f}+\left(\nabla\boldsymbol{u_f}\right)^T\right)-\frac{2}{3}\nabla\cdot\boldsymbol{u_f}\,\boldsymbol{I}\right]\tag{6.5}$$

The term $\langle\rho_f\rangle^f\langle\boldsymbol{u'_f u'_f}\rangle^f$ in Eq. (6.4) represents the Reynolds stress which is determined via turbulence modelling. This will be presented in the sequel. The last two terms on the right-hand side of Eq. (6.4), i.e., $-\left(\frac{\phi_V^2\,\mu_f}{K}\,\langle\boldsymbol{u_f}\rangle^f+\frac{\phi_V^3\,C}{2}\langle\rho_f\rangle^f\left|\langle\boldsymbol{u_f}\rangle^f\right|\langle\boldsymbol{u_f}\rangle^f\right)$, is the flow resistance due to the presence of beads and the parameters K and C are determined empirically. In this study, we follow the conclusion drawn by Sun et al. [145] to compute these two parameters using the revisited Ergun's equation [43]:

$$K=\frac{d_s^2\,\phi_V^3}{180\,(1-\phi_V)^2}\tag{6.6}$$

$$C=\frac{3.6\,(1-\phi_V)}{d_s\,\phi_V^3}\tag{6.7}$$

- Energy conservation equations:

The volume averaged thermal energy equation of the fluid phase writes:

$$\frac{\partial}{\partial t}\left(\phi_V \langle\rho_f\rangle^f \langle C_f\rangle^f \langle T_f\rangle^f\right) + \nabla\cdot\left(\phi_V \langle\rho_f\rangle^f \langle C_f\rangle^f \langle T_f\rangle^f \langle \boldsymbol{u_f}\rangle^f\right)$$
$$= \nabla\cdot\left(\phi_V \lambda_{f_{eff}} \nabla\langle T_f\rangle^f\right) - a_v\, h_{sf}\left(\langle T_f\rangle^f - \langle T_s\rangle^s\right) \quad (6.8)$$
$$+ \frac{\nabla V}{V}(\phi_V - \phi_A)\left(\lambda_{f_{eff}} \nabla\langle T_f\rangle^f - \langle\rho_f\rangle^f \langle C_f\rangle^f \langle T_f\rangle^f \langle \boldsymbol{u_f}\rangle^f\right)$$

where T_f is the fluid temperature, C_f is the fluid specific heat capacity, h_{sf} is the convective heat transfer coefficient, a_v is the interfacial area per unit volume and $\lambda_{f_{eff}}$ is the fluid effective thermal conductivity. The parameter a_v can be expressed as follows for sphere packings:

$$a_v = \frac{6\,(1-\phi_V)}{d_s} \quad (6.9)$$

The coefficient h_{sf} is used to compute the convective heat exchange between the solid beads and the fluid. Due to the complexity of interfacial heat transfer, h_{sf} is obtained from empirical correlations. Such correlations are developed based on the fluid-to-particle Nusselt number (Nu) defined as:

$$\mathrm{Nu} = \frac{h_{sf}\, d_s}{\lambda_f} \quad (6.10)$$

where λ_f is the thermal conductivity of the fluid. In this study, the correlation of Wakao et al. [72] is used:

$$\mathrm{Nu} = 2 + 1.1\,\mathrm{Re_{ds}}^{0.6}\,\mathrm{Pr}^{1/3} \quad (6.11)$$

where $\mathrm{Re_{ds}}$ is the Reynolds number based on particle size and Pr is the the Prandtl number. These two parameters are calculated as follows:

$$\mathrm{Re_{d_s}} = \frac{\langle\rho_f\rangle^f\, \phi_V \left|\langle \boldsymbol{u_f}\rangle^f\right| d_s}{\mu_f} \quad (6.12)$$

$$\mathrm{Pr} = \frac{\mu_f \langle C_f\rangle^f}{\lambda_f} \quad (6.13)$$

For the solid beads, the volume averaged energy equation writes:

$$\frac{\partial}{\partial t}\left[(1-\phi_V)\,\langle\rho_s\rangle^s\,\langle C_s\rangle^s\,\langle T_s\rangle^s\right] = \nabla\cdot\left[(1-\phi_V)\,\lambda_s\,\nabla\langle T_s\rangle^s\right] - a_v\,h_{sf}\left(\langle T_s\rangle^s - \langle T_f\rangle^f\right) + \frac{\nabla V}{V}\,\lambda_s\,\nabla\langle T_s\rangle^s\,(\phi_A-\phi_V) \tag{6.14}$$

where ρ_s, T_s, C_s and λ_s represent the density, temperature, specific heat capacity and thermal conductivity of the beads. Note that the maximum radius of the non-constant REV used to determine ϕ_V and ϕ_A is 2.75 d_s (see Part I of the study). For a wall distance d_{wall} larger that this value (i.e., $d_{wall}/d_s \geq 2.75$), the size of the REV remains constant, i.e., $\nabla V = 0$, and the source terms are null. When $d_{wall}/d_s \leq 0.3$, no obvious difference between ϕ_V and ϕ_A is observed (see Figure 5.4). The difference between ϕ_V and ϕ_A mainly occurs in the range of $0.3 < d_{wall}/d_s < 2.75$. All the source terms presented in the governing equations (Eq. (6.1), Eq. (6.4), Eq. (6.8) and Eq. (6.14)) are implemented in the simulation with UDFs.

6.5.2 Input material properties

The material properties of the ceramic beads, acrylic pipe and air are summarized and reported in Table 6.1. These values are used as input parameters in the numerical study. Note that the air density (ρ_f) is determined by the ideal gas law for compressible fluids in the numerical simulation with the specific gas constant $R_{specific}$=287.055 J/(kg·K). The thermal conductivity of air (λ_f) and acrylic (λ_w), the specific heat capacity of air (C_f) and acrylic (C_w), and the air viscosity (μ_f) are all considered as temperature dependent and are implemented in the simulation with UDFs.

Table 6.1: Material properties of ceramic, air and acrylic.

Material	Parameters	Value or function	Unit	Reference
Ceramic	Density (ρ_s)	2580±30	kg/m^3	Measured by the buoyancy technique, ASTM D792 [108]
	Thermal conductivity (λ_s)	2.09	W/(m·K)	Kingery [146]
	Specific heat capacity (C_s)	846.7±17	J/(kg·K)	Measured by DSC Q2000, TA Instruments [147]
	Diameter range	5.78×10^{-3} ~ 6.70×10^{-3}	m	Measured
	Average diameter (d_s)	6.27×10^{-3}	m	Measured
Air	Thermal conductivity (λ_f)	$2.5143\times10^{-3} + 7.7288\times10^{-5}\ T + 8.6248\times10^{-11}\ T^2$	W/(m·K)	Rasmussen [148]
	Specific heat capacity (C_f)	$1.0535\times10^{3} - 3.8738\times10^{-1}\ T + 8.9321\times10^{-4}\ T^2 - 4.2048\times10^{-7}\ T^3$	J/(kg·K)	Rasmussen [148]
	Dynamic viscosity (μ_f)	$1.716\times10^{-5} \times (\frac{T}{273.15})^{1.5} \times \frac{383.55}{T + 110.4}$	Pa·s	Sutherland [149]
Acrylic	Density (ρ_w)	1170±10	kg/m^3	Measured by the buoyancy technique, ASTM D792 [108]
	Thermal conductivity (λ_w)	$8.3338\times10^{-5}\ T + 1.7149\times10^{-1}$	W/(m·K)	Eiermann and Hellwege [11]
	Specific heat capacity (C_w)	$4.0289\ T + 166.95$	J/(kg·K)	Gaur et al. [150]

6.5.3 Additional turbulence source terms induced by the granular bed

With the Boussinesq hypothesis, the Reynolds stress in Eq. (6.4) is computed as:

$$
\begin{aligned}
&-\langle\rho_f\rangle^f \langle \boldsymbol{u'_f u'_f}\rangle^f \\
&\qquad = \mu_t \left[\nabla \langle \boldsymbol{u_f}\rangle^f + \left(\nabla \langle \boldsymbol{u_f}\rangle^f\right)^T\right] \\
&\qquad -\frac{2}{3}\left(\langle\rho_f\rangle^f \langle k_f\rangle^f + \mu_t \nabla\cdot\langle \boldsymbol{u_f}\rangle^f\right)\boldsymbol{I}
\end{aligned}
\tag{6.15}
$$

where $\boldsymbol{I}$ is the unit matrix and μ_t is the eddy viscosity which writes:

$$
\mu_t = C_\mu \langle\rho_f\rangle^f \frac{\left(\langle k_f\rangle^f\right)^2}{\langle\epsilon\rangle^f} \tag{6.16}
$$

where C_μ is the $k-\epsilon$ model constant, $\langle k_f\rangle^f$ and $\langle\epsilon\rangle^f$ denote the turbulence kinetic energy and the dissipation rate. In Ansys Fluent, the conservation equations for $\langle k_f\rangle^f$ and $\langle\epsilon\rangle^f$ are written based on the void fraction of the porous medium:

$$
\begin{aligned}
&\frac{\partial}{\partial t}\left(\phi_V \langle\rho_f\rangle^f \langle k_f\rangle^f\right) + \nabla\cdot\left(\phi_V \langle\rho_f\rangle^f \langle k_f\rangle^f \langle \boldsymbol{u_f}\rangle^f\right) \\
&\qquad = \nabla\cdot\left[\phi_V \left(\mu_f + \frac{\mu_t}{\sigma_k}\right)\nabla\langle k_f\rangle^f\right] + \phi_V \langle G_k\rangle^f - \phi_V \langle\rho_f\rangle^f \langle\epsilon\rangle^f \\
&\qquad + \phi_V \langle S_k\rangle^f
\end{aligned}
\tag{6.17}
$$

$$
\begin{aligned}
&\frac{\partial}{\partial t}\left(\phi_V \langle\rho_f\rangle^f \langle\epsilon\rangle^f\right) + \nabla\cdot\left(\phi_V \langle\rho_f\rangle^f \langle\epsilon\rangle^f \langle \boldsymbol{u_f}\rangle^f\right) \\
&\qquad = \nabla\cdot\left[\phi_V \left(\mu_f + \frac{\mu_t}{\sigma_\epsilon}\right)\nabla\langle\epsilon\rangle^f\right] \\
&\qquad + \frac{\phi_V \langle\epsilon\rangle^f}{\langle k_f\rangle^f}\left(C_{\epsilon1} \langle G_k\rangle^f - C_{\epsilon2} \langle\rho_f\rangle^f \langle\epsilon\rangle^f\right) + \phi_V C_{\epsilon2} \langle S_\epsilon\rangle^f
\end{aligned}
\tag{6.18}
$$

where G_k is the generation of turbulent kinetic energy due to the fluid velocity gradient, The parameters $C_{\epsilon1}$, $C_{\epsilon2}$, σ_k and σ_ϵ, are the standard $k-\epsilon$ turbulence model constants. In this study, the values proposed by Launder and Spalding [151] are used: $C_{\epsilon1}$=1.14, $C_{\epsilon2}$=1.92, σ_k=1, σ_ϵ=1.3 and C_μ=0.09.

This modelling approach neglects the influence of beads on the turbulent kinetic energy and dissipation rate, which can be true when the pore scale is large enough and has little interactions with the eddies. For packed beds, however, the turbulent kinetic energy and dissipation rate are likely to be underestimated without a proper definition of the additional source terms $\langle S_k \rangle^f$ and $\langle S_\epsilon \rangle^f$ in Eq. (6.17) and (6.18). Guo et al. [48] evaluated several different models for $\langle S_k \rangle^f$ and $\langle S_\epsilon \rangle^f$ in a case of isothermal gas flow in a sphere packing. Their results showed the model proposed by Nakayama and Kuwahara [152] (Eq. (6.19) and (6.20)) gives the most reasonable eddy viscosity μ_t. In this study, we make use of this model to perform the simulation.

$$\langle S_k \rangle^f = \epsilon_\infty \langle \rho_f \rangle^f \tag{6.19}$$

$$\langle S_\epsilon \rangle^f = \frac{\epsilon_\infty^2}{k_\infty} \langle \rho_f \rangle^f \tag{6.20}$$

where ϵ_∞ and k_∞ are model constants, which are determined as follows:

$$\epsilon_\infty = 39\, \phi_V^2\, (1-\phi_V)^{2.5}\, \frac{\left|\langle \boldsymbol{u_f} \rangle^f\right|^3}{d_s} \tag{6.21}$$

$$k_\infty = 3.7\, \phi_V^{1.5}\, (1-\phi_V)\, \left|\langle \boldsymbol{u_f} \rangle^f\right|^2 \tag{6.22}$$

In pure fluid regions (i.e., $\phi_V = 1$), these terms are null.

6.5.4 Boundary conditions

The simulation starts by setting the initial conditions (i.e., at $t = 0$): $\langle T_f \rangle^f = \langle T_s \rangle^s = T_{in}$ and $\langle \boldsymbol{u_f} \rangle^f = 0$. A schematic diagram is given in Figure 6.3 illustrating the boundaries used in the simulation. At the inlet, an adiabatic boundary condition is applied for the bead phase. The temperature and velocity are specified for the fluid in the axial z direction:

$$\langle T_f \rangle^f = T_{in}(t), \qquad \left|\langle \boldsymbol{u_f} \rangle^f\right| = u_{in}(t) \tag{6.23}$$

During the test, T_{in} and u_{in} do not remain constant in time. As mentioned above, T_{in} is measured by the thermocouple placed at the inlet, whereas u_{in} is calculated as:

$$u_{in}(t) = \frac{T_{in}(t)}{P_{in}(t)} \cdot Q_{ro} \cdot \sqrt{\frac{P_{ref}}{T_{ro}(t)} \cdot \frac{P_{ro}(t)}{T_{ref}}} \cdot \frac{1}{\pi R_{bed}^2} \tag{6.24}$$

where R_{bed} is the radius of the granular bed, P_{ref} and T_{ref} are the standard pressure (101325 Pa) and temperature (21 °C) used to correct the reading of the rotameter Q_{ro}. The air inlet velocity u_{in} and temperature T_{in} are plotted in Figure 6.4a. With these data, the Reynolds number $\mathrm{Re_{ds}}$ of the test is determined, which varies between 400 and 450. This indicates a turbulent flow regime [153].

Four heat flux sensors are placed on the outer surface of the acrylic pipe (see Figure 6.2) to evaluate the heat loss. In the simulation, the measured heat flux values are given in negative (Figure 6.4b) representing the heat loss of the system and are directly imposed on the outer surface of the wall. The heat flux values between two measurement points are extrapolated linearly.

At the outlet, the fluid pressure $\langle p \rangle^f$ is considered as the atmospheric pressure. This is done by setting the gauge pressure to 0 in the simulation.

A symmetry condition is imposed on the central axis of the granular bed (at $r = 0$):

$$\frac{\partial \langle T_f \rangle^f}{\partial r} = \frac{\partial \langle T_s \rangle^s}{\partial r} = \frac{\partial \langle \boldsymbol{u_f} \rangle^f}{\partial r} = 0 \tag{6.25}$$

All the time dependent boundary conditions are implemented in the simulation using UDFs.

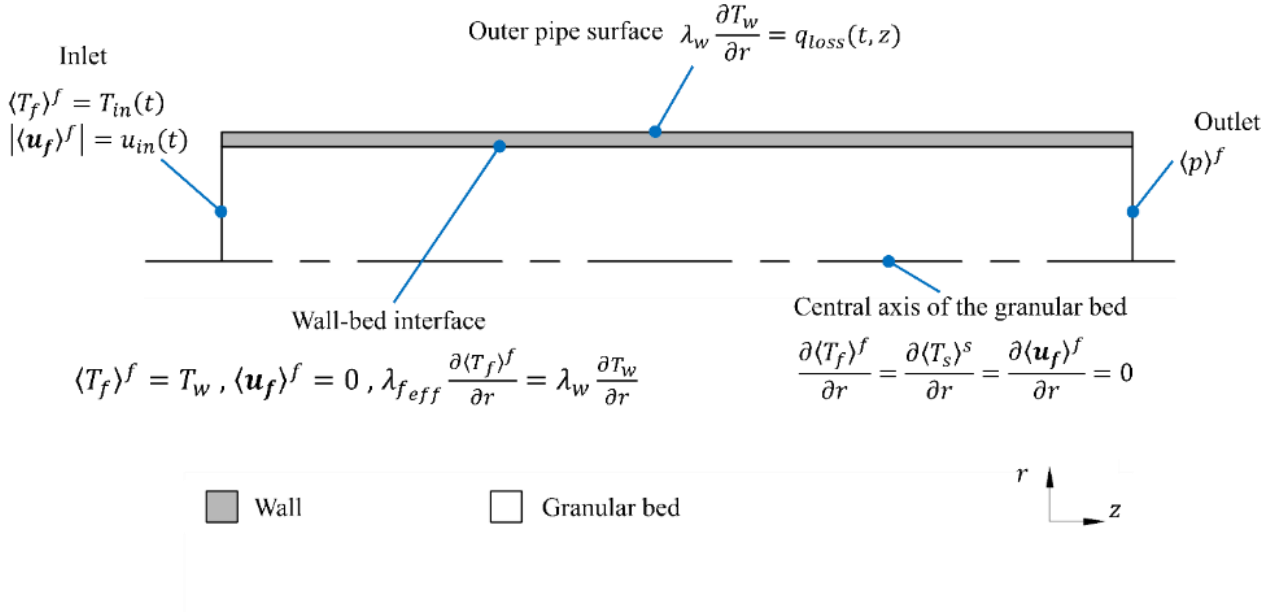

Figure 6.3: Schematic diagram of the 2D axisymmetric numerical model and boundary conditions.

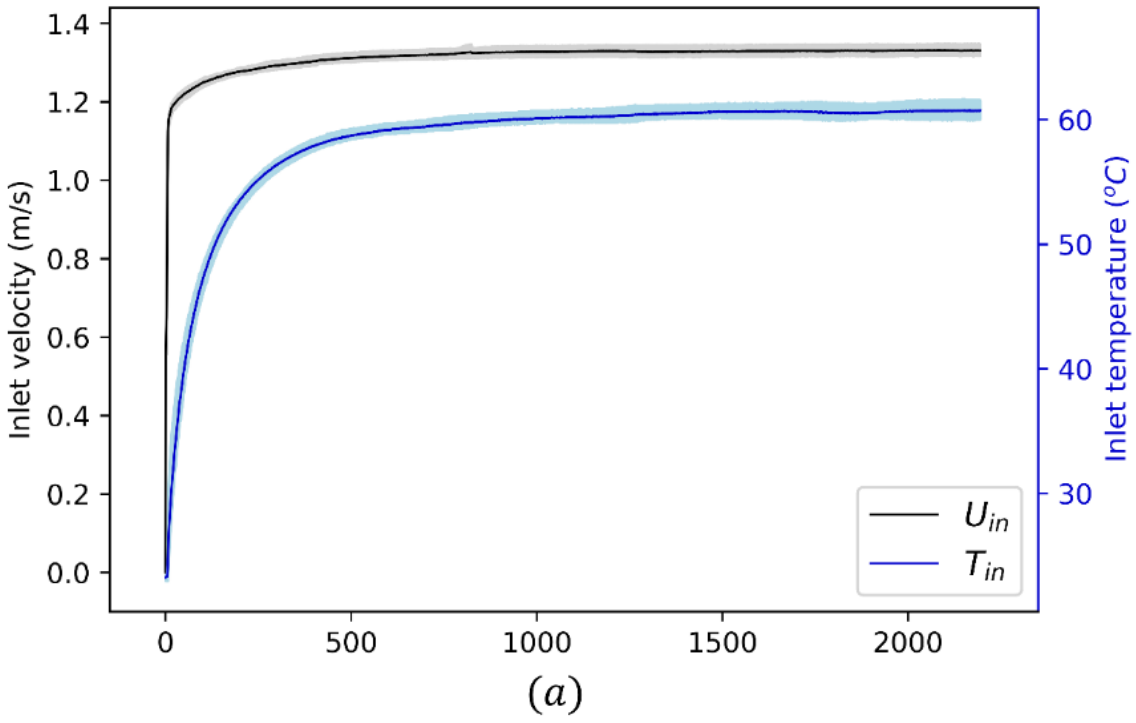

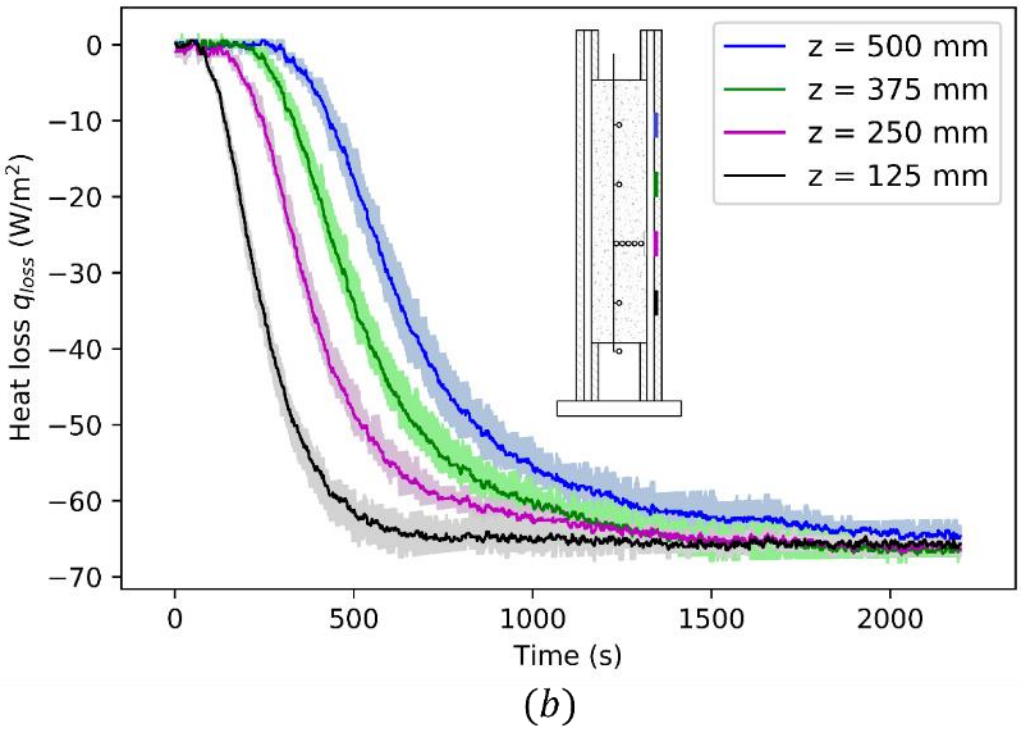

Figure 6.4. Experimental data of boundary conditions as a function of time: (a) inlet air velocity and temperature; (b) heat flux values on the outer pipe wall with colors indicating different positions (shaded areas are the range of three repeated tests, solid lines are averaged values used in the simulation).

Due to disagreements found in the published literature, the thermal boundary condition at the interface between the granular bed and the wall was determined from the experimental data. A typical radial temperature profile at z = 250 mm measured during the test is shown in Figure 6.5. The fluid temperature measured at multiple radial positions is plotted as scattered points considering the errors in positioning of $\pm$0.5 mm and in temperature of $\pm$1.1 ℃. The upper limit of the radial fluid temperature profile is extrapolated with errors of 0.5 mm and 1.1 ℃ on all the data points, whereas the lower limit is plotted by imposing -0.5 mm and -1.1 ℃. The area between is shaded, which represents the possible region of radial fluid temperature distribution. The extrapolated fluid temperatures at the wall are then compared with the measured wall temperature. The differences ΔT_w are plotted in time throughout the test (Figure 6.6). The area between the minimum and maximum values is shaded. At about 500 seconds, the heat flux from the granular

bed to the wall reaches a maximum (also see Figure 6.13). This intensifies the temperature change and causes higher measurement errors. As a result, the maximum value of ΔT_w increases. Considering the possible errors of the test, it is reasonable to assume a continuous temperature profile at the interface. The conditions at the wall then write:

$$\langle T_f \rangle^f = T_w$$

$$\lambda_{f_{eff}} \frac{\partial \langle T_f \rangle^f}{\partial r} = \lambda_w \frac{\partial T_w}{\partial r} \tag{6.26}$$

$$\langle \boldsymbol{u_f} \rangle^f = 0$$

where T_w is the wall temperature, λ_w is the thermal conductivity of the wall and $\lambda_{f_{eff}}$ is the effective conductivity of the fluid.

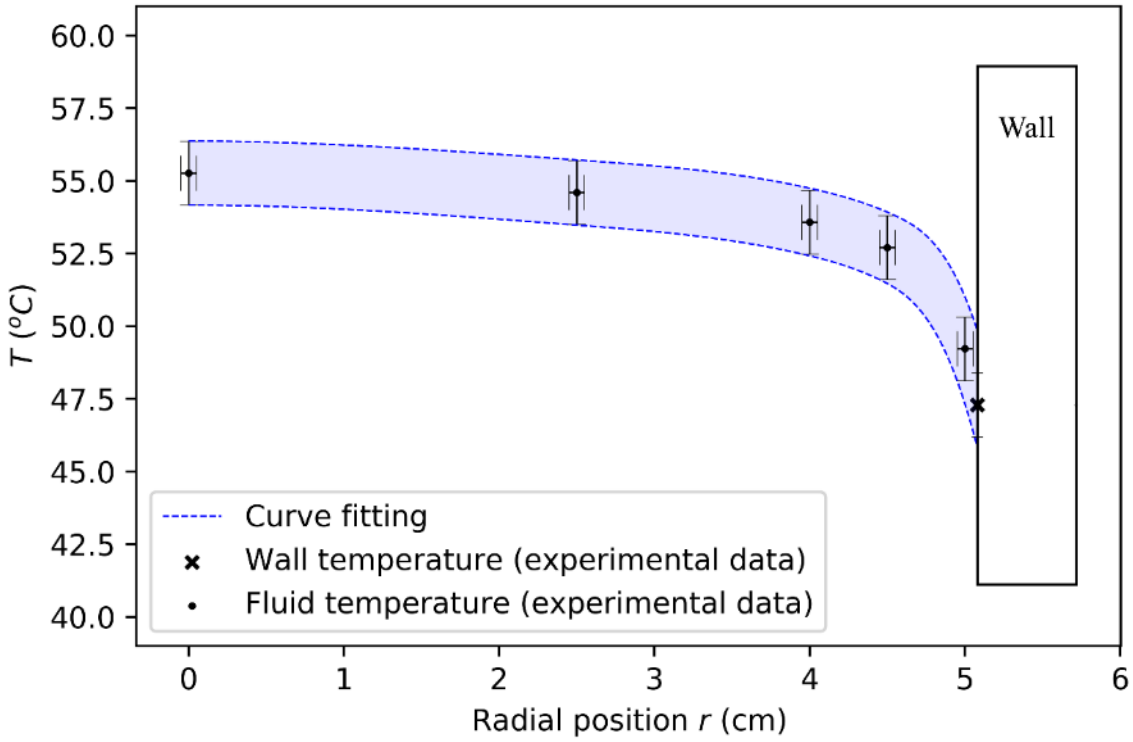

Figure 6.5: Experimental radial temperature profile at z = 250 mm including five measured data points of fluid temperature and the inner pipe wall temperature. The graph plots the upper and lower limits of temperature distribution considering errors of $\pm$0.5 mm and $\pm$1.1 °C.

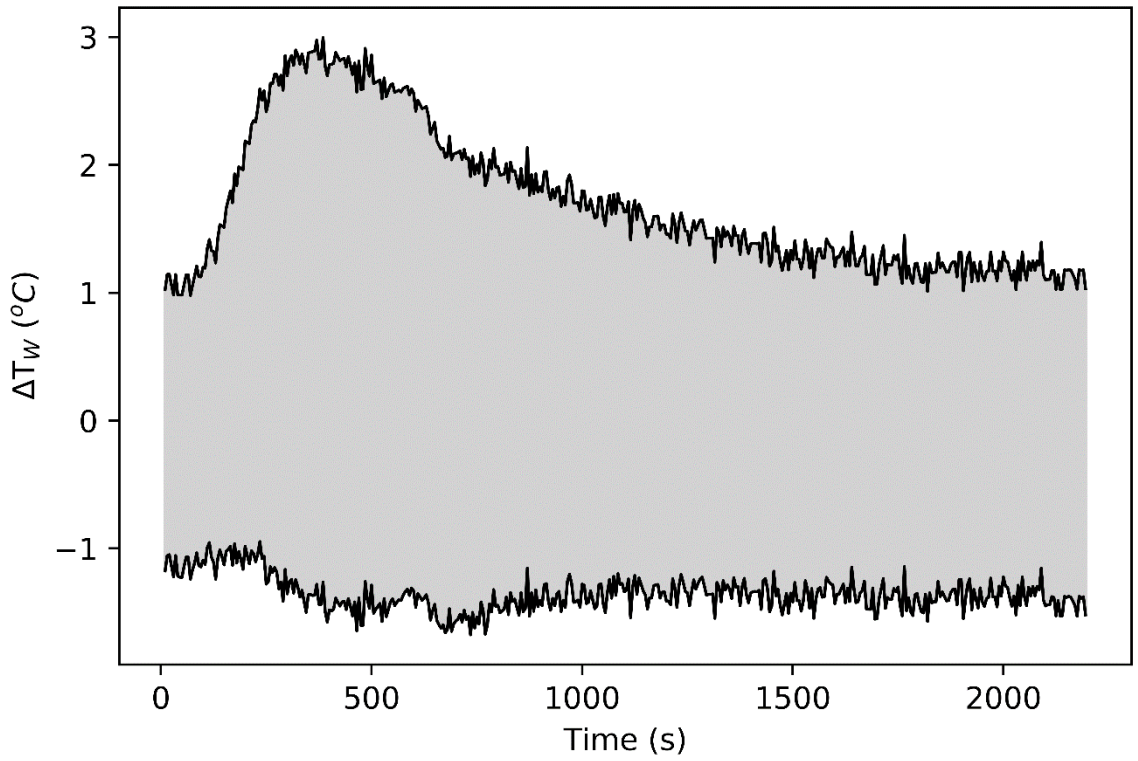

Figure 6.6: The range of difference between the extrapolated fluid temperature and the measured wall temperature at the inner pipe surface throughout the test.

6.5.5 Convergence and grid independence

To confirm the choice of the mesh and verify the convergence of the numerical simulation, studies on the mesh size and time step were performed. The simulation domain is discretized with quadrilateral elements and the near-wall region is completely resolved. Three cases with different radial mesh growth rates were created: 1.05, 1.1 and 1.15. With a total simulation time of 500 seconds, the radial temperature profiles at z = 250 mm were compared. As the maximum deviation between these cases remains below 0.1 ℃, the radial mesh size growth rate of 1.15 is used in the simulation.

In the z direction, three cases of different axial mesh sizes were created: 1.7 mm, 3.5 mm and 7 mm. The fluid temperature evolution in time was compared at multiple axial positions, namely at z = 125, 250, 375, 500 mm along the granular bed centerline. As the maximum difference between

different cases in fluid temperature is below 0.1 ℃, the axial mesh of 7 mm is used, and the result is considered as grid independent.

The convergence of the time step was also investigated for three different values of Δt = 0.5, 1 and 2 seconds. For 500 seconds simulations, deviations of ~0.25 ℃ in axial fluid temperature evolutions were found with Δt = 2 seconds compared to the other cases. Hence, the time step of 1 second will be used in the numerical analysis.

6.6 Results and discussions

6.6.1 Comparison between numerical and experimental results

Firstly, the numerical results are compared with the experimental data: Figure 6.7a shows the temperature evolution at four axial positions along the packed bed, Figure 6.7b plots the temperature profile at four axial positions on the outer surface of pipe, Figure 6.8 shows the radial temperature profile at an axial position of 250 mm and Figure 6.9 plots the 2D numerical results of the fluid and wall temperature evolution. Remind that the experimental data measured by thermocouples are ‘pointwise quantities’, whereas the numerical results given by volume averaged equations are ‘averaged quantities’ (excluding values on the wall). Ideally, the temperature should be measured experimentally in the whole REV to validate the numerical predictions, but this is not possible in practice. Despite that limitation, a satisfactory agreement is observed between the numerical results and the experimental observations. Overall, it is reasonable to conclude that the temperature evolutions are well predicted for axial and radial positions in the granular bed and on the wall surfaces.

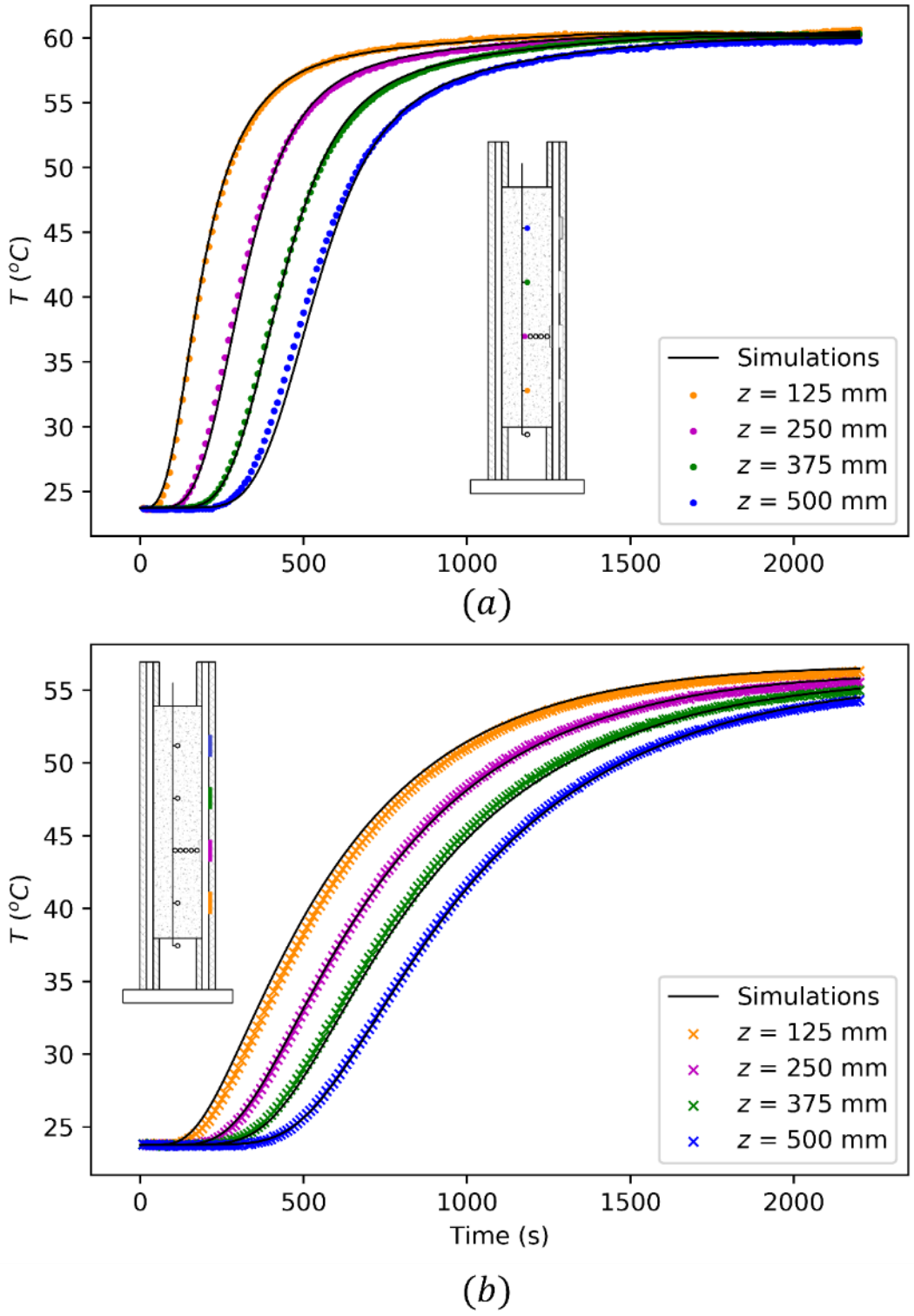

Figure 6.7: Comparison between numerical predictions (solid curves) and experimental data (scatter points) with colors to distinguish between different axial positions: (a) fluid temperature evolution along the granular bed centerline; (b) surface temperature evolution on the outer pipe.

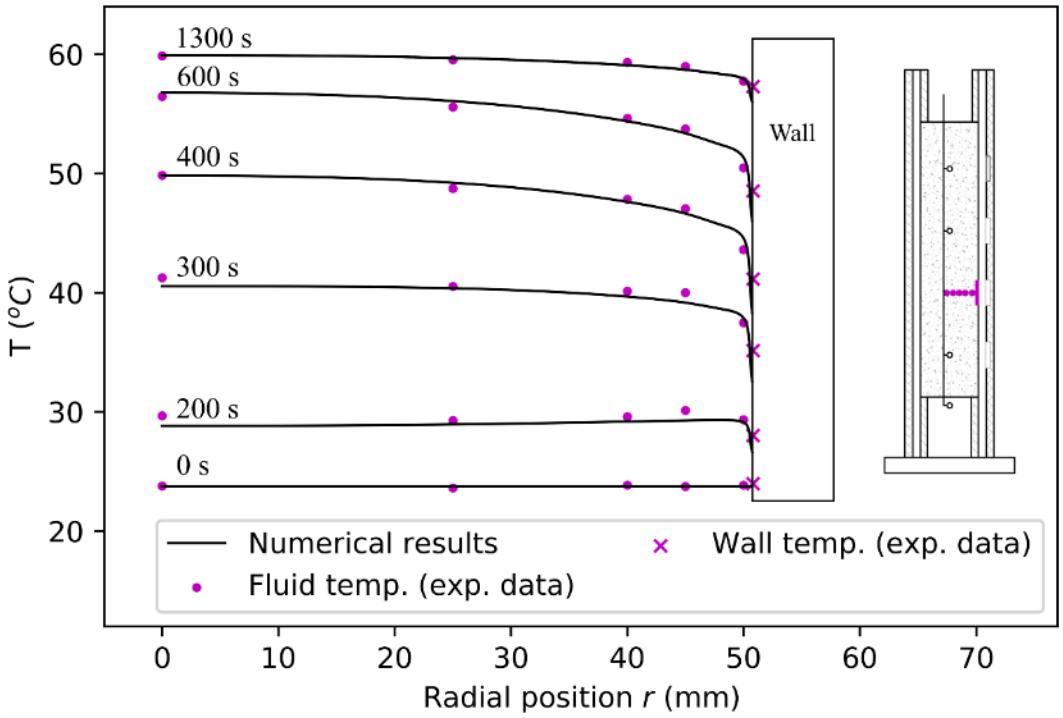

Figure 6.8: Comparisons between the numerical predictions (solid curves) and experimental data (scatter points) of the radial temperature profile at z = 250 mm.

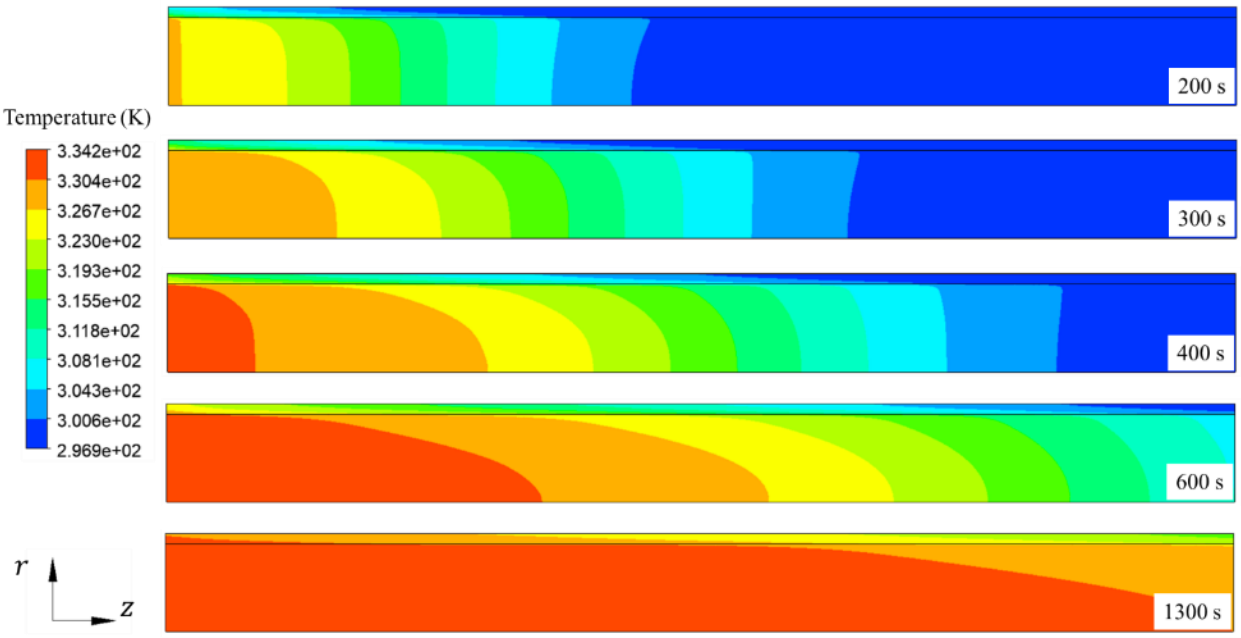

Figure 6.9: Numerical contour plots of the fluid and wall temperatures at different times.

6.6.2 Effect of the convective heat transfer coefficient (h_{sf}) between the fluid and beads

Although the predictive capability of the numerical model was verified, the selection of the empirical correlation for the heat transfer coefficient h_{sf} can be further justified. In this work, the correlation of Wakao et al. [72] (Eq. (6.11)) was used, but many other models have been proposed in the literature. Some of them are plotted in Figure 6.10 with Re_{ds} ranging from 100 to 550.

In front of such different correlations, the question arises about which one to select, especially when the validation ranges of Re_{ds} overlap. To investigate this, note that all the empirical correlations shown in Figure 6.10 lie within $\pm 50\%$ of the one proposed by Wakao et al. [72] (Eq. (6.11)). Therefore, the value of h_{sf} was varied by $\pm 50\%$ in the numerical model to study the impact on numerical predictions. Results are reported in Figure 6.11a for the axial temperature and in Figure 6.11b for the outer pipe surface temperature. The maximum deviation of the axial temperature profile is not significant (less than 3°C). This can be explained by a scale analysis of the fluid phase energy conservation equation (Eq. (6.8)): the convection term (i.e., the second term on the left-hand side) is slightly larger than the interfacial flux term (i.e., the second term on the right-hand side), and is 4 orders of magnitude higher than the other terms. This shows that the coefficient h_{sf} is not the only deciding factor. Note that this can be different in the laminar case at low flow velocity. Furthermore, increasing the value of h_{sf} results in a faster decrease of $\langle T_f \rangle^f - \langle T_s \rangle^s$ (i.e., the solid beads will be heated faster). This further neutralizes the influence of h_{sf} on the fluid temperature profile. However, it should be noted that increasing h_{sf} by 50% results in a larger Biot number for beads. The assumption of neglecting the temperature gradient in a particle is not strictly met. A more sophisticated model of heat transfer may be needed to provide more accurate predictions.

For the outer pipe surface, the three temperature profiles are nearly overlapped throughout the test (Figure 6.11b). Near the wall, the interfacial heat flux between the fluid and beads is less important as porosity increases. The weak response between the coefficient h_{sf} and the wall temperature is therefore not surprising. Overall, it may be concluded that h_{sf} is not a critical parameter of the numerical model. Using another existing correlation (within the range of $\pm 50\%$ from the one obtained with Eq. (6.11)) will not significantly change the temperature predictions.

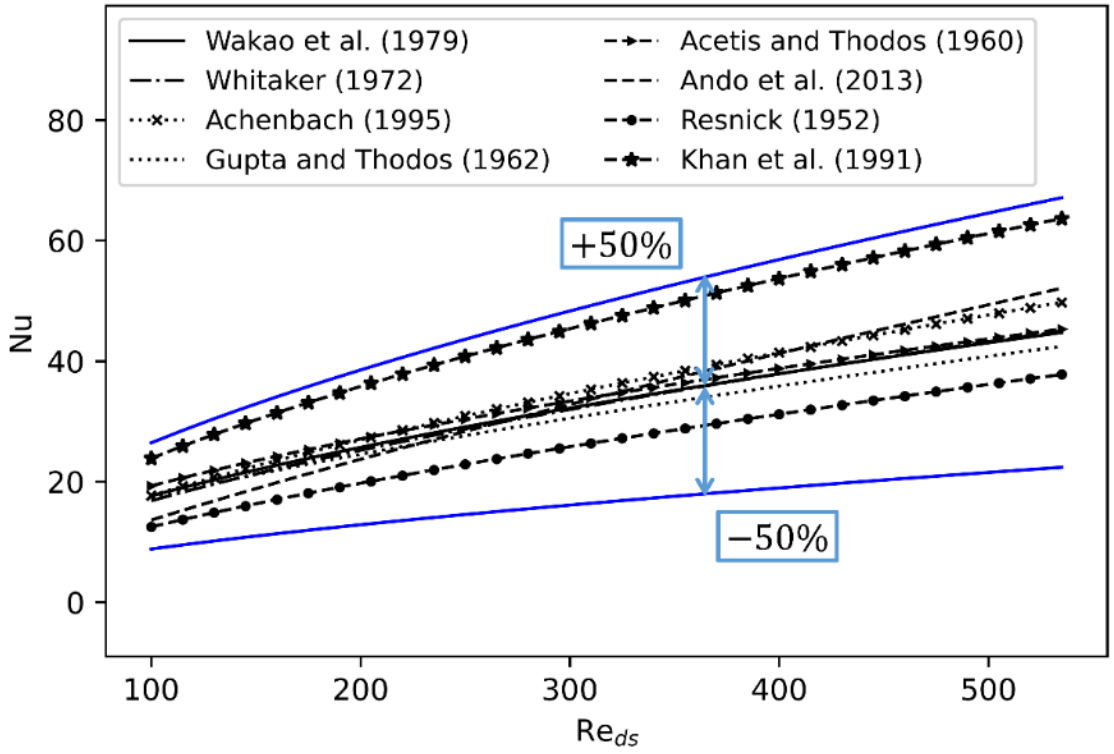

Figure 6.10: Existing fluid-to-particle convective heat transfer correlations for bead packings with Pr = 0.71.

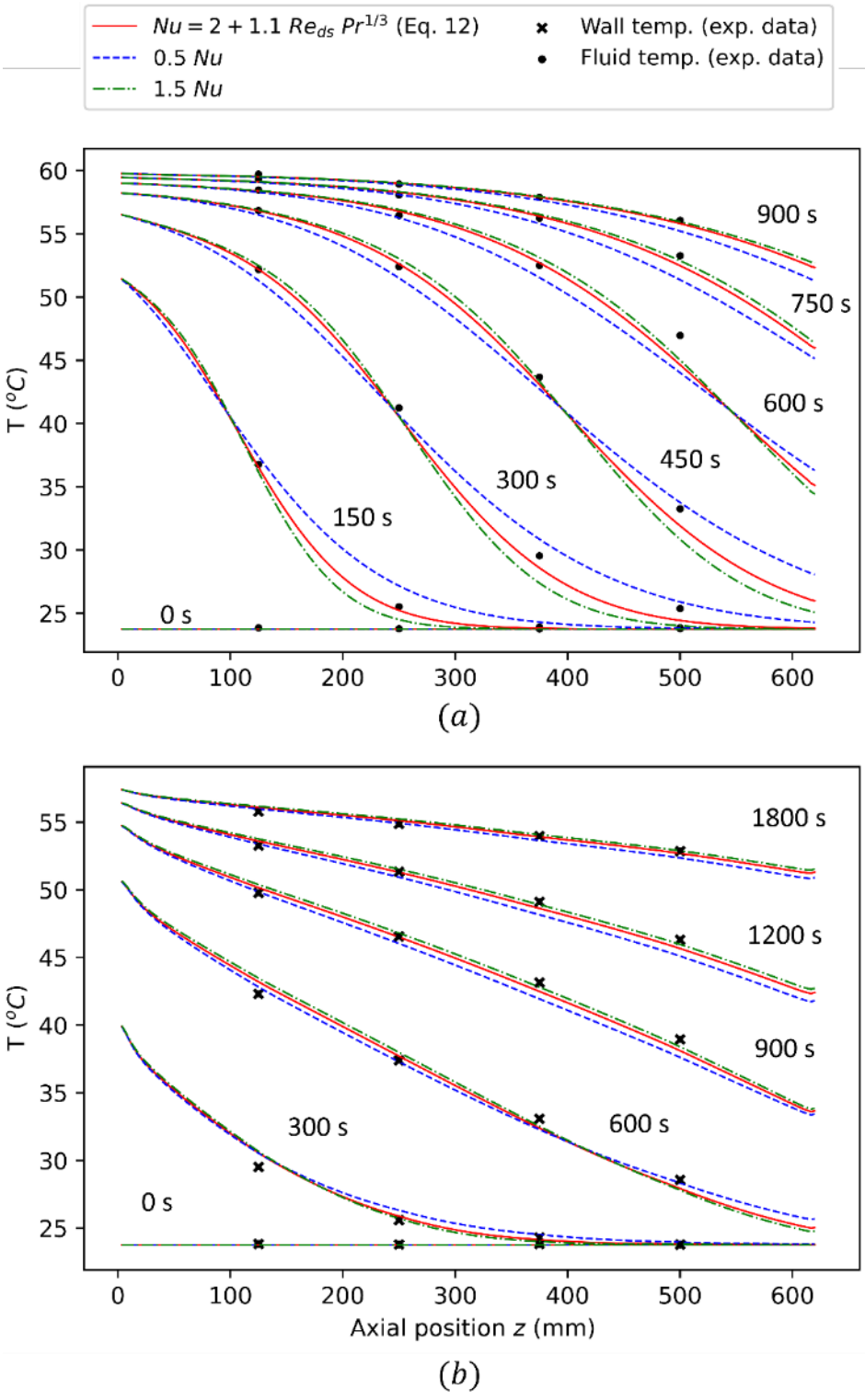

Figure 6.11: Comparison between predicted temperature profiles for different Nu and experimental data: (a) fluid temperature along the centerline of the bead packing; (b) outer pipe wall temperature.

6.6.3 Turbulence modelling

As mentioned previously, additional source terms (Eq. (6.19) and (6.20)) were considered to compensate for the possible underestimation on the turbulent energy induced by beads. Although the presence of these terms has been discussed in modelling the eddy viscosity μ_t [48] and predicting the temperature evolution inside packed beads [74], their importance in modelling the wall-to-bed heat transfer has not yet been investigated. On the other hand, several published studies [60, 61, 75] used the laminar flow model to predict the forced convective heat transfer in the homogeneous region of porous media, which showed good agreement with experimental results. The necessity of turbulence modelling is therefore justified by comparing the numerical results of three different models. The first model is laminar without any turbulent effect. The second one is the standard $k-\epsilon$ turbulence model without additional source terms, i.e., $\langle S_k \rangle^f$ and $\langle S_\epsilon \rangle^f$ are null. The third model includes the additional sources of turbulent quantities induced by the presence of beads (i.e., the standard $k-\epsilon$ turbulence model with additional source terms given by Eq. (6.19) and (6.20)).

Comparing the results of the axial temperature evolution (Figure 6.12a), there are no obvious differences between models. This agrees with the conclusion of Burström et al. [74]. In numerical simulations, turbulence affects the temperature profile in the packed beads only through the effective thermal conductivity of the fluid ($\lambda_{f\,eff}$):

$$\lambda_{f_{eff}} = \lambda_f + \frac{\langle C_f \rangle^f \, \mu_t}{\mathrm{Pr_t}} \tag{6.27}$$

where $\mathrm{Pr_t}$ is the turbulent Prandtl number. Note that the effect of hydrodynamic dispersion on the fluid effective thermal conductivity is included in μ_t through two additional terms, namely the turbulent kinetic energy $\langle S_k \rangle^f$ and the dissipation rate $\langle S_\epsilon \rangle^f$. The enhancement of thermal convection between phases has already been lumped into the heat transfer coefficient h_{sf}. Meanwhile, due to the high velocity and low thermal conductivity of air, the thermal convection is predominant. As a result, all three models provide similar predictions for the temperature distribution inside the bead packing.

Approaching the wall, as the volume fraction of solid beads decreases, the thermal conduction of air gradually becomes important. The values of $\lambda_{f_{eff}}$ near the wall determined by Model 3 (i.e., $k-\epsilon$ turbulence model with additional sources) are up to 70 and 3 times greater than the ones given by Model 1 (i.e., laminar model) and Model 2 (i.e., $k-\epsilon$ turbulence model without additional sources) respectively. In Figure 6.13, the experimental heat flux passing through the pipe wall at z = 250 mm is compared with the predictions of three different models. Despite a slight overestimation, Model 3 gives satisfactory predictions while Model 1 and 2 underestimate the heat transfer rate near the wall. It should be noted that the additional source terms (Eq. (6.19) and (6.20)) applied in Model 3 were originally derived from a square array of porosity 0.75. Compared to our study, the application of these terms can overestimate the turbulent quantities for two possible reasons: a higher porosity than that of square arrays gives larger eddy scales; squares are likely to create more eddies than spheres. The underestimation of the heat transfer rate by Model 1 and 2 can further be revealed by the outer pipe surface temperature evolution (Figure 6.12b): only the third model gives a good agreement with experiments. These results show that the turbulent and additional sources should be properly considered to predict the evolution of the wall temperature for fully turbulent cases.

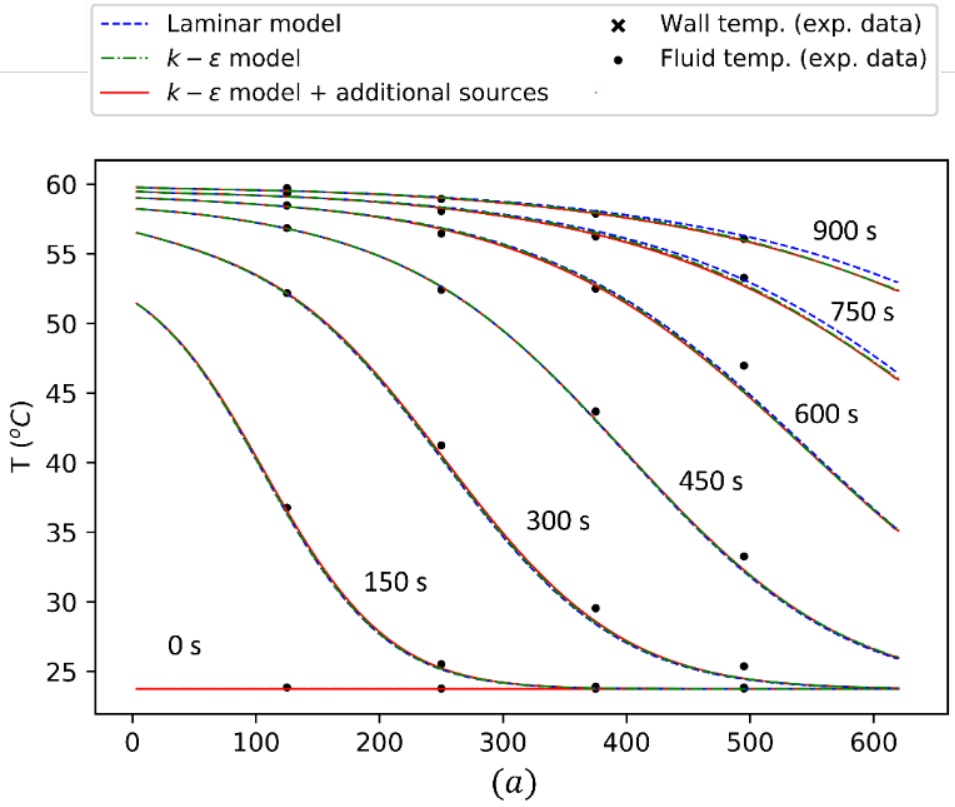

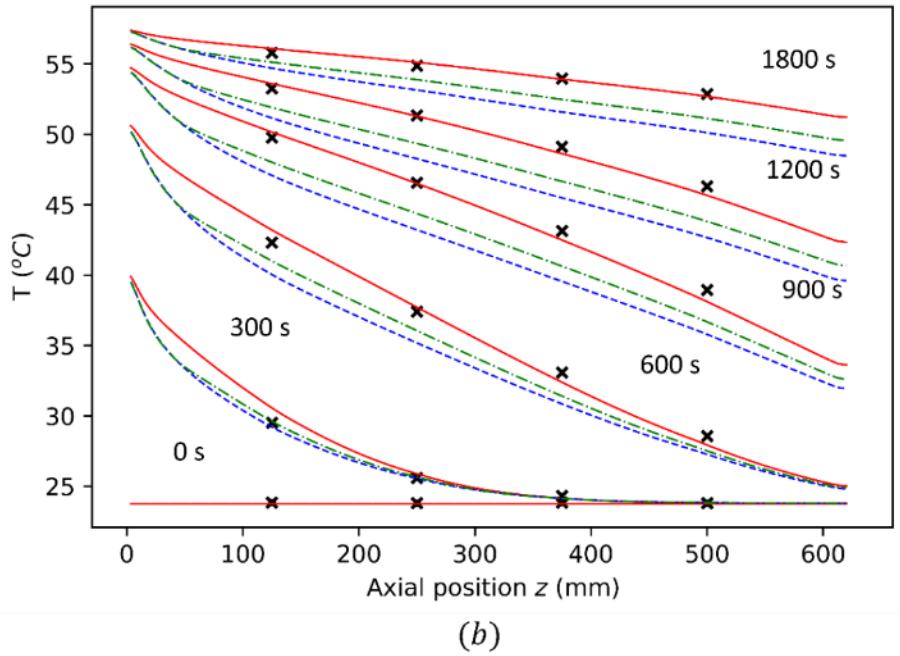

Figure 6.12: Comparisons between predicted temperature profiles using different models and experimental data: (a) fluid temperature along the centerline of the bead packing; (b) outer pipe wall temperature.

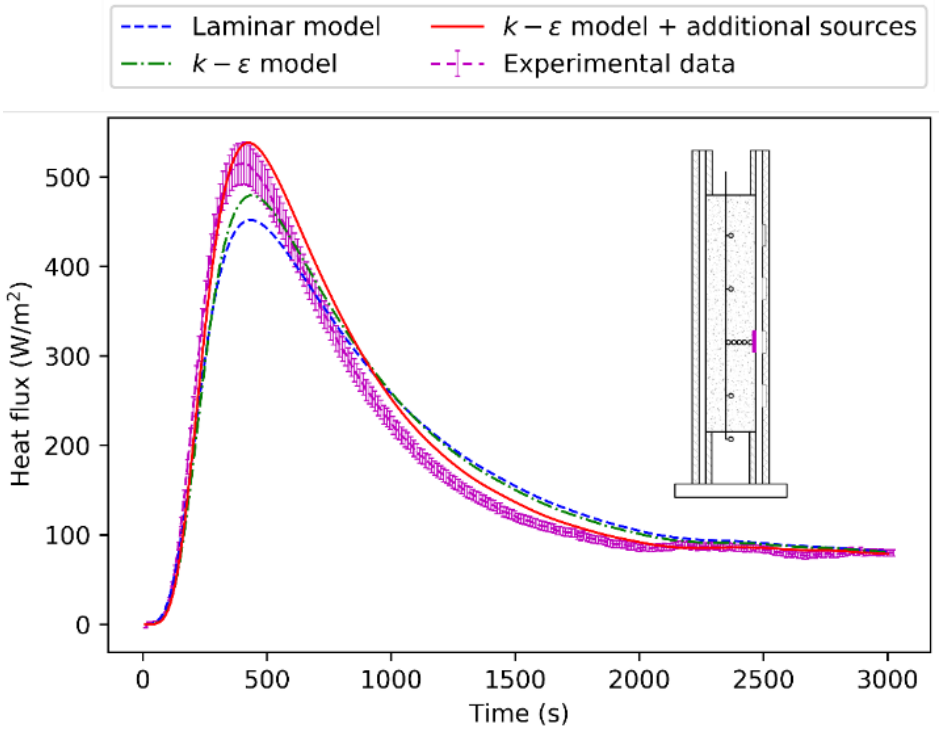

Figure 6.13: Comparisons between predictions of different models and experimental data of heat flux passing through the inner pipe wall at z = 250 mm with 5% measurement errors.

6.6.4 Radial porosity distribution

As mentioned previously, a proper determination of the radial porosity profile is essential to model transport phenomena in packed beds. As several exponential porosity models have been proposed, the selection of a proper one remains an issue. In fact, different exponential porosity models have been compared to predict physical phenomena in bead packings, such as the cross-sectional flow velocity field [54], the porosity of the entire packing structure [127], the radial coordination number for sphere packings [56], etc. The importance of predicting the temperature evolution has barely been investigated. In this study, the exponential porosity profile is determined with a non-constant REV approach directly from the packing structure and implemented in the simulation as a piecewise linear function. The predictions are compared with four empirical porosity models proposed in the literature (see Table 5.1). In these four cases, each empirical porosity profile is used to model both ϕ_V and ϕ_A. The bulk porosity value ϕ_b is 0.4 in all cases. The temperature profiles predicted using a constant porosity (i.e., $\phi_V = 0.4$ everywhere in the granular bed) are also plotted. Along the centerline of the bead packing, different predicted fluid temperature profiles do not exhibit large differences. This shows that using a constant porosity is a reasonable simplification to predict the temperature in homogenous regions of the granular bed, which has been considered in several published works [58, 60, 73]. However, these models show a large discrepancy when predicting the wall temperature of the outer pipe (Figure 6.14). The constant porosity model largely underestimates the wall temperature evolution because it does not take into account the porosity variations near the wall. The model proposed by Vortmeyer and Schuster [54] and the one proposed by Cheng and Hsu [126] overestimate the wall temperature, since the near wall regions described by these two models are wider than the others (see Figure 5.5). On the other hand, predictions with the models of Hunt and Tien [124], White and Tien [125] and the piecewise linear fitted function agree well with experimental data. As shown in Part I, these three models correlate the ϕ_V numerical results with relatively high R^2 values (i.e., 0.94, 0.79 and 0.97, respectively).

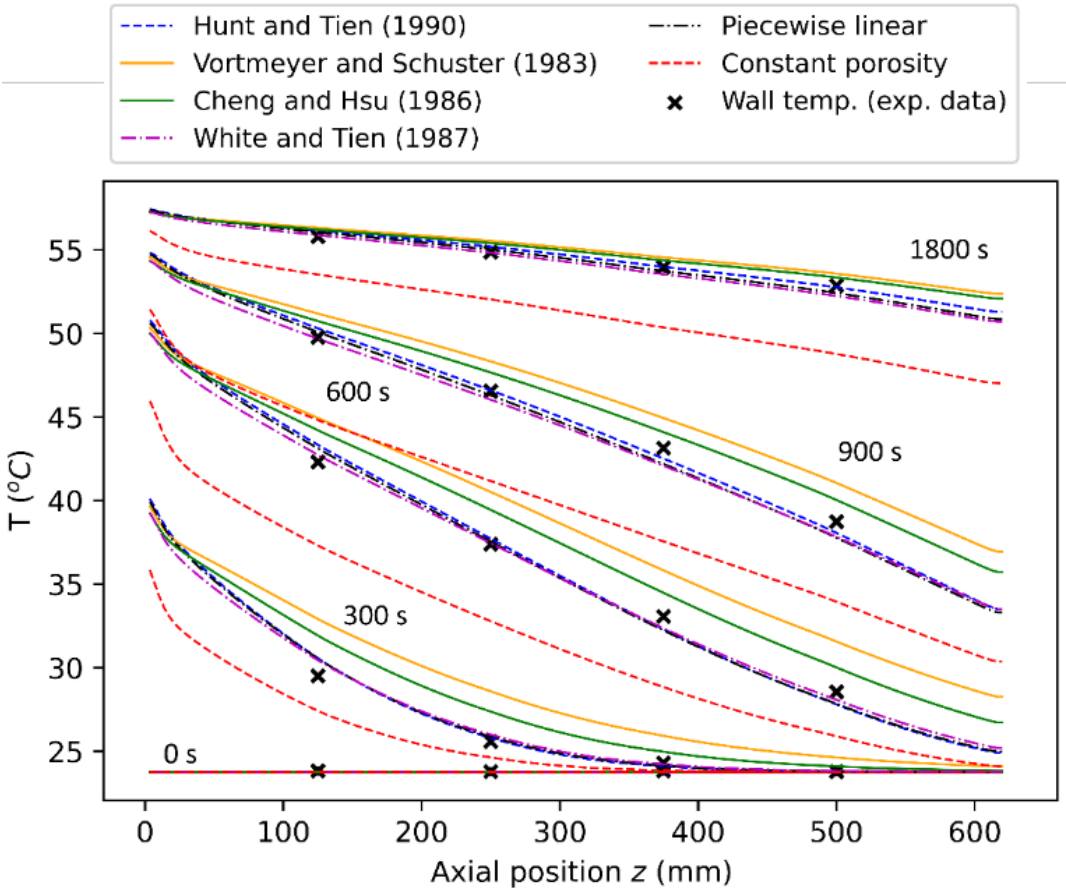

Figure 6.14: Comparisons between predicted outer pipe wall temperatures using different porosity models and experimental data.

6.7 Conclusion

A framework was proposed to model the forced convective heat transfer from a monodisperse bead packing to its containing wall. In Part I, the macroscopic transport equations were derived using the method of volume averaging and a non-constant REV to eliminate the incompatibility of quantities at the wall. This subsequently allowed determining the granular bed radial porosity profile directly from the packing structure. In Part II, the model was verified by experiments performed with a cylindrical packed bed of ceramic beads heated with air in fully turbulent regime. At the wall-bed interface, a continuous temperature profile was observed. With the derived governing equations, a 2D transient axisymmetric numerical simulation was performed and compared to the experiment. The transient temperature field in the packed bed and on the wall

surface is accurately predicted. The influence of the empirical parameters included in the model was also discussed. For the fluid temperature profile along the centerline of the beads, modelling turbulence does not lead to obvious differences compared to a laminar model, and the influence of the heat transfer coefficient h_{sf} is quite limited. Moreover, the coefficient h_{sf} has nearly no effect on the evolution of the bounding wall temperature. In contrast, the turbulence model is an important factor to predict the wall heating process. By comparing different models, we demonstrated that both the turbulence energy and the dissipation rate induced by the fluid movement and the presence of beads must be considered to predict the temperature evolution. Finally, as explained previously, the proposed framework is only valid for large bed-to-particle ratios (higher than 10). For smaller bed-to-particle ratios, future work would be probably needed.

6.8 Acknowledgements

This work was supported by the *National Science & Engineering Research Council of Canada* (NSERC) (Discovery Grants). Authors also gratefully acknowledge the *Research Center for High Performance Polymer and Composite Systems* (CREPEC) and the "*Fonds de recherche du Québec - Nature et technologies*" (FRQNT) for their partial financial support. Authors also express their sincere thanks to Christian-Charles Martel, technical assistant, for his support in the laboratory.

CHAPTER 7 ARTICLE 4: EXPERIMENTAL AND NUMERICAL INVESTIGATION OF WALL TEMPERATURE IN A HEATED PIPE FILLED WITH BEADS

Yixun Sun, Cédric Béguin, Philippe Causse, Brahim Benmokrane and François Trochu

Submitted to *International Journal of Heat and Mass Transfer* on 08/10/2021

7.1 Chapter overview

Within the modeling framework proposed in Chapter 5 and validated in Chapter 6, the influence of several design parameters on the heating efficiency is studied for a heated pipe filled with beads. This third article was submitted to International Journal of Heat and Mass Transfer. The parametric study emphasizes the importance of reducing the wall thickness and volumetric heat capacity. This largely shortens the time to reach wall temperature uniformity and represents an important optimization feature in the design of granular molds.

7.2 Abstract

Placing granular materials inside empty channels with coolant or heat transfer fluids flowing through is an effective way to increase the heat transfer rate to the wall. Although this approach has been used in different engineering fields, a particular goal is seldom considered in some applications, namely the temperature uniformity of the bounding wall. As temperature varies along the flow direction, a non-uniform temperature field appears on the wall. This bears consequences in some applications such as in electronics, battery cooling or composite manufacturing. In the present study, the uniformity of the wall temperature is investigated numerically for a typical cylindrical pipe filled with monodisperse ceramic beads and heated by air flow. Numerical simulations based on *Reynolds-averaged Navier-Stokes* (RANS) *Computational Fluid Dynamics* (CFD) are performed to analyze the heat transfer to the bounding wall. Because of the uncertainty mentioned in the literature, the applicability of an empirical model reflecting additional sources of

production and dissipation of turbulent energy due to beads is firstly evaluated. By comparing the numerical predictions of temperature fields with experimental data, a damping function is needed to adjust these additional source terms to better fit experimental data for bulk Reynolds numbers between 100 and 700. A parametric study is then conducted to assess the effect of various parameters on the wall temperature uniformity. Results shows that wall materials of low volumetric heat capacity and a reduced wall thickness greatly shorten the duration to reach thermal uniformity. A less pronounced enhancement also exists for larger thermal conductivity of the wall material. However, using beads of lower volumetric heat capacity does not have a major influence on the uniformity of the wall temperature.

KEYWORDS: Bead packings, forced convection, wall temperature, thermal uniformity

7.3 Nomenclature

a_V interfacial area per unit volume, m^{-1}

C inertial resistance factor, m^{-1}

C_f air specific heat capacity, J/(kg K)

C_s ceramic beads specific heat capacity, J/(kg K)

C_w acrylic specific heat capacity, J/(kg K)

$C_{\epsilon 1}$, $C_{\epsilon 2}$, C_μ turbulence model coefficients

d_s beads diameter, m

d_w pipe wall thickness, m

D_w bead packing diameter, m

f_d damping factor

g gravitational acceleration, m/s^2

h_{sf} convective heat transfer coefficient, $W/(m^2 K)$

I unit matrix

K permeability, m^2

k_f turbulent kinetic energy, m^2/s^2

p pressure, Pa

P_{ref} reference pressure of rotameter, Pa

P_{ro} air pressure at rotameter, Pa

Pr Prandtl number

$\mathrm{Pr_t}$ turbulent Prandtl number

q_{loss} heat loss at the outer wall surface, W/m^2

Q_{ro} air flow rate before entering the test section, m^3/s

r radial coordinate

$\mathrm{Re_{in}}$ Reynolds number based on the particle diameter and inlet flow velocity

$\mathrm{Re_s}$ Reynolds number based on the particle diameter and local fluid velocity

S_{ave} average deviation between predicted and measured temperature values per data point, K

S_k additional source of turbulent kinetic energy, $kg/(s^3 m)$

S_ϵ additional source of dissipation rate, $kg/(s^4 m)$

t time, s

T_f air temperature, K

T_s ceramic beads temperature, K

T_{ref} reference temperature of rotameter, K
T_{ro} air temperature at rotameter, K
T_{oil} oil temperature, K
T_{in} inlet air temperature, K
u_{in} inlet air velocity, m/s
u_f local air velocity, m/s
$u_f{}'$ deviation from the average flow velocity, m/s
V averaging volume, m^3
V_f averaging volume for the fluid, m^3
V_s averaging volume for the beads, m^3
y^+ dimensionless wall distance
z axial coordinate

Abbreviations

CFD Computational Fluid Dynamics
DSC Differential Scanning Calorimetry
PCI Peripheral Component Interconnect
RANS Reynolds Averaged Navier-Stokes
REV Representative Elementary Volume
SCFM Standard Cubic Feet per Minute

Greek letters

ϵ dissipation rate, m^2/s^3
σ_k, σ_ϵ urbulence model coefficients
ρ_f air density, kg/m^3
ρ_s ceramic beads density, kg/m^3
ρ_w acrylic density, kg/m^3
ϕ_V void fraction of averaging volume
ϕ_b bulk porosity of the packing
μ_f air dynamic viscosity, Pa · s
μ_t eddy viscosity, kg/(m s)
λ_f air thermal conductivity, W/(m K)
λ_s ceramic beads thermal conductivity, W/(m K)
λ_w acrylic thermal conductivity, W/(m K)
λ_{fe} effective thermal conductivity of air, W/(m K)
$\bar{\bar{\tau}}$ stress tensor

7.4 Introduction

When a coolant or heat transfer fluid flows through a porous medium placed inside a container, forced convection occurs between the fluid and the bounding wall. This phenomenon was investigated in several engineering fields because the presence of the porous medium intensifies fluid mixing and enhances heat transfer. This approach was used to add or remove rapidly heat through the bounding wall in packed bed reactors [156], in micro-porous heat exchangers [118], in heat sinks used for electronics cooling [157], etc. Several studies were conducted to analyze the heat transfer enhancement resulting from the flow through a porous medium and identify the best tuning parameters. Jiang et al. [113] studied experimentally the forced convection in parallel channels filled with porous materials. They showed that channels filled with sintered bronze porous medium increases 15 times the local heat transfer coefficient for water and about 30 times for air

compared with empty channels. Demirel et al. [114] studied the forced convection in rectangular ducts filled with different low thermal conductivity granular materials (polyvinyl chloride Raschig rings and polystyrene spheres). They showed that the grain shape has nearly no effect on the wall-to-bed heat transfer, but the rate of heat transfer increases with the particle size. Seto et al. [158] analyzed the flow and heat transfer of sphere-packed pipes with small pipe-to-sphere diameter ratios ($1.3 < D_w/d_s < 3$, where D_w is the diameter of the packing, and d_s the sphere diameter). Their results showed that the wall-to-bed heat transfer coefficient increases with the value of D_w/d_s and can be from 4.5 to 12 times greater than in unfilled pipes.

Apart from the investigations mentioned above, the heat transfer enhancement was also confirmed by [159-161]. In most published works, the temperature uniformity of the containing wall is not a major concern. However, wall temperature variations can be critical in some applications. In electronics cooling, large temperature variations in cooling channels create undesirable thermal stresses due to the different thermal expansion coefficients of materials. This impacts negatively the reliability and reduces lifetime [162, 163]. In composite manufacturing by resin injection, Désilets [10] heated an uncured composite part through the wall of a channel filled with porous material. Uniform heating is required because temperature variations on the wall surface affects the polymerization rate of the resin, which may result in uneven shrinkage and the creation of residual stresses. Based on our literature survey, the wall temperature uniformity has been investigated in micro-channels with nanofluids [164, 165], channels filled with foam structures [166], channels of micro-pin-fin [162] and pipes with a wick structure on the inner surface [167, 168]. On the other hand, the uniformity of wall temperature for channels filled with packed spherical beads has not been studied thoroughly. Channels filled with beads are widely used structures, which combines the advantages of relatively low pressure drop with rapid heat exchange [169]. Compared to many porous foam structures, bead packings are easy to prepare. This leads to many potential applications requiring rapid and uniform heat transfer through the channel wall.

Numerical simulation is a powerful tool to assist in the investigation and design of such systems. Compared to experiments, the numerical approach can provide a reasonable description of transport phenomena in bead packings at a much lower cost. Several studies [74, 170-172] used *Reynolds-averaged Navier-Stokes* (RANS) *Computational Fluid Dynamics* (CFD) approach to model the heat transfer in packed beds. Burström et al. [74] showed the importance of considering additional sources of turbulent energy production and dissipation rates induced by beads. The

source terms were determined with the model proposed by Nakayama and Kuwahara [152] for fully turbulent flows (Reynolds number based on the particle diameter Re_s > 300) passing through square arrays. Note that the validity of this model was questioned by Guo et al. [173] for low Re_s values. Therefore, our study also intends to validate its application range of Re_s.

The main objective here is to examine the uniformity of wall temperature for a typical cylindrical channel filled with packed beads and heated by air flow. This is investigated after an experimental validation on the modelling framework by considering additional turbulent sources induced by beads. With the validated model, the influence of multiple design parameters (i.e., particle size, wall and particle materials, wall thickness, inlet pressure) is also investigated. The article begins by describing the experimental setup and test procedure (Section 2). The numerical model is presented in Section 3. This includes the governing equations, input parameters, boundary conditions and a study of mesh dependency. In Section 4, the numerical results are compared with experiments to validate the N-K turbulent model. A parametric study is also presented, and the effect of various parameters on the uniformity of wall temperature is discussed. Finally, the conclusion states the most important factors governing the efficiency of the wall-to-bed heat transfer.

7.5 Experimental setup and test procedure

7.5.1 Experimental setup

An experimental setup was designed and built to study the wall-to-bed heat transfer for beads packed in a cylindrical pipe. The system is depicted schematically in Figure 7.1. It consists of a heating circuit and a test section. The testing fluid is supplied by the laboratory compressed air system. A valve and rotameter (FL4613-V, OMEGA) are installed to control and measure the flow rate. The observed reading of the rotameter is denoted Q_{ro}, which is measured at the pressure P_{ro} and temperature T_{ro}. The error on Q_{ro} reading is ~1%. Before entering the test section, the air flow passes through the heat exchanger which is connected to a closed heating circuit. This allows transferring the thermal energy to the air flow. In the heating circuit, thermal oil (Ucon 50HB-660, Dow Inc.) is used as heat transfer fluid and is electrically heated. The oil is stored in a tank and pumped into the circuit through a one-inch-diameter pipe at constant speed. A J-type thermocouple

is mounted on the heating circuit to measure the oil temperature T_{oil}. All the pipes and the oil tank are insulated to reduce heat loss.

The details of the test section are given in Figure 7.2. Held by two identical metallic perforated plates and mesh layers on the top and bottom, a packed bed of ceramic spheres (0.625 m in length) is placed in a vertical acrylic pipe of inner diameter 0.1016 m (4 inches) and 6.35×10^{-3} m (0.25 inches) thick. The acrylic pipe is covered outside by a 1.27×10^{-2} m (0.5 inch) thick insulation layer (flexible rubber foam insulation tube, McMaster # 4463K148). The lower perforated plate is supported by an acrylic sleeve of outer diameter 0.1016 m (4 inches) and height of 0.2 m. Note that an insulation layer covers the inner surface of the sleeve to avoid excessive heating of the pipe wall. The inlet pressure P_{in} is measured by a pressure sensor (Hoskin Scientific, type E14) installed 0.02 m below the bottom of the granular bed. The measurement error of the pressure sensor is 0.25%. Five K-type thermocouples are placed on a metallic rack fixed on the lower perforated plate along the central axis of the cylinder. Among these thermocouples, one is located 0.01 m below the lower perforated plate to measure the inlet air temperature T_{in}. The other four thermocouples measure the fluid temperature at several axial positions (i.e., z = 0.125, 0.25, 0.375 and 0.5 m) in the granular bed. At similar axial positions, four heat flux sensors (PHFS-01 FluxTeq) are mounted on the outer pipe surface. These flux sensors are equipped with thermocouples, which allow measuring the wall temperatures and heat fluxes at the same time. The flux values are used to evaluate the heat loss caused by natural convection. The positioning errors for all sensors are considered as $\pm5\times10^{-4}$ m in the radial and axial directions. The measurement errors of thermocouples and heat flux sensors are ±1.1 K and 5% respectively. All the signals are detected by two National Instrument data acquisition cards (PCI-6036E, 16-Analog-Input Multifunction DAQ) plugged into the *Peripheral Component Interconnect* (PCI) of a computer. A LabVIEW interface is programmed to operate the electrical heater and pump. It is also used to perform data acquisition.

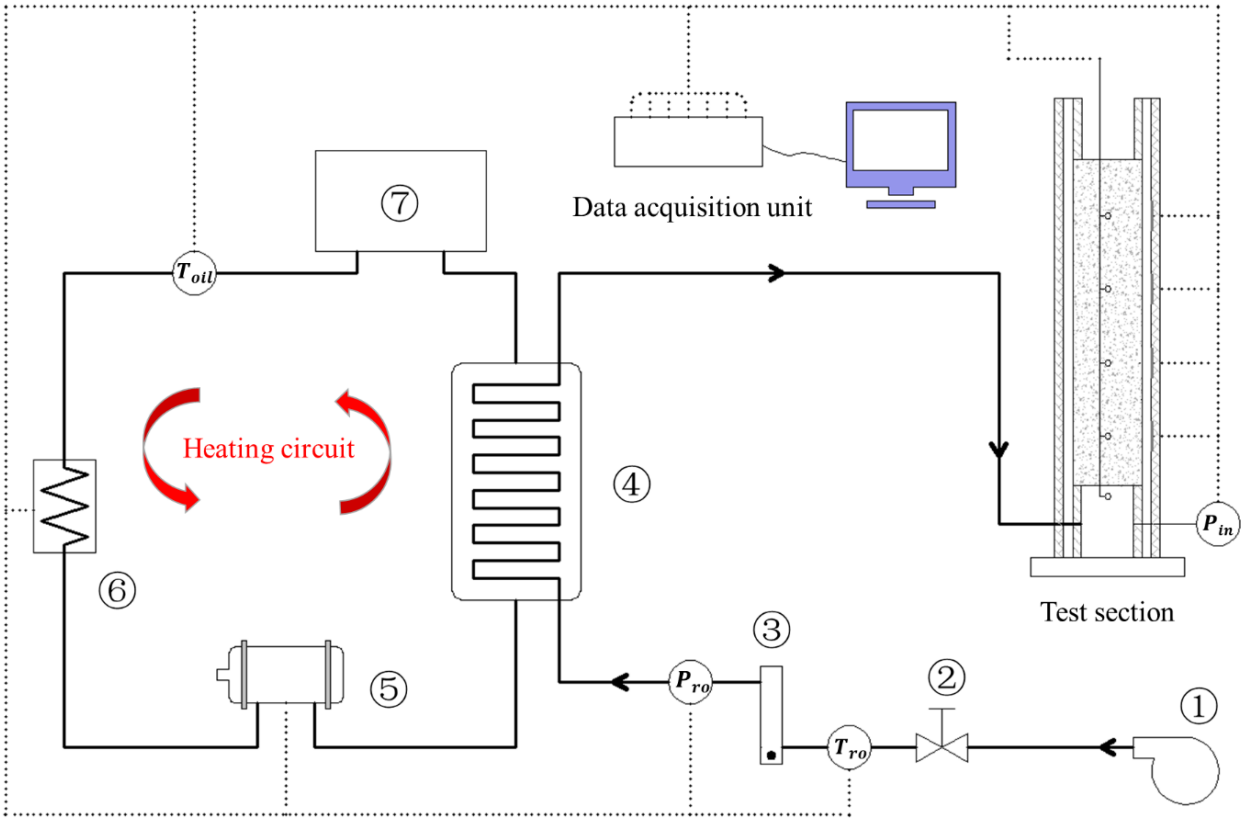

Figure 7.1: Schematic of the experimental setup: (1) compressed air supply; (2) valve; (3) rotameter; (4) heat exchanger; (5) pump; (6) electrical heater; (7) oil tank; the dashed lines represent wires.

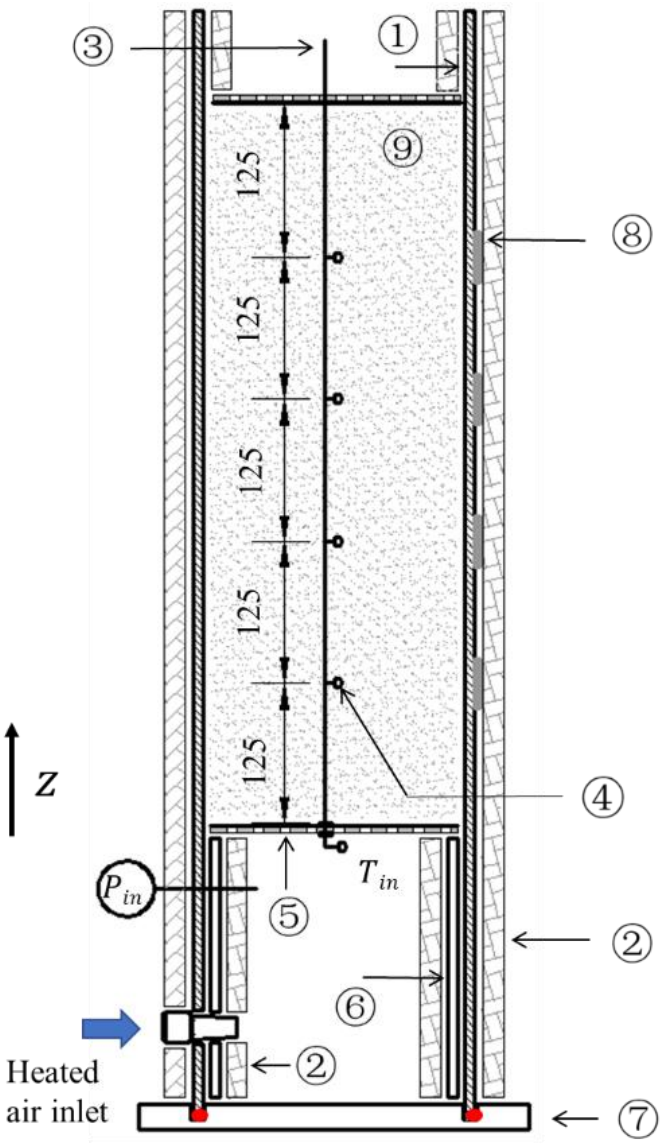

Figure 7.2: Schematic of the test section (unit: mm): (1) acrylic pipe of 4 inches inner diameter; (2) insulation layer; (3) metallic rack; (4) thermocouple; (5) mesh layer and porous plate; (6) acrylic ‘sleeve’; (7) acrylic base with groove and O-ring; (8) heat flux sensor; (9) ceramic bead packing.

7.5.2 Test procedure

A typical test starts by circulating and heating the thermal oil in the heating circuit. A PID controller (implemented in the LabVIEW program) automatically operates the electrical heater by monitoring the real-time temperature of oil T_{oil}. The value of T_{oil} is maintained at 338.15±0.8 K throughout the test. The valve is then opened manually to let air flow in the testing device. The air flow rate Q_{ro} is regulated by tuning the control knob of the rotameter to a desired value. Note that the flow rate Q_{ro} is observed for P_{ro} and T_{ro}. Since air is compressible, Q_{ro} should be corrected for further use. This will be presented in detail in the next section. Passing through the heat exchanger, air is heated from T_{ro} to 333.15±1.5 K before entering the test section. All the temperature, pressure and heat flux values are measured and recorded every second during the test. The experiment stops when the temperatures measured on the outer pipe surface stabilize and reach $T_{in} - 2$ K.

In this study, tests at Q_{ro} = 3.3×10^{-3} and 4.25×10^{-3} m^3/s (i.e., 7 and 9 Standard Cubic Feet per Minute) were performed with three monodisperse granular beds for the same bead material (i.e., ceramic), but with different particle sizes. The density of the ceramic material (ρ_s) was measured at ~296.15 K following the buoyancy technique described in standard ASTM D792 [108]. This subsequently allowed measuring the particle size by weighing a large number of randomly selected beads (~1500 beads of each size) one by one. The diameter of each bead was calculated by assuming a perfect spherical shape. The mean diameters (d_s) thus determined are 3.3×10^{-3}, 6.3×10^{-3} and 9.4×10^{-3} m (Table 6.1).

7.6 Numerical analysis

Numerical simulations were performed with the commercial software Ansys Fluent [144]. Six cases were analyzed to compare with the experiments performed with three different bead packings and two inlet flow rates. The computational domain in all the cases is 2D axisymmetric. This takes the bead packing and its containing wall into account, namely from the lower to the upper surfaces without the insulation layer outside. The standard $k-\epsilon$ turbulent model with enhanced wall function is used. Due to the low temperature range, thermal radiation was neglected. The governing equations, the input material properties, empirical parameters, and boundary conditions are presented in the sequel.

7.6.1 Governing equations

The governing equations for the flow and heat transfer in granular beds were developed based on the local volume averaging technique [74]. For sake of brevity, the fluid phase intrinsic volume average of a quantity ψ over a *Representative Elementary Volume* (REV) is defined as follows:

$$\langle \psi \rangle^f = \frac{1}{V_f} \int_{V_f} \psi \, dV = \frac{1}{\phi_V \, V} \int_{V_f} \psi \, dV \tag{7.1}$$

where V is the volume of the REV and V_f represents the fluid volume in the REV. The parameter ϕ_V is the void fraction of the REV defined as:

$$\phi_V = \frac{1}{V} \int_{V_f} dV \tag{7.2}$$

Similarly, the solid phase (i.e., beads) intrinsic volume average writes:

$$\langle \psi \rangle^s = \frac{1}{V_s} \int_{V_s} \psi \, dV = \frac{1}{(1 - \phi_V) \, V} \int_{V_s} \psi \, dV \tag{7.3}$$

where V_s represents the beads volume in the REV. For wall-confined randomly packed beads, the distribution of ϕ_V is not constant in the radial direction. In the context of RANS CFD simulations, such profiles can be well described by the exponential porosity models in which the value of ϕ_V decreases exponentially from the wall to the bulk porosity ϕ_b in the center region of the bed. The model proposed by Hunt and Tien [124] is used in this study:

$$\phi_V = \phi_b \left[1 + a \exp\left(-8 \, \frac{0.5 \, D_w - r}{d_s} \right) \right] \tag{7.4}$$

where D_w is the diameter of the bead packing, r the radial coordinate, and a the adjustable parameter to obtain $\phi_V = 1$ at the wall. With the nomenclature given in Eq. (7.1) and Eq. (7.3), the conservation equations of mass, momentum and energy in the packed bed stand as follows:

- Mass conservation:

$$\frac{\partial\left(\phi_V \langle\rho_f\rangle^f\right)}{\partial t} + \nabla \cdot \left(\phi_V \langle\rho_f\rangle^f \langle \boldsymbol{u_f}\rangle^f\right) = 0 \tag{7.5}$$

where ρ_f is air density, t the time, and $\boldsymbol{u_f}$ the air velocity.

- Momentum conservation:

$$\begin{aligned} &\frac{\partial}{\partial t}\left(\phi_V \langle\rho_f\rangle^f \langle \boldsymbol{u_f}\rangle^f\right) + \nabla \cdot \left(\phi_V \langle\rho_f\rangle^f \langle \boldsymbol{u_f}\rangle^f \langle \boldsymbol{u_f}\rangle^f\right) \\ &\qquad = -\phi_V \nabla\langle p\rangle^f + \nabla\left(\phi_V \langle\bar{\bar{\tau}}\rangle^f\right) + \phi_V \langle\rho_f\rangle^f \boldsymbol{g} \\ &-\nabla \cdot \left(\phi_V \langle\rho_f\rangle^f \langle \boldsymbol{u'_f u'_f}\rangle^f\right) - \left(\frac{\phi_V^2 \mu_f}{K} \langle \boldsymbol{u_f}\rangle^f + \frac{\phi_V^3 C}{2} \langle\rho_f\rangle^f \left|\langle \boldsymbol{u_f}\rangle^f\right| \langle \boldsymbol{u_f}\rangle^f\right) \end{aligned} \tag{7.6}$$

where $\langle \boldsymbol{u_f}\rangle^f \langle \boldsymbol{u_f}\rangle^f$ represents the tensor product of the averaged fluid velocity, p the pressure, $\boldsymbol{g}$ the gravitational acceleration, μ_f the fluid viscosity, K the permeability of the granular bed, C the inertial resistance factor, and $\bar{\bar{\tau}}$ the stress tensor calculated as follows where $\boldsymbol{I}$ is the unit matrix:

$$\bar{\bar{\tau}} = \mu\left[\left(\nabla \boldsymbol{u_f} + \left(\nabla \boldsymbol{u_f}\right)^T\right) - \frac{2}{3}\nabla \cdot \boldsymbol{u_f} \boldsymbol{I}\right] \tag{7.7}$$

As presented in more details in the sequel, the term $\langle\rho_f\rangle^f \langle \boldsymbol{u'_f u'_f}\rangle^f$ in Eq. (7.6) represents Reynolds stress determined by turbulence modelling. The last two terms on the right-hand side of Eq. (7.6), i.e., $-\left(\frac{\phi_V^2 \mu_f}{K} \langle \boldsymbol{u_f}\rangle^f + \frac{\phi_V^3 C}{2} \langle\rho_f\rangle^f \left|\langle \boldsymbol{u_f}\rangle^f\right| \langle \boldsymbol{u_f}\rangle^f\right)$, model the flow resistance due to the presence of beads. As verified in a previous investigation [145], the parameters K and C can be determined empirically by the revisited Ergun's equation [43] as follows:

$$K = \frac{d_s^2 \phi_V^3}{180 (1-\phi_V)^2} \tag{7.8}$$

$$C = \frac{3.6 (1-\phi_V)}{d_s \phi_V^3} \tag{7.9}$$

- Energy conservation:

The volume averaged thermal energy equation of the fluid phase writes:

$$\frac{\partial}{\partial t}\left(\phi_V \langle\rho_f\rangle^f \langle C_f\rangle^f \langle T_f\rangle^f\right) + \nabla\cdot\left(\phi_V \langle\rho_f\rangle^f \langle C_f\rangle^f \langle T_f\rangle^f \langle \boldsymbol{u_f}\rangle^f\right) = \nabla\cdot\left(\phi_V \lambda_{fe} \nabla\langle T_f\rangle^f\right) - a_V h_{sf}\left(\langle T_f\rangle^f - \langle T_s\rangle^s\right) \tag{7.10}$$

where T_f is the fluid temperature, C_f the fluid specific heat capacity, h_{sf} the convective heat transfer coefficient, a_V the interfacial area per unit volume, and λ_{fe} the fluid effective thermal conductivity which takes the turbulent energy into account:

$$\lambda_{fe} = \lambda_f + \frac{\langle C_f\rangle^f \mu_t}{\mathrm{Pr_t}} \tag{7.11}$$

where μ_t is the eddy viscosity, λ_f the fluid thermal conductivity, and $\mathrm{Pr_t}$ the turbulent Prandtl number considered as a constant value of 0.85. Note that the effect of hydrodynamic dispersion on the fluid effective thermal conductivity is included in μ_t through two additional terms, namely the turbulent kinetic energy $\langle S_k\rangle^f$ and the dissipation rate $\langle S_\epsilon\rangle^f$, which will be presented in the following section. The parameter a_V can be expressed as follows for sphere packings [74]:

$$a_V = \frac{6\,(1-\phi_V)}{d_s} \tag{7.12}$$

The coefficient h_{sf} models the convective heat exchange between the solid beads and the fluid. In this study, this coefficient is obtained by the correlation of Wakao et al. [72]:

$$h_{sf} = \frac{(2 + 1.1\ \mathrm{Re_s}^{0.6}\ \mathrm{Pr}^{1/3})\ \lambda_f}{d_s} \tag{7.13}$$

where $\mathrm{Re_s}$ is the Reynolds number based on particle size and Pr is the Prandtl number. The dimensionless number $\mathrm{Re_s}$ and Pr are defined as follows:

$$\mathrm{Re_s} = \frac{\langle\rho_f\rangle^f\ \phi_V\ \left|\langle \boldsymbol{u_f}\rangle^f\right|\ d_s}{\mu_f} \tag{7.14}$$

$$\mathrm{Pr} = \frac{\mu_f \langle C_f \rangle^f}{\lambda_f} \tag{7.15}$$

For the solid particle phase, the volume averaged energy equation writes:

$$\frac{\partial}{\partial t}[(1-\phi_V)\,\rho_s\,C_s\,\langle T_s\rangle^s] = \nabla\cdot[(1-\phi_V)\,\lambda_s\,\nabla\langle T_s\rangle^s] - a_V\,h_{sf}\left(\langle T_s\rangle^s - \langle T_f\rangle^f\right) \tag{7.16}$$

where ρ_s, T_s, C_s and λ_s represent the density, temperature, specific heat capacity and thermal conductivity of the beads.

7.6.2 Input parameters for fluid, beads and wall properties

The material properties of the ceramic beads, acrylic pipe and air are summarized in Table 6.1. The density of beads (ρ_s) and of the acrylic pipe (ρ_w) was measured at room temperature (~296.15 K) [108]. The air density (ρ_f) was determined by the ideal gas law for compressible fluids. The specific heat capacity of beads (C_s) was measured by the Differential Scanning Calorimetry (DSC Q2000, TA Instruments) [147]. Note that the thermal conductivity of air (λ_f) and acrylic (λ_w), the specific heat capacity of air (C_f) and acrylic (C_w), and the air viscosity (μ_f) were computed using temperature dependent functions implemented in the simulations with *User Defined Functions* (UDFs).

Table 7.1: Input parameters for beads, air and acrylic pipe

Material	Parameters	Value or function	Unit	Ref.
Ceramic beads	Density (ρ_s)	2580	kg/m^3	Measured
	Thermal conductivity (λ_s)	2.09	W/(m·K)	[146]
	Specific heat capacity (C_s)	846.7	J/(kg·K)	Measured
	Average diameter (d_s)	3.3×10^{-3} / 6.3×10^{-3} / 9.4×10^{-3}	m	Measured

Air	Air density (ρ_f)	Ideal gas law, $R_{specific}$ =287.055 J/(kg·K)	kg/m^3	-
	Thermal conductivity (λ_f)	$2.5143\times10^{-3} + 7.7288\times10^{-5}\ T + 8.6248\times10^{-11}\ T^2$	W/(m·K)	[148]
	Specific heat capacity (C_f)	$1.0535\times10^{3} - 3.8738\times10^{-1}\ T + 8.9321\times10^{-4}\ T^2 - 4.2048\times10^{-7}\ T^3$	J/(kg·K)	[148]
	Dynamic viscosity (μ_f)	$1.716\times10^{-5} \times (\frac{T}{273.15})^{1.5} \times \frac{383.55}{T + 110.4}$	Pa·s	[149]
Acrylic pipe	Density (ρ_w)	1170	kg/m^3	Measured
	Thermal conductivity (λ_w)	$8.3338\times10^{-5}\ T + 1.7149\times10^{-1}$	W/(m·K)	[174]
	Specific heat capacity (C_w)	$4.0289\ T + 166.95$	J/(kg·K)	[150]
	Internal pipe diameter (D_w)	0.1016	m	Measured
	Pipe wall thickness (d_w)	6.35×10^{-3}	m	Measured

7.6.3 Boundary conditions

The simulation starts with the following initial conditions:

$$\langle T_f \rangle_{t=0}^{f} = \langle T_s \rangle_{t=0}^{s} = T_{in}(0)$$
$$\langle \boldsymbol{u_f} \rangle_{t=0}^{f} = 0 \tag{7.17}$$

where $T_{in}(0)$ denotes the inlet fluid temperature at the initial time. The detailed boundary conditions used in the simulation are described in Figure 7.3. At the inlet, the temperature and velocity (in the z direction) are specified for the fluid phase:

$$\langle T_f \rangle^{f} = T_{in}(t)$$
$$\left| \langle \boldsymbol{u_f} \rangle^{f} \right| = u_{in}(t) \tag{7.18}$$

During the test, T_{in} and u_{in} do not remain constant in time. The value of T_{in} is measured by the thermocouple directly, whereas u_{in} is computed by the following equation:

$$u_{in}(t) = \frac{T_{in}(t)}{P_{in}(t)} \cdot Q_{ro} \cdot \sqrt{\frac{P_{ref}}{T_{ro}(t)} \cdot \frac{P_{ro}(t)}{T_{ref}}} \cdot \frac{4}{\pi D_w^2} \tag{7.19}$$

where D_w is the diameter of the granular bed, P_{ref} and T_{ref} are the reference pressure (101325 Pa) and temperature (291.15 K) of the rotameter. Typical examples are given in Figure 7.4a, where $u_{in}(t)$ and $T_{in}(t)$ are plotted for the 9.4×10^{-3} m bead packing with Q_{ro} = 7 and 9 Standard Cubic Feet per Minute (SCFM).

The curves of heat loss $q_{loss}(t,z)$ measured by four heat flux sensors on the outer pipe surface are shown in Figure 7.4b. The heat fluxes are given in negative and imposed directly as boundary condition representing the heat loss of the system. The heat flux values between two measurement points are computed by linear interpolation. At the wall-bed interface, the continuity of temperature and of the heat flux are applied together with a no-slip boundary condition:

$$\begin{aligned} \langle T_f \rangle^f &= T_w \\ \lambda_{fe} \frac{\partial \langle T_f \rangle^f}{\partial r} &= \lambda_w \frac{\partial T_w}{\partial r} \\ \langle \boldsymbol{u_f} \rangle^f &= 0 \end{aligned} \tag{7.20}$$

where T_w is the wall temperature. Symmetry conditions are implemented along the central axis:

$$\frac{\partial \langle T_f \rangle^f}{\partial r} = \frac{\partial \langle T_s \rangle^s}{\partial r} = \frac{\partial \langle \boldsymbol{u_f} \rangle^f}{\partial r} = 0 \tag{7.21}$$

At the outlet, the fluid pressure $\langle p \rangle^f$ is considered as the atmospheric pressure. This is done by setting the gauge pressure to zero in the simulation. All the time and position dependent boundary conditions mentioned above are implemented in Fluent using UDFs.

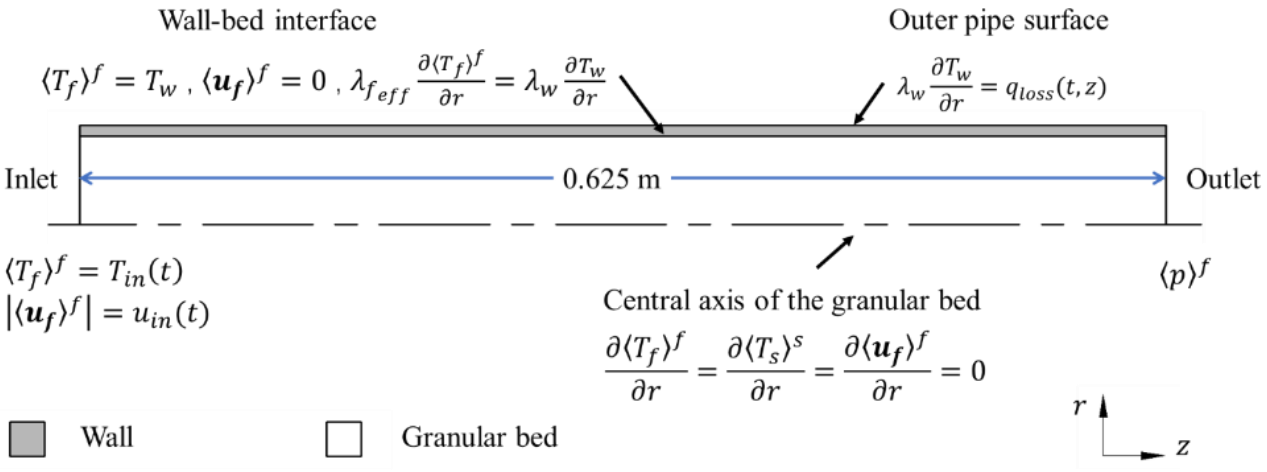

Figure 7.3: Schematic diagram of the 2D axisymmetric numerical model and boundary conditions.

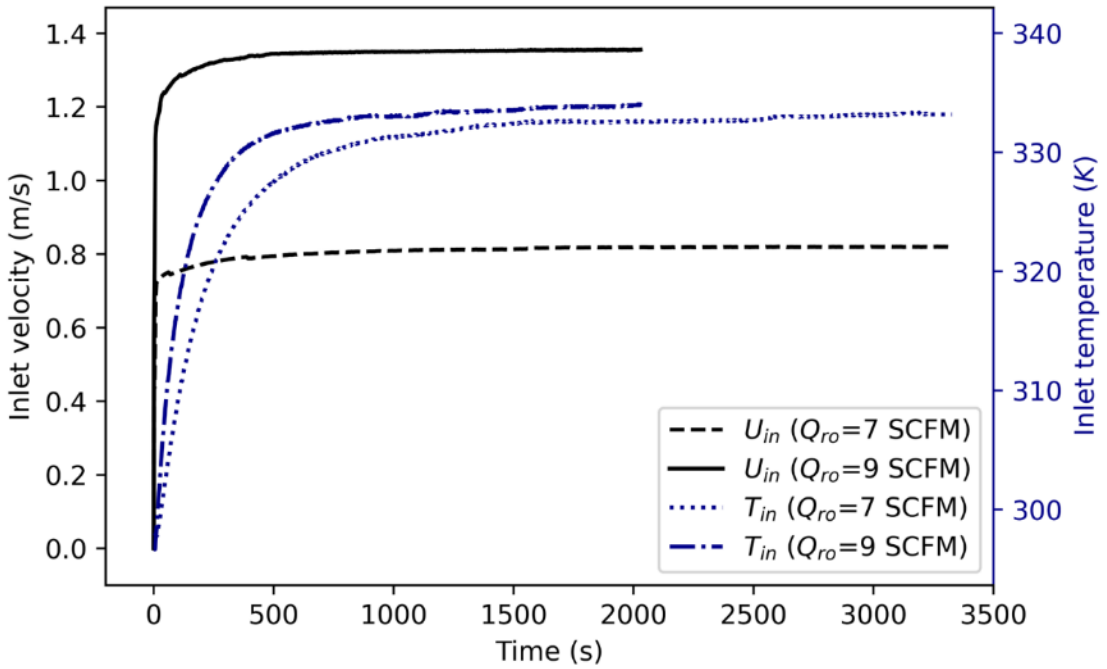

(a)

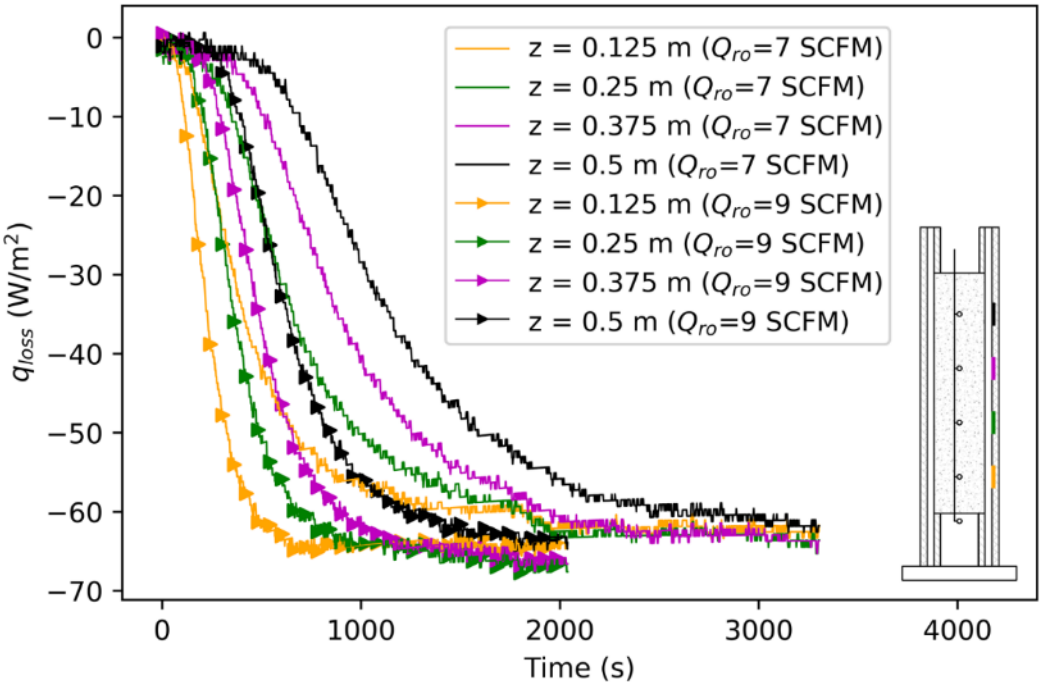

(b)

Figure 7.4: Typical experimental results used as boundary conditions in the numerical model (selected cases: 9.4×10^{-3} m bead packing with inlet flow rate Q_{ro} = 7 and 9 SCFM): (a) inlet velocity $u_{in}(t)$ and inlet temperature $T_{in}(t)$; (b) heat loss at the outer wall $q_{loss}(t,z)$ with colors indicating the axial positions.

7.6.4 Turbulence modelling

Based on Boussinesq hypothesis, the term $\langle\rho_f\rangle^f\langle \boldsymbol{u'_f u'_f}\rangle^f$ in Eq. (7.6) is computed as follows [175]:

$$-\langle\rho_f\rangle^f\langle \boldsymbol{u'_f u'_f}\rangle^f = \mu_t\left[\nabla\langle \boldsymbol{u_f}\rangle^f + \left(\nabla\langle \boldsymbol{u_f}\rangle^f\right)^T\right] - \frac{2}{3}\left(\langle\rho_f\rangle^f\langle k_f\rangle^f + \mu_t\,\nabla\cdot\langle \boldsymbol{u_f}\rangle^f\right)\boldsymbol{I} \qquad (7.22)$$

where $\langle k_f\rangle^f$ denotes the turbulent kinetic energy, $\boldsymbol{I}$ the unit matrix, and μ_t the eddy viscosity which writes:

$$\mu_t = C_\mu \langle \rho_f \rangle^f \frac{\left(\langle k_f \rangle^f\right)^2}{\langle \epsilon \rangle^f} \tag{7.23}$$

where C_μ is the constant of the $k-\epsilon$ turbulence model and $\langle \epsilon \rangle^f$ is the dissipation rate. The transport equations for $\langle k_f \rangle^f$ and $\langle \epsilon \rangle^f$ are developed in Ansys Fluent based on the volume fraction of fluid in the porous medium [144]:

$$\begin{aligned} &\frac{\partial}{\partial t}\left(\phi_V \langle \rho_f \rangle^f \langle k_f \rangle^f\right) + \nabla \cdot \left(\phi_V \langle \rho_f \rangle^f \langle k_f \rangle^f \langle \boldsymbol{u_f} \rangle^f\right) \\ &\quad = \nabla \cdot \left[\phi_V \left(\mu_f + \frac{\mu_t}{\sigma_k}\right) \nabla \langle k_f \rangle^f\right] + \phi_V \langle G_k \rangle^f - \phi_V \langle \rho_f \rangle^f \langle \epsilon \rangle^f \\ &\quad + \phi_V \langle S_k \rangle^f \end{aligned} \tag{7.24}$$

$$\begin{aligned} &\frac{\partial}{\partial t}\left(\phi_V \langle \rho_f \rangle^f \langle \epsilon \rangle^f\right) + \nabla \cdot \left(\phi_V \langle \rho_f \rangle^f \langle \epsilon \rangle^f \langle \boldsymbol{u_f} \rangle^f\right) \\ &\quad = \nabla \cdot \left[\phi_V \left(\mu_f + \frac{\mu_t}{\sigma_\epsilon}\right) \nabla \langle \epsilon \rangle^f\right] \\ &\quad + \frac{\phi_V \langle \epsilon \rangle^f}{\langle k_f \rangle^f} \left(C_{\epsilon 1} \langle G_k \rangle^f - C_{\epsilon 2} \langle \rho_f \rangle^f \langle \epsilon \rangle^f\right) + \phi_V C_{\epsilon 2} \langle S_\epsilon \rangle^f \end{aligned} \tag{7.25}$$

where G_k is the turbulent kinetic energy generated due to the fluid velocity gradient, the parameters $C_{\epsilon 1}$, $C_{\epsilon 2}$, σ_k and σ_ϵ are the standard $k-\epsilon$ turbulence model constants. The values of Launder and Spalding [151] are used: $C_{\epsilon 1}$=1.14, $C_{\epsilon 2}$=1.92, σ_k=1, σ_ϵ=1.3 and C_μ=0.09.

This approach neglects the turbulent kinetic energy and dissipation rate induced by the beads. This approach can be true when the porosity is large, or if the porous medium has little interactions with the flow. In granular packings, the values of $\langle k_f \rangle^f$ and $\langle \epsilon \rangle^f$ are likely underestimated. Therefore, the additional source terms $\langle S_k \rangle^f$ and $\langle S_\epsilon \rangle^f$ in Eq. (7.24) and Eq. (7.25) are needed. In this study, the N-K model proposed by Nakayama and Kuwahara [152] is used:

$$\langle S_k \rangle^f = \epsilon_\infty \langle \rho_f \rangle^f \tag{7.26}$$

$$\langle S_\epsilon \rangle^f = \frac{\epsilon_\infty^2}{k_\infty} \langle \rho_f \rangle^f \tag{7.27}$$

where ϵ_∞ and k_∞ are model constants, which are determined as:

$$\epsilon_\infty = 39\ \phi_V^2\ (1-\phi_V)^{2.5}\ \frac{\left|\langle \boldsymbol{u_f} \rangle^f\right|^3}{d_s} \tag{7.28}$$

$$k_\infty = 3.7\ \phi_V^{1.5}\ (1-\phi_V)\ \left|\langle \boldsymbol{u_f} \rangle^f\right|^2 \tag{7.29}$$

Although studies confirmed that the N-K model provides reasonable predictions of eddy viscosity and temperature evolution for fully turbulent flows in packed beds [74, 173], its validation range is not well established. To investigate this issue, the applicability of the N-K model will be evaluated in the sequel by comparing the numerical predictions of temperature profile with experimental data at various Reynolds numbers $\mathrm{Re_s}$.

7.6.5 Grid independence

The mesh independence and the convergence of time steps were validated prior to conduct the numerical simulations. As multiple simulations need to be performed, this was verified with the case of the maximum $\mathrm{Re_s}$, i.e., 9.4×10^{-3} m packing with Q_{ro} = 9 SCFM. The simulation domain was discretized with quadrilateral elements. Due to large solution gradients, the near-wall region was resolved with the dimensionless wall distance $y^+ < 1.5$. In the radial direction, three cases with different radial mesh growth rates were created, namely 1.05, 1.1 and 1.15. At 500 seconds, the radial temperature profiles at z = 0.25 m were compared (Figure 7.5). The maximum deviation between these cases was below 0.1 K. Therefore, the radial mesh growth rate of 1.15 was used in the simulations.

In the axial direction, three cases with different mesh sizes (Δz) were created, namely 1.7×10^{-3}, 3.5×10^{-3} and 7×10^{-3} m. The fluid temperature evolution at z = 0.125, 0.25, 0.375, 0.5 m along the granular bed centerline was compared in time (Figure 7.6). As the maximum difference was below 0.1 K after 500 seconds, 7×10^{-3} m was used, so the result can be considered as grid independent.

The convergence of the time step was studied for three cases: Δt = 0.5, 1 and 2 seconds. At 500 seconds, deviations of ~0.25 K were found for Δt = 2 seconds when comparing the axial fluid temperature evolutions at z = 0.125, 0.25, 0.375, 0.5 m (Figure 7.7). Hence, a time step of 1 second was used in the numerical analysis.

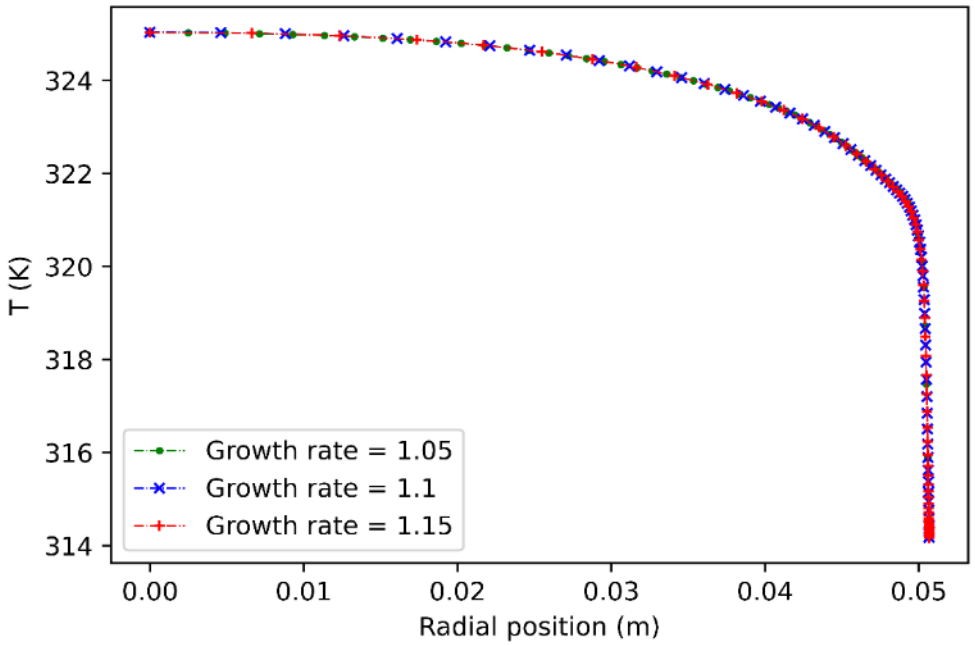

Figure 7.5: Comparison of the 9.4×10^{-3} m bead packing radial temperature profile at 500 seconds and axial position z = 0.25 m obtained in 3 numerical cases using different mesh growth rates in the radial direction.

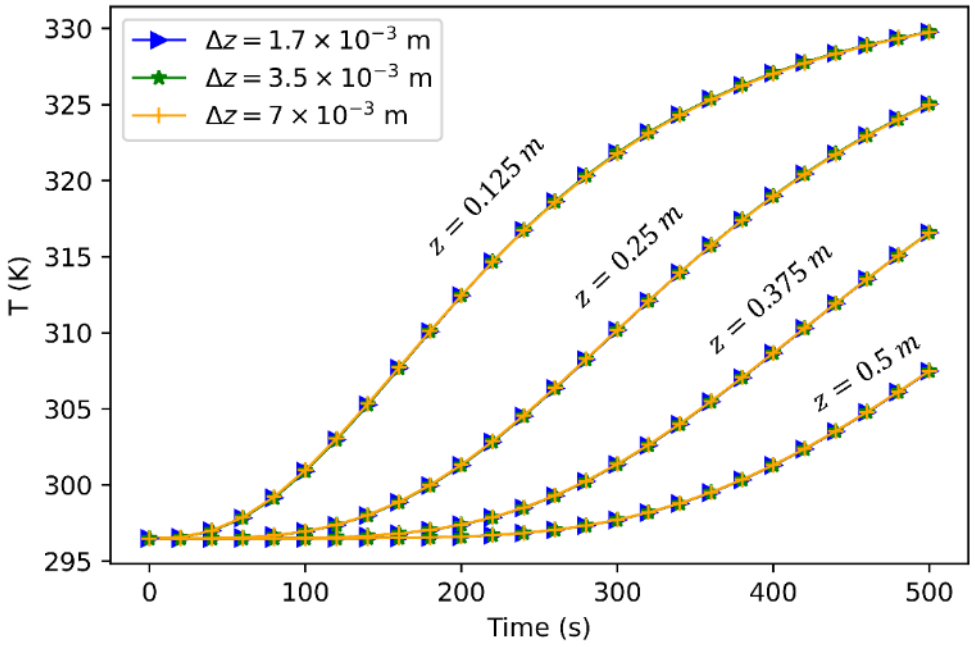

Figure 7.6: Comparison of the 9.4×10^{-3} m bead packing temperature evolution at different axial positions along the centerline of the granular bed obtained in 3 numerical cases using different axial mesh sizes (Δz).

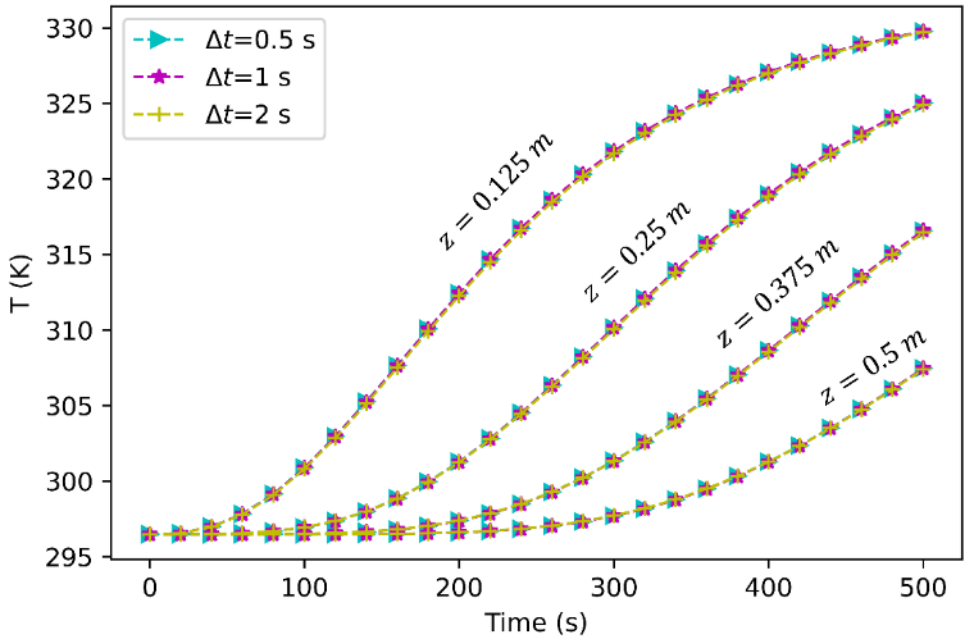

Figure 7.7: Comparison of the 9.4×10^{-3} m bead packing temperature evolution at different axial positions along the centerline of the granular bed obtained in 3 numerical cases using different time steps (Δt).

7.7 Results and discussion

7.7.1 Application range of the additional turbulence source model

To evaluate the suitability of the N-K model (i.e., Eq. (7.26) and Eq. (7.27)), numerical predictions are compared with experiments. A typical comparison of the 6.3×10^{-3} m bead packing with Q_{ro} = 9 SCFM is shown in Figure 7.8. In this test case, the N-K model (Eq. (7.26) and Eq. (7.27)) is used. The predictions of the fluid temperature along the centerline of the packing (Figure 7.8a) and on the outer pipe surface (Figure 7.8b) are compared with measurements and show good agreement. Despite this, the use of N-K model does not always predict well the experimental observations. To quantify the differences between measurements and predictions, the average deviation per data point S_{ave} is introduced and computed as follows:

$$S_{ave} = \frac{1}{n} \sum_{i=1}^{n} \left| T_{exp,i} - T_{sim,i} \right| \tag{7.30}$$

where $T_{exp,i}$ and $T_{sim,i}$ represent the i-th measured and predicted temperatures respectively and n is the total number of measured data points. Regarding the fluid temperature evolutions measured at four axial positions (i.e., at z = 0.125, 0.25, 0.375 and 0.5 m), the S_{ave} values in all cases remain below 0.5 K. This represents a good agreement between predictions and measurements. Differences of S_{ave} between predictions with and without additional turbulent sources are below 0.2 K. This shows that no obvious difference occurs with the N-K model in terms of axial fluid temperature predictions inside the granular bed. In numerical simulations, turbulence affects the fluid temperature through the effective thermal conductivity λ_{fe} and the convection between the fluid and beads. Due to the low thermal conductivity of air, the thermal convection is predominant. However, its influence on convection has already been lumped into the heat transfer coefficient h_{sf} which is directly computed from the empirical correlation. As a result, additional sources do not significantly change the temperature predictions along the centerline. In contrast, the temperature evolution predicted on the outer pipe wall are significantly different with and without additional turbulent sources (Figure 7.9a). In order to consider each case, the Reynolds number $\mathrm{Re_{in}}$ in abscissa of Figure 7.9 was calculated with the particle diameter d_s and the stabilized inlet flow velocity u_{in} (e.g., the inlet velocity after 500 seconds in Figure 7.4b). This is different from Eq. (7.14) and can be considered as a representative of the case. Regarding large Reynolds number ($\mathrm{Re_{in}} > 300$), the absence of additional sources causes higher deviations by underestimating the temperature evolution (Figure 7.9a). For lower Reynolds numbers ($\mathrm{Re_{in}} < 300$), the N-K model overestimates the temperatures and causes higher deviations. To take this into account, a better description of experimental data can be obtained by combining a multiplicative damping factor f_d in the N-K model:

$$\langle S_k \rangle^f = f_d \, \epsilon_\infty \, \langle \rho_f \rangle^f \tag{7.31}$$

$$\langle S_\epsilon \rangle^f = f_d \, \frac{\epsilon_\infty^2}{k_\infty} \, \langle \rho_f \rangle^f \tag{7.32}$$

The damping factor f_d can be expressed as a function of the Reynolds number. However, it is more appropriate to use the localized Reynolds number Re_s (Eq. (7.14)) instead of $\mathrm{Re}_{\mathrm{in}}$ to develop this function. As described by Eq. (7.4), the porosity of the granular packing decreases exponentially from the wall to the bulk porosity in the center of the granular bed. The flow velocity is therefore relatively low in the central region of the packing and increases near the wall. This indicates an uneven distribution of turbulent energy in the cross-section, which is difficult to describe with a constant Reynolds number $\mathrm{Re}_{\mathrm{in}}$. Based on the cases tested, the following functions are proposed in our investigation:

$$\begin{aligned} f_d &= 0 \quad (\mathrm{Re}_s \le 800) \\ f_d &= 3\left(\frac{\mathrm{Re}_s - 800}{100}\right)^2 - 2\left(\frac{\mathrm{Re}_s - 800}{100}\right)^3 \quad (800 < \mathrm{Re}_s < 900) \\ f_d &= 1 \quad (\mathrm{Re}_s \ge 900) \end{aligned} \tag{7.33}$$

With this damping term in the N-K model, the predictions and experimental data of the temperature profile on the outer pipe surface are compared and shown in Figure 7.9b. As the values of S_{ave} in all cases remain below 0.5 K, it is reasonable to conclude that the temperature evolution can be predicted correctly in the granular bed and on the outer wall surface.

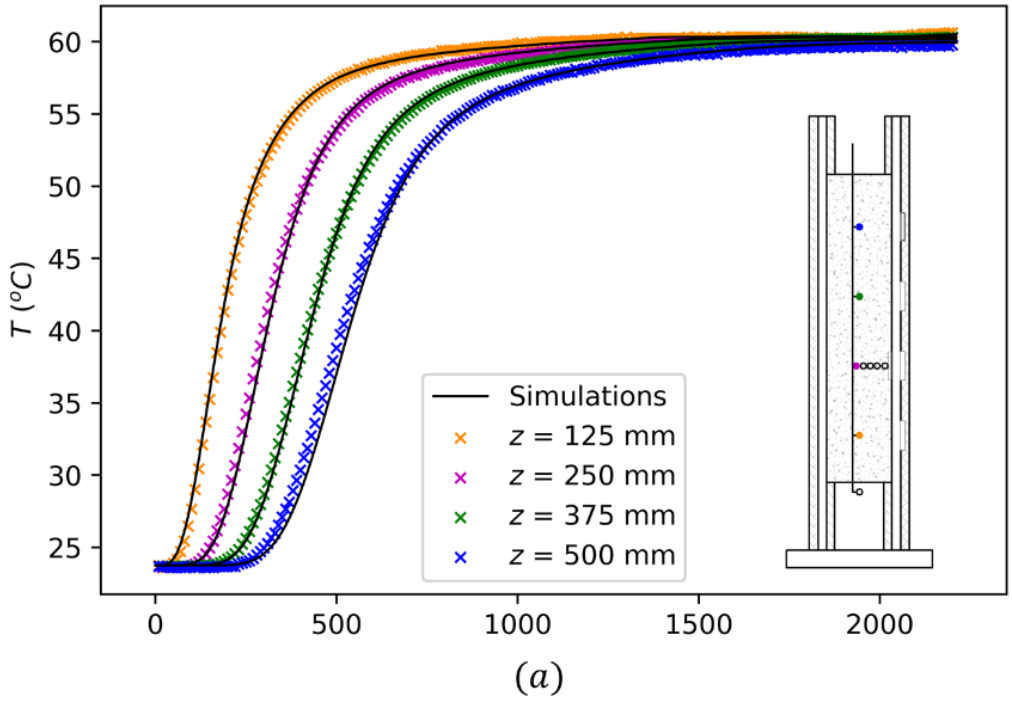

Figure 7.8: Comparison between numerical predictions (solid curves) and experimental data (scatter points) of 6.3×10^{-3} m bead packing with Q_{ro} = 9 SCFM: (a) fluid temperature evolution along the granular bed centerline; (b) outer pipe surface temperature evolution. Colors are used to distinguish different axial positions.

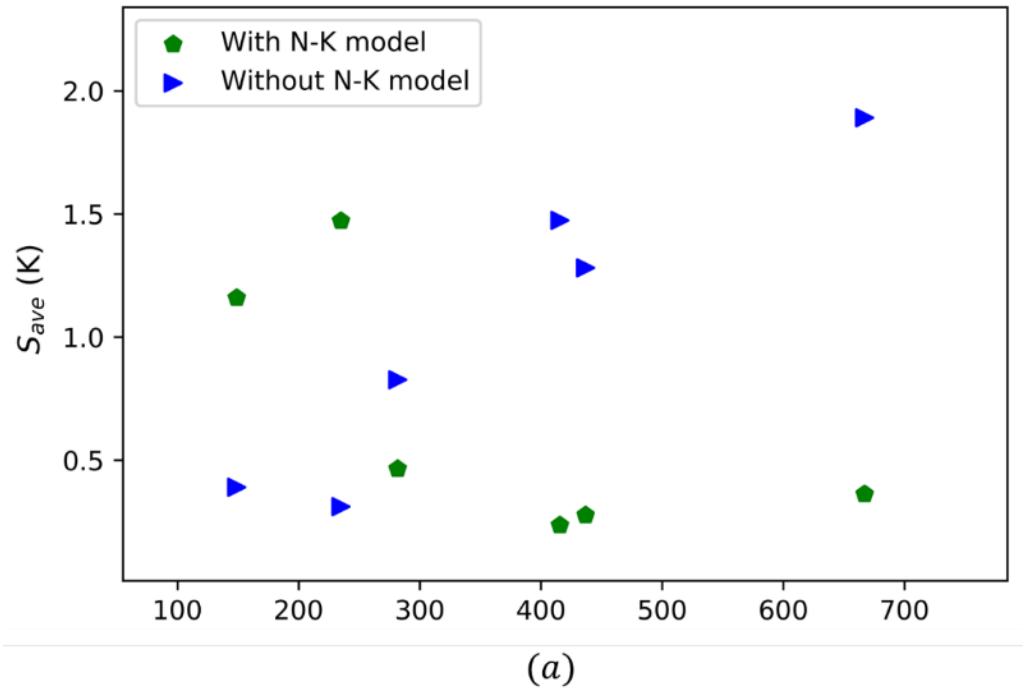

(a)

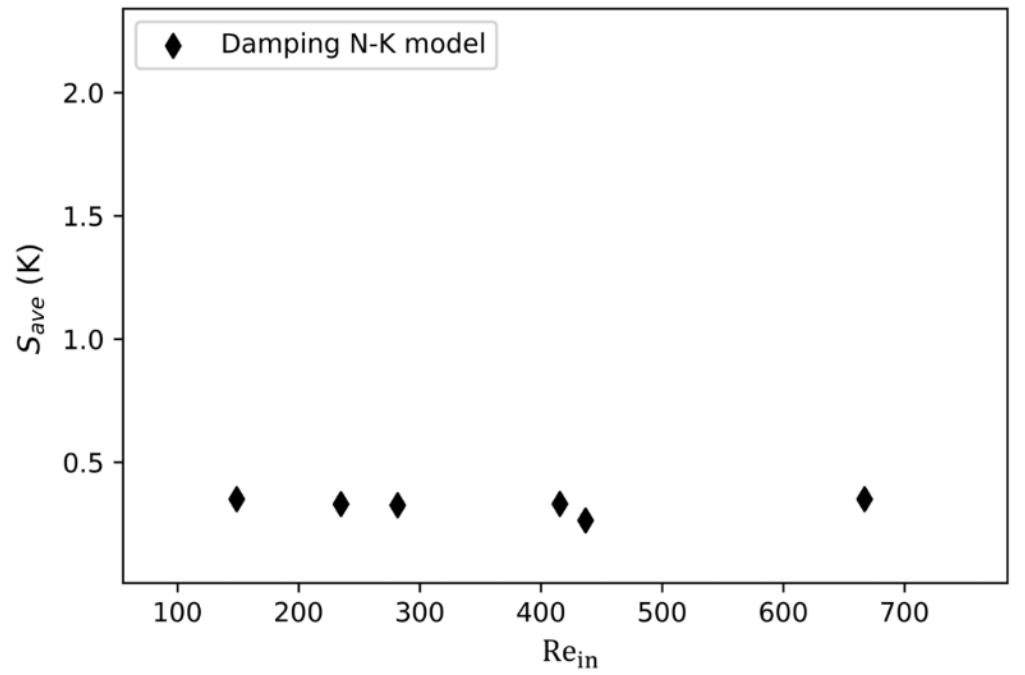

(b)

Figure 7.9: Comparisons of the average deviation S_{ave} between experimental data and numerical predictions of temperature on the outer surface of the pipe for the cases tested. Numerical results are obtained: (a) with and without the N-K model; (b) with the damping N-K model.

7.7.2 Parametric study

After verifying the predictive capability of the numerical model, the temperature uniformity of a typical cylindrical wall was investigated numerically. The 2D axisymmetric numerical model presented in Figure 7.4a was reused with modified boundary conditions to create the following baseline case:

a) The initial temperature is set at 296.15 K for the fluid, beads and wall.
b) The constant inlet flow temperature is 333.15 K.
c) The pressure inlet condition is applied with a pressure difference ΔP between the inlet and outlet of 2000 Pa.
d) No heat loss is considered on the outer pipe surface, i.e., $\partial T_w/\partial r = 0$.
e) The particle diameter d_s is 5×10^{-3} m.

The heating time $t_{heating}$ for the temperature difference between the inlet fluid and the bounding wall to become smaller than 2 K is introduced as an indicator of wall temperature uniformity and heating efficiency. A shorter heating time means a better wall thermal uniformity. The effect of different parameters was studied by varying each parameter separately from the baseline case while keeping the other parameters fixed. Six parameters were evaluated, namely the particle size (d_s), wall thickness (d_w), pressure difference (ΔP), wall thermal conductivity (λ_w), particle volumetric heat capacity ($\rho_s C_s$) and wall volumetric heat capacity ($\rho_w C_w$).

Figure 7.10 shows the evolution of $t_{heating}$ for different particle sizes ranging from 2×10^{-3} to 10×10^{-3} m. Since the thermal convection is predominant in the wall-to-bed heat transfer, the change in heating time agrees with the general trend of the flow velocity. As d_s increases, the flow resistance of the packed bed decreases (Eq. (7.8) and (7.9)), which results in a higher flow velocity. However, this influence decreases as d_s becomes larger. The evolution of $t_{heating}$ is therefore well correlated with the power law function shown in Figure 7.10. Another influence comes from the radial porosity distribution. According to Eq. (7.4), the flow channel (i.e., the high-speed flow region due to the increase in local porosity) near the wall becomes thinner with smaller beads. This gives a lower turbulent kinetic energy, which also reduces the heat transfer rate. In the current investigation, the column-to-particle diameter ratio is always kept larger than 10, which stays in the validation range of the exponential porosity model [53]. Further increase in particle size may

lead to a decrease of the heat transfer rate [158]. However, our model is not appropriate to predict this trend. In the current investigation, the column-to-particle diameter ratio D_w/d_s always remains larger than 10 since the governing equations were derived by volume averaging. This normally requests a large ratio D_w/d_s to obtain meaningful averaged physical parameters at a certain location, which also stays in the validation range of the exponential porosity model [53]. For low column-to-particle size ratios (i.e., $D_w/d_s < 10$), the *Direct Numerical Simulation* (DNS) method is commonly used to study transport phenomena in packed beds [142, 176]. The influence of ΔP on $t_{heating}$ shows a similar pattern (Figure 7.11), since the particle size is closely related to the pressure drop through the granular bed. Consequently, it is suggested to increase the particle size and the pressure drop to shorten $t_{heating}$.

The effect of d_w and $\rho_w C_w$ on $t_{heating}$ is shown in Figure 7.12 and Figure 7.13 respectively. These two parameters possess a similar influence, and the experimental data can be correlated linearly, since both factors are directly related to the total amount of energy required to heat the wall. Compared with parameters d_s and ΔP, $t_{heating}$ is more sensitive to d_w and $\rho_w C_w$: to reach 70% $t_{heating}$ of the baseline case, d_s and ΔP need to be increased by around 94% and 150%, whereas d_w and $\rho_w C_w$ only need to decrease by 54% and 40% respectively. Figure 7.14 compares different values of $t_{heating}$ obtained with various wall thermal conductivities λ_w ranging from 0.05 to 180 W/(m·K). Despite the sharp decrease for low λ_w values, i.e., for $\lambda_w < 5$ W/(m·K), the influence of the wall material conductivity rapidly flattens and becomes less pronounced than the above-mentioned factors. By increasing λ_w from 5 to 180 W/(m·K), $t_{heating}$ only decreases by ~17%.

The effect of the particle volumetric heat capacity $\rho_s C_s$ is plotted in Figure 7.15. Increasing the value of $\rho_s C_s$ means that more energy is needed to heat the particles, which results in a longer heating time. However, this parameter does not play a major role. Increasing the value of $\rho_s C_s$ by 50% results in a small increase of 16% of $t_{heating}$. Another important parameter could be the thermal conductivity of the beads λ_s, which affects the heating time in a more complex way. However, in the current model, the interaction between the solid wall and the beads is neglected because of the low thermal conductivity and small contact areas between the spheres and the bounding wall. With highly conductive particles, this model may be inadequate [177]. Furthermore, the conductivity of particles affects the temperature profile of the granular bed in both the axial and

radial directions, which in turn changes the efficiency of the wall-to-bed heat transfer. Further work would therefore be needed to assess in more details the influence of the beads thermal conductivity.

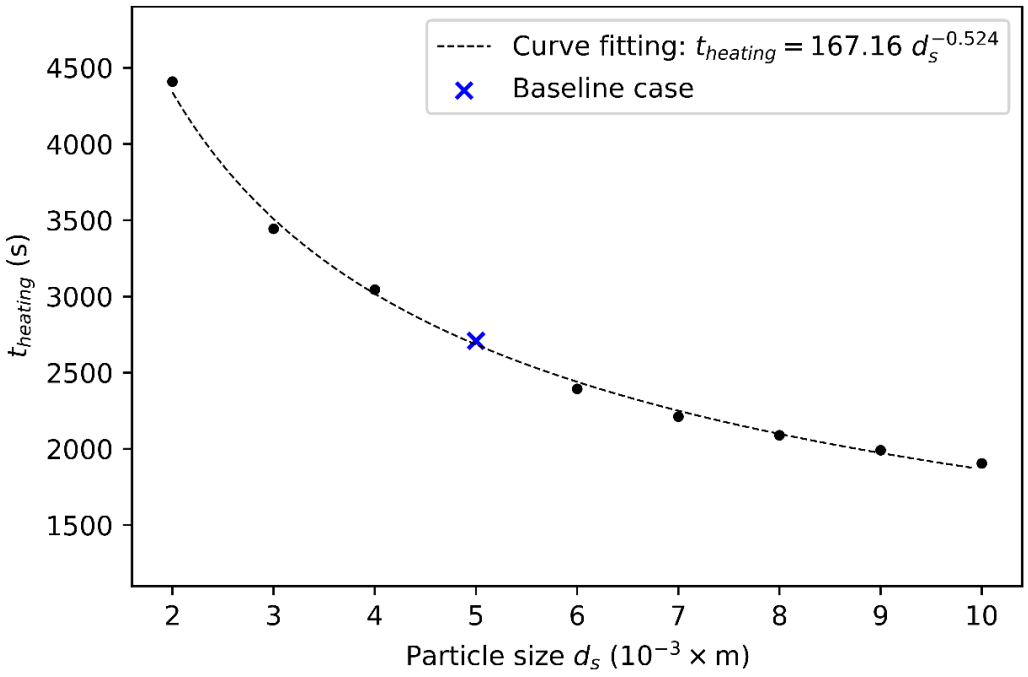

Figure 7.10: Variations in $t_{heating}$ as a function of particle size.

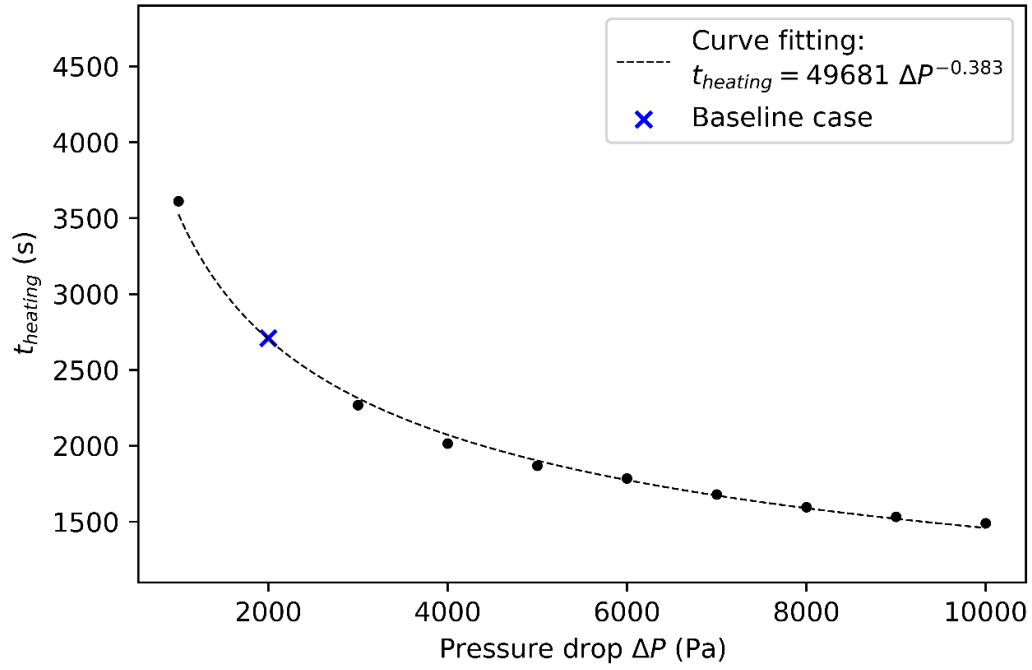

Figure 7.11: Variations in $t_{heating}$ as a function of pressure drop.

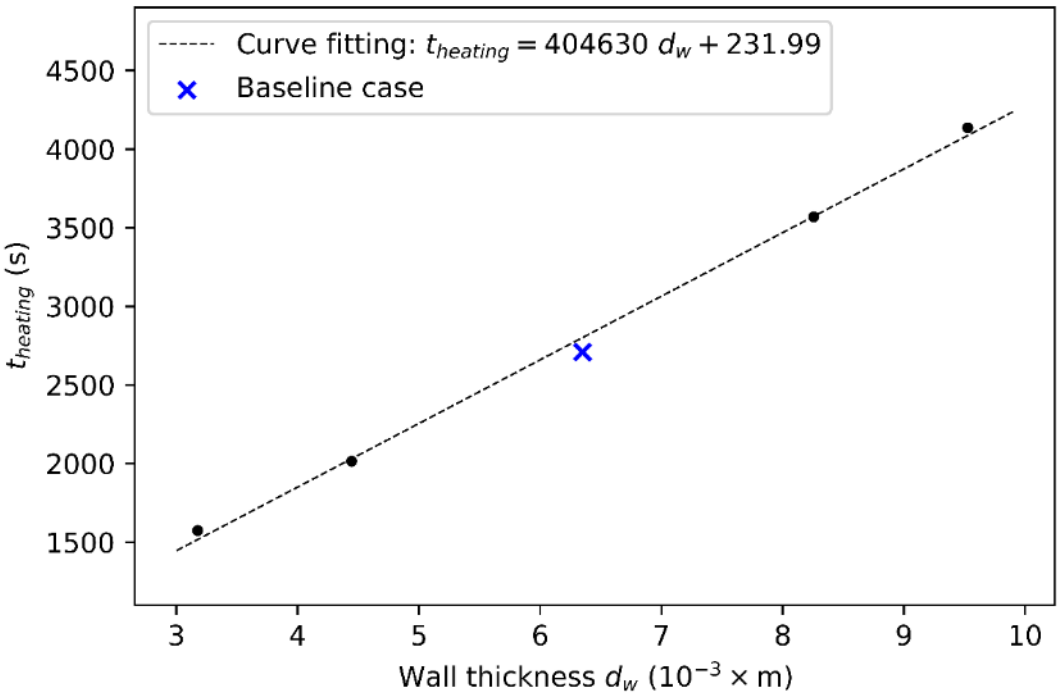

Figure 7.12: Variations in $t_{heating}$ as a function of wall thickness.

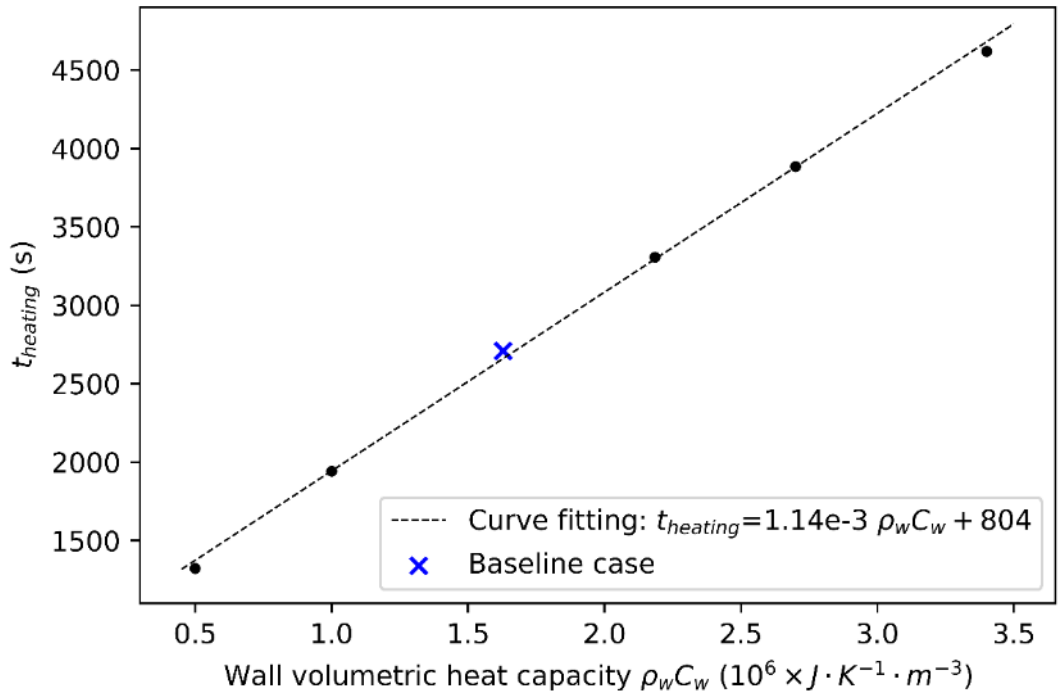

Figure 7.13: Variations in $t_{heating}$ as a function of wall volumetric heat capacity.

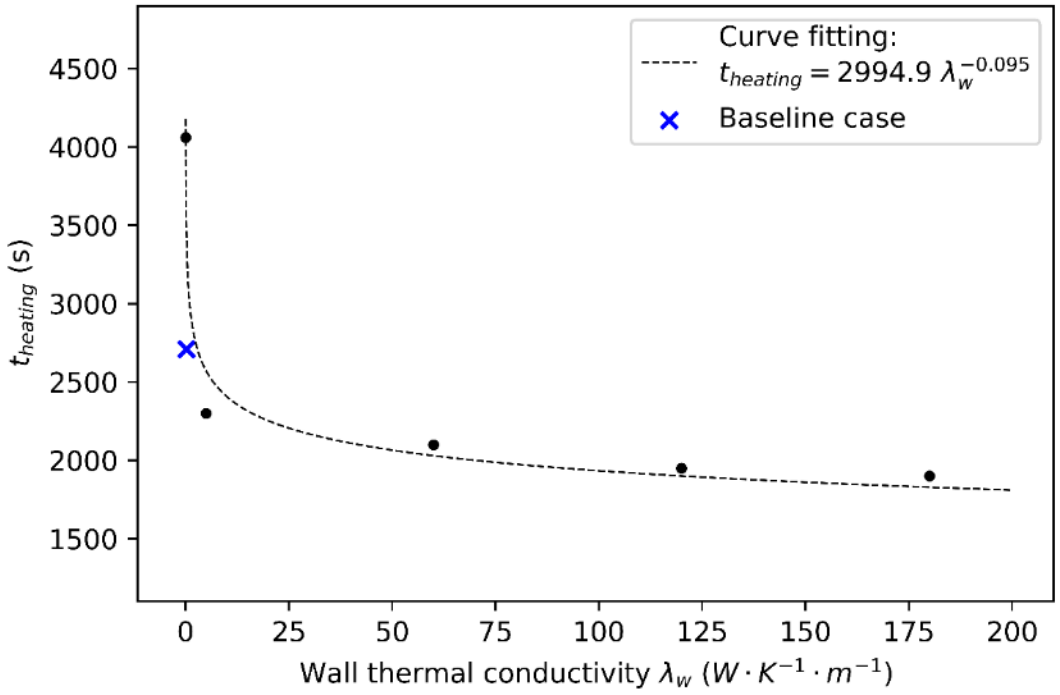

Figure 7.14: Variations in $t_{heating}$ as a function of wall thermal conductivity.

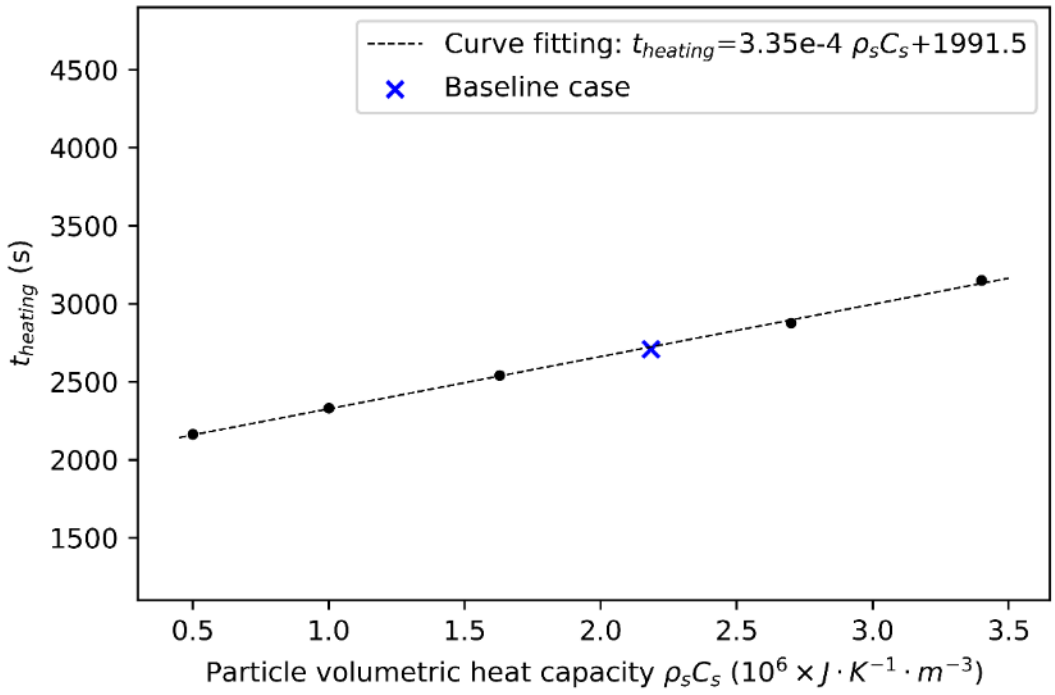

Figure 7.15: Variations in $t_{heating}$ as a function of bead volumetric heat capacity.

7.8 Conclusion

In this study, the applicability of the N-K model (Eq. (7.26) and (7.27)) was investigated to predict the wall temperature during heating of bead packings contained in cylindrical pipes. The numerical modelling framework described in [74] was used to study the heat transfer in bead packings heated by an air flow. The N-K model was found not to be applicable at low Reynolds numbers (Re_{in} < 300), since it overestimates the heat transfer rate between the wall and the beads. On the other hand, the N-K model is necessary at high Reynolds numbers (Re_{in} > 300) to compute additional turbulent sources induced by the presence of beads. Based on experimental measurements, a damping function was combined with the original N-K model to improve the accuracy of temperature predictions up to values of average deviation per data point below 0.5 K in all cases.

The uniformity of the wall temperature was also investigated numerically. A parametric study showed that reducing the wall thickness as well as volumetric heat capacity play a key role. Both factors reduce the total amount of energy required to heat the wall, therefore largely shortening the time required to reach a uniform temperature on the wall. Increasing the inlet flow rate and particle size has also an effect, but to a lower extent. Note that the study on particle size was conducted for large bed-to-particle ratios (higher than 10), which remain in the validation range of the exponential radial porosity model proposed by Hunt and Tien [124]. Therefore, future investigations are suggested to cover the analysis for low bed-to-particle ratios (smaller than 10). Finally, changing the particle volumetric heat capacity or using a highly conductive material for the wall do not play a major role.

7.9 Acknowledgements

This work was supported by the *National Science & Engineering Research Council of Canada* (NSERC) (Discovery Grants). Authors also gratefully acknowledge the *Research Center for High Performance Polymer and Composite Systems* (CREPEC) and the "*Fonds de recherche du Québec - Nature et technologies*" (FRQNT) for their partial financial support. Authors also express their sincere thanks to Christian-Charles Martel, technical assistant, for his support in the laboratory.

CHAPTER 8 ARTICLE 5: HEATING ANALYSIS FOR AN INNOVATIVE CONCEPT OF INJECTION MOLDS BASED ON GRANULAR MATERIALS

Yixun Sun, Philippe Causse, Cédric Béguin, Brahim Benmokrane and François Trochu

Submitted to *Applied Thermal Engineering* on 09/10/2021

8.1 Chapter overview

This chapter presents the article submitted to Applied Thermal Engineering, which introduces an innovative concept of molds using granular materials. The advantages of this design have been presented in detail in Chapter 2. In this new chapter, the heating performance of a granular mold is examined numerically using the modelling framework proposed and studied in Chapter 4 to Chapter 7. The mold dimensions, the material selection and the test conditions are based on similar investigations published in the scientific literature. This allows making reasonable comparisons with conventional methods, which confirm the heating performance of this innovative concept.

8.2 Abstract

This paper investigates an innovative concept of injection mold containing granular materials, which can be heated or cooled by circulating a fluid through the packed bed. This design simplifies the heating process since no autoclave, oven or complex heating system is needed. It also brings several possible advantages in terms of tooling costs and heating uniformity. In this study, the heating performance of granular molds is investigated numerically using flow and heat transfer simulations. Firstly, it is shown that thermal uniformity can be reached within a reasonable duration compared to conventional molds with ducts. The influence of several design parameters on the heating efficiency is also investigated through a parametric study. Results show that skin materials of low volumetric heat capacity and a reduced mold skin thickness improve the heating performance. Using beads of lower volumetric heat capacity or mold skin of higher thermal conductivity do not have a major influence on the heating performance.

KEYWORDS: granular material, mold heating, thermal uniformity

8.3 Introduction

As structures made of Fiber Reinforced Polymers (FRP) are lighter and have a high rigidity and strength, FRP have been increasingly used in different industries in recent years. To fabricate such structures, reinforcing fibers are impregnated by a liquid thermosetting resin and heat is delivered to the composite part to initiate the polymerization of the resin. Heating represents a critical issue since uniformity and speed of the polymerization reaction have a direct impact on the quality of the part. The commonly used approach is to heat the part indirectly via gas (e.g., nitrogen) circulation inside an autoclave or an oven. As applications of advanced high-performance composites grow in aircrafts, vehicles, boating, wind energy and even infrastructure, composite parts are getting much larger and more complex. The size of autoclaves needs to be increased accordingly. However, the cost to acquire and operate large autoclaves tend to be significantly large [3, 4]. To reduce cost and improve heating efficiency, alternative heating methods have been proposed without autoclaves or ovens. Many of them embed the heating elements in the mold and heat the part directly through the mold surface. Such approach uses heat transfer fluids (e.g., oil, gas, steam, etc.) [29, 178, 179], electrical resistance heaters [20] or inductive heating elements [180]. Compared with the other methods, using heat transfer fluids comes up with some practical advantages since it is easy to control the maximum temperature and because the heating system can be used ‘reversely’ for cooling before demolding the composite part. One of the most commonly used methods is to circulate the heat transfer fluid through ducts embedded (or drilled) in the mold and several studies have been conducted to analyze the thermal performance of such heating system. Abdalrahman et al. [179] showed that the fluid channel cross-sectional geometry has little influence on heating efficiency and that the parallel piping layout is the most efficient for heating. Ding et al. [178] studied an oil-heated tool embedded with parallel pipes. They showed that the time to reach thermal uniformity mainly depends on the flow rate. In addition, compared with laminar flows, a fully turbulent flow drastically shortens the heating time. Collomb et al. [181] compared heating channels of rectangular and circular cross-sections to optimize design parameters. They concluded that using low thermal inertia materials for the mold improves the heating performance. The ‘technological parameters’ (e.g., pump capacity, fluid properties, heating device

parameters) also need to be considered for the design and sizing of an injection mold. Molds with ducts come with a higher cost for the installation and repair of ducts, especially for large molds. It is also difficult to evaluate the heat loss along the pipes [182]. Finally, ducts cannot always follow the shape of complex parts [9], which brings another major limitation.

Recently, a novel mold concept based on granular materials was proposed [11]. This approach has the potential to overcome the above-mentioned limitations, while keeping the advantages of using a heat transfer fluid. The design of a granular mold is schematically depicted in Figure 8.1. The core of the mold consists of a cavity packed with a granular material and covered by a rigid mold skin reproducing the shape of the molded part. Seal of the cavity is achieved by standard grooves and rubber. The mold skin is heated (or cooled) by passing a fluid through the granular bed. The outer surface of the cavity wall is covered by insulation layers to reduce the heat loss. Compared with conventional heating methods, this design can bring significant savings on tooling, because the same granular mold can be reused to make different parts by replacing only the mold skin. Machining a full metallic mold or fabricating a ribbed tool would be indeed much more expensive. The work required to install heating ducts can also be saved. Another advantage over heating ducts lies in the ability to follow the geometry of the molded part with the deformable granular material packed in the mold. Finally, continuous flow lines through the granular bed provide an enhanced heat transfer rate with the mold skin [113]. Compared with discrete heating ducts or electrical wires, this can also improve the heating uniformity of the molded part. However, granular molds are a new concept. Their thermal efficiency still needs to be investigated.

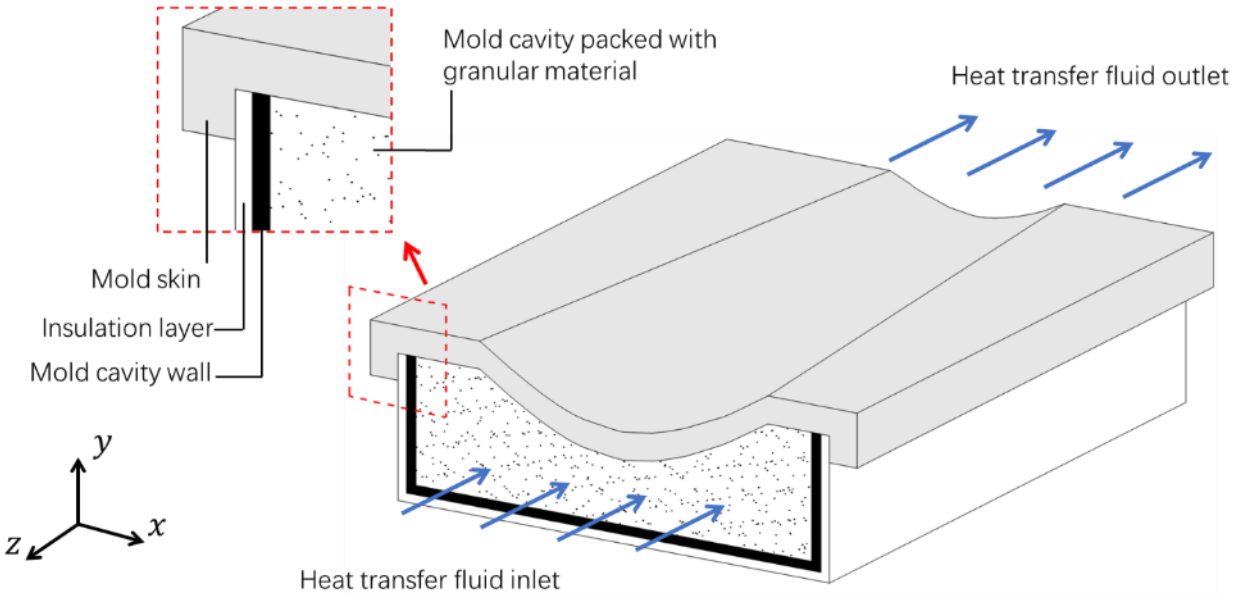

Figure 8.1: Schematic of a granular mold (the heat transfer fluid is injected in the z direction)

The objective of this study is to assess the thermal performance of granular molds by numerical simulation. The first part of the article describes the numerical model. This includes the dimensions of the model, the governing equations, the input parameters and the boundary conditions. The second section investigates through a parametric study the influence of several design parameters on the heating uniformity of the mold skin.

8.4 Numerical Analysis

The test case considered is a planar square mold having side of 1 meter (Figure 8.2a). The cavity has a height (h_{cav}) of 50 mm and is filled with monodisperse ceramic beads packed randomly. The size of beads (d_p) is assumed to be 10 times smaller than the cavity height (i.e., d_p= 5 mm). Hot air is injected in the z direction and passes through the granular bed to heat the mold skin. As no heat loss is considered, the computational domain is simplified as a 2D symmetric domain (Figure 8.2b) with the mold skin and half of the mold cavity. The thickness of the skin (d_w) is 3 mm. Two typical materials are tested for the mold skin, namely aluminum and FRP. Numerical simulations are performed with the commercial software Ansys Fluent. Reynolds-averaged Navier-Stokes

(RANS) Computational Fluid Dynamics (CFD) is used to simulate the flow and heat transfer. The governing equations, the input material properties and the boundary conditions are presented in the sequel.

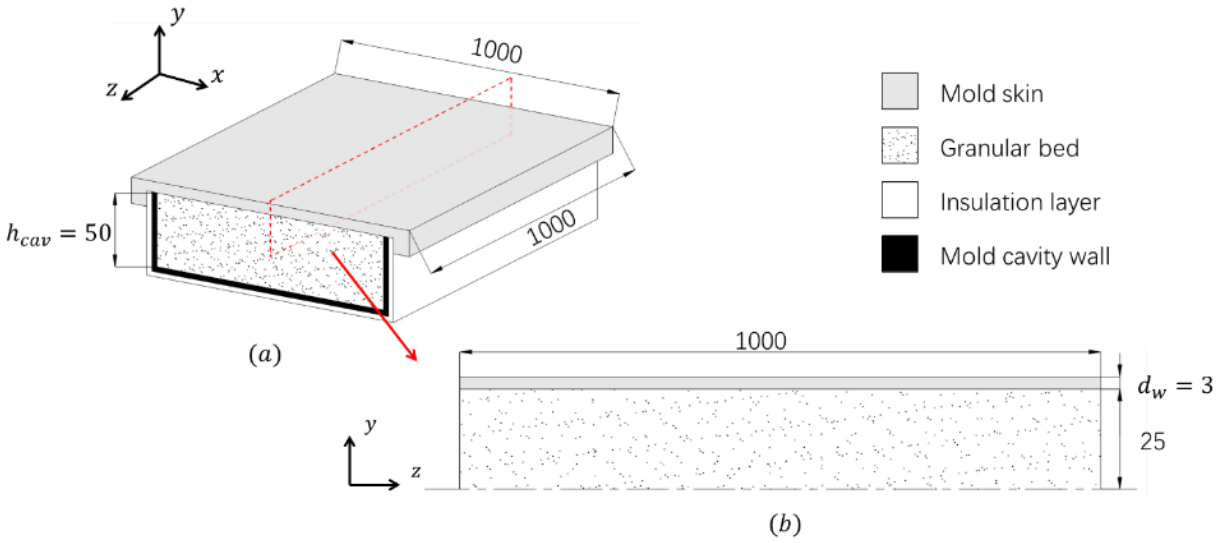

Figure 8.2: Schematic of the test case: (a) structure of the granular mold covered by a flat square skin and filled with monodisperse ceramic beads; (b) 2D symmetric computational domain (dimensions in mm).

8.4.1 Governing equations

The governing equations for flow and heat transfer in a wall-confined granular medium were developed in a prior work of Sun et al. [183] using a non-constant Representative Elementary Volume (REV) and the local volume averaging technique. The mass, momentum and energy conservation equations stand as follows:

- Mass conservation:

$$\frac{\partial\left(\phi_V \langle\rho_f\rangle^f\right)}{\partial t} + \nabla \cdot \left(\phi_V \langle\rho_f\rangle^f \langle \boldsymbol{u_f} \rangle^f\right) = 0 \tag{8.1}$$

where ϕ_V is porosity, ρ_f the air density, t the time, and $\boldsymbol{u_f}$ the air velocity. The symbol $\langle\,\rangle^f$ represents the fluid phase intrinsic average over a REV, which writes:

$$\langle\,\rangle^f = \frac{1}{V_f}\int_{V_f} dV = \frac{1}{\phi_V\, V}\int_{V_f} dV \tag{8.2}$$

where V is the REV volume and V_f represents the fluid volume in the REV. The value of ϕ_V does not remain constant near the wall. For RANS CFD simulations, the variation of ϕ_V near the wall is appropriately described by the model of Hunt and Tien [124], which was verified in our previous investigation [183]:

$$\phi_V = 0.4\left[1 + 1.5\exp\left(-8\,\frac{d_{wall}}{d_p}\right)\right] \tag{8.3}$$

where d_p is the diameter of beads, and d_{wall} the distance to the mold skin. Note that this porosity model is generally considered as valid for channel-to-particle size ratio larger than 10 (i.e., $h_{cav}/d_p \geq 10$).

- Momentum conservation:

$$\begin{aligned}&\frac{\partial}{\partial t}\left(\phi_V\,\langle\rho_f\rangle^f\,\langle\boldsymbol{u_f}\rangle^f\right) + \nabla\cdot\left(\phi_V\,\langle\rho_f\rangle^f\,\langle\boldsymbol{u_f}\rangle^f\langle\boldsymbol{u_f}\rangle^f\right)\\ &= -\,\phi_V\,\nabla\langle p\rangle^f + \nabla\left(\phi_V\,\langle\bar{\bar{\tau}}\rangle^f\right) + \phi_V\,\langle\rho_f\rangle^f\,\boldsymbol{g} - \nabla\cdot\left(\phi_V\,\langle\rho_f\rangle^f\langle\boldsymbol{u'_f u'_f}\rangle^f\right)\\ &-\left(\frac{180\,(1-\phi_V)^2}{d_p^2\,\phi_V}\,\mu_f\,\langle\boldsymbol{u_f}\rangle^f + \frac{1.8\,(1-\phi_V)}{d_p}\,\langle\rho_f\rangle^f\,\left|\langle\boldsymbol{u_f}\rangle^f\right|\langle\boldsymbol{u_f}\rangle^f\right)\end{aligned} \tag{8.4}$$

where $\langle\boldsymbol{u_f}\rangle^f\langle\boldsymbol{u_f}\rangle^f$ represents the tensor product of the averaged fluid velocity, p the pressure, $\boldsymbol{g}$ the gravitational acceleration, μ_f the fluid viscosity, and $\bar{\bar{\tau}}$ the stress tensor. The term $\langle\rho_f\rangle^f\langle\boldsymbol{u'_f u'_f}\rangle^f$ represents the Reynolds stress computed with the standard $k-\epsilon$ turbulence model.

- Energy conservation:

The thermal energy equation of the fluid phase writes:

$$\begin{aligned}&\frac{\partial}{\partial t}\left(\phi_V\,\langle\rho_f\rangle^f\,\langle C_f\rangle^f\,\langle T_f\rangle^f\right) + \nabla\cdot\left(\phi_V\,\langle\rho_f\rangle^f\,\langle C_f\rangle^f\,\langle T_f\rangle^f\,\langle\boldsymbol{u_f}\rangle^f\right)\\ &= \nabla\cdot\left(\phi_V\,\lambda_{fe}\,\nabla\langle T_f\rangle^f\right) - \frac{6\,(1-\phi_V)}{d_p}\,h_{sf}\left(\langle T_f\rangle^f - \langle T_s\rangle^s\right)\end{aligned} \tag{8.5}$$

where T_f is the fluid temperature, C_f the fluid specific heat capacity, h_{sf} the convective heat transfer coefficient, and λ_{fe} the effective thermal conductivity of the fluid. The coefficient h_{sf} is computed from the correlation of Wakao et al. [72]:

$$h_{sf} = \frac{(2 + 1.1\ \mathrm{Re_p}^{0.6}\ \mathrm{Pr}^{1/3})\ \lambda_f}{d_p} \tag{8.6}$$

where λ_f is the thermal conductivity of the fluid, $\mathrm{Re_p}$ the Reynolds number based on the particle size, and Pr the the Prandtl number. The parameters $\mathrm{Re_{dp}}$ and Pr are defined as follows:

$$\mathrm{Re}_p = \frac{\langle \rho_f \rangle^f\ \phi_V\ \left| \langle \boldsymbol{u_f} \rangle^f \right|\ d_p}{\mu_f} \tag{8.7}$$

$$\mathrm{Pr} = \frac{\mu_f\ \langle C_f \rangle^f}{\lambda_f} \tag{8.8}$$

For solid particles, the volume averaged energy equation writes:

$$\begin{aligned} &\frac{\partial}{\partial t}\left[(1-\phi_V)\ \rho_s\ C_s\ \langle T_s \rangle^s\right] \\ &\qquad = \nabla \cdot \left[(1-\phi_V)\ \lambda_s\ \nabla \langle T_s \rangle^s\right] - \frac{6\ (1-\phi_V)}{d_p}\ h_{sf}\ \left(\langle T_s \rangle^s - \langle T_f \rangle^f\right) \end{aligned} \tag{8.9}$$

where ρ_s, T_s, C_s and λ_s represent the density, temperature, specific heat capacity and thermal conductivity of beads. The symbol $\langle\ \rangle^s$ represents the solid bead phase intrinsic volume average, which is similar to (8.1):

$$\langle\ \rangle^s = \frac{1}{V_s} \int_{V_s} dV = \frac{1}{(1-\phi_V)\ V} \int_{V_s} dV \tag{8.10}$$

where V_s denotes the volume of beads in the REV.

8.4.2 Input material properties of fluid, beads and mold

The material properties used as input parameters in the numerical study are reported in Table 8.1: Material properties of ceramic, air, aluminum and FRP. The FRP material is assumed to be isotropic with a typical thermal conductivity value in the through-thickness direction. (In practice, such materials are generally orthotropic with a much larger thermal conductivity in the in-plane direction). Note that the air density (ρ_f) is determined by the ideal gas law for compressible fluids. The thermal conductivity (λ_f), the specific heat capacity (C_f) and the viscosity (μ_f) of air are described by temperature dependent functions implemented in the simulations by User Defined Functions (UDFs).

Table 8.1: Material properties of ceramic, air, aluminum and FRP

	Material	Parameters	Value or function	Unit	Ref.
Mold filler	Ceramic	Density (ρ_s)	2580	kg/m^3	[145]
		Thermal conductivity (λ_s)	2.09	W/(m·K)	
		Specific heat capacity (C_s)	846.7	J/(kg·K)	
		Particle diameter (d_p)	0.005	m	-
Heat transfer fluid	Air	Thermal conductivity (λ_f)	$2.5143\times10^{-3} + 7.7288\times10^{-5}\ T + 8.6248\times10^{-11}\ T^2$	W/(m·K)	[148]
		Specific heat capacity (C_f)	$1.0535\times10^{3} - 3.8738\times10^{-1}\ T + 8.9321\times10^{-4}\ T^2 - 4.2048\times10^{-7}\ T^3$	J/(kg·K)	
		Dynamic viscosity (μ_f)	$1.716\times10^{-5} \times (\frac{T}{273.15})^{1.5} \times \frac{383.55}{T + 110.4}$	Pa·s	[149]
Mold skin	Aluminum	Density	2702	kg/m^3	[178]
		Thermal conductivity	237	W/(m·K)	
		Specific heat capacity	903	J/(kg·K)	
	FRP	Density	1600	kg/m^3	[179]

		Thermal conductivity	0.64	W/(m·K)	
		Specific heat capacity	1075	J/(kg·K)	

8.4.3 Boundary conditions

The initial temperature is 298.15 K for the air, beads and mold skin. Figure 8.3 shows the detailed boundary conditions used in the simulations. At the inlet, air is injected at 363.15 K in the z direction. The pressure difference ΔP between the inlet and outlet is 8000 Pa. At the skin-bed interface, a no-slip boundary condition and continuous temperature profile are applied:

$$\langle \boldsymbol{u_f} \rangle^f = 0 \, , \langle T_f \rangle^f = T_w \, , \lambda_{fe} \frac{\partial \langle T_f \rangle^f}{\partial y} = \lambda_w \frac{\partial T_w}{\partial y} \tag{8.11}$$

where T_w and λ_w represent the temperature and the thermal conductivity of the mold skin. Symmetrical boundary conditions are applied in the center of the mold cavity:

$$\frac{\partial \langle T_f \rangle^f}{\partial y} = \frac{\partial \langle T_s \rangle^s}{\partial y} = \frac{\partial \langle \boldsymbol{u_f} \rangle^f}{\partial y} = 0 \tag{8.12}$$

No heat loss is considered on the outer surface of the mold skin, i.e., $\partial T_w / \partial y = 0$.

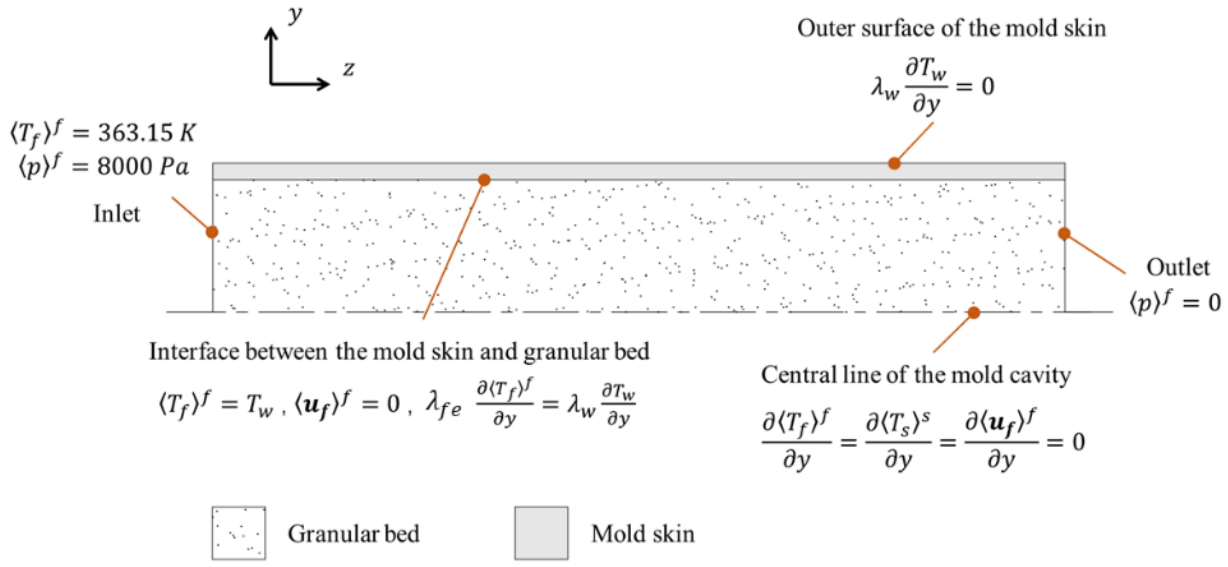

Figure 8.3: Schematic diagram of the 2D symmetric model and boundary conditions.

8.5 Results and discussions

To evaluate the heating performance, an indicator $t_{heating}$ is defined as the heating time until the temperature difference between the inlet fluid and the coldest point on the mold skin becomes less than 2 K. A shorter heating time means a better thermal uniformity and higher efficiency. For the two materials tested, i.e., aluminum and FRP, the values of $t_{heating}$ are 1470 and 1275 seconds respectively. This is comparable to the heating time of conventional molds with ducts (see Table 8.2), which shows that the granular mold concept is promising in terms of heating efficiency. Thanks to the support provided the granular material, the thickness of the skin can be reduced to a few millimeters. This decreases the influence of the material conductivity in the through-thickness direction. As a result, a shorter heating time is obtained with a FRP skin compared to an aluminum one. This is different from conventional molds with ducts, because metallic molds usually possess a shorter heating time than composite ones [184]. This feature suggests that the mold skin could be 3D printed (possibly with a complex geometry) while keeping the mold heating efficiency, since printable materials usually exhibit a low thermal conductivity [185].

Various parameters can influence the heating time of a granular mold. To investigate this, a parametric study was conducted using the case with aluminum skin as baseline. The influence of each parameter was investigated separately and compared with the baseline case while keeping the other factors fixed. The effect of skin thickness d_w and volumetric heat capacity $\rho_w C_w$ on the heating time is shown in Figure 8.4 and Figure 8.5 respectively. The influence of these two parameters is similar, since they are both related to the total amount of energy required to heat the mold skin: to reach 70% of the baseline case, d_w and $\rho_w C_w$ need to be varied by 62 % and 80 %. In comparison, the influence of the particle volumetric heat capacity $\rho_s C_s$ is even less important as illustrated in Figure 8.6: decreasing this parameter by 77% only decreases the heating time by 13%. The effect of the mold skin thermal conductivity λ_w is plotted in Figure 8.7. The curve decreases sharply at low λ_w values and remains nearly constant for large values. This shows that using highly conductive skin materials does not have a huge impact on the heating efficiency. The thermal conductivity λ_s of beads affects the heating performance of the mold in a more complex way. In the current model, the heat conduction between the mold skin and the particles is neglected due to a low λ_s value and the small contact area between spherical beads and the flat mold skin. With

highly conductive beads or particles of irregular shape, this assumption could be inadequate [177]. Further work would be needed to investigate such situations.

Figure 8.8 shows the variations of heating time for different bead sizes ranging from 2 to 5 mm. As the beads diameter increases, the average flow velocity $\langle \boldsymbol{u_f} \rangle^f$ increases (Eq. (8.6)). Since convection is a dominant factor to heat the mold skin, a higher $\langle \boldsymbol{u_f} \rangle^f$ results in smaller values of $t_{heating}$. Furthermore, according to Eq. (8.4), the flow channel in the granular bed near the mold skin (i.e., the high-speed flow region due to the increase in local porosity) becomes thicker with large beads. This gives a higher turbulent kinetic energy, which also boosts the heat transfer rate. Therefore, larger beads are preferable. To remain within in the validation range of the numerical model, the size ratio h_{cav}/d_p is kept at 10 and the effect of the cavity height h_{cav} (defined in Figure 8.2) is studied (Figure 8.9). The results show that $t_{heating}$ decreases for larger cavity heights, but the reduction becomes gradually smaller. On the other hand, the inlet air flow rate increases with h_{cav}, which means more energy is required to heat the inlet air. The total required energy (Q_{air}) may be estimated as follows:

$$Q_{air} = C_f \, \rho_f \, u_f \, A_{inlet} \, t_{heating} \, \Delta T \tag{8.13}$$

where C_f, ρ_f and u_f are respectively the inlet air specific heat capacity, density and velocity determined at 363.15 K and 8000 Pa. The parameter A_{inlet} is the inlet area, i.e., here $h_{cav} \times 1\ m$. The temperature increment ΔT is considered as the difference between the initial and inlet temperatures, i.e., 363.15 K – 298.15 K. The energy Q_{air} plotted in Figure 8.10 increases linearly with h_{cav}. From this point of view, it is less efficient to excessively increase the cavity height. In addition, the maximum inlet flow rate, pressure, and thermal energy are limited by the power of the air blower and heater. Therefore, the trade-off between Q_{air} and $t_{heating}$ must be considered for each operational condition.

Table 8.2: Summary of published results on the heating performance of conventional flat molds with heating ducts

Ref.	Fluid	Mold material	Dimen-sions (mm)	Heating time (s)	Crite-rion of the heating time	Temp-erature range (°C)	Adiabatic boundary condition	Notes
[181]	Water / thermal oil	Steel	d_{duct}=8, d_{surf}=16, s_{duct}=16	910 (water), 3659 (thermal oil)	T_{min} = 72°C	25 to 80	Yes	Numerical study using 2D symmetric model
[178]	Thermal oil	Alumi-num	Square tool surface of 450 on a side, th_{tot}=22.5 , d_{duct}=10.5	~9000 (Re_D = 2300), ~300 (Re_D = 10000)	T_{min} = 180 °C	20 to 180	Yes	Numerical study using 3D numerical model
[186]	Water	FRP and Alepoxy	Square tool surface of 500 on a side; th_{tot}=22.5 , d_{duct}=10	600	T_{min} = 81°C	17 to 90	-	Experimental study of mold with parallel ducts. Total flow rate is 15.68 L/min
[184]	Thermal oil	Stainless steel / Com-posite	d_{duct}=8, d_{surf}=8 to 20, s_{duct}=24	~460 (Stainless steel), ~470 (composite)	T_{min} = 180°C	120 to 185	Yes	Numerical study with 2D symmetric model. The heat transfer coefficient between the fluid and channel wall is assumed as 1500 $Wm^{-2}K^{-1}$
[187]	Thermal oil	Alumi-num	Rectangular tool surface of 1780×900, th_{tot}=75, d_{duct}=9	~3600	T_{min} = 70°C	20 to 70	-	Experimental investigation, the flow velocity in the duct is 2.02 m/s

(Here d_{duct} is the diameter of the duct, d_{surf} the vertical distance between the ducts and the mold surface, s_{duct} the distance between ducts, th_{tot} the total thickness of the mold, Re_D the Reynolds number based on d_{duct}, and T_{min} the minimum temperature of the mold surface during heating.)

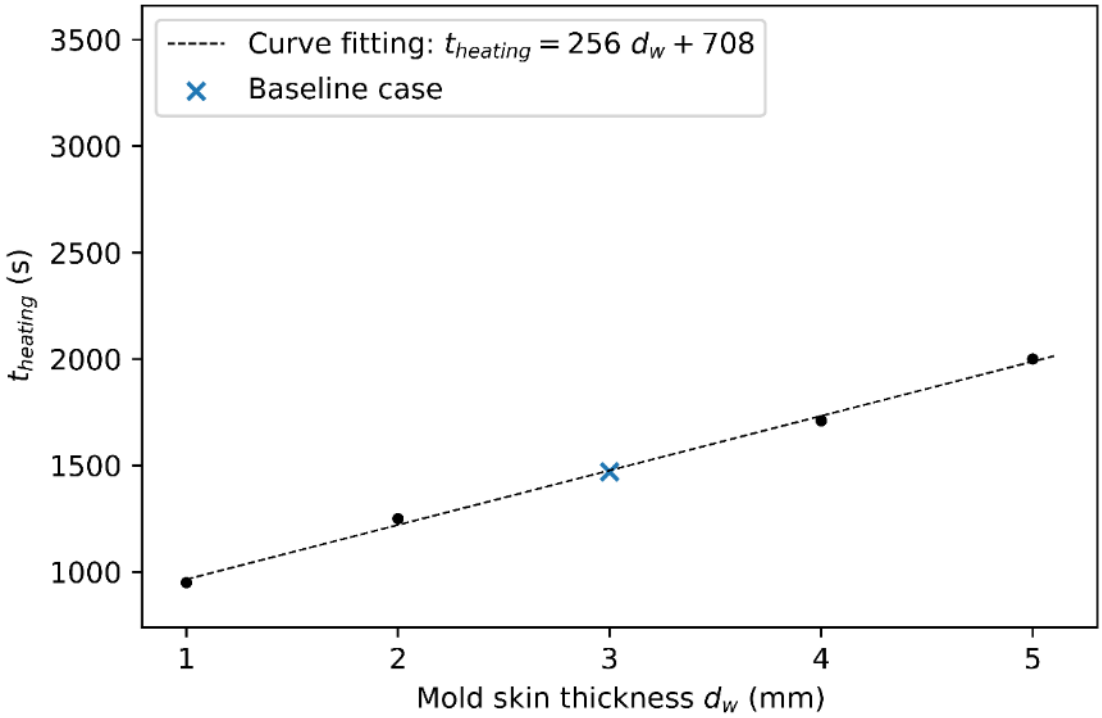

Figure 8.4: Variations in $t_{heating}$ as a function of mold skin thickness.

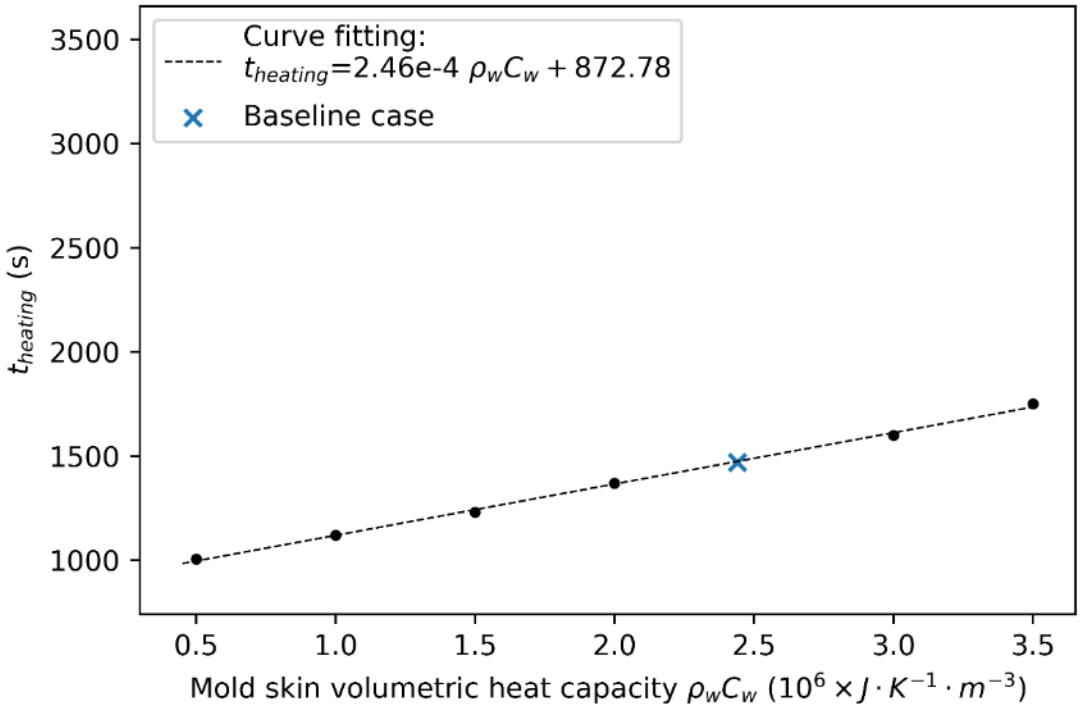

Figure 8.5: Variations in $t_{heating}$ as a function of skin volumetric heat capacity.

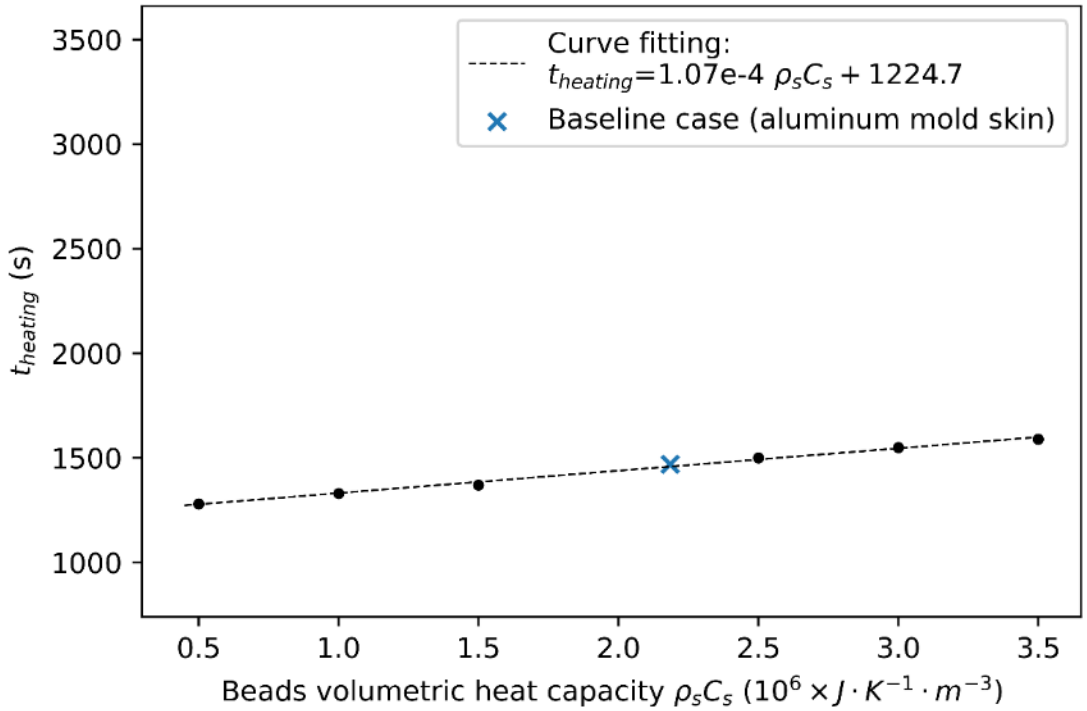

Figure 8.6: Variations in $t_{heating}$ as a function of bead volumetric heat capacity.

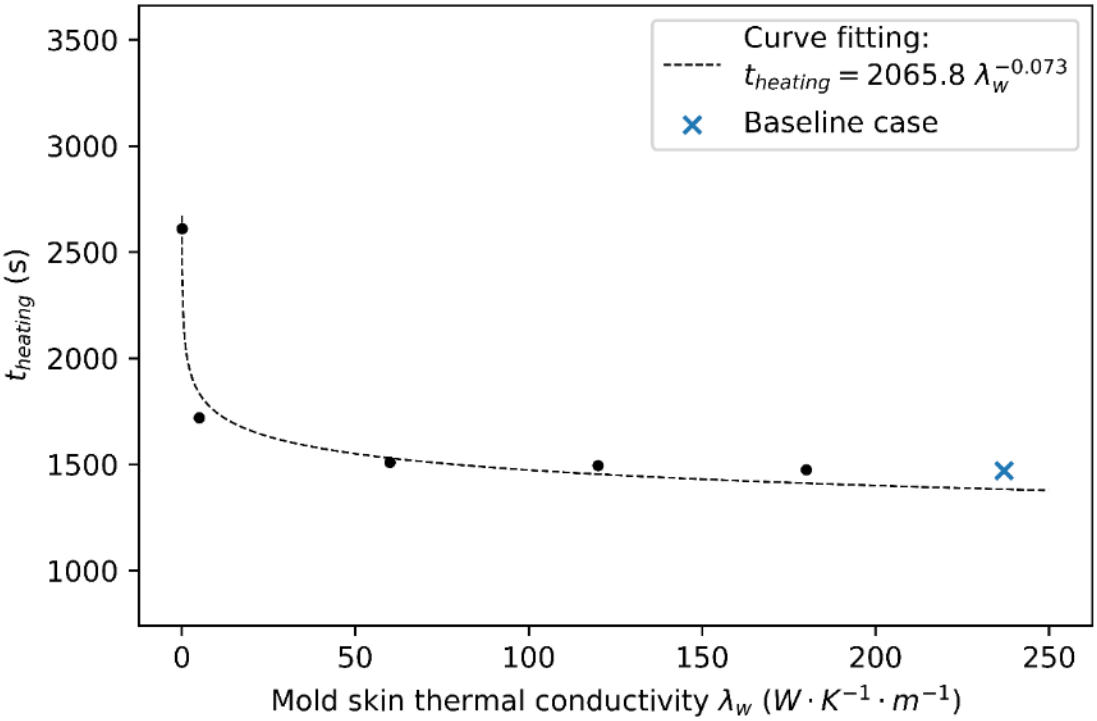

Figure 8.7: Variations in $t_{heating}$ as a function of mold skin thermal conductivity.

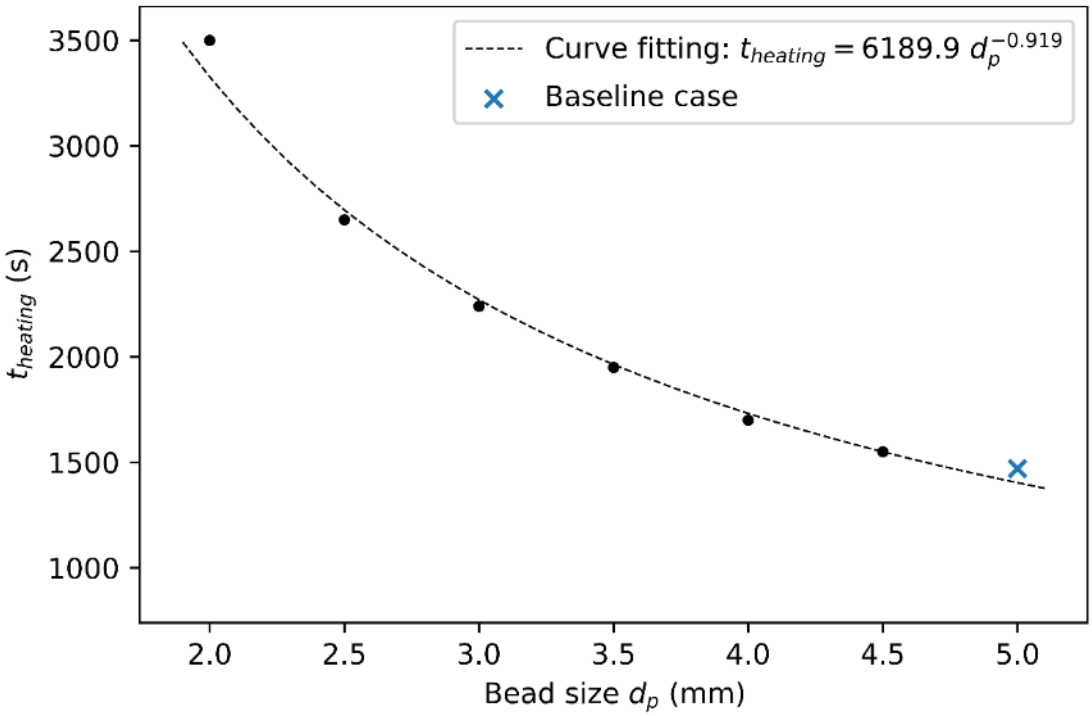

Figure 8.8: Variations in $t_{heating}$ as a function of bead size.

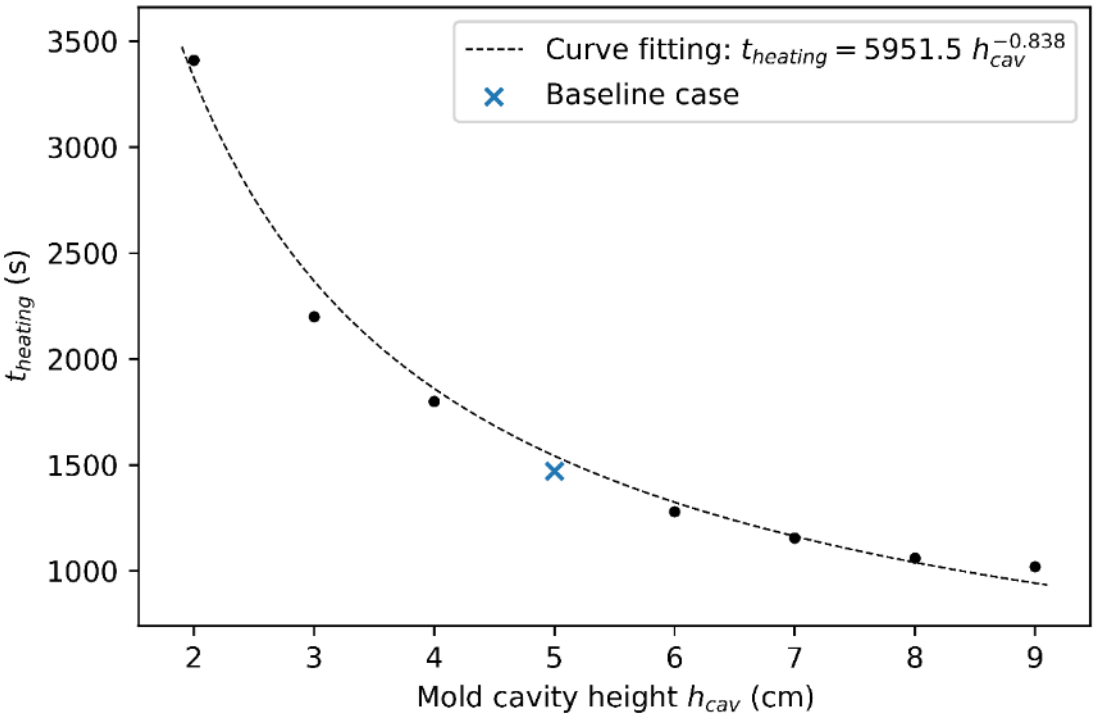

Figure 8.9: Variations in $t_{heating}$ as a function of the mold cavity height. Note that h_{cav}/d_p remains equal to 10 for all cases tested.

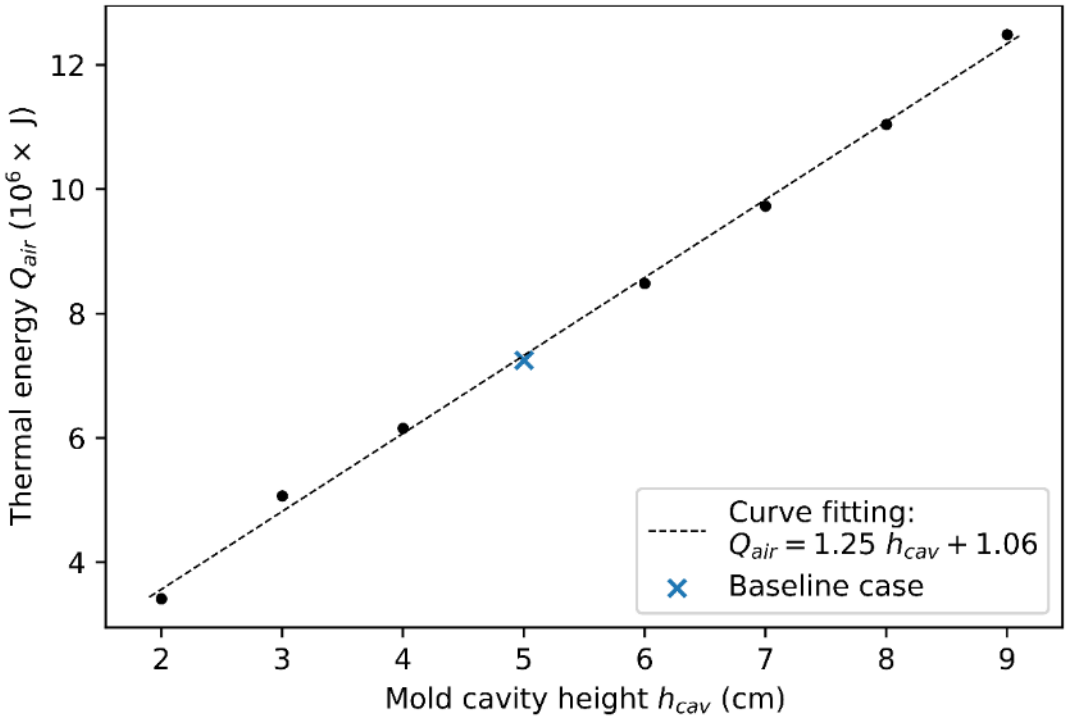

Figure 8.10: Variations in Q_{air} as a function of the mold cavity height.

8.6 Conclusion

This work investigated the heating efficiency of a new concept of injection mold possessing a porous core made of granular material and heated by a circulating fluid. Apart from the benefits of using heat transfer fluids, this innovative approach also brings the following potential advantages:

(a) The mold is reusable for parts of different shapes by changing only the mold skin, which can reduce significantly tooling costs.

(b) The mold skin takes the shape of the molded part and is supported by closely packed beads in the cavity. This feature brings advantage in conforming the part geometry over the mold with heating ducts, since standard pipes usually cannot follow the shape of complex parts.

(c) The injected fluid heats the mold skin continuously. Compared with discrete heating sources (e.g., ducts), granular heating can improve temperature uniformity.

The heating performance of a planar granular mold was evaluated numerically. With hot air injected, the mold surface can reach a uniform temperature within a reasonable time for both

composite and aluminum skins. A parametric study showed that reducing the skin thickness and volumetric heat capacity plays a key role in decreasing the heating time, whereas changing the particle volumetric heat capacity or using higher thermally conductive materials for the skin do not have a major impact. This widens the selection of bead and skin materials and enhances the potential of further reducing the tooling costs. Finally, within the model validation range, it is preferable to use larger beads and increase the cavity height. However, this is limited by the power of the air blower and heater that supply hot air at the inlet. In the future, experimental and numerical studies will be conducted to apply this innovative mold concept in composite manufacturing.

8.7 Acknowledgement

This work was supported by the National Science & Engineering Research Council of Canada (NSERC) (Discovery Grants). Authors also gratefully acknowledge the Research Center for High Performance Polymer and Composite Systems (CREPEC) and the “Fonds de recherche du Québec - Nature et technologies” (FRQNT) for their partial financial support.

CHAPTER 9 GENERAL DISCUSSION

This thesis investigated an innovative tooling concept for composite manufacturing based on packed granular materials held in the mold case. The surface of the mold skin can be heated by circulating a heat transfer fluid through the granular bed. This new approach is considered as a potential solution to overcome several limitations of conventional molds and reduce tooling costs. Machining a full metallic mold is no longer necessary with reusable granular molds that can be adapted to fabricate different parts by changing only the mold skin.

The study starts from the characterization of permeability (Chapter 4), which is a key parameter to describe flows in porous media. Based on the conventional falling head method, a modified version was proposed, which considers the influence of the gravity, the pressure loss of the setup and fluid viscosity. These issues were not considered in the scientific literature. The modified falling head test retains the simplicity of conventional tests and enlarges the test range using silicon oil as test fluid instead of water.

In the following part of the thesis, the governing equations of wall-bounded granular media were derived using a non-constant spherical REV. The size of the REV varies close to the wall and becomes equivalent to a point on the wall. This approach allows addressing problems connected with the incompatibility of physical variables at the wall-bed interface. The use of non-constant REV also leads to a direct determination of the exponential porosity profile of monodisperse granular beds. Such profiles are shown in Article 2 (Chapter 5) to depend only on the dimensionless distance to the wall (d_{wall}/d_s). This result is in agreement with the model of Hunt and Tien [124]. The derived governing equations were then validated experimentally for cylindrical granular beds packed with ceramic beads heated by air flow. This was presented in Article 3 (Chapter 6). The temperatures predicted in the granular bed and on the wall agree closely with experimentally measured values. A parametric study was then conducted in Article 4 (Chapter 7) using the above-mentioned modelling framework. Several suggestions are proposed to reduce the time required to reach the uniformity of the wall temperature. This helps improve the temperature uniformity of the granular mold. Finally, a comparison of heating times between granular molds and conventional molds with heating ducts was presented in Article 5 (Chapter 8) and confirmed the heating efficiency of this new tooling concept.

CHAPTER 10 CONCLUSION AND RECOMMENDATIONS

10.1 Summary of works

The granular mold is an innovative tooling concept for composite manufacturing. The originality of this technique lies in the use of granular materials held in the mold case. This allows the surface of the mold can be heated by circulating a heat transfer fluid through the granular bed. This is considered as a potential solution to overcome several limitations of conventional heating methods. This thesis investigated this tooling concept numerically using the modelling framework developed based on volume-averaged governing equations in porous media.

The study begins by the characterization of permeability using a modified falling head method. This method enlarges the test range by two orders of magnitude (up to ~10^{-8} m^2) compared to the conventional falling head test. The results exhibit a good consistency and repeatability, and the revisited Ergun's equation was recommended to predict the permeability of bead packings. The governing equations of wall-bounded granular media were derived using a non-constant spherical REV. The derived governing equations were then validated experimentally. The important parameters were disscussed and the discussion leads to the following results:

- The turbulence of the flow must be modelled especially near the wall. Both the turbulent energy and dissipation rate induced by the fluid motion and the presence of beads must be considered.
- In a fully turbulent flow, the influence of the heat transfer coefficient between the beads and the fluid is quite limited, which has no obvious effect on the evolution of the wall temperature.
- At the wall-bed interface, measurements show that the difference between the fluid and wall temperatures is negligible. Therefore, a continuous temperature boundary condition is considered in the numerical simulation.
- The function of Nakayama and Kuwahara [152] models correctly the additional turbulent sources in fully turbulent flows ($Re_{dp} > 300$). However, it overestimates the heat transfer rate of flow for $Re_{dp} < 300$. Therefore, a damping function was proposed to be combined with the Nakayama and Kuwahara model to improve the accuracy of temperature predictions.

A parametric study was also conducted using the above-mentioned modelling framework. Several suggestions are proposed to reduce the time required to reach the uniformity of the wall temperature:

- Reducing the wall thickness and its volumetric heat capacity play a key role, since both parameters are related to the total amount of thermal energy required to heat the wall.
- Increasing the inlet flow rate and particle size also has an effect, but to a lower extent. Note that the current study is only suited for the bed-to-particle size ratios higher than 10.
- Reducing the particle volumetric heat capacity or excessively increasing the thermal conductive of the wall do not play a great role.

10.2Limitations and recommendations for future research

Current limitations and recommendations for future improvements are listed below:

- The method to enlarge the range of the conventional falling head test is described in Chapter 4 (Article 1). However, the exact test capability (i.e., the exact upper limit of the test range) of the modified falling head test was not determined. This parameter depends on the properties of the test fluid, the apparatus size, the resolution of the electronic scale, etc. Predicting the test capability could assist in improving the design of new experimental setups and in selecting appropriate test fluids.
- The porosity profile is only analyzed in Chapter 5 for three monodisperse bead packings. Practically, the granular beds are often mixtures of beads of different sizes. The methodology presented in this thesis is applicable to such packings, which can be studied in future investigations.
- The bed-to-wall heat transfer investigated here is limited to small beads (D_{bed}/d_s higher than 10). The flow and heat transfer mechanisms for D_{bed}/d_s < 10 have not been studied.
- The heating efficiency of granular molds was only investigated numerically with a mold of simple geometry (i.e., a flat plate). In the future, experimental and numerical studies are expected for more complex geometry to apply this new tooling concept in composite manufacturing.

REFERENCES

[1] M. M. Schwartz, "Composite materials. Volume 2: Processing, fabrication, and applications," 1997.

[2] P. Hubert, G. Fernlund, and A. Poursartip, "Autoclave processing for composites," in *Manufacturing techniques for polymer matrix composites (PMCs)*: Elsevier, 2012, pp. 414-434.

[3] C. Campbell Flake, "Chapter 6: Curing: It's a Matter of Time (t), Temperature (T) and Pressure (P)," in *Manufacturing Processes for Advanced Composites*, vol. 1, 2004, pp. 175-221.

[4] T. Centea, L. K. Grunenfelder, and S. R. Nutt, "A review of out-of-autoclave prepregs–Material properties, process phenomena, and manufacturing considerations," *Composites Part A: Applied Science and Manufacturing,* vol. 70, pp. 132-154, 2015.

[5] H. S. Bromley, "Investigation of integrally-heated tooling and thermal modeling methodologies for the rapid cure of aerospace composites," Massachusetts Institute of Technology, 2015.

[6] R. Stewart, "New mould technologies and tooling materials promise advances for composites," *Reinforced Plastics,* vol. 54, no. 3, pp. 30-36, 2010.

[7] L. Progoulakis, "Heated tooling for aerospace composites manufacture," University of Plymouth, 2004.

[8] G. Marsh, "Mould tool heating–the oven-free alternative'," *Reinforced Plastics,* vol. 47, no. 11, pp. 38-41, 2003.

[9] T. Oppelt, J. Schulze, H. Stein, and B. Platzer, "Comparison of Methods for Mould Surface Heating – Part 1: Review," *International Polymer Science and Technology,* vol. 39, no. 12, pp. 1-8, 2012/12/01 2012.

[10] J.-F. Désilets, "Développement et optimisation d'un procédé de mise en forme par injection d'une pièce complexe à épaisseur variable en matériaux composites," École Polytechnique de Montréal, 2011.

[11] J. Borland, "Adjustable support for preformed mold," Patent US9211660B2, 2015.

[12] J. C. Borland, "Deflector Embedded In A Thermal System of Discrete Units," ed: Google Patents, 2020.

[13] T. Brocks, M. Y. Shiino, M. O. H. Cioffi, H. J. C. Voorwald, and A. Caporalli Filho, "Experimental RTM manufacturing analysis of carbon/epoxy composites for aerospace application," *Materials Research,* vol. 16, pp. 1175-1182, 2013.

[14] G. Wang, G. Zhao, H. Li, and Y. Guan, "Research of thermal response simulation and mold structure optimization for rapid heat cycle molding processes, respectively, with steam heating and electric heating," *Materials & Design,* vol. 31, no. 1, pp. 382-395, 2010/01/01/ 2010.

[15] S. Payette, "Heated Tool Processing of Out-of-Autoclave Composite Materials," McGill University, 2015.

[16] A. Smith, K. Goyette, and C. Kazanas, "Development of a heated tooling solution to improve process flexibility for out-of-autoclave prepregs," in *SAMPE Tech 2013 Conference*, 2013, pp. 21-24.

[17] R. Lucas and H. Danford, "Case studies: low cost, high-strength, large carbon foam tooling," *Sampe Journal*, vol. 45, no. 1, 2009.

[18] J. M. Blacker, D. J. Merriman, and R. D. Lucas, "Out-of-autoclave composites manufacturing with electrically heated carbon foam tooling," in *SAMPE 2010 Conference and Exhibition "New Materials and Processes for a New Economy", May 17, 2010 - May 20, 2010*, Seattle, WA, United states, 2010, p. Seattle and Eastern Canada SAMPE Chapters: Soc. for the Advancement of Material and Process Engineering.

[19] Z. Shayfull, S. Sharif, A. M. Zain, M. Ghazali, and R. M. Saad, "Potential of conformal cooling channels in rapid heat cycle molding: a review," *Advances in Polymer Technology*, vol. 33, no. 1, 2014.

[20] N. Athanasopoulos, G. Koutsoukis, D. Vlachos, and V. Kostopoulos, "Temperature uniformity analysis and development of open lightweight composite molds using carbon fibers as heating elements," *Composites Part B: Engineering*, vol. 50, pp. 279-289, 2013/07/01/ 2013.

[21] S.-C. Chen, W.-R. Jong, and J.-A. Chang, "Dynamic mold surface temperature control using induction heating and its effects on the surface appearance of weld line," *Journal of Applied Polymer Science*, https://doi.org/10.1002/app.24070 vol. 101, no. 2, pp. 1174-1180, 2006/07/15 2006.

[22] R. Abdalrahman, S. Grove, A. Kyte, and M. J. Rizvi, "Numerical Studies of Integrally-Heated Composite Tooling."

[23] Y. Ding, W. Chiu, and X. Liu, "Numerical investigation on thermal response of oil-heated tool for manufacture of composite products," *Composite structures*, vol. 47, no. 1-4, pp. 491-495, 1999.

[24] V. Coenen, M. Hatrick, H. Law, D. Brosius, A. Nesbitt, and D. Bond, "A feasibility study of Quickstep processing of an aerospace composite material," in *Proceedings of SAMPE-EUROPE, Paris*, 2005.

[25] L. Davies, R. Day, D. Bond, A. Nesbitt, J. Ellis, and E. Gardon, "Effect of cure cycle heat transfer rates on the physical and mechanical properties of an epoxy matrix composite," *Composites science and technology*, vol. 67, no. 9, pp. 1892-1899, 2007.

[26] A. Ogale, P. Potluri, B. Rittenschober, U. Beier, and J. Schlimbach, "OUT-OF-AUTOCLAVE CURING OF COMPOSITES FOR HIGH TEMPERATURE AEROSPACE APPLICATIONS."

[27] E. Ruiz and F. Trochu, "Manufacture of composites by a flexible injection process using a double or multiple cavity mold," ed: Google Patents, 2011.

[28] F. Trochu, S. Soukane, and B. Touraine, "Flexible injection: a novel LCM technology for low cost manufacturing of high performance composites. Part II: numerical model," *Proceedings FPCM9*, vol. 35, 2008.

[29] E. Ruiz, L. Briones, E. Allard, and F. Trochu, "Flexible injection: a novel LCM technology for low cost manufacturing of high performance composites. Part I: experimental investigation," *Proceedings FPCM9*, vol. 34, 2008.

[30] S.-Y. Shih, S.-C. Nian, and M.-S. Huang, "Comparison between single- and multiple-zone induction heating of largely curved mold surfaces," *International Communications in Heat and Mass Transfer*, vol. 75, pp. 24-35, 2016/07/01/ 2016.

[31] L. Schaal, "RocTool launches an innovative composites process: Light Induction Tooling," *Reinforced Plastics*, vol. 61, no. 3, pp. 173-175, 2017/05/01/ 2017.

[32] S. B. Donna Dawson, Jeff Sloan, "JEC World 2016, the full report," 2016.

[33] Y. Mahmoudi, K. Hooman, and K. Vafai, "Convective Heat Transfer in Porous Media," 2019.

[34] M. Quintard, "Introduction to heat and mass transport in porous media," *Porous media interaction with high temperature and high speed ows, STO-AVT-261. VKI*, p. 33, 2015.

[35] Y. Mahmoudi, K. Hooman, and K. Vafai, *Convective heat transfer in porous media*. CRC Press, 2019.

[36] H. Darcy, "Les fontaines publiques de la ville de Dijon, Dalmont," *Paris: Dalmont*, 1856.

[37] J. Bear, *Dynamics of fluids in porous media*. New York: Dover Publications, INC., 2013.

[38] H. Brinkman, "A calculation of the viscous force exerted by a flowing fluid on a dense swarm of particles," *Flow, Turbulence and Combustion*, vol. 1, no. 1, p. 27, 1949.

[39] R. Givler and S. Altobelli, "A determination of the effective viscosity for the Brinkman–Forchheimer flow model," *Journal of Fluid Mechanics*, vol. 258, pp. 355-370, 1994.

[40] J.-L. Auriault, "On the domain of validity of Brinkman's equation," *Transport in porous media*, vol. 79, no. 2, pp. 215-223, 2009.

[41] H. Teng and T. Zhao, "An extension of Darcy's law to non-Stokes flow in porous media," *Chemical engineering science*, vol. 55, no. 14, pp. 2727-2735, 2000.

[42] S. Ergun, "Fluid Flow through Packed Columns," *Journal of Chemical Engineering Progress*, vol. 48, no. 2, pp. 89-94, 1952.

[43] I. Macdonald, M. El-Sayed, K. Mow, and F. Dullien, "Flow through porous media-the Ergun equation revisited," *Industrial & Engineering Chemistry Fundamentals*, vol. 18, no. 3, pp. 199-208, 1979.

[44] J. Bear, *Dynamics of fluids in porous media*. New York: Dover Publications, INC., 1972.

[45] P. Vardanega, "State of the art: permeability of asphalt concrete," *Journal of Materials in Civil Engineering*, vol. 26, no. 1, pp. 54-64, 2012.

[46] J. G. H. Borkink and W. K.R, "Significance of the radial porosity profile for the description of heat transport in wall-cooled packed beds," *Chemical Engineering Science*, vol. 49, no. 6, pp. 863-876, 1994/01/01/ 1994.

[47] C. E. Schwartz and J. Smith, "Flow distribution in packed beds," *Industrial & Engineering Chemistry*, vol. 45, no. 6, pp. 1209-1218, 1953.

[48] B. Guo, A. Yu, B. Wright, and P. Zulli, "Simulation of Turbulent Flow in a Packed Bed," *Chemical Engineering & Technology,* vol. 29, no. 5, pp. 596-603, 2006.

[49] K. Ridgway and K. J. Tarbuck, "Voidage fluctuations in randomly-packed beds of spheres adjacent to a containing wall," *Chemical Engineering Science,* vol. 23, no. 9, pp. 1147-1155, 1968/09/01/ 1968.

[50] W. Zhang, K. E. Thompson, A. H. Reed, and L. Beenken, "Relationship between packing structure and porosity in fixed beds of equilateral cylindrical particles," *Chemical Engineering Science,* vol. 61, no. 24, pp. 8060-8074, 2006.

[51] G. E. Mueller, "Radial porosity in packed beds of spheres," *Powder Technology,* vol. 203, no. 3, pp. 626-633, 2010.

[52] J. S. Goodling, R. I. Vachon, W. S. Stelpflug, S. J. Ying, and M. S. Khader, "Radial porosity distribution in cylindrical beds packed with spheres," *Powder Technology,* vol. 35, no. 1, pp. 23-29, 1983/05/01/ 1983.

[53] A. De Klerk, "Voidage variation in packed beds at small column to particle diameter ratio," *AIChE journal,* vol. 49, no. 8, pp. 2022-2029, 2003.

[54] D. Vortmeyer and J. Schuster, "Evaluation of steady flow profiles in rectangular and circular packed beds by a variational method," *Chemical Engineering Science,* vol. 38, no. 10, pp. 1691-1699, 1983.

[55] S. M. White and C. L. Tien, "Analysis of flow channeling near the wall in packed beds," *Wärme - und Stoffübertragung,* vol. 21, no. 5, pp. 291-296, 1987/09/01 1987.

[56] W. Van Antwerpen, C. Du Toit, and P. G. Rousseau, "A review of correlations to model the packing structure and effective thermal conductivity in packed beds of mono-sized spherical particles," *Nuclear Engineering and design,* vol. 240, no. 7, pp. 1803-1818, 2010.

[57] M. Cascetta, G. Cau, P. Puddu, and F. Serra, "A comparison between CFD simulation and experimental investigation of a packed-bed thermal energy storage system," *Applied Thermal Engineering,* vol. 98, pp. 1263-1272, 2016.

[58] M. A. Zanoni, J. L. Torero, and J. I. Gerhard, "Determination of the interfacial heat transfer coefficient between forced air and sand at Reynold's numbers relevant to smouldering combustion," *International Journal of Heat and Mass Transfer,* vol. 114, pp. 90-104, 2017.

[59] N. Mertens, F. Alobaid, L. Frigge, and B. Epple, "Dynamic simulation of integrated rock-bed thermocline storage for concentrated solar power," *Solar Energy,* vol. 110, pp. 830-842, 2014.

[60] C. Xu, X. Li, Z. Wang, Y. He, and F. Bai, "Effects of solid particle properties on the thermal performance of a packed-bed molten-salt thermocline thermal storage system," *Applied Thermal Engineering,* vol. 57, no. 1-2, pp. 69-80, 2013.

[61] A. Bruch, J. Fourmigué, and R. Couturier, "Experimental and numerical investigation of a pilot-scale thermal oil packed bed thermal storage system for CSP power plant," *Solar Energy,* vol. 105, pp. 116-125, 2014.

[62] T. Esence, A. Bruch, S. Molina, B. Stutz, and J.-F. Fourmigué, "A review on experience feedback and numerical modeling of packed-bed thermal energy storage systems," *Solar Energy,* vol. 153, pp. 628-654, 2017.

[63] R. Anderson, S. Shiri, H. Bindra, and J. F. Morris, "Experimental results and modeling of energy storage and recovery in a packed bed of alumina particles," *Applied Energy,* vol. 119, pp. 521-529, 2014.

[64] X. Nie, R. Evitts, R. Besant, and J. Bolster, "A new technique to determine convection coefficients with flow through particle beds," *Journal of heat transfer,* vol. 133, no. 4, 2011.

[65] E. Achenbach, "Heat and flow characteristics of packed beds," *Experimental thermal and fluid science,* vol. 10, no. 1, pp. 17-27, 1995.

[66] A. S. Gupta and G. Thodos, "Mass and heat transfer in the flow of fluids through fixed and fluidized beds of spherical particles," *AI Ch. E.(Am. Inst. Chem. Engrs.) J.,* vol. 8, 1962.

[67] J. D. Acetis and G. Thodos, "Mass and heat transfer in flow of gases through spherical packings," *Industrial & Engineering Chemistry,* vol. 52, no. 12, pp. 1003-1006, 1960.

[68] H. Resnick, "Simultaneous heat and mass transfer in a diffusion-controlled chemical reaction," Massachusetts Institute of Technology, 1952.

[69] E. C. Nsofor and G. A. Adebiyi, "Measurements of the gas-particle convective heat transfer coefficient in a packed bed for high-temperature energy storage," *Experimental Thermal and Fluid Science,* vol. 24, no. 1-2, pp. 1-9, 2001.

[70] S. W. Pen, R. W. Besant, and G. Strathdee, "Heat and mass transfer in granular potash fertilizer with a surface dissolution reaction," *The Canadian Journal of Chemical Engineering,* vol. 78, no. 6, pp. 1076-1086, 2000.

[71] S. Whitaker, "Forced convection heat transfer correlations for flow in pipes, past flat plates, single cylinders, single spheres, and for flow in packed beds and tube bundles," *AIChE Journal,* vol. 18, no. 2, pp. 361-371, 1972.

[72] N. Wakao, S. Kaguei, and T. Funazkri, "Effect of fluid dispersion coefficients on particle-to-fluid heat transfer coefficients in packed beds: correlation of Nusselt numbers," *Chemical engineering science,* vol. 34, no. 3, pp. 325-336, 1979.

[73] A. Abdulla and K. Reddy, "Comparative study of single and multi-layered packed-bed thermal energy storage systems for CSP plants," *Applied Solar Energy,* vol. 53, no. 3, pp. 276-286, 2017.

[74] P. E. Burström, V. Frishfelds, A.-L. Ljung, T. S. Lundström, and B. D. Marjavaara, "Modelling heat transfer during flow through a random packed bed of spheres," *Heat and Mass Transfer,* vol. 54, no. 4, pp. 1225-1245, 2018.

[75] P. Gangapatnam, R. Kurian, and S. Venkateshan, "Numerical simulation of heat transfer in metal foams," *Heat and Mass Transfer,* vol. 54, no. 2, pp. 553-562, 2018.

[76] J. A. Ochoa-Tapia and S. Whitaker, "Heat transfer at the boundary between a porous medium and a homogeneous fluid: the one-equation model," *Journal of Porous Media,* vol. 1, no. 1, 1998.

[77] J. Hager, R. Wimmerstedt, and S. Whitaker, "Steam drying a bed of porous spheres: theory and experiment," *Chemical engineering science,* vol. 55, no. 9, pp. 1675-1698, 2000.

[78] F. Radjai, J.-N. Roux, and A. Daouadji, "Modeling granular materials: century-long research across scales," *Journal of Engineering Mechanics,* vol. 143, no. 4, p. 04017002, 2017.

[79] B. Abdelgawad, "Design of a gas-solid fluidized bed reactor at high temperature and high pressure," École Polytechnique de Montréal, 2013.

[80] M. Amani, M. Ameri, and A. Kasaeian, "The experimental study of convection heat transfer characteristics and pressure drop of magnetite nanofluid in a porous metal foam tube," *Transport in Porous Media,* vol. 116, no. 2, pp. 959-974, 2017.

[81] S. Esna Ashari, A. Das, and G. Buscarnera, "Model-Based Assessment of the Effect of Surface Area Growth on the Permeability of Granular Rocks," *Journal of Engineering Mechanics,* vol. 144, no. 5, p. 04018023, 2018.

[82] J. Gomez, R. Chalaturnyk, and G. Zambrano-Narvaez, "Experimental Investigation of the Mechanical Behavior and Permeability of 3D Printed Sandstone Analogues Under Triaxial Conditions," *Transport in Porous Media,* pp. 1-17, 2018.

[83] P. Guo, D. Stolle, and S. X. Guo, "An Equivalent Spherical Particle System to Describe Characteristics of Flow in a Dense Packing of Non-spherical Particles," *Transport in Porous Media,* pp. 1-28, 2019.

[84] V. Andres-Valeri, L. Juli-Gandara, D. Jato-Espino, and J. Rodriguez-Hernandez, "Characterization of the Infiltration Capacity of Porous Concrete Pavements with Low Constant Head Permeability Tests," *Water,* vol. 10, no. 4, p. 480, 2018.

[85] K. D. Hall, "Comparison of falling-head and constant-head techniques: Estimating field permeability of hot-mix asphalt pavements," *Transportation research record,* vol. 1891, no. 1, pp. 23-31, 2004.

[86] V. Ranieri, P. Colonna, J. J. Sansalone, and A. Sciddurlo, "Measurement of hydraulic conductivity in porous mixes," *Transportation Research Record,* vol. 2295, no. 1, pp. 1-10, 2012.

[87] L. Allen Cooley and E. Ray Brown, "Selection and Evaluation of Field Permeability Device for Asphalt Pavements," *Transportation Research Record,* vol. 1723, no. 1, pp. 73-82, 2000.

[88] M. A. F. Zarandi, K. M. Pillai, and B. Barari, "Flow along and across glass-fiber wicks: Testing of permeability models through experiments and simulations," *AIChE Journal,* vol. 64, no. 9, pp. 3491-3501, 2018.

[89] D. Johnson, F. Arriaga, and B. Lowery, "Automation of a falling head permeameter for rapid determination of hydraulic conductivity of multiple samples," *Soil Science Society of America Journal,* vol. 69, no. 3, pp. 828-833, 2005.

[90] J. J. Assaad and J. Harb, "Use of the falling-head method to assess permeability of freshly mixed cementitious-based materials," *Journal of Materials in Civil Engineering,* vol. 25, no. 5, pp. 580-588, 2012.

[91] S. Ergun, "Fluid flow through packed columns," *Chemical Engineering Progress,* vol. 48, no. 6, pp. 89-94, 1952.

[92] S. Galvan, C. Pla, N. Cueto, J. Martínez-Martínez, M. García del Cura, and D. Benavente, "A comparison of experimental methods for measuring water permeability of porous building rocks," 2014.

[93] M. Wilson, W. Hoff, R. Brown, and M. Carter, "A falling head permeameter for the measurement of the hydraulic conductivity of granular solids," *Review of Scientific Instruments,* vol. 71, no. 10, pp. 3942-3946, 2000.

[94] A. Pedescoll, P. Knowles, P. Davies, J. García, and J. Puigagut, "A comparison of in situ constant and falling head permeameter tests to assess the distribution of clogging within horizontal subsurface flow constructed wetlands," *Water, Air, & Soil Pollution,* vol. 223, no. 5, pp. 2263-2275, 2012.

[95] L. Chu and T. Fwa, "Functional sustainability of single-and double-layer porous asphalt pavements," *Construction and Building Materials,* vol. 197, pp. 436-443, 2019.

[96] A. Pedescoll, R. Samsó, E. Romero, J. Puigagut, and J. García, "Reliability, repeatability and accuracy of the falling head method for hydraulic conductivity measurements under laboratory conditions," *Ecological engineering,* vol. 37, no. 5, pp. 754-757, 2011.

[97] R. Batezini and J. Balbo, "Study on the hydraulic conductivity by constant and falling head methods for pervious concrete," *Revista IBRACON de Estruturas e Materiais,* vol. 8, no. 3, pp. 248-259, 2015.

[98] K.-W. Lee, S. Wang, L. Lu, E. Jabbari, B. L. Currier, and M. J. Yaszemski, "Fabrication and characterization of poly (propylene fumarate) scaffolds with controlled pore structures using 3-dimensional printing and injection molding," *Tissue engineering,* vol. 12, no. 10, pp. 2801-2811, 2006.

[99] G. F. Sandoval, I. Galobardes, R. S. Teixeira, and B. M. Toralles, "Comparison between the falling head and the constant head permeability tests to assess the permeability coefficient of sustainable Pervious Concretes," *Case studies in construction materials,* vol. 7, pp. 317-328, 2017.

[100] A. Silva, J. Hetherman, and D. Calnan, "Low-gradient permeability testing of fine-grained marine sediments," in *Permeability and Groundwater Contaminant Transport*: ASTM International, 1981.

[101] H. Nightingale and W. Bianchi, "Rapid measurement of hydraulic conductivity changes in slowly permeable soils," *Soil Science,* vol. 110, no. 4, pp. 221-228, 1970.

[102] T. Fwa, S. Tan, and C. Chuai, "Permeability measurement of base materials using falling-head test apparatus," *Transportation Research Record: Journal of the Transportation Research Board,* no. 1615, pp. 94-99, 1998.

[103] K. Noborio *et al.*, "A new and simple method for measuring in situ field-saturated hydraulic conductivity using a falling-head single cylinder," *Paddy and Water Environment,* vol. 16, no. 1, pp. 81-87, 2018.

[104] L. Nagy, A. Tabácks, and T. Huszák, "Comparison of permeability testing methods," in *Proceedings of the 18th International Conference on Soil Mechanics and Geotechnical Engineering,* Paris, 2013, pp. 399-402.

[105] H. Li, M. Kayhanian, and J. T. Harvey, "Comparative field permeability measurement of permeable pavements using ASTM C1701 and NCAT permeameter methods," *Journal of Environmental Management,* vol. 118, pp. 144-152, 2013.

[106] M. Kaczmarek, "Role of inertia in falling head permeability test," *International journal for numerical and analytical methods in geomechanics,* vol. 33, no. 18, pp. 1963-1970, 2009.

[107] L. C. d. S. Ozelim and A. L. Cavalcante, "Combining Microtomography, 3D Printing, and Numerical Simulations to Study Scale Effects on the Permeability of Porous Media," *International Journal of Geomechanics,* vol. 19, no. 2, p. 04018194, 2018.

[108] O. Adamidis and G. S. P. Madabhushi, "Use of viscous pore fluids in dynamic centrifuge modelling," *International Journal of Physical Modelling in Geotechnics,* vol. 15, no. 3, pp. 141-149, 2015.

[109] C. A. Schneider, W. S. Rasband, and K. W. Eliceiri, "NIH Image to ImageJ: 25 years of image analysis," *Nature methods,* vol. 9, no. 7, p. 671, 2012.

[110] G. Beavers, E. Sparrow, and D. Rodenz, "Influence of bed size on the flow characteristics and porosity of randomly packed beds of spheres," *Journal of Applied Mechanics,* vol. 40, no. 3, pp. 655-660, 1973.

[111] N. Vernet *et al.*, "Experimental determination of the permeability of engineering textiles: Benchmark II," *Composites Part A: Applied Science and Manufacturing,* vol. 61, pp. 172-184, 2014.

[112] D. May, A. Aktas, and A. Yong, "International Benchmark Exercises on Textile Permeability and Compressibility Characterization," 2018.

[113] P.-X. Jiang, M. Li, T.-J. Lu, L. Yu, and Z.-P. Ren, "Experimental research on convection heat transfer in sintered porous plate channels," *International Journal of Heat and Mass Transfer,* vol. 47, no. 10, pp. 2085-2096, 2004.

[114] Y. Demirel, B. Abu-Al-Saud, H. Al-Ali, and Y. Makkawi, "Packing size and shape effects on forced convection in large rectangular packed ducts with asymmetric heating," *International journal of heat and mass transfer,* vol. 42, no. 17, pp. 3267-3277, 1999.

[115] K. Habibi, A. Mosahebi, and H. Shokouhmand, "Heat transfer characteristics of reciprocating flows in channels partially filled with porous medium," *Transport in porous media,* vol. 89, no. 2, pp. 139-153, 2011.

[116] J. Zhu, S. S. Araya, X. Cui, S. L. Sahlin, and S. K. Kær, "Modeling and Design of a Multi-Tubular Packed-Bed Reactor for Methanol Steam Reforming over a Cu/ZnO/Al2O3 Catalyst," *Energies,* vol. 13, no. 3, p. 610, 2020.

[117] S. M. Kuo and C. L. Tien, "Heat transfer augmentation in a foam-material filled duct with discrete heat sources," in *InterSociety Conference on Thermal Phenomena in the Fabrication and Operation of Electronic Components. I-THERM '88,* 1988, pp. 87-91.

[118] B. Boyd and K. Hooman, "Air-cooled micro-porous heat exchangers for thermal management of fuel cells," *International Communications in Heat and Mass Transfer,* vol. 39, no. 3, pp. 363-367, 2012.

[119] I. A. Badruddin *et al.*, "Conjugate heat transfer in an annulus with porous medium fixed between solids," *Transport in Porous media,* vol. 109, no. 3, pp. 589-608, 2015.

[120] S. Whitaker, *The method of volume averaging*. Springer Science & Business Media, 2013.

[121] J. P. Du Plessis and J. H. Masliyah, "Mathematical modelling of flow through consolidated isotropic porous media," *Transport in Porous Media,* vol. 3, no. 2, pp. 145-161, 1988.

[122] K. Ridgway and K. Tarbuck, "Radial voidage variation in randomly‐packed beds of spheres of different sizes," *Journal of Pharmacy and Pharmacology,* vol. 18, no. S1, pp. 168S-175S, 1966.

[123] N. Zobel, T. Eppinger, F. Behrendt, and M. Kraume, "Influence of the wall structure on the void fraction distribution in packed beds," *Chemical engineering science,* vol. 71, pp. 212-219, 2012.

[124] M. Hunt and C. Tien, "Non-Darcian flow, heat and mass transfer in catalytic packed-bed reactors," *Chemical Engineering Science,* vol. 45, no. 1, pp. 55-63, 1990.

[125] S. White and C. Tien, "Analysis of flow channeling near the wall in packed beds," *Wärme- und Stoffübertragung,* vol. 21, no. 5, pp. 291-296, 1987.

[126] P. Cheng and C. Hsu, "Fully-developed, forced convective flow through an annular packed-sphere bed with wall effects," *International journal of heat and mass transfer,* vol. 29, no. 12, pp. 1843-1853, 1986.

[127] C. G. Du Toit, "Radial variation in porosity in annular packed beds," *Nuclear engineering and design,* vol. 238, no. 11, pp. 3073-3079, 2008.

[128] D. A. Nield and A. Bejan, *Convection in porous media*. Springer, 2006.

[129] J. A. Ochoa-Tapia and S. Whitaker, "Heat transfer at the boundary between a porous medium and a homogeneous fluid," *International Journal of Heat and Mass Transfer,* vol. 40, no. 11, pp. 2691-2707, 1997.

[130] F. J. Valdés-Parada, B. t. Goyeau, and J. A. Ochoa-Tapia, "Jump momentum boundary condition at a fluid–porous dividing surface: derivation of the closure problem," *Chemical engineering science,* vol. 62, no. 15, pp. 4025-4039, 2007.

[131] J. P. Du Plessis and J. H. Masliyah, "Flow through isotropic granular porous media," *Transport in porous media,* vol. 6, no. 3, pp. 207-221, 1991.

[132] W. G. Gray, "Local volume averaging of multiphase systems using a non-constant averaging volume," *International journal of multiphase flow,* vol. 9, no. 6, pp. 755-761, 1983.

[133] J. A. Ochoa-Tapia and S. Whitaker, "Bulk and surface diffusion in porous media: an application of the surface-averaging theorem," *Chemical Engineering Science,* vol. 48, no. 11, pp. 2061-2082, 1993.

[134] C. Kloss, C. Goniva, A. Hager, S. Amberger, and S. Pirker, "Models, algorithms and validation for opensource DEM and CFD–DEM," *Progress in Computational Fluid Dynamics, an International Journal,* vol. 12, no. 2-3, pp. 140-152, 2012.

[135] V. Clausnitzer and J. Hopmans, "Determination of phase-volume fractions from tomographic measurements in two-phase systems," *Advances in water resources,* vol. 22, no. 6, pp. 577-584, 1999.

[136] A. Faghri and Y. Zhang, "4 - GENERALIZED GOVERNING EQUATIONS FOR MULTIPHASE SYSTEMS: AVERAGING FORMULATIONS," in *Transport Phenomena in Multiphase Systems*, A. Faghri and Y. Zhang, Eds. Boston: Academic Press, 2006, pp. 238-330.

[137] O. Laguerre, S. B. Amara, and D. Flick, "Heat transfer between wall and packed bed crossed by low velocity airflow," *Applied thermal engineering,* vol. 26, no. 16, pp. 1951-1960, 2006.

[138] T. J. Hanrattry, "Nature of wall heat transfer coefficient in packed beds," *Chemical Engineering Science,* vol. 3, no. 5, pp. 209-214, 1954.

[139] E. Tsotsas and E.-U. Schlünder, "Heat transfer in packed beds with fluid flow: remarks on the meaning and the calculation of a heat transfer coefficient at the wall," *Chemical Engineering Science,* vol. 45, no. 4, pp. 819-837, 1990.

[140] Y. Yi, X. Bai, F. Kuwahara, and A. Nakayama, "Analytical and Numerical Study on Thermally Developing Forced Convective Flow in a Channel Filled with a Highly Porous Medium Under Local Thermal Non-Equilibrium," *Transport in Porous Media,* vol. 136, no. 2, pp. 541-567, 2021.

[141] M. Winterberg and E. Tsotsas, "Impact of tube-to-particle-diameter ratio on pressure drop in packed beds," *American Institute of Chemical Engineers. AIChE Journal,* vol. 46, no. 5, p. 1084, 2000.

[142] T. Eppinger, K. Seidler, and M. Kraume, "DEM-CFD simulations of fixed bed reactors with small tube to particle diameter ratios," *Chemical Engineering Journal,* vol. 166, no. 1, pp. 324-331, 2011.

[143] A. G. Dixon, "Heat transfer in fixed beds at very low (< 4) tube-to-particle diameter ratio," *Industrial & engineering chemistry research,* vol. 36, no. 8, pp. 3053-3064, 1997.

[144] I. Ansys, "ANSYS FLUENT theory guide," *Canonsburg, Pa,* vol. 794, 2019.

[145] Y. Sun, P. Causse, B. Benmokrane, and F. Trochu, "Permeability Measurement of Granular Porous Materials by a Modified Falling-Head Method," *Journal of Engineering Mechanics,* vol. 146, no. 9, p. 04020101, 2020/09/01 2020.

[146] W. Kingery, "Thermal conductivity: XIV, conductivity of multicomponent systems," *Journal of the American Ceramic Society,* vol. 42, no. 12, pp. 617-627, 1959.

[147] L. C. Thomas, "Modulated DSC paper# 9: Measurement of accurate heat capacity values," *TA Instruments, New Castle, DE,* 2005.

[148] K. Rasmussen, "Calculation methods for the physical properties of air used in the calibration of microphones," 1997.

[149] W. Sutherland, "LII. The viscosity of gases and molecular force," *The London, Edinburgh, and Dublin Philosophical Magazine and Journal of Science,* vol. 36, no. 223, pp. 507-531, 1893.

[150] U. Gaur, S. f. Lau, B. B. Wunderlich, and B. Wunderlich, "Heat capacity and other thermodynamic properties of linear macromolecules VI. Acrylic polymers," *Journal of Physical and Chemical Reference Data,* vol. 11, no. 4, pp. 1065-1089, 1982.

[151] B. E. Launder and D. B. Spalding, "The numerical computation of turbulent flows," *Computer Methods in Applied Mechanics and Engineering,* vol. 3, no. 2, pp. 269-289, 1974.

[152] A. Nakayama and F. Kuwahara, "A Macroscopic Turbulence Model for Flow in a Porous Medium," *Journal of Fluids Engineering,* vol. 121, no. 2, pp. 427-433, 1999.

[153] N. F. Jouybari, M. Maerefat, and M. E. Nimvari, "A macroscopic turbulence model for reacting flow in porous media," *Transport in Porous Media,* vol. 106, no. 2, pp. 355-381, 2015.

[154] K. Ando, H. Hirai, and Y. Sano, "An accurate experimental determination of interstitial heat transfer coefficients of ceramic foams using the single blow method," *Open Transport Phenomena Journal,* Article vol. 5, no. 1, pp. 7-12, 2013.

[155] J. A. Khan, D. E. Beasley, and B. Alatas, "Evaporation from a packed bed of porous particles into superheated vapor," *International journal of heat and mass transfer,* vol. 34, no. 1, pp. 267-280, 1991.

[156] S. Afandizadeh and E. A. Foumeny, "Design of packed bed reactors: guides to catalyst shape, size, and loading selection," *Applied Thermal Engineering,* vol. 21, no. 6, pp. 669-682, 2001/04/01/ 2001.

[157] S. Kuo and C. Tien, "Heat transfer augmentation in a foam-material filled duct with discrete heat sources," in *InterSociety Conference on Thermal Phenomena in the Fabrication and Operation of Electronic Components. I-THERM'88,* 1988, pp. 87-91: IEEE.

[158] N. Seto, K. Yuki, H. Hashizume, and A. Sagara, "Heat transfer enhancement in sphere-packed pipes under high Reynolds number conditions," *Fusion Engineering and Design,* vol. 83, no. 7-9, pp. 1102-1107, 2008.

[159] W. Shao *et al.*, "Experimental and numerical measurements of the channel packed with disordered cement granules regarding the heat transfer performance," *Applied Energy,* vol. 251, p. 113244, 2019.

[160] P. Dhiman, N. Thakur, A. Kumar, and S. Singh, "An analytical model to predict the thermal performance of a novel parallel flow packed bed solar air heater," *Applied energy,* vol. 88, no. 6, pp. 2157-2167, 2011.

[161] H. Peng, R. Li, X. Ling, and H. Dong, "Modeling on heat storage performance of compressed air in a packed bed system," *Applied energy,* vol. 160, pp. 1-9, 2015.

[162] M. Vilarrubí *et al.*, "Experimental and numerical study of micro-pin-fin heat sinks with variable density for increased temperature uniformity," *International Journal of Thermal Sciences,* vol. 132, pp. 424-434, 2018.

[163] C. Leng, X.-D. Wang, T.-H. Wang, and W.-M. Yan, "Optimization of thermal resistance and bottom wall temperature uniformity for double-layered microchannel heat sink," *Energy Conversion and Management,* vol. 93, pp. 141-150, 2015.

[164] S. P. Jang and S. U. Choi, "Cooling performance of a microchannel heat sink with nanofluids," *Applied Thermal Engineering,* vol. 26, no. 17-18, pp. 2457-2463, 2006.

[165] P. Mashaei and M. Shahryari, "Effect of nanofluid on thermal performance of heat pipe with two evaporators; application to satellite equipment cooling," *Acta Astronautica,* vol. 111, pp. 345-355, 2015.

[166] A. Bayomy, M. Saghir, and T. Yousefi, "Electronic cooling using water flow in aluminum metal foam heat sink: Experimental and numerical approach," *International Journal of Thermal Sciences,* vol. 109, pp. 182-200, 2016.

[167] Z. Tian *et al.*, "Code development and analysis on the operation of liquid metal high temperature heat pipes under full condition," *Annals of Nuclear Energy,* vol. 160, p. 108396, 2021/09/15/ 2021.

[168] C. Wang, D. Zhang, S. Qiu, W. Tian, Y. Wu, and G. Su, "Study on the characteristics of the sodium heat pipe in passive residual heat removal system of molten salt reactor," *Nuclear Engineering and Design,* vol. 265, pp. 691-700, 2013/12/01/ 2013.

[169] Z. Guo, Z. Sun, N. Zhang, M. Ding, and J. Wen, "Experimental characterization of pressure drop in slender packed bed (1< D/d< 3)," *Chemical Engineering Science,* vol. 173, pp. 578-587, 2017.

[170] M. Cascetta, F. Serra, S. Arena, E. Casti, G. Cau, and P. Puddu, "Experimental and numerical research activity on a packed bed TES system," *Energies,* vol. 9, no. 9, p. 758, 2016.

[171] M. Behnam, A. G. Dixon, M. Nijemeisland, and E. H. Stitt, "A New Approach to Fixed Bed Radial Heat Transfer Modeling Using Velocity Fields from Computational Fluid Dynamics Simulations," *Industrial & Engineering Chemistry Research,* vol. 52, no. 44, pp. 15244-15261, 2013/11/06 2013.

[172] A. Tongkratoke, A. Pramuanjaroenkij, A. Chaengbamrung, and S. Kakac, "Development of mathematical modeling for nanofluids as porous media in heat transfer technology," *Heat Pipe Science and Technology, An International Journal,* vol. 7, no. 1-2, 2016.

[173] B. Guo, A. Yu, B. Wright, and P. Zulli, "Simulation of turbulent flow in a packed bed," *Chemical Engineering & Technology: Industrial Chemistry‐Plant Equipment‐Process Engineering‐Biotechnology,* vol. 29, no. 5, pp. 596-603, 2006.

[174] K. Eiermann and K. x. Hellwege, "Thermal conductivity of high polymers from− 180° C. to 90° C," *Journal of Polymer Science,* vol. 57, no. 165, pp. 99-106, 1962.

[175] P. Wellinger, P. Uhl, B. Weigand, and J. Rodriguez, "Analysis of turbulence structures and the validity of the linear Boussinesq hypothesis for an infinite tube bundle," *International Journal of Heat and Fluid Flow,* p. 108779, 2021.

[176] S. Das, N. G. Deen, and J. A. M. Kuipers, "A DNS study of flow and heat transfer through slender fixed-bed reactors randomly packed with spherical particles," *Chemical Engineering Science,* vol. 160, pp. 1-19, 2017/03/16/ 2017.

[177] X.-L. Ouyang, P.-X. Jiang, and R.-N. Xu, "Thermal boundary conditions of local thermal non-equilibrium model for convection heat transfer in porous media," *International journal of heat and mass transfer,* vol. 60, pp. 31-40, 2013.

[178] Y. Ding, W. K. Chiu, and X. L. Liu, "Numerical investigation on thermal response of oil-heated tool for manufacture of composite products," *Composite Structures,* vol. 47, no. 1, pp. 491-495, 1999/12/01/ 1999.

[179] R. Abdalrahman, S. Grove, A. Kyte, and M. J. Rizvi, "Numerical simulation and design optimisation of an integrally-heated tool for composite manufacturing," *Materials & Design*, vol. 64, pp. 477-489, 2014/12/01/ 2014.

[180] S. C. Chen, H. S. Peng, J. A. Chang, and W. R. Jong, "SIMULATIONS AND VERIFICATIONS OF INDUCTION HEATING ON A MOLD PLATE," *International Communications in Heat and Mass Transfer*, vol. 31, no. 7, pp. 971-980, 2004/10/01/ 2004.

[181] J. Collomb, P. Balland, P. Francescato, Y. Gardet, D. Leh, and P. Saffré, "Thermomechanical Optimization and Comparison of a Low Thermal Inertia Mold with Rectangular Heating Channels and a Conventional Mold," *Advances in Materials Science and Engineering*, vol. 2019, p. 3261972, 2019/05/02 2019.

[182] "Mould tool heating – the oven-free alternative," *Reinforced Plastics*, vol. 47, no. 11, pp. 38-41, 2003/12/01/ 2003.

[183] Y. Sun, C. Béguin, P. Causse, B. Benmokrane, and F. Trochu, "Convective Heat Transfer between a Bead Packing and its Bounding Wall: Part I - Theory (under review)," *Transport in Porous Media*, 2021.

[184] J. Collomb, P. Balland, P. Francescato, Y. Gardet, D. Leh, and P. Saffré, "Thermo-mechanical simulations for the comparison of heating channels geometries for composite material injection tools," *Applied Thermal Engineering*, vol. 126, pp. 204-211, 2017/11/05/ 2017.

[185] P. Bere, C. Neamtu, and R. Udroiu, "Novel Method for the Manufacture of Complex CFRP Parts Using FDM-based Molds," *Polymers*, vol. 12, no. 10, 2020.

[186] R. Abdalrahman, S. Grove, A. Kyte, and M. J. Rizvi, "Numerical simulation and experimental verification of heating performance of an integrally water-heated tool," *Journal of Reinforced Plastics and Composites*, vol. 35, no. 8, pp. 671-687, 2016/04/01 2016.

[187] Y. Ding, W. K. Chiu, X. L. Liu, and B. Whittingham, "Modelling of thermal response of oil-heated tools due to different flow rates for the manufacture of composite structures," *Composite Structures*, vol. 54, no. 4, pp. 477-488, 2001/12/01/ 2001.